Error-Induced Beam Degradation in Fermilab's Accelerators

by

Sung-Yong Phil Yoon

Submitted in Partial Fulfillment

of the

Requirements for the Degree

Doctor of Philosophy

Supervised by

Professor Arie Bodek

Doctor Weiren Chou

Department of Physics and Astronomy

The College

Arts and Sciences

University of Rochester

Rochester, New York

2008

Curriculum Vitae

The dissertation author was born in Seoul, Republic of Korea. He studied at the State University of New York at Stony Brook and received the Bachelor of Arts degree in physics in 1999. He enrolled in graduate school in the Department of Physics and Astronomy at University of Rochester in the Fall of 1999 and began graduate studies in physics. He was supported in part by the GAAAN Fellowship from the U.S. Department of Education during his first three years of study. After receiving the Master of Arts degree in 2001, he enrolled in the Joint University-Fermilab PhD Program in Accelerator Physics to pursue his doctoral research in high-energy/high-intensity particle accelerators under the supervision of Professor Arie Bodek of University of Rochester and Doctor Weiren Chou of Fermilab.

Acknowledgments

There are a number of people whom I would like to thank throughout my Ph.D. graduate program. My apologies first to those who I inadvertently fail to list on this page.

First and foremost, I am grateful to Prof. Arie Bodek and the staff members of the physics and astronomy department at University of Rochester. They have provide continuous support throughout my graduate program. In particular, I would like to thank Prof. Bodek for serving as a home-institution advisor and Ms. Barbara Warren and Ms. Sue Brightman at the department for having well taken care of all administrative work for me. As a result, this doctoral dissertation can be published.

Along with two dissertation co-advisors, three other faculty members from different branches of physics constituted the Ph.D. committee: Prof. W. Schröder (physics and chemistry), Prof. A. Bodek (experimental particle physics), Dr. W. Chou (accelerator physics), Prof. M. Alonso (optics), and Prof. A. Jordan (theoretical condensed matter). I would like to thank them for their valuable time and efforts.

I would also like to thank the committee members of the University-Fermilab joint Ph.D. program in Accelerator Physics: Dr. R. Rubinstein at Fermilab Directorate, Dr. M. Syphers of the Accelerator Division Headquarters, and all the other program committee members. They have maintained the Accelerator Physics Ph.D. program for the past years. At the time of my application, there were a few people who helped me enroll in the University-Fermilab joint Ph.D. program in one way or another. I would also like to express my gratitude to Dr. R. Tesarek, Dr. W. C. Chang and Dr. L. H. Li, and Prof. L. Orr. Thanks to their help, this dissertation in accelerator physics has come into existence.

Throughout my work on the Booster modeling, I have interacted with most of the staff members in Fermilab Booster group: Mr. R. Tomlin, Mr. J. Lackey, Dr. F. Garcia, Mr. T. Sullivan, and Mr. W. Pellico. Dr. E. Prebys, head of the proton source department, scheduled my presentations on the Booster modeling at Budker seminars for the past years.

Since the very first draft of my dissertation was around, both Prof. Bodek and Dr. Chou have made time-consuming efforts to revise and edit every draft line by line and word by word. Through their help, all the draft versions have been molded and shaped into the present version.

Abstract

In Part I, three independent models of Fermilab's Booster synchrotron are presented. All three models are constructed to investigate and explore the effects of unavoidable machine errors on a proton beam under the influence of space-charge effects.

The first is a *stochastic noise model*. Electric current fluctuations arising from power supplies are ubiquitous and unavoidable and are a source of instabilities in accelerators of all types. A new noise module for generating the Ornstein-Uhlenbeck (O-U) stochastic noise is first created and incorporated into the existing Object-oriented Ring Beam Injection and Tracking (ORBIT-FNAL) package. After being convinced with a preliminary model that the noise, particularly non-white noise, does matter to beam quality, we proceeded to measure directly current ripples and common-mode voltages from all four Gradient Magnet Power Supplies (GMPS). Then, the current signals are Fourier-analyzed. Based upon the power spectra of current signals, we tune up the Ornstein-Uhlnbeck noise model. As a result, we are able to closely match the frequency spectra between current measurements and the modeled O-U stochastic noise. The stochastic noise modeled upon measurements is applied to the Booster beam in the presence of the full space-charge effects. This noise model, accompanied by a suite of beam diagnostic calculations, manifests that the stochastic noise, impinging upon the beam and coupled to the space-charge effects, can substantially enhance the beam degradation process throughout the injection period.

The second model is a *magnet misalignment model*. It is the first time to utilize the latest beamline survey data for building a *magnet-by-magnet* misalignment model. Given as-found survey fiducial coordinates, we calculate all types of magnet alignment errors (station error, pitch, yaw, roll, twists, etc.) are implemented in the model. We then follow up with statistical analysis to understand how each type of alignment errors are currently distributed around the Booster ring. The ORBIT-FNAL simulations with space charge

included show that rolled magnets, in particular, have substantial effects on the Booster beam. This survey-data-based misalignment model can predict how much improvement in machine performance can be achieved if prioritized or selected realignment work is done. In other words, this model can help us investigate different realignment scenarios for the Booster. In addition, by calculating average angular kicks from all misaligned magnets, we expect this misalignment model to serve as guidelines for resetting the strengths of corrector magnets.

The third model for the Booster is a *time-structured multi-turn injection model*. Microbunch-injection scenarios with different time structures are explored in the presence of longitudinal space-charge force. Due to the radio-frequency (RF) bucket mismatch between the Booster and the 400-MeV transferline, RF-phase offsets can be parasitically introduced during the injection process. Using the microbunch multiturn injection, we carry out ESME-ORBIT-combined simulations. This combined simulation allows us to investigate realistic charge-density distribution under full space-charge effects. The growth rates of transverse emittances turned out to be 20 % in both planes. This microbunch-injection scenarios is also applicable to the future 8-GeV Superconducting Linac Proton Driver and the upgraded Main Injector at Fermilab.

In Part II, the feasibility of momentum-stacking method of proton beams is investigated. When the Run2 collider program at Fermilab comes to an end around year 2009, the present antiproton source can be available for other purposes. One possible application is to convert the antiproton accumulator to a proton accumulator, so that the beam power from the Main Injector could be enhanced by a factor of four. Through adiabatic processes and optimized parameters of synchrotron motion, we demonstrate with an aid of the ESME code that up to four proton batches can be stacked in the momentum acceptance available for the Accumulator ring. This momentum-stacking method is expected to be a part of Fermilab's SuperNuMI (SNuMI) project.

Contents

List of Tables

List of Figures

Chapter 1

Introduction

> *dixitque Deus fiat lux et facta est lux*
>
> -Genesis 1:3

The subject of this dissertation[1] is the investigation of enhanced beam degradation phenomena in Fermilab's Booster Synchrotron and Accumulator Storage Ring. Enhancement of beam degradations, caused by unavoidable machine[2] imperfections coupled to space charge are simulated using four independent models including three Booster models and one Accumulator model. This introductory chapter provides a synopsis of our work on modeling of error-induced beam degradation phenomena in present and future accelerators at Fermilab. Fermilab's accelerator and computing facilities are extensively used in this work.

1.1 Motivations

Advanced computational tools for the realistic modeling and reliable simulation of particle accelerators are needed for:

---

[1] This dissertation is created by TeX kpathsea version 3.4.5.

[2] We refer to an accelerator as a machine in this dissertation.

(1) Lattice[3] designs for future accelerators.

(2) Investigation of various operating scenarios with different parameters for present and future machines.

(3) Investigation of beam instabilities and the adverse effects of machine-imperfections.

In all three applications, cost savings are realized through the better understanding and predictive power that are provided by modeling tools. More realistic modeling and simulation are now possible through recent advances in computer technology, such as Message-Passing Interface (MPI) [1] for multiprocessor applications.

In order to explore and understand the effects of known machine errors on a beam, the following four models are investigated:

(1) Stochastic noise model (for the Booster).

(2) Misalignment model (for the Booster).

(3) Time-structured multiturn injection model (for the Booster).

(4) Momentum-stacking model (for the Proton Accumulator).

The above-mentioned four accelerator models are motivated by accelerator physics issues that affect current machine performance at Fermilab.

Booster Models: The accelerator physics mechanisms in the Booster that result in beam losses at injection are of great importance. Beam losses in the Booster mostly occur during the first $2 \sim 3$ msec of the machine cycle, and space-charge effects contribute to these losses. However, given the operational beam intensity and injection energy, space-charge effects alone cannot entirely account for the large beam losses. In our models, it is demonstrated that other factors couple to space-charge effects, and together are responsible for the large beam-losses in the Booster. These other factors include stochastic fluctuations

---

[3] Lattice refers to a repetitive pattern of bending (dipole) and focusing (quadrupole) magnets in an accelerator.

arising from noise in power supplies and misaligned beamline elements, and RF[4]-bucket mismatch during the multiturn injection process.

Accumulator Model: The proton accumulator ring[5] is under consideration as one of the options for a future accelerator upgrade at Fermilab. This upgrade is to take place after the termination of the Run 2 collider program around the year 2009. The accumulator upgrade calls for stacking multiple batches of the Booster proton beam in the present Antiproton Accumulator ring using the RF-stacking method. Using the momentum-stacking method, a factor of four increase in the Fermilab Main Injector beam intensity could be achieved (even in the presence of longitudinal space-charge effects).

1.2 Methodology

1.2.1 Computational Modeling Tools

We investigate the consequence of error-induced beam degradation in two Fermilab accelerators: the Booster synchrotron and the Accumulator ring. Our computational modeling involves multiparticle tracking in each ring. The macroparticles [6] are tracked in a self-consistent manner in six-[7], or two[8]-dimensional phase spaces in the presence of longitudinal (1-D), or transverse (2-D), or full (3-D) space-charge forces. The simulation yields various beam parameters such as particle distributions and the evolution of beam emittance. We use the ORBIT-FNAL package and ESME code in the modeling of the beams.

---

[4] RF stands for Radio Frequency, used interchangeably with the term high frequency in accelerator physics context.

[5] In this context, we refer to a circular-type accelerator as a ring.

[6] In practice, it is not feasible to simulate and track the same number of particles as in actual machine operation. As such, we use macroparticles, each of which represents some fraction of total charge in a machine.

[7] including both transverse and longitudinal phase space dimensions

[8] including longitudinal phase space only

The Object-oriented Ring Beam Injection and Tracking (ORBIT) [2], a three-dimensional C^{++} computer package, has been developed by the accelerator physics group of the Spallation Neutron Source (SNS) at Oak Ridge National Laboratory (ORNL). The ORBIT-FNAL code is a Fermilab version of ORBIT that has been developed for application to Fermilab accelerators. During the course of modeling the Booster with the ORBIT-FNAL package, various new features and methods have been developed and implemented. The one-dimensional code ESME [3], authored by J. MacLachlan of Fermilab, is mainly designed for modeling RF gymnastics and longitudinal beam dynamics. In our simulations, the Booster lattice [9] and machine parameters including space-charge forces are all used in the stochastic noise model, the misalignment model, and a multiturn injection model.

1.2.2 Booster: Stochastic Noise Model

For the stochastic noise model for the Booster, we first designed and added a new noise module to the ORBIT-FNAL package. This noise module can generate Ornstein-Uhlenbeck stochastic noise, employing the Ornstein-Uhlenbeck (O-U hereafter) stochastic process [4] and the Langevin-like stochastic differential equation [5]. In the first stage of modeling, we simulate various parameters, including space-charge effects, to find out if dynamic (time-dependent) noise has any adverse influence on the Booster beam at the time of injection. The results from this initial model [6] simulation demonstrate that dynamic noise, combined with the space-charge effects, leads to an enhancement in beam degradation in the Booster. Moreover, our preliminary findings are consistent with what was found earlier from an idealized and simplified model [7] of collective space-charge modes coupled with dynamic noise. As we are certain that there is noise in the Booster Gradient Magnet Power

---

[9] The term Lattice refers to the repetitive pattern of bending (dipole) and focusing (quadrupole) magnets in an accelerator

Supply (GMPS)[10] system, we proceed to devise methods for measurement and analysis of ripples in the electric current[11] in the Booster GMPS. Repeated measurements and analyses confirm that a substantial amount of noise is present in the GMPS system. We are also able to extract stochastic noise parameters by a Fourier-analysis of our measurements. The new noise module with stochastic noise parameters now can model and generate realistic power-supply noise that can be applied to the Booster beam in the presence of space-charge. Our stochastic noise model is the first simulation of the effects of noise (modeled on noise measurements) on a beam in a real synchrotron over a long period of time. For more realistic beam simulations, we inject and track 330,000 macroparticles with the new noise module fully parallelized on several dozen processor nodes in local workstation clusters.

We conclude that when noise is combined with space-charge effects, synergism between noise and machine errors induces enhancements in beam degradation in the Booster, thus resulting in beam losses.

Figure 1.1 illustrates the processes involved in modeling Booster power-supply noise.
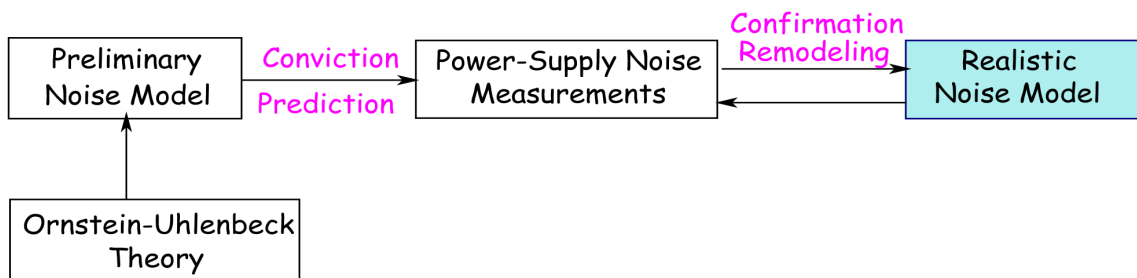
Figure 1.1: Modeling the effect of noise arising from the Booster power supply

---

[10] We often refer to the Booster Gradient Magnet Power Supply (GMPS) of the Booster as just plain Power Supply for convenience.

[11] A more technical term for this kind of noise is electromagnetic interference.

1.2.3   Booster: Misalignment Model

In constructing the Booster misalignment model, we employ the latest survey data [8, 9], and investigate the effect of each type of alignment error. It is the first time that the latest magnet survey data is used in modeling the Booster. This is done in collaboration with the Fermilab Survey and Alignment Geodesy (SAG) Group. In general, during the design stage of an accelerator, the required tolerance of magnet alignment error is determined by modeling and simulation. Since we are working on modeling misalignment for the existing Booster machine (with the latest magnet survey data at hand), we proceed to construct a magnet-by-magnet alignment model. Given the coordinates of survey fiducial points, we first calculated the magnitudes[12] and orientations[13] of each type of alignment error at each individual magnet. We then perform a statistical analysis to determine which type of alignment errors are presently present in the Booster ring. After obtaining a good understanding of the present distributions of all types of alignment errors in the Booster magnet system, we upgrade the Error module of the ORBIT-FNAL accordingly. By including the magnet-by-magnet alignment errors in the code, the ORBIT-FNAL is now capable of simulating Booster alignment errors. To achieve the best accuracy, our model treats each magnet individually (i.e. there are no identical magnets in our misalignment model). Consequently, this survey-data-based alignment model can now predict the improvement in machine performance that can achieved if some fraction of total magnets in the Booster ring are realigned. Since a complete realignment is very time consuming, our misalignment model can be used to prioritize which magnets should be corrected first in a magnet realignment effort.

---

[12] for translational alignment errors

[13] for rotational alignment errors

Our studies with the misalignment model indicate that in particular, misalignments of rolled combined-function magnets[14] have a sizeable effect on the beam (in the presence of space-charge effects at injection energy).

Figure 1.2 in the following page illustrates how the misalignment modeling has been implemented.

Raw Survey Data
as-found survey measurements
of fiducial-point coordinates

• Transverse-error calculations
• Rotational-error calculations

• Statistical Calculations (mean and rms)
  from distributions of each type of errors.

Ringwide Error Distribution
68 % CL Exclusion

Angular Kick Calculations
(for new corrector settings)

3-D ORBIT FNAL
(numerical calculations)

• beam diagnostic calculations
• SC simulations with partially
  realigned magnets.
  (realignment scenario)

Figure 1.2: Modeling of the Booster Magnet Misalignment

1.2.4 Booster: Time-Structured Multiturn-Injection Model

In the Booster microbunch model, multiturn-injection methods with a train of microbunches are explored in the presence of longitudinal space-charge effects. This modeling is carried out with the aid of the ESME code. First, one microbunch is generated, and

---

[14]A combined-function magnet is for both bending and focusing charged-particle beams.

then a train of four or five microbunches are injected into a synchronous RF bucket[15] at different times.[16] The synchronous injection is repeated over 11 injection turns with a certain amount of phase shift. Because of the RF-bucket mismatch between the 400-MeV transfer line and the Booster ring, uncontrolled phase shifts can be induced during the injection process. The ESME simulation with this microbunch-injection model demonstrates that there is no significant longitudinal beam loss for each injection method. Since this injection method is for a linac-to-ring transition, we can speculate that this microbunch-injection method can also be applied to the injection method for a future 8-GeV-linac proton driver and an upgraded Main Injector.

1.2.5   Proton Accumulator: Momentum-Stacking Model

Here we model a future proton Accumulator at Fermilab. In order to maximize the proton beam intensity, proton pulses from the Booster can be debunched and accumulated within the momentum acceptance of the Proton Accumulator ring. In the process of optimizing the desired performance of a Proton Accumulator, it is crucial to minimize the emittance dilution that originates from longitudinal space-charge forces. This is accomplished by finding optimal synchrotron parameters.

The momentum-stacking model, including longitudinal space-charge effects, demonstrates that up to four unbunched proton batches injected from the Booster can be stacked up within the momentum acceptance of the present Antipoton-Accumulator ring.

Therefore, proton stacking can be used in the present Antiproton-Accumulator ring, and it can be used as a Proton-Accumulator in a future Fermilab upgrade. An outline of the proton-stacking process is illustrated in Figure 1.3.

---

[15] a standing RF bucket

[16] at different phase ($\Delta\theta$). Common coordinates in longitudinal phase space are (θ, $\Delta E/\omega_0$). The azimuthal angle for an entire ring is 2π. The phase (θ) coordinate can be converted to a time coordinate.

Figure 1.3: Proton-stacking cycle

1.3 Dissertation Layout

The dissertation consists of two parts. In part I we focus on the three Booster models: (1) stochastic noise model, (2) misalignment model, and (3) multiturn injection model with microbunches. The measurement-based stochastic noise model is discussed in chapters 2, 3 and 4. The implementation and inclusion of the Ornstein-Uhlenbeck stochastic noise model into the new noise module is presented in chapter 2. The experimental techniques of measuring noise in the Booster power supplies are discussed in chapter 3. The ramifications of the presence of real noise coupled to space-charge effects are discussed in chapter 4. The misalignment model utilizing the most up-to-date survey data for each individual gradient magnet is discussed in chapters 5 and 6. The multiturn injection model with microbunches is discussed in chapter 7. The modeling of the Proton Accumulator ring is presented in Part II. We investigate the feasibility of the proposed momentum-stacking method of proton beams for the Accumulator as one of the choices for a future accelerator-upgrade plans at Fermilab. The content of various chapters are illustrated in the block diagram of Figure 1.4.

Figure 1.4: The synoptic view of dissertation organization

1.4   The Fermilab Accelerator Complex

The Fermilab accelerator complex consists of seven accelerators including the Electrostatic Pre-accelerator, the Proton Linear Accelerator (Linac) , the 8-GeV Booster synchrontron, the Main Injector synchrontron, the Tevatron synchrontron, the Proton Accumulator ring, and the Debuncher. The accelerator complex also includes the Switchyard and a number of beamlines. In this dissertation we only model the Booster and the Proton Accumulator. These two accelerators are reviewed in the next two sub-sections.

1.4.1   Booster Synchrotron

Overview

The 8-GeV Booster synchrotron is the very first synchrotron in this chain of accelerators. As necessary, additional details on specific systems of the Booster are described in the next few chapters in Part I. Here, we introduce the main features of the Booster.

The Booster [10] is a rapid-cycling, 15-Hz alternating-gradient synchrotron with a mean radius of 75.47 meters. A 400-MeV beam-line transfers the proton beam from the Linac to the Booster. the beam is bent down vertically to a level of 15 feet below ground. The Booster lattice is composed of 24-fold superperiods [11]. Each period (or magnet cell) consists of four 10-foot long combined-function magnets, which serve both as bending magnets and as main gradient magnets. There are a total of 96 main gradient magnets. The combined-function magnets both focus and bend the beam around the design orbit. The 18 RF ferrite-tuned cavity[17] resonators, located in several long straight sections, are used to accelerate and to longitudinally focus a beam over the 33-msec ramping portion of a sinusoidal current waveform.

---

[17] The term ferrite refers to variable permeability materials for fast-tuned cavities. The ferrite-tuned cavities are used when varying resonance frequencies are needed to follow the varying revolution frequency of the beam.

For the magnet system, a resonator power-supply system utilizes a 15-Hz DC-biased sinusoidal current waveform to excite the main magnets which are connected in series. The multiturn injection system increases the Booster intensity by accumulating successive injection of Linac beams on top of each other. Proton beams at the extraction energy of 8.0 GeV can be extracted to two different locations: (1) to the Main Injector by way of the MI-8 transferline, and (2) to a beam dump in the MI-8 line. An aerial view of the Booster (which is located behind Wilson Hall) is shown in Figure 1.5 (a) [12].

(a) The Booster synchrotron

(b) The Accumulator ring

Figure 1.5: Aerial views

Injection [13–15]

All of the Booster models presented in this dissertation involve processes that occur during injection. Therefore, we include further details on the injection system into the Booster.

The extraction of H$^-$ ions at 400 MeV from the Linac begins after an area which is referred to as the *400-MeV area*—this area begins after the last Coupled-Cavity-Linac (CCL)[18] RF cavity that is powered by klystron[19] tank # 7.

As shown in Figure 1.6, the 400-MeV Linac beam can be directed into any of three beamlines at the end of the Linac enclosure. Linac beam pulses, not deflected by the 400-MeV chopper, are veered into one of two beam-dump lines: dump #1 and dump #2.
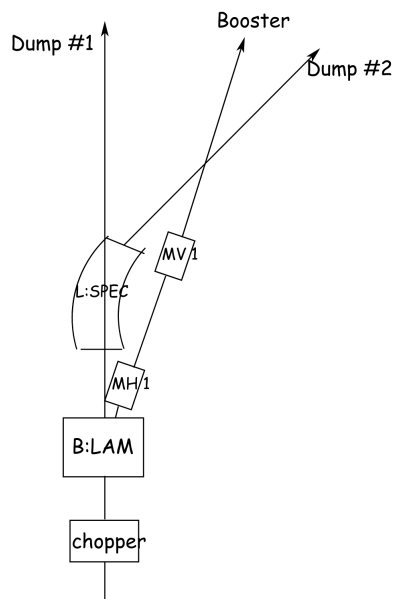
Figure 1.6: 400-MeV area

When the 40° spectrometer magnet (L:SPEC in Figure 1.6) is powered on, the beam is directed to *dump* #2, in which a wire scanner measures the beam momentum. This is used to display the average momentum and momentum spread in the beamline. On the other

---

[18] The Coupled-Cavity Linac (CCL) is a serial array of resonant cavities that are coupled together to form a multicavity accelerating structure. The CCL operates at a higher accelerating gradient for acceleration of beams. The velocity range is usually in the range of $0.4 < \beta < 1.0$. In 1993, the Fermilab linac was upgraded from an energy of 200 MeV to 400 MeV with the CCL in order to reduce the space-charge effects.

[19] A klystron is a high-gain radio-frequency amplifier.

(a) Wire Scanner; Corrector Package; ORBUMP 3

(b) 400-MeV Chopper

Figure 1.7: Instruments located in the 400-MeV area: *photo courtesy of the Booster group*

hand, when the spectrometer magnet is off, the beam is directed to dump #1. This transport line is used to measure the transverse emittances and is solely used for beam studies. The third transfer line brings the beam to to the Booster. The transfer line will be referred to in this dissertation as the *400-MeV Transferline* (or just the Transferline) leading to the Booster.

The aforementioned 400-MeV chopper (see Figure 1.7) is a pulsed electric deflector composed of a pair of parallel charged plates. It is located downstream of the last coupled-cavity-linac RF cavity. The chopper selects what portion of the beam enters the Booster, and is used to control the Booster, Main injector and Tevatron. The duration of chopper pulse determines the number of Booster turns that are used. For the normal mode of operation (e.g. antiproton production) and for NuMI [16, 17] operations, 11 turns of the Booster beam are used. The portion of the beam that is deflected by the chopper and quadrupoles, passes through the field region of a Lambertson magnet.

The final section of the 400-MeV line is designed for lattice-parameter matching. In the first part of the matching section, the transverse phase ellipse of the beam is rotated to achieve efficient injection. In order to make a FDOODF[20] configuration, seven quadrupoles are used in the matching section. Another device that is located in the phase matching section is a klystron-driven cavity which is called the Debuncher. The main function of the Debuncher is to reduce the momentum spread of the beam. Prior to the injection process, the Transferline lattice must be matched to that of the Booster.

Utilizing the last two quadrupoles[21] (B:Q16 and B:Q17) in the Transferline, the lattice match is fulfilled. These quadrupoles are replicas of the upstream lattice of long-straight section 1. The Q16 and Q17 are focusing and de-focusing quadrupoles, respectively. The duplicate quadrupoles are aligned with the main gradient magnets located just upstream of the injection location.

To reduce the peak current in the Linac, a multiturn injection method is used for Booster operation. Beams injected during the 11 injection turns are accumulated laterally in the Booster aperture.

The Transferline intersects the Booster ring at the injection girder. At the girder, a DC septum magnet, shown in Figure 1.8, eliminates the horizontal bend angle in the upstream. The H^- beam from the Linac is injected into the Fermilab Booster ring using a DC septum magnet and four pulsed magnets that cause a local *orbit-bump* (ORBUMP). The DC septum magnet bends the incoming H^- beam parallel to the circulating beam. The ORBUMP 1 and ORBUMP 2 magnets merge both incoming and circulating beams, after which they pass through a carbon stripping foil. The ORBUMP 3 and ORBUMP 4[22] restore the circulating orbit. The injected beam is then stacked on a trajectory lateral to the Booster

---

[20]By convention, F, D, and O represent a focusing magnet, a de-focusing magnet, and a drift section in which there is no magnetic field, respectively.

[21] These two quadrupoles are not shown in Figure 1.6

[22] At present, the 3-ORBUMP method is in use as in Figure 1.9 [14, 18]. The Figure 1.9 is created based upon one of J. Lackey's original drawings.
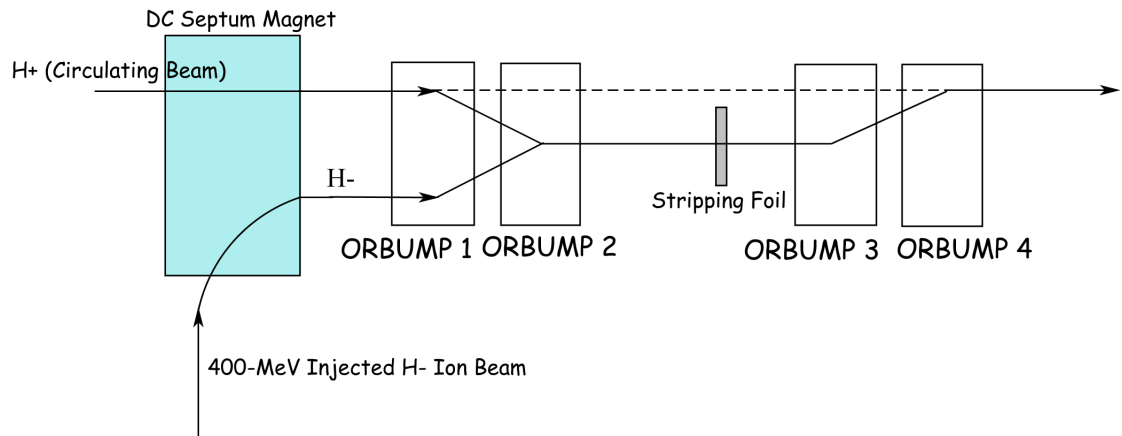
Figure 1.8: Injection layout of 4-ORBUMP method

closed orbit—radial separation is about 8 cm. The circulating beam transverses through the field-free region of the septum magnet without deflection. Both injected and circulating beams pass through the upstream ORBUMP magnets. As shown in Figure 1.8 these dipole magnets bend the circulating beam outward and the injected beam inward. Note that the injected beam carries negative charge (H^-), and the circulating beam positive charge (H^+). The injection trajectory places the beam on a carbon stripping foil located in between OR-BUMP magnets. While H^- ions and circulating beam pass through the stripping foil, both electrons of each H^- ion are stripped off, and the negative ions convert to protons. The downstream ORBUMP magnets then curve the proton beam radially inwards, or towards the closed orbit. The remaining unstripped H^- ions, or H^0 are directed outwards and end in the H^- detector: this process is termed *injection dump*. The beam from the Linac is injected into the Booster at the $45°$ [14] point (around the ring from the extraction point) which is located at long straight-section 3.
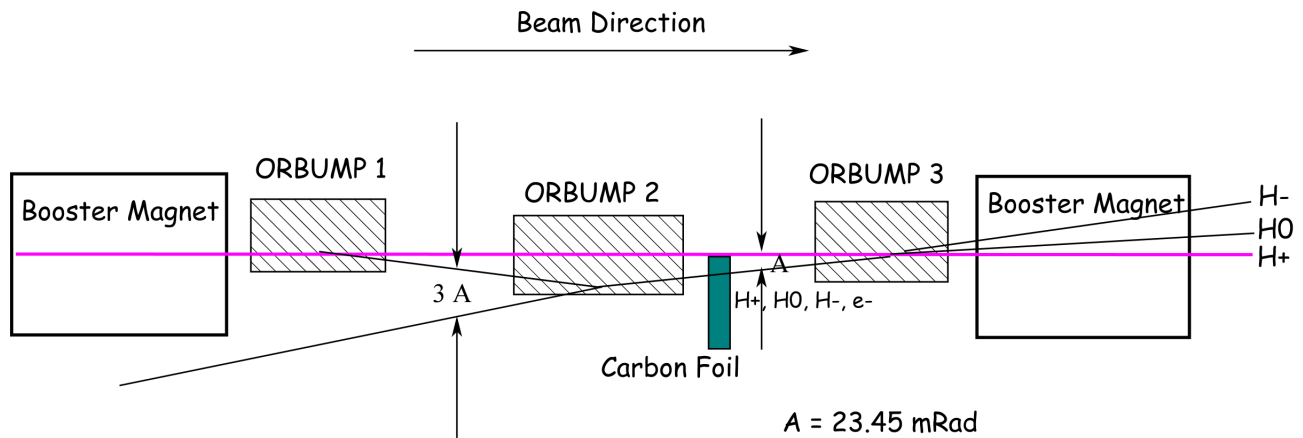
Figure 1.9: New injection layout of 3-ORBUMP method

1.4.2 Accumulator

The Accumulator is an antiproton source. It is a triangle-shaped storage ring for an-tiprotons as shown in Figure 1.5 (b). It is housed in the same radiation enclosure as the Debuncher, and its function is to accumulate antiprotons. Antiprotons are produced by di-recting a proton beam on to the p-bar[23] production target. The antiproton Accumulator is a DC (unbunched) machine with a large momentum acceptance. We find that it is possi-ble to accumulate several Booster proton batches in the present Antiproton-Accumulator ring. Therefore, it is possible to use the present Antiproton-Accumulator ring as a Proton-Accumulator for use in a future Fermilab upgrade. After the completion of this dissertation, the plans for a Fermilab upgrade now includes the Recycler[24] as illustrated by Figure 1.10.
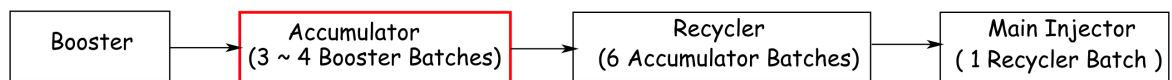
Figure 1.10: An updated Proton-stacking method

---

[23] We use the terms antiproton and p-bar interchangeably.

[24] As the Recycler is out of the scope of this dissertation, we do not discuss here.

Chapter 2

Booster Stochastic Noise Model

Make a joyful noise unto the Lord.

-Ps. 98:4, KJV

In this chapter we describe the design of a new stochastic noise module that is used for modeling noise[1] in the Booster power supply system. We first define stochastic processes and some of the associated concepts. We then introduce the Ornstein-Uhlenbeck (O-U) stochastic process. We follow with derivations of the statistical properties of the O-U process that are implemented in the new noise module for the ORBIT-FNAL package. We also describe how the new noise module generates the O-U stochastic noise and applies the modeled noise to macroparticles[2] in the simulation.

2.1 Motivation

Fluctuations that are observed in particle accelerator systems are expected as is common in other natural systems. Here we define a collection of charged particles as the *system*,

---

[1] In this context, we refer noise to electrical current fluctuations.

[2] In the context of the simulation of charged-particle beams, a macroparticle represents a fraction of total charge in an accelerator. We consider it to be a *representative* particle, or simulation particle.

and all the beamline components for accelerating and guiding particles as the *environment*. The system of charged particles then perceives the environment as a source of noise, or fluctuations. External noise[3] is intrinsic to particle accelerators due to unavoidable machine imperfections; e.g., electric current ripples in power supplies, ground vibration motion, etc. These noise sources have a significant impact on a beam. They cause a dilution of the beam emittance, formation of beam halo, and enhance beam losses. The physical noise is modeled as exponentially-driven Gaussian stochastic noise with the properties of the O-U process [4, 7, 26]. We select the O-U process for our investigations into the influence of external noise on the Booster beam.

2.2 Stochastic Process

A stochastic process[4] $\xi(t)$ is a process in which the variable ξ does not depend on the independent variable t in a predictable fashion. Here, $\mathcal{W}(\xi t)$ represents a *probability density function*. A stochastic process is completely defined by the following set of probability distributions:

- $\mathcal{W}_1(\xi, t)d\xi$: probability of finding ξ in the range of $(\xi, \xi + d\xi)$ at time t

- $\mathcal{W}_2(\xi_1, t_1; \xi_2, t_2)\, d\xi_1 d\xi_2$: joint probability of finding ξ in the range $(\xi_1, \xi_1 + d\xi_1)$ at time t_1 and in the range $(\xi_2, \xi_2 + d\xi_2)$ at time t_2.

- … … …

- $\mathcal{W}_n(\xi_1, t_1; \xi_2, t_2; \ldots; \xi_n, t_n)d\xi_1 d\xi_2 d\xi_3 \ldots d\xi_n$: joint probability of finding a series of values of ξ in the ranges $d\xi_1, d\xi_2, d\xi_3, \ldots, d\xi_n$ at times $t_1, t_2, t_3, \ldots, t_n$.

---

[3] External noise means fluctuations generated by a stochastic (random) process. The stochastic properties of random force are well understood.

[4] In this dissertation, we interchangeably use the terms stochastic process, stochastic function, random process, random function, and process.

The above functions should also obey the following conditions:

- $\mathcal{W}_n' \geqslant 0$

- $\mathcal{W}_n(\xi_1, t_1; \xi_2, t_2; \ldots ; \xi_n, t_n)$ is a symmetric function.[5]

- $W_k(\xi_1, t_1; \ldots ; \xi_k, t_k) = \int \ldots \int d\xi_{k+1} \ldots d\xi_n W_n(\xi_1, t_1; \ldots ; \xi_n, t_n)$, where $k < n$.

2.2.1 Pure Stochastic Processes

A pure stochastic process occurs when two successive processes are not correlated at all as shown in Eqn. (2.1). This implies that a pure process is a stochastic process without memory. Pure processes are primarily used in mathematical models and are not typical in the physical world.

$$\mathcal{W}_2(\xi_1, t_1 ; \xi_2, t_2) = \mathcal{W}_1(\xi_1, t_1) \cdot \mathcal{W}_1(\xi_2, t_2) \tag{2.1}$$

2.3 Langevin Equation

In 1905, the theory of the Brownian movement was first formulated by Einstein and Smoluchowski [19, 20]. In 1908, P. Langevin introduced the concept of the equation of motion of a stochastic variable (i.e. the position coordinate of a Brownian particle). The Langevin equation [5] was the first example of a stochastic differential equation.[6] Langevin writes the equation of motion for a Brownian particle according to Newton's second law

---

[5] For a symmetric function the value of the function does not change with an interchange of two of its arguments: $f(a, b) = f(b, a)$

[6] A stochastic differential equation is a differential equation with a stochastic (random) term. Therefore, its solution is also a random function.

with the assumption that a Brownian particle is subject to two forces.

$$m \frac{d^2x(t)}{dt^2} = \underbrace{-\zeta \frac{dx(t)}{dt}}_{\text{systematic force: dissipation}} + \underbrace{\mathcal{F}(t)}_{\text{stochastic force: fluctuation}} \quad (2.2)$$

Here, m, x, and ζ represent the particle mass, displacement, and the friction coefficient, respectively. The first term $(-\zeta \dot{x}(t)^7)$ on the right-hand side of Eqn. (2.2) represents the viscous drag as a function of time, or dynamic friction. The second term $\mathcal{F}(t)$ represents fluctuations which could be from white noise, or non-white noise[8]. Since we model physical noise, *non-white* noise, or *off-white* noise is used in our investigation. The following assumptions are made about the fluctuation part $\mathcal{F}(t)$:

(1) $\mathcal{F}(t)$ is a function of time only, and independent of $x(t)$.

(2) The variation rate of $\mathcal{F}(t)$ is much faster than the velocity of a Brownian particle, $dx(t)/dt$.

(3) $\langle \mathcal{F}(t) \rangle = 0$

The expressions above define the statistical properties of $\mathcal{F}(t)$. There is a great advantage in using Langevin equation instead of using the more complex Fokker-Plank Equation (FPE).[9] The Langevin's method is much easier to understand than the FPE since it is based upon the time evolution of a stochastic variable, whereas the FPE applies to the time evolution of the probability distribution. As such, Langevin equation allows us to forgo the

---

[7] The notations, $\dot{x}$ and $\ddot{x}$, denote dx/dt and d^2x/dt^2, respectively.

[8] *White noise* is noise with a flat frequency spectrum.

[9] The probability density function is not conserved in the presence of stochastic force, so we can use the Fokker-Plank Equation for a Brownian particle as follows:

$$\frac{\partial \mathcal{P}(\xi, t)}{\partial t} = \alpha \frac{\partial (\xi \mathcal{P})}{\partial \xi} + \mathcal{D} \frac{\partial^2 \mathcal{P}}{\partial \xi^2},$$

where $\mathcal{P} = \mathcal{P}(\xi, t)$, α is an average drift-velocity constant, and $\mathcal{D}$ is a diffusion constant.

calculation of the diffusion coefficient, thus reducing mathematical complexity. In summary, Langevin equation allows us to build an effective but far more simplified model for the Booster power-supply noise.

2.4 Markov Processes

Markov processes involve the use of *conditional probability*. We define the conditional probability $\mathcal{P}(\xi_1 \mid \xi_2, t)d\xi_2$ as the *probability* that given ξ_1 one can find ξ in the range $(\xi_2, \xi_2 + d\xi_2)$ at time t later.

$$\mathcal{W}_2(\xi_1, \xi_2, t) = \mathcal{W}_1(\xi_1)\mathcal{P}_2(\xi_1 \mid \xi_2, t) \tag{2.3}$$

In general, the following conditions need to be satisfied:

$$\left.\begin{array}{r}
\mathcal{P}_2(\xi_1 \mid \xi_2, t) \geqslant 0 \\[4pt]
\displaystyle\int d\xi_2 \mathcal{P}_2(\xi_1 \mid \xi_2, t) = 1 \\[4pt]
\mathcal{W}_1(\xi_2) = \displaystyle\int \mathcal{W}_1(\xi_1)\mathcal{P}_2(\xi_1 \mid \xi_2, t)\, d\xi_1
\end{array}\right\} \tag{2.4}$$

Accordingly, the Markov process is defined as follows [21]:

$$\mathcal{P}_n(\xi_1\, t_1, \xi_2\, t_2, \ldots, \xi_{n-1}\, t_{n-1} \mid \xi_n\, t_n) = \mathcal{P}_2(\xi_{n-1}\, t_{n-1} \mid \xi_n\, t_n) \tag{2.5}$$

The form of Eqn. (2.5) implies that all the $\mathcal{P}_n$ for $n > 2$ can be derived, when only $\mathcal{P}_2$ is known. That is,

Knowledge of the present is sufficient to determine the future.

2.4.1 Ornstein-Uhlenbeck Stochastic Processes

The O-U process is a Gaussian-Markovian process with an exponentially decreasing autocorrelation function and a finite autocorrelation time [4].

$$\langle \xi(t)\xi(t') \rangle = \mathcal{A}^2 \cdot \exp(-\omega_{ac}|t - t'|), \tag{2.6}$$

in which ω_{ac} is an autocorrelation frequency, and $\mathcal{A}$ is a constant. O-U processes are defined by

$$\mathcal{W}_1(\xi_1\, t) = \frac{1}{\mathcal{A}\sqrt{\pi/\omega_{ac}}} \cdot \exp\left(-\frac{1}{2}\frac{\xi^2}{\mathcal{A}^2/2\omega_{ac}}\right) \tag{2.7}$$

According to the Doob's theorem [23], the O-U process is the only stochastic process with all of the following properties:

(1) Gaussian process

(2) stationary process

(3) Markovian process

In order to construct a simplified stochastic noise model, it is necessary to make the most of the Markovian property. Of all the stochastic processes, the Ornstein-Uhlenbeck stochastic process is a convenient choice for modeling Booster noise. In particular, if a process is invariant to translations in time (e.g. a shift in time (τ)) then the process is called a *stationary process* [21, 24]. For a stationary process we can make simplifications.

$$\langle \xi(t_1 + \tau)\xi(t_2 + \tau) \cdots \xi(t_n + \tau) \rangle = \langle \xi(t_1)\xi(t_2) \cdots \xi(t_n) \rangle \tag{2.8}$$

where $\xi(t)$ is the stochastic function and $\langle \ldots \rangle$ is the statistical average. This above implies:

(1) Since the underlying mechanisms causing the fluctuations do not change with time,

the stochastic properties of a stationary process are conserved.

(2) The important parameter in the O-U stochastic process is *relative time* and not the absolute time.

$$\langle\, \xi(t_1 - \tau)\xi(t_1)\, \rangle = \langle\, \xi(t_1)\xi(t_1 + \tau)\, \rangle \tag{2.9}$$

Therefore, the autocorrelation function $\Gamma(t,\, t')$ for a stationary process is a function of $|t - t'|$ only.

(3) The ensemble average and the time average are the same, which leads to the ergodic property.

2.5 Color of Noise

White Noise, Non-White Noise, and Colored Noise

In optics, the frequency spectrum of white light is flat. By analogy, the term *white noise* is used to describe noise with a flat frequency spectrum. White noise is not typically present in a real world. Therefore, we can only use white noise in idealized mathematical models for fast-fluctuating forces. The term *colored noise* refers to noise with a frequency spectrum which rapidly decreases with increasing frequency. In the following subsections we discuss some of the important stochastic parameters.

2.5.1 Autocorrelation Function

The mean and the standard deviation of a stochastic variable ξ do not provide much information on the process of interest. We are more interested in a measure of the influence of $\xi(t)$ on $\xi(t + \Delta t)$. This statistical quantity is referred to as *autocorrelation*

function $\Gamma(t,\ t+\Delta t)$ [25].

$$\Gamma(\ t,\ t'\ ) = \lim_{T\ \to\ \infty} \frac{1}{T} \int_0^T dt\ \xi(t)\xi(\ t'\ ), \qquad (2.10)$$

where $0 < t < t'$, and $t' = t + \Delta t$. As in Eqn. (2.10), the autocorrelation function is a time average of a product of stochastic variables at t and t' over an arbitrary large time T. In the case of external fluctuations, the variables of interest can vary appreciably for the duration of the autocorrelation time [26]. Therefore, we consider noise with finite autocorrelation time to be colored noise. For white noise [21], the autocorrelation function is,

$$\langle\ \xi(t)\cdot\xi(t')\ \rangle = \mathcal{A}^2\cdot\delta(\ t\ -\ t'\ ), \qquad (2.11)$$

where $0 < t < t'$, $t' = t + \Delta t$, and $\delta(t)$ is the Dirac-δ function. As in Eqn. (2.11), when a stochastic noise is uncorrelated in time, or the autocorrelation time approaches asymptotically to zero ($\tau_{ac} \to 0$), the noise with a very short memory can be treated as *white noise*. As was mentioned earlier, perfect white noise never occurs in nature, and is only an idealized mathematical model. *Colored noise*, on the other hand, has a longer memory span, so the autocorrelation function $\Gamma(t,\ t')$ can be an exponential function of time, but *not* δ-correlated.

$$\langle\ \xi(t)\cdot\xi(t')\ \rangle = \mathcal{A}^2\cdot\Gamma(\ t,\ t'\ ), \qquad (2.12)$$

where $t' = t + \Delta t$, $\Gamma(\ t,\ t'\ ) = \exp(\ -\omega_{ac}|t\ -\ t'|)$, and $\mathcal{A} = S_N\cdot\omega_{ac} = \sigma$.

Here S_N is the noise strength, and ω_{ac} is the *autocorrelation frequency* (the reciprocal of the autocorrelation time). The autocorrelation function $\Gamma(\ t,\ t'\ )$ can be viewed as a measure for the rapidity of the fluctuations (the memory time of the stochastic process under study.)

The span of the memory time determines the color of stochastic noise.

2.6 Stochastic Properties of the Noise

Let us consider a 1st-order linear stochastic differential equation[10] of the form of Langevin equation.

$$\dot{\eta}(t) = -\omega \cdot \eta(t) + \xi(t),$$
$$\text{where } \dot{\eta} = \frac{d\eta}{dt}, \ \omega = \omega_{ac}. \tag{2.13}$$

As explained in Eqn. (2.2), the second term in Eqn. (2.13) is from external fluctuations. The fluctuations are external noise with finite ω_{ac}, or τ_{ac} (i.e. O-U noise). Eqn. (2.13) is Langevin equation, in which η, ω, and ξ are the stochastic function, autocorrelation frequency, and O-U stochastic noise source, respectively. The O-U noise ξ is a function of time, and ω is a constant The autocorrelation function of ξ is given in Eqn. (2.12) for the case of no spatial dependence. Ornstein and Uhlenbeck [4], Doob [23], and van Kampen [21] use the integration method to find the statistical properties of colored noise, or non-white noise from Langevin equation. We, on the other hand, solve Langevin equation as a 1st-order differential equation. The general solution of a 1st-order inhomogeneous differential equation is a linear superposition of a homogeneous solution (η_h) and a particular solution (η_p).

$$\eta(t) = \eta_h(t) + \eta_p(t) \tag{2.14}$$

A homogeneous solution for the differential equation (DE) is,

$$\eta_h(t) = \eta(0) \cdot \exp(-\omega t), \tag{2.15}$$

A particular solution for the DE is:

$$\eta_p(t) = \exp(-\omega t) \cdot \int_0^t ds \cdot \exp(+\omega s) \cdot \xi(s) \tag{2.16}$$

---

[10] A stochastic differential equation is a differential equation in which the coefficients are random functions of the independent variable, usually time.

Hence,

$$
\begin{aligned}
\eta(t) &= \eta_h(t) + \eta_p(t) \\
&= \eta(0) \cdot \exp(-\omega\, t) + \exp(-\omega\, t) \cdot \int_0^t ds \cdot \exp(\omega\, s) \cdot \xi(s) \\
&= \eta(0) \cdot \exp(-\omega\, t) + \int_0^t ds \cdot \exp[-\omega(t - s)] \cdot \xi(s)
\end{aligned}
\tag{2.17}
$$

From here, the stochastic process at the next time step $t + \Delta t$ can be obtained.

$$
\begin{aligned}
\eta(t + \Delta t) &= \eta(0) \cdot \exp[-\omega(t + \Delta t)] + \int_0^{t+\Delta t} ds \cdot \exp[-\omega \cdot (t + \Delta t - s)] \cdot \xi(s) \\
&= \exp[-\omega\Delta t] \cdot \{\eta(0) \cdot \exp[-\omega t] + \int_0^t ds \cdot \exp[-\omega(t - s)] \cdot \xi(s) \\
&\quad + \int_t^{t+\Delta t} ds \cdot \exp[-\omega(t - s)] \cdot \xi(s)\} \\
&= \exp[-\omega\Delta t] \cdot \eta(t) + \underbrace{\int_t^{t+\Delta t} ds \cdot \exp[-\omega(t + \Delta t - s)] \cdot \xi(s)}_{\mathcal{H}(t,\, t + \Delta t)}
\end{aligned}
\tag{2.18}
$$

Let $\mathcal{H}(t, t + \Delta t)$ be the second term of Eqn. (2.18).

$$
\mathcal{H}(t,\, t + \Delta t) \equiv \int_t^{t+\Delta t} ds \cdot \exp[-\omega(t + \Delta t - s)] \cdot \xi(s)
\tag{2.19}
$$

We transform the variables of integration from s and s' to $\tilde{s}$ and $\tilde{s}'$.

$$
\left.
\begin{aligned}
\tilde{s} &\equiv s - t \\
\int_t^{t+\Delta t} ds &\longrightarrow \int_0^{\Delta t} d\tilde{s}
\end{aligned}
\right\}
\tag{2.20}
$$

and obtain

$$
\begin{aligned}
\mathcal{H}(0,\, \Delta t) &= \int_0^{\Delta t} d\tilde{s} \cdot \exp[-\omega(\Delta t - \tilde{s})] \cdot \xi(\tilde{s} + t) \\
&= \exp[-\omega\Delta t] \cdot \int_0^{\Delta t} d\tilde{s} \cdot \exp[\omega\tilde{s}] \cdot \xi(\tilde{s} + t)
\end{aligned}
\tag{2.21}
$$

$$\mathcal{H}^2(0,\,\Delta t) = \exp[-2\omega\Delta t] \cdot \int_0^{\Delta t} d\tilde{s} \cdot \int_0^{\Delta t} d\tilde{s}' \cdot \exp[\omega(\tilde{s}+\tilde{s}')] \cdot \xi(\tilde{s}+t) \cdot \xi(\tilde{s}'+t) \quad (2.22)$$

The statistical properties of a random variable can be investigated by the calculations of various moments.

We calculate the first and the second central moments by averaging Eqns. (2.21) and (2.22) over an ensemble of particles. The first two moments determine the complete statistical properties of the noise because it is a Gaussian process. Gaussian white noise has zero mean. For zero-mean Gaussian, the 1st moment vanishes.

$$\langle \mathcal{H}(0,\Delta t) \rangle = 0 \quad (2.23)$$

Accordingly, keeping in mind that the O-U process is a stationary process, the 2nd moments boil down to

$$
\begin{aligned}
\langle (\mathcal{H}(0,\Delta t) - \langle \mathcal{H}(0,\Delta t)\rangle)^2 \rangle &= \langle \mathcal{H}^2(0,\Delta t) \rangle \\
&= \exp[-2\omega\Delta t] \cdot \int_0^{\Delta t} d\tilde{s} \int_0^{\Delta t} d\tilde{s}' \cdot \exp[\omega(\tilde{s}+\tilde{s}')] \cdot \langle \xi(\tilde{s}) \cdot \xi(\tilde{s}') \rangle \\
&= A^2 \exp[-2\omega\Delta t] \cdot \int_0^{\Delta t} d\tilde{s} \cdot \exp[2\omega\tilde{s}] \\
&= \frac{A^2}{2\omega} \cdot \{1 - \exp[-2\omega\Delta t]\}
\end{aligned}
\quad (2.24)
$$

The O-U noise module can generate stochastic noise with a desired strength according to the measurements (refer to section 4.3.3). This is done by using a scaling factor χ to multiply Eqn. (2.24). This module is designed to generate O-U stochastic noise $\eta(t)$ applied to macroparticles as a magnetic field perturbation term: *autocorrelation time (τ_{ac}), time step (Δt), noise strength ($A = \sigma$)*

2.7 Overview of ORBIT/ORBIT-FNAL

The ORBIT/ORBIT-FNAL[11] is a modularized C++code. It is mainly designed for particle injection, tracking and a variety of beam dynamics calculations in high-intensity proton rings. It is intended for detailed simulation of both realistic machine problems and of idealized situations. The ORBIT⋆ can track particles in 6D phase space by transporting herds[12] of interacting particles through a series of nodes representing elements, or diagnostic devices in the accelerator lattice. During tracking, the ORBIT⋆ can perform a variety of actions (transfer matrix operation, space-charge calculations, streaming information to output files, etc.) on macroparticles at specified nodes around the ring.

2.7.1 Physics Modules and SuperCode Shell

Since ORBIT⋆ is a C++ open source code, it is designed to allow the development of various programming modules in parallel. Depending on their research interests, module developers can provide ORBIT⋆ with additional physics modules. Physics modules operate within the *SuperCode* driver shell [27]. The followings can be accomplished with the interactive programming shell:

(1) To execute interpreted script files as well as compiled physics modules.

(2) To customize simulation sequences within a script.

---

[11] We will refer to ORBIT/ORBIT-FNAL as *ORBIT⋆* for short.

[12] A group of macroparticles is called *herd*.

2.8 Algorithm of the New Noise Module

In addition to 28 existing modules in total[13], we add a new Noise module to the ORBIT-FNAL package. First, the new noise module generates Gaussian white noise directly from uniform random deviates. Combining this generated Gaussian white noise with inputs of noise parameters, Gaussian *non-white* noise can be generated.

2.8.1 Box-Muller-Like Transformation:

Non-White Noise Generation

The Box-Muller method [28, 29] is used to generate independent Gaussian random deviates from independent uniform random deviates. However, by implementing algorithms for Eqn. (2.24) in addition to the Box-Muller algorithm, the variant of the method is also capable of generating exponentially-driven Gaussian colored noise. The method requires a good uniform random number generator to generate independent uniformly-distributed random numbers. First, a pair of random numbers between 0 and 1 is generated. As shown in Figure 2.1 (a), α_1 and α_2 are independent random variables from the same rectangular probability density function on (0, 1). Consider the random variables

$$\left.\begin{aligned}
\beta_1 &= (-2\ln\alpha_1)^{\frac{1}{2}} \cdot \cos(2\pi\alpha_2) \\
\beta_2 &= (-2\ln\alpha_1)^{\frac{1}{2}} \cdot \sin(2\pi\alpha_2)
\end{aligned}\right\} \tag{2.25}$$

The coordinates of (β_1, β_2) are a pair of independent random variables from the same normalized Gaussian distribution of zero mean. Because α_1 and α_2 are chosen in between 0 and 1, their logarithmic values are negative. The minus sign is thereby introduced to make the argument positive inside the square root in Eqn. (2.25). The joint probability-density

---

[13] We build ORBIT-FNAL from a CVS version of ORBIT of SNS dated December 2005

function of β_1 and β_2 are:

$$\begin{aligned}
\mathcal{F}(\beta_1, \beta_2) &= \frac{1}{2\pi} \cdot \exp\left[-\frac{1}{2}(\beta_1{}^2 + \beta_2{}^2)\right] \\
&= \frac{1}{\sqrt{2\pi}} \exp\left[-\frac{\beta_1{}^2}{2}\right] \cdot \frac{1}{\sqrt{2\pi}} \exp\left[-\frac{\beta_2{}^2}{2}\right] \\
&= \mathcal{F}(\beta_1) \cdot \mathcal{F}(\beta_2)
\end{aligned} \tag{2.26}$$

We just verified that the random variables (β_1, β_2) are independent. We can speculate

(a) unit square   **(b)** unit circle
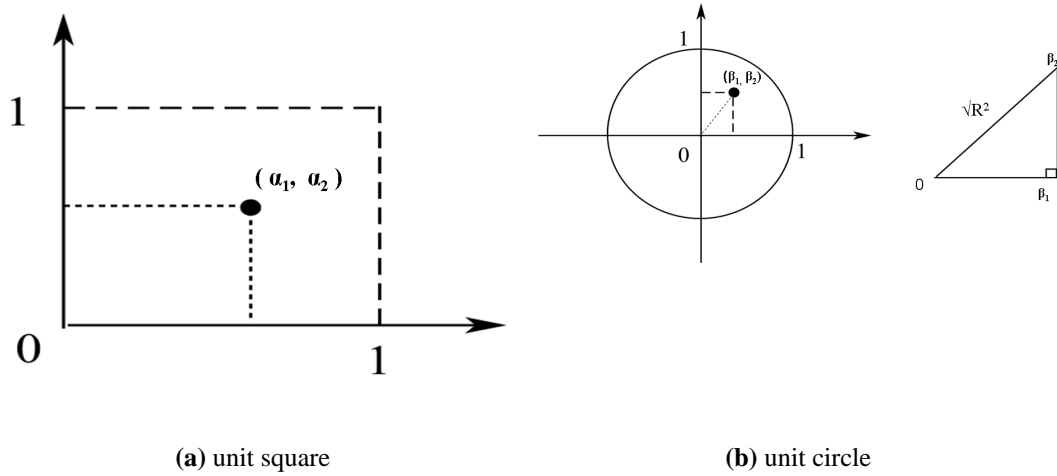
Figure 2.1: Box-Muller transformation

further that the probability density function $\mathcal{F}(\beta_1, \beta_2)$ is constant on an unit circle. Also, a random angle of θ, which is uniformly distributed in the interval $(0, 2\pi)$, can be defined as below:

$$\theta = \arctan(\beta_1/\beta_2) \tag{2.27}$$

As illustrated by Figure 2.1 (b), we define R^2 as squared length of a radius as in Eqn. (2.28). The R^2, which is a random number within a unit circle, can be used for α_1, or α_2 within a

unit square.

$$R^2 \stackrel{\text{def}}{=} \beta_1^2 + \beta_2^2 \tag{2.28}$$

As long as the value of R^2 lies in the range of $(0, 1)$, i.e., within a unit circle centered around the origin, the pair of random deviates (β_1 and β_2) define the coordinates of a point inside the unit circle. It is convenient to use three random deviates (β_1, β_2, and R) in place of the trigonometric functions:

$$\left. \begin{aligned} \cos \theta &= \beta_1 / \sqrt{R^2} \\ \sin \theta &= \beta_2 / \sqrt{R^2} \end{aligned} \right\} \tag{2.29}$$

From here, a pair of new random deviates (γ_1 and γ_2) can be defined:

$$\left. \begin{aligned} \gamma_1 &= \frac{\beta_1}{\sqrt{R^2}} \cdot \sqrt{-2 \cdot \ln R^2} \\ \gamma_2 &= \frac{\beta_2}{\sqrt{R^2}} \cdot \sqrt{-2 \cdot \ln R^2} \end{aligned} \right\} \text{ for white noise} \tag{2.30}$$

The above is for the case of *white noise*. In the case of *non-white noise*, or *colored noise* the second moments of $\mathcal{H}(t, t + \Delta t)$, which has already been derived as in Eqn. (2.24), are inserted inside the square root as follows:

$$\left. \begin{aligned} \gamma_1 &= \frac{\beta_1}{\sqrt{R^2}} \cdot \sqrt{-2 \cdot \langle \mathcal{H}^2 \rangle \cdot \ln R^2} \\ \gamma_2 &= \frac{\beta_2}{\sqrt{R^2}} \cdot \sqrt{-2 \cdot \langle \mathcal{H}^2 \rangle \cdot \ln R^2} \end{aligned} \right\} \text{ for non-white noise, or colored noise} \tag{2.31}$$

We can view what is derived in Eqn. (2.31) as the 2nd moments of $\mathcal{H}(t, t + \Delta t)$ mounted on a carrier of the white-noise generator. Consequently, depending on the values of autocorrelation time and time step, the module is fully capable of generating a wide spectra of stochastic noise, ranging from white noise, near-white noise, off-white noise to colored noise.

2.8.2   Next Step

In the end, two Gaussian random deviates (γ_1 and γ_2) are obtained from two input uniform deviates. In order to generate exponentially-driven Gaussian noise, the exponential factor $\exp(-\omega\Delta t)$ is first multiplied by the stochastic noise $\eta(t)$ at present time t. Then a rms (root-mean-square) value of $\mathcal{H}(0,\Delta t)$ is added to compute the noise at the next time step $t + \Delta t$, as redescribed in Eqn. (2.31). The form of Eqn. (2.18) implies that to generate $\eta(t+\Delta t)$, one needs to know $\eta(t)$ only. This takes advantage of the powerful Markov property of the O-U process.

$$
\begin{aligned}
\eta(t+\Delta t) &= \exp(-\omega\,\Delta t)\cdot\eta(t) + C_w\cdot\sqrt{\langle\,\mathcal{H}(t,\,t+\Delta t)^2\,\rangle} \\
&= \exp(-\omega\,\Delta t)\cdot\eta(t) + \underbrace{C_w\cdot\sqrt{\langle\,\mathcal{H}(0,\,\Delta t)^2\,\rangle}}_{\gamma_1,\,\text{or}\,\gamma_2}.
\end{aligned}
\tag{2.32}
$$

Here C_w represents random deviates from a rectangular distribution, (or white noise). The second term on the right-hand side of Eqn. (2.32) corresponds to the Eqn. (2.31).

2.8.3   Class Hierarchy

When adding a new module to the ORBIT-FNAL we need to pay attention on the class[14] design. New noise-related classes created in the module need to fit into the existing class hierarchies of the entire package. A lot of effort goes into the class design for this noise module. Consequently, the new noise module is simple and effective, and is capable of generating a broad spectrum of stochastic noise. Figure 2.2 illustrates the class hierarchy of the noise module.   There are four new methods implemented in the noise module:

(1) The *addRandomNoiseNode* for inserting a noise node at a desired location around a ring. The noise adder location is where the noise source is located. In the case of the

---

[14]In C++language, a class is a user-defined type. It contains member functions, or methods that manipulate data members declared inside a class.
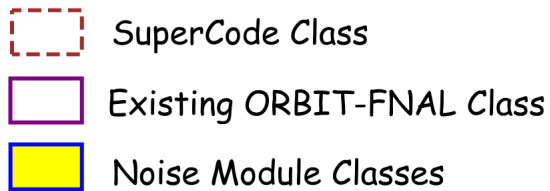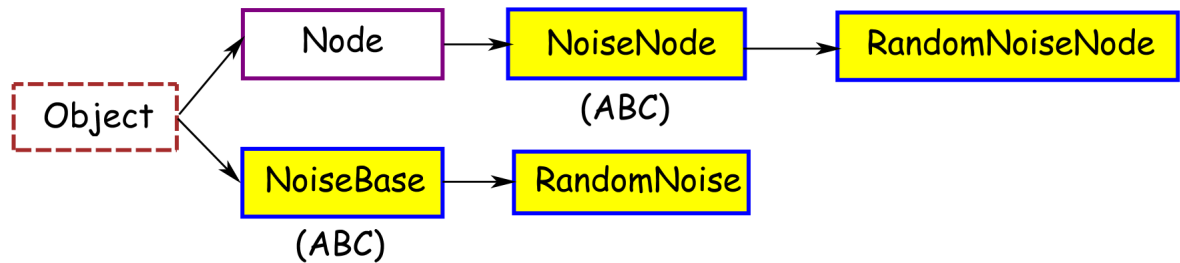
Figure 2.2: The class hierarchy in the Noise module: *base class → derived class*

Booster, the source of noise is taken to be one of the Booster power supplies. (2) The *showNoise()* method, which is for streaming the primary input noise parameters (*autocorrelation time, time step, and noise strength*) and the secondary parameters, such as node order, noise color (*white, or non-white*), etc. (3 and 4) noise-node activator and deactivator methods. These methods are available for use in a SuperCode script. Excerpts from the Noise module descriptor file, *Noise.mod* are shown in Figure 2.3.

```
Void addRandomNoiseNode( const String &nName,    const Integer &oindex,
                         const String &fNoise,   const String   &fHalo,
                         const Real   &dT,       const Real    &corrTime,
                         const Real   &Strength, const Integer &nSteps )
                         -- " A routine to add a RandomNoiseNode " ;


Void  showNoise()              -- " Show noise parameters. ";


Void activateRandomNoiseNodes()      -- " Activates all RandomNoiseNodes. ";
Void deactivateRandomNoiseNodes()   -- " Deactivate all RandomNoiseNodes. ";
```

Figure 2.3: The methods implemented in the Noise module descriptor file

Figure 2.4 is a schematic showing the interconnection between Physics Modules and the SuperCode Shell.

2.8.4   Features of the New Noise Module

Key features of the new Noise module are listed below:

(1) The new module is configured to generate a broad spectra of stochastic noise per user input. (*autocorrelation time*, *time step*, and *noise strength*)

(2) The module enables statistical properties of the random noise to be controlled via input script file.

(3) The module is completely parallelized with the Message-Passing Interface (MPI).

(4) The module calculates a suite of beam diagnostic calculations: *transverse rms emittances, longitudinal rms emittance, transverse actions, longitudinal action, halo amplitudes, position amplitudes, and angle amplitudes.*
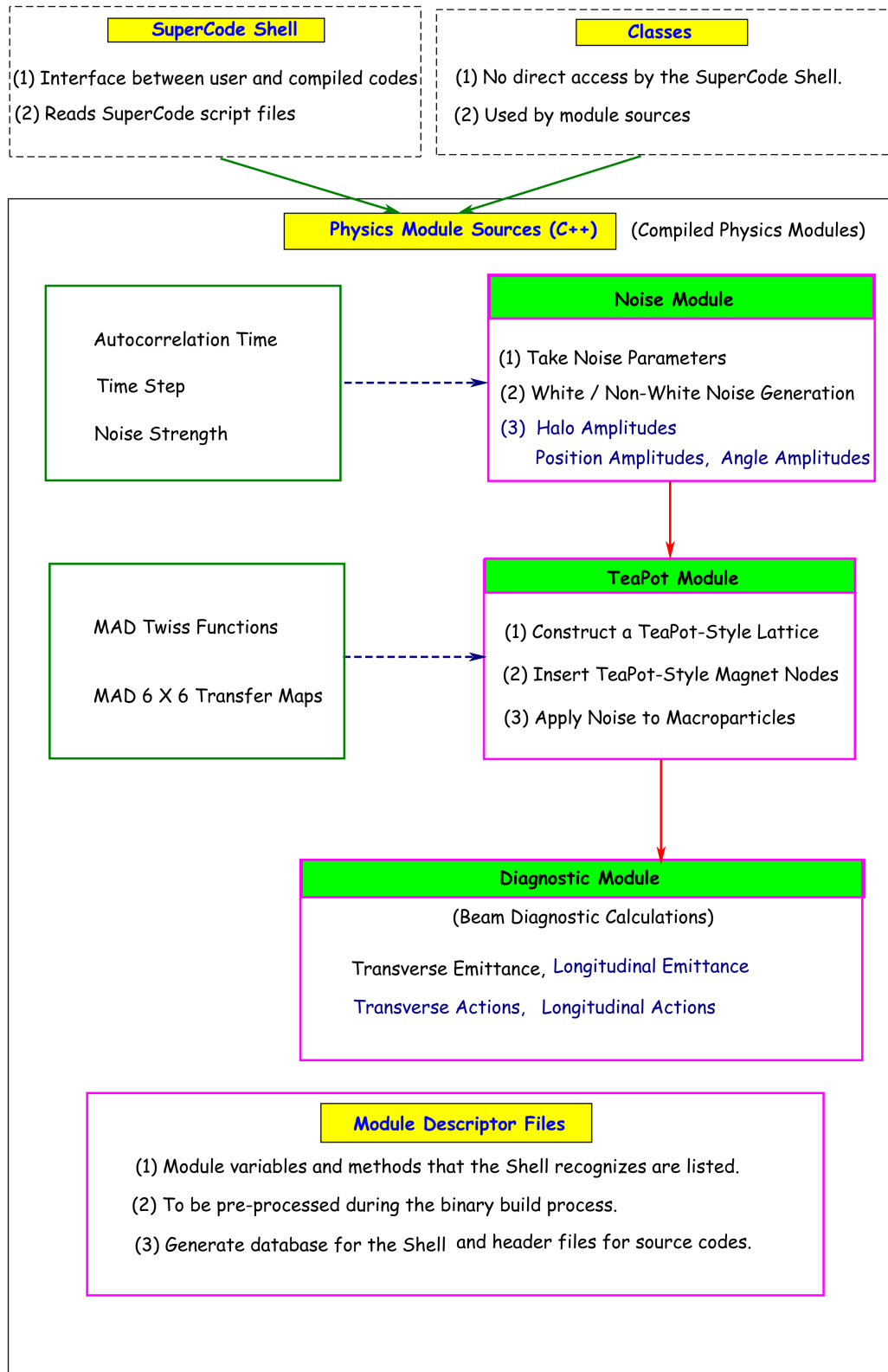
Figure 2.4: Connections between Physics Modules and SuperCode Shell: the items in dark blue are new parallelized calculations implemented in each module.

2.9   Method of Applying Noise to Macroparticles

In ORBIT⋆, a few different methods are available for reading in the lattice information such as Twiss functions[15] and transfer maps that are computed by MAD[16] [30]. One of the methods, *buildTPlattice(...)* , is for reading in a TEAPOT[17]-style lattice[18] [31].

We first convert to a TEAPOT-style lattice from the MAD design lattice of the Booster with the aid of SNS/ORNL's Python scripts. During the course of converting the lattices from one format to another, we are able to understand the new structure of the TEAPOT-style lattice. We then upgrade the lattice-reading method to *buildTPlatticeI(...)* accordingly, such that the TeaPot module can fully understand the Fermilab's Booster lattice in TEAPOT format.

2.9.1   Internal Algorithm

The following steps describe how the upgraded TeaPot module applies stochastic noise, generated from the Noise module, to macroparticles.

(1) The new method of *Void buildTPlatticeI (...)* reads in lattice elements and their attributes (length, magnet-face angles, field gradient, etc.) line by line.

(2) To each of the main gradient magnets of the Booster, one Booster power supply[19] identifier is assigned. (i_{GMPS} = 1, 2, 3, 4)

---

[15]When a beam is propagated through a series of magnets, its phase-space ellipse changes, keeping the area preserved. The Twiss functions, or Twiss parameters (β, α, γ) characterize the orientation and shape of phase-space ellipse.

[16] MAD (Methodical Accelerator Design) is an accelerator-design tool for charged-particle optics in alternating-gradient accelerators and beamlines.

[17]TEAPOT is an accelerator-modeling code handling all beamline elements as thin elements except for drift. Upon reading a lattice file, TEAPOT converts all thick elements (lenses) to thin elements.

[18]A TEAPOT-style lattice is a lattice file containing all information of beamline elements written in TEAPOT syntax.

[19] GMPS (Gradient Magnet Power Supply)

(3) After reading through the line for each individual main gradient magnet, *kml, pole, and skew* values defined below are determined:

    (a) *kml*: integrated multipole gradient

    (b) *pole*: number of poles (dipole=2, quadrupole=4, sextupole=6, etc.)

    (c) *skew*: skew index

(4) Sum up the magnetic field gradients of all orders.

(5) Reading in Twiss functions from the MAD calculation outputs.

(6) According to the sum of magnetic field gradients in all combinations, the type of each magnet is determined. The types of the magnet element available in the module are:

    (a) *multipole (Mult)*

    (b) *combined-function multipole (MultCF)*

    (c) *bend (Bend)*

    (d) *combined-function bend (BendCF)*

    (e) *quadrupole (Quad)*

    (f) *combined-function quadrupole (QuadCF)*

    (g) *solenoid (Soln)*

    (h) *kicker (Kick)*

The names specified in the parentheses above are variable names used to represent the type of each magnet element in the module. If the magnet-field gradient is set to zero, then a magnet element is handled as a *drift* element.

(7) Insert a TeaPot-style magnet node that is determined in the previous step to which the corresponding magnet is. *All of the new TEAPOT-style magnet-node adders take*

one independent stochastic noise generator implemented in the new Noise module. One noise generator is invoked by the associated GMPS identifier. We create and incorporate the additional methods for the Booster lattice into the TeaPot module as shown in Figures 2.5 and 2.6. For the Booster design lattice (version 1.1), all elements are categorized into the following choices only:

<p align="center">*Drift, Bend, BendCF* and *Mult*</p>

By means of providing the number of tracking steps for each type of magnet element, the TeaPot module performs symplectic tracking, breaking up each element into shorter lengths. The hard-edge fringe-field effects of the magnet elements are included. At the location of each TeaPot node, the magnetic field gradient is perturbed by the amount of input noise with a specified magnitude. Because current fluctuations are directly proportional to magnetic-field fluctuations, the current ripple measurements are translated into field fluctuations as in Eqn. (2.33).

$$\widetilde{\mathcal{K}_{imag}} = \mathcal{K}_{imag} + \Delta\mathcal{K}_{imag} = \mathcal{K}_{imag} \cdot \left(1 + \Delta\mathcal{K}/\mathcal{K}_{imag}\right) \tag{2.33}$$

In the Booster design lattice, focusing and de-focusing gradient magnets have different gradient strengths $\mathbf{K}$ ($\mathcal{K}_D$, or $\mathcal{K}_F$). The gradient strength [20], ($\mathbf{K}$) is factored out to normalize $\Delta\mathbf{K}$ with its own gradient strength. Then, the fluctuation of gradient strength arising from current fluctuation is introduced as a perturbation term for each magnetic field calculation. As a consequence, macroparticles will experience perturbed fields as they propagate through each main gradient magnet element. It should be pointed out that a string of 24 gradient magnets in a quadrant of the entire magnet system are connected *in series*. (cf. chapter 3). As such, the field fluctuations due to *current* fluctuations, or ripples, are preserved; that is, *there is no current attenuation.*

---

[20] K_F = -0.0577069 and K_D = 0.0542195 ($1/\text{m}^2$).

```
Void  buildTPlatticeI ( const String    &MADTwissFile, const String    &MADLATFile,
                        const Integer   &nstepTPD,   const Integer    &fringeD,
                        const Integer   &nstepTPM,   const Integer    &fringeM,
                        const Integer   &nstepTPQ,   const Integer    &fringeQ,
                        const Integer   &nstepTPB,   const Integer    &fringeB,
                        const Integer   &nstepTPS,   const Integer    &fringeS,
                        const Integer   &nstepTPK,   const Integer    &fringeK,
                        const Subroutine &sub )
```

(a) Method for constructing a TeaPot-style lattice

```
Void  addTPB2 ( const String  &nName,   const Integer  &order,
                const Real    &bx,      const Real     &by,
                const Real    &ax,      const Real     &ay,
                const Real    &ex,      const Real     &epx,
                const Real    &length,  const String   &et,
                const Real    &tilt,    const Real     &theta,
                const Integer &ea1,     const Real     &ea2,
                const Integer &nSteps,
                const Integer &fringeIN, const Integer &fringeOUT,
                const Subroutine &sub )
```

(b) Method for inserting a TeaPot-style Bending magnet with a noise source

```
Void  addTPBCF2 ( const String  &nName,   const Integer   &order,
                  const Real    &bx,      const Real      &by,
                  const Real    &ax,      const Real      &ay,
                  const Real    &ex,      const Real      &epx,
                  const Real    &length,  const String    &et,
                  const Real    &tilt,    const Real      &theta,
                  const Real    &ea1,     const Real      &ea2,
                  const Integer &vectnum, const IntegerVector &pole,
                  const RealVector &kl, const IntegerVector &skew,
                  const Integer &nSteps,
                  const Integer &fringeIN, const Integer &fringeOUT,
                  const Subroutine &sub )
```

(c) Method for inserting a TeaPot-style Quadrupole magnet with a noise source

Figure 2.5: New TeaPot-style magnet-node adders to a ring (I)

```
Void  addTPQ2 ( const String  &nName, const Integer &order,
                const Real    &bx,        const Real     &by,
                const Real    &ax,        const Real     &ay,
                const Real    &ex,        const Real     &epx,
                const Real    &length,   const String    &et,
                const Real    &tilt
                const Real    &kq,    const Integer &nsteps,
                const Integer   &fringeIN, const Integer &fringeOUT,
                const Subroutine &sub )
```

(a) Method for inserting a TeaPot-style Combined-Function Quadrupole magnet with a noise source

```
Void  addTPM2 ( const String   &nName, const Integer &order,
                const Real    &bx,        const Real     &by,
                const Real    &ax,        const Real     &ay,
                const Real    &ex,        const Real     &epx,
                const Real    &length,  const String  &et,
                const Real    &tilt
                const Integer   &pole,  const Real    &kl,
                const Integer   &skew, const Integer   &nsteps,
                const Integer   &fringeIN, const Integer  &fringeOUT,
                const Subroutine &sub )
```

(b) Method for inserting a TeaPot-style Multipole magnet with a noise source

Figure 2.6: New TeaPot-style magnet-node adders to a ring (II)

Measurements of Noise Originating from Booster Power Supplies

In the preceding chapter, we described a theoretical model of stochastic noise that is implemented in the new noise module of ORBIT-FNAL. In this chapter, we first examine the Booster Gradient-Magnet Power-Supply System (GMPSS). We then present methods of measuring and analyzing noise originating from the GMPSS. The stochastic noise model is then tuned to represent these measurements. In particular, the frequency spectrum of the measured physical noise is used to tune the Ornstein-Uhlenbeck noise in our model. Since the Booster power-supply noise is characterized by O-U stochastic noise parameters, as introduced in Chapter 2, we extracted characteristic noise parameters from a series of measurements. Consequently, our stochastic noise model provides a realistic representation of the Booster noise originating from GMPSS.

3.1   Gradient-Magnet Power-Supply System

The Gradient-Magnet Power-Supply System (GMPSS) for the Booster synchrotron powers a total of 96 main gradient magnets. A resonance system is selected in order to

reduce the size and cost of the power-supply system. The Booster magnet system consists of 48 LC-resonant magnet cells. Each individual magnet cell consists of a focusing magnet (F), a de-focusing magnet (D), a choke, and a capacitor bank. Equivalent circuits for each cell component are drawn in Figure 3.1. In the equivalent circuit, each gradient magnet (focusing, or de-focusing magnet) is represented by an inductor (L). Figure 3.2 illustrates the equivalent-circuit arrangement of 96 main gradient magnets and 4 GMPS'. In turn, 48 focusing and 48 de-focusing magnets are connected in series by common buses (front bus and back bus). The gradient magnets are powered by 4 GMPS' that are symmetrically inserted in the LC-resonant system. Each GMPS drives current at a fundamental frequency of 15 Hz through a string of 12 magnet cells. Hence, the GMPS voltages to ground (V_{+G} and V_{-G}) can be kept as low as possible.

The GMPSS includes dual three-phase Silicon Controlled Rectifier (SCR) bridges connected in series, and is fed by a 12-phase 13.8-kV bus with shunt (or stray) capacitors connected to ground. A schematic of the SCR module built inside each GMPS unit is drawn in Figure 3.3. The SCR module generates both AC and DC components of the GMPS current as in Eqn. 3.2. Table 3.1 summarizes the structure of the Booster Gradient-Magnet Power-Supply System.

Table 3.1: The Booster Gradient-Magnet System

Component	No.
LC-resonant magnet cells	48
Focusing magnets	48
De-focusing magnets	48
Chokes	48
Capacitor Banks	48
GMPS	4
Gradient Magnets / cell	2
Choke / cell	1
Magnet cells / GMPS	12

In this magnet excitation mode, a sinusoidal-wave current is superimposed on a mean

current of about 500 A. Figure 3.4(a) shows the current waveform sampled directly from the main bus line around the GMPS 1 unit. Frequency and period of the current are shown in the shaded boxes. Figures 3.4(b) and (c) show ACNET (Accelerator Control NETwork) lumberjack plots of peak current and minimum current. Here, the peak current is 967 (A) and the minimum current is 103 (A). The DC output of the power supply is filtered with a L-C network to smooth the differential-mode sawtooth waveform from the power supplies. An additional magnet, referred to as *a reference magnet*, is connected in series with the ring magnets to map and track the magnetic field in the Booster. The rate of change of the magnetic field, B-dot ($\dot{B}$), can be detected using a B-dot coil located in the gap of the reference magnet. This B-dot coil samples the magnet-current transductor signal at its maximum and minimum values. The maximum and minimum values of the magnet current are set via the control system (B:VIMAX and B:VIMIN) as shown in Figure 3.4. The Booster operates in fast-cycling mode implemented as a resonant system. The fast-cycling operation involves a DC-biased sine-wave current at a frequency of 15-Hz. The sinusoidal ramp of the magnetic field and current are,

$$
\begin{aligned}
B &= \sum_{i=0}^{\infty} B_i \, \cos(i\omega t + \theta_i) \\
&= B_{dc} - B_{ac}\cos(30\pi t)
\end{aligned}
\tag{3.1}
$$

$$
\begin{aligned}
I &= \sum_{i=0}^{\infty} I_i \, \cos(i\omega t + \theta_i) \\
&= I_{dc} - I_{ac}\cos(2\pi f t) \\
&= 535 - 432\cos(30\pi t) \; (A),
\end{aligned}
\tag{3.2}
$$

where dc, ac, and f denote the DC and AC components, and the fundamental frequency of 15 Hz, respectively. Power supplies GMPS 1 and GMPS 2 are located in the West Booster Gallery, and GMPS 3 and GMPS 4 are located in the East Booster Gallery. Figure 3.5 shows the rack of GMPS 1, GMPS 3 and GMPS 4 units located in the Booster gallery.

Each of the Booster main magnets both steers (or bends) radially and focuses the beam in transverse directions. As such, the Booster lattice is unique in that it is composed of *combined-function magnets*. The magnets are placed on girders as shown in Figure 3.6(a). Each magnet girder is composed of a focusing and a de-focusing magnet, a choke, a capacitor bank, a corrector package, a Beam-Position Monitor (BPM), and an ion pump.

3.1.1 Choke and Capacitor Banks

A large amount of energy is stored in the magnetic field in the Booster. Therefore, large capacitor banks with DC chokes to pass the DC current are used. The capacitor banks and chokes are distributed around the ring. A modular approach is used in which two magnets together with their resonant capacitor and choke form one LC-resonant cell. A second winding on each choke is used to provide coupling between resonant cells. The winding ratio is one to one. Because of resonant system, energy is exchanged between magnets and the capacitor bank, and the power supply makes up the energy loss in the system. Hence, distributed capacitor banks and chokes proved to be the most economic system. The magnitude of DC-biased rms current ($I_{rms, mag}$) that is transmitted to a string

of magnets is,

$$\widetilde{I^2}_{mag} = I^2_{rms,\,mag}$$

$$= \frac{1}{2\pi} \int_0^{2\pi} (I_{dc} + I_{ac,\,mag} \cos\theta)^2 \, d\theta$$

$$= \frac{1}{2\pi} \int_0^{2\pi} \left(2\pi \cdot I_{dc}^2 + \frac{I_{ac,\,mag}^2}{2} \int_0^{2\pi} (1 \, - \, \cos 2\theta) \, d\theta \right)$$

$$= I_{dc}^2 + \frac{I_{ac,\,mag}^2}{2} \tag{3.3}$$

$$\widetilde{I}_{mag} = \sqrt{\left(I_{dc}^2 + \frac{1}{2} \cdot I_{ac,\,mag}^2 \right)}$$

$$= 616 \; (A),$$

where $\theta = \omega t = 30\pi\,t$

Choke current can be computed as follows:

$$L_{mag} I_{mag} = L_{choke} I_{choke}$$

$$I_{choke} = \frac{L_{mag}}{L_{choke}} \times I_{ac,\,mag}$$

$$= \frac{21.4 \; mH}{42.0 \; mH} \times 432 \; A$$

$$= 220 \; (A)$$

$$\hat{I}_{choke} = I_{dc} + I_{choke} = 755 \; (A) \tag{3.4}$$

$$\check{I}_{choke} = I_{dc} - I_{choke} = 315 \; (A)$$

$$\widetilde{I}_{choke} = I_{rms,\,choke} = \sqrt{I_{dc}^2 \, + \, \frac{1}{2} \cdot I_{ac,\,choke}^2}$$

$$= 557 \; (A)$$

Peak stored energy at each magnet is,

$$
\begin{aligned}
\hat{E}_{mag} &= \frac{1}{2} \cdot L_{mag}\hat{I}_{mag}^2 \\
&= \frac{1}{2} \cdot (21.4 \, mH) \, (967 \, A)^2 \\
&= 10.0 \, (kJ)
\end{aligned}
\tag{3.5}
$$

Thus, total peak stored energy at all magnets is,

$$
\begin{aligned}
\hat{E}_{mag, \, tot} &= 48 \, \times \, \frac{1}{2} \cdot L_{mag}\hat{I}_{mag}^2 \\
&= 480.0 \, (kJ)
\end{aligned}
\tag{3.6}
$$

Peak stored energy at each choke is,

$$
\begin{aligned}
\hat{E}_{choke} &= \frac{1}{2} L_{choke}\hat{I}_{choke}^2 \\
&= \frac{1}{2} (42.0 \, mH) \, (220 \, + \, 535 \, A)^2 \\
&= 12.0 \, (kJ)
\end{aligned}
\tag{3.7}
$$

Therefore, total peak stored energy at all chokes is,

$$
\begin{aligned}
\hat{E}_{choke, \, tot} &= 48 \, \times \, \frac{1}{2} L_{choke}\hat{I}_{choke}^2 \\
&= 576.0 \, (kJ)
\end{aligned}
\tag{3.8}
$$

Table 3.2 summarizes the calculations that are associated with the LC-resonant cell. Two magnet girders form one of twenty-four superperiods of the Booster. Figures 3.6 (b) and (c) show tapered pole faces of a combined-function magnet when its physical aperture is viewed from the beam direction.

Table 3.2: Magnet Resonant Cell Components

L_{D-mag}	(D-magnet inductance)	10.7 (mH)
L_{F-mag}	(F-magnet inductance)	10.7 (mH)
L_{choke}	(choke inductance)	42.0 (mH)
I_{dc}	(DC-bias current)	535 (A)
$\hat{I}_{mag}$	(maximum magnet current)	967 (A)
$\check{I}_{mag}$	(minimum magnet current)	103 (A)
$I_{ac,\,mag}$	(amplitude of magnet current)	432 (A)
$\widetilde{I}_{mag}$	(rms magnet current)	616 (A)
$\hat{I}_{choke}$	(maximum choke current)	755 (A)
$\check{I}_{choke}$	(minimum choke current)	315 (A)
$\widetilde{I}_{choke}$	(rms choke current)	557 (A)
$I_{ac,\,choke}$	(amplitude of choke current)	220 (A)
$\hat{E}_{mag,\,tot}$	(peak total energy at magnets)	480.0 (kJ)
$\hat{E}_{choke,\,tot}$	(peak total energy at chokes)	576.0 (kJ)
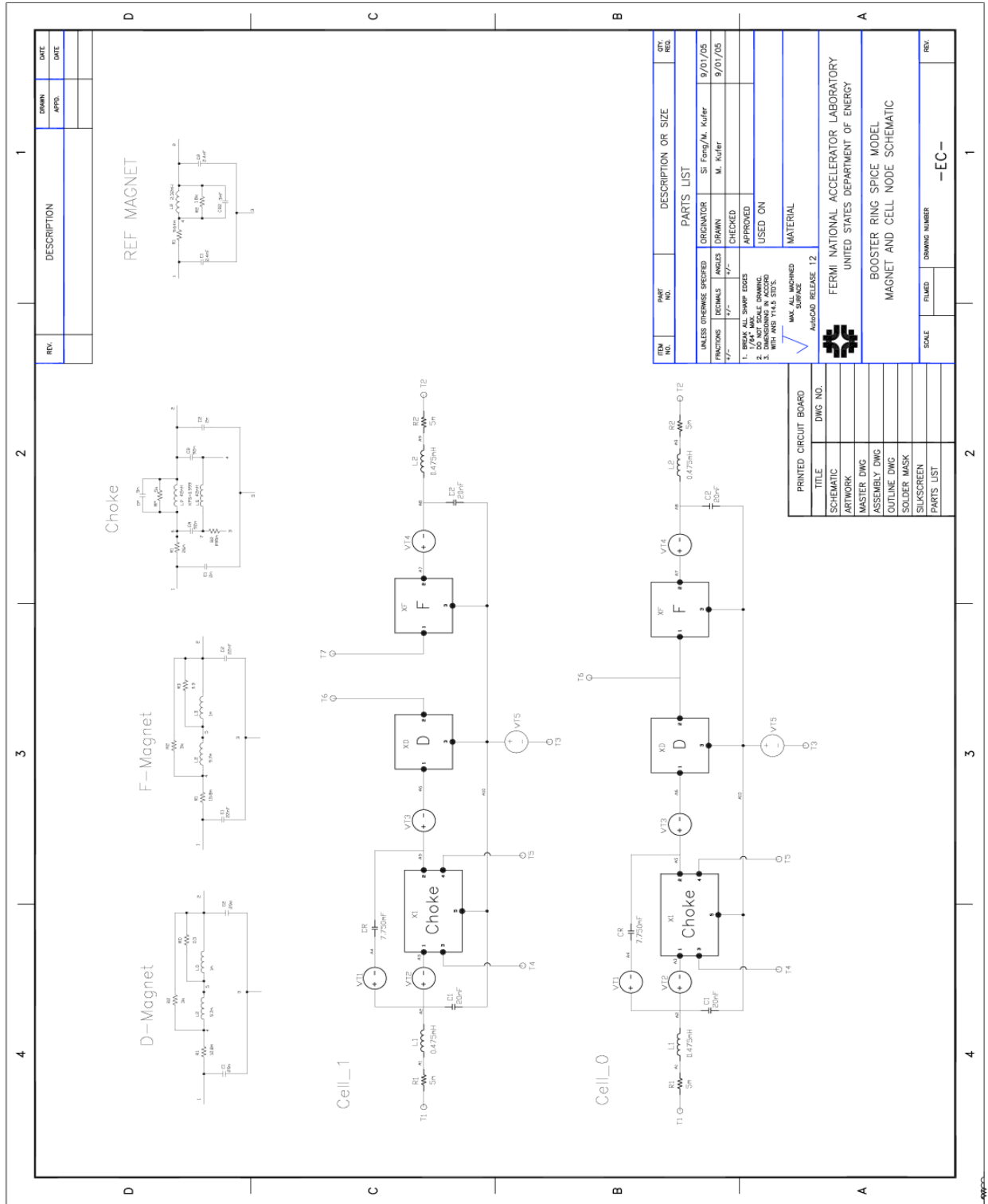
Figure 3.1: The equivalent circuits of a LC-resonant magnet cell for the Booster
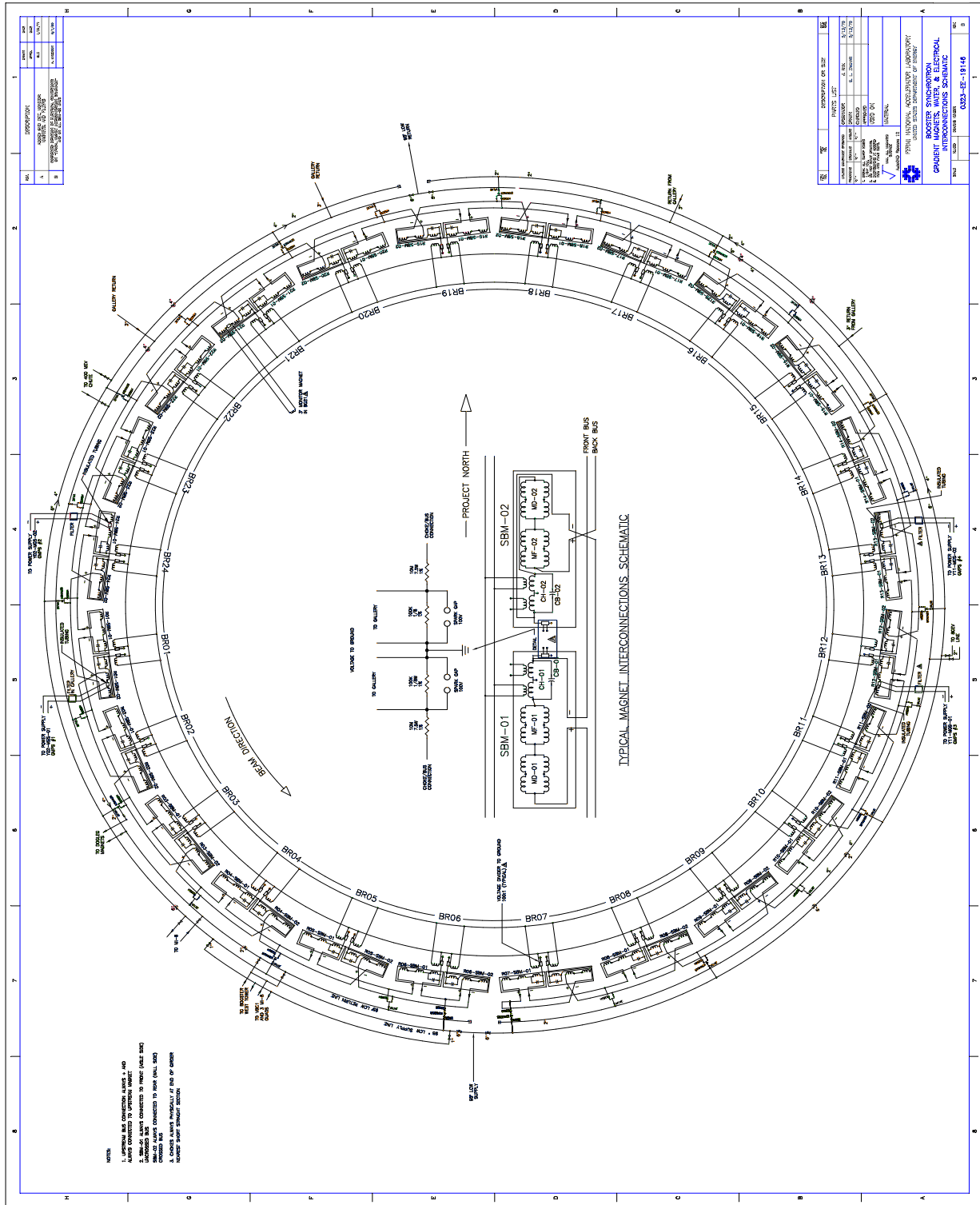
Figure 3.2: Schematic of the interconnection of Booster gradient magnets and GMPS'
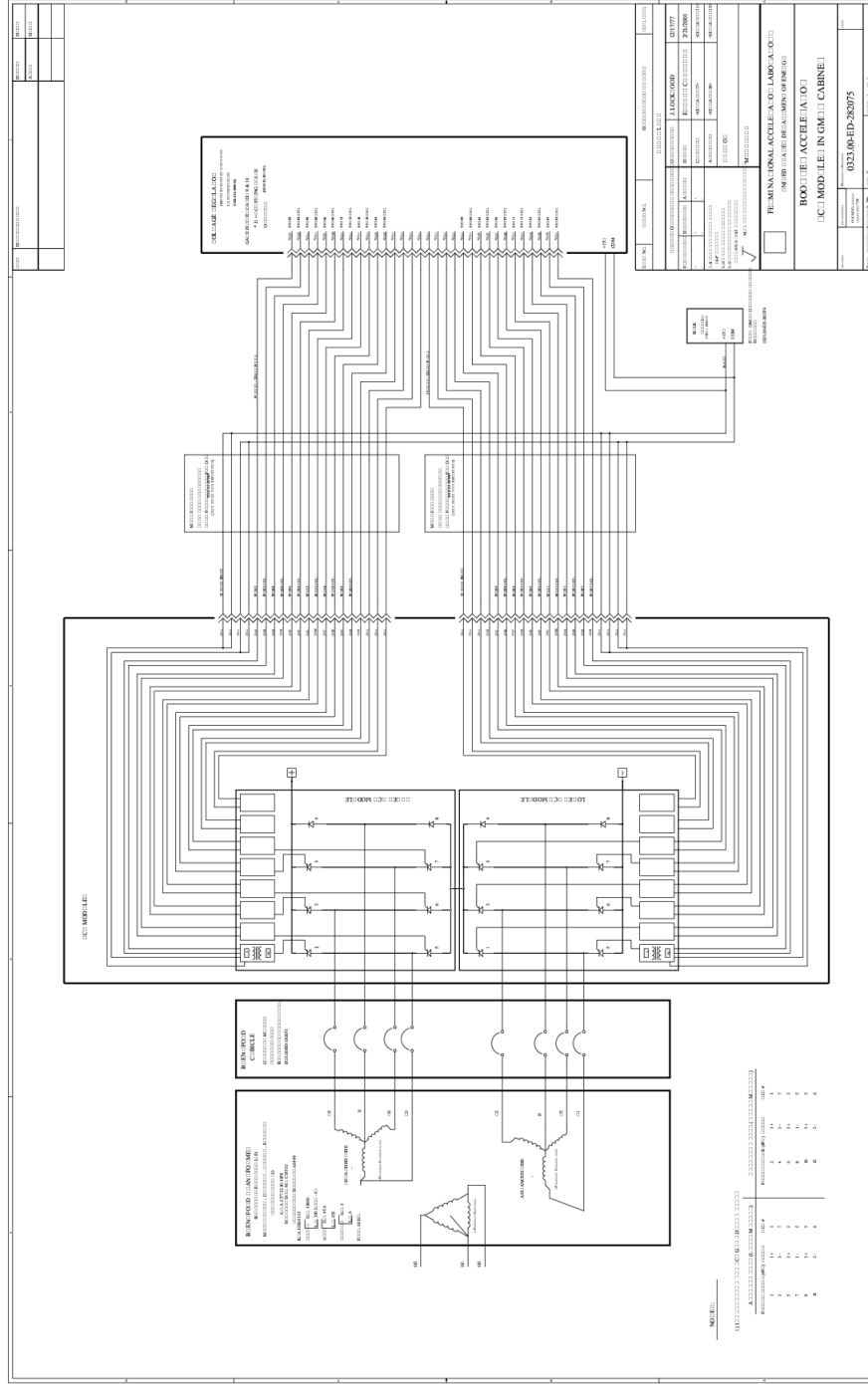
Figure 3.3: Three-Phase Silicon-Controlled Modulator (SCR) in a GMPS unit
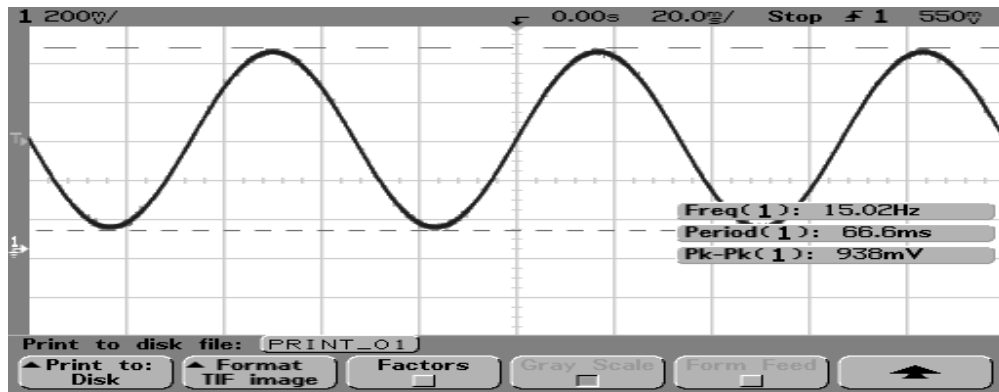
(a) 15-Hz Current waveform at GMPS 1
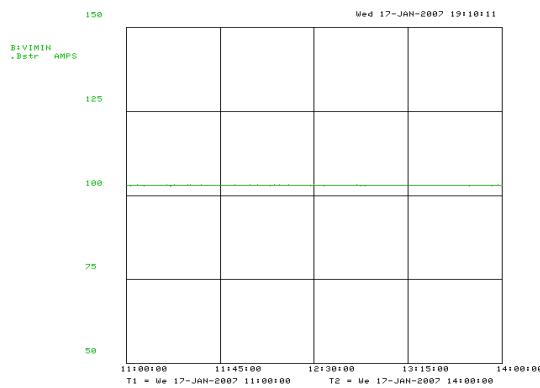
(b) minimum current (B:VIMIN)
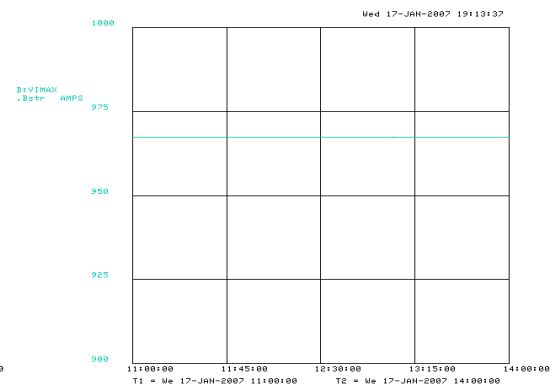
(c) maximum current (B:VIMAX)

Figure 3.4: ACNET (Accelerator Control NETwork) lumberjack plots of the Booster GMPS currents. The ACNET device name is indicated on the left-hand side of (b) and (c).

(a) GMPS rack

(b) GMPS 3 and GMPS 4

Figure 3.5: GMPS units

(a) Two Booster combined-function magnets on a girder
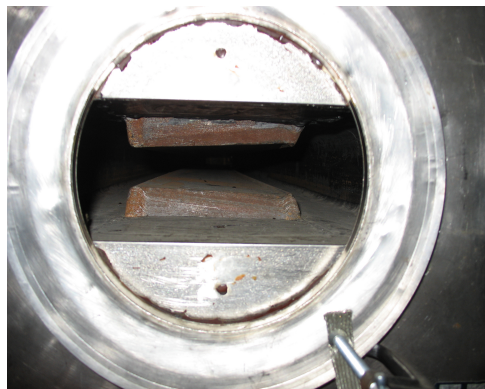
(b) physical aperture
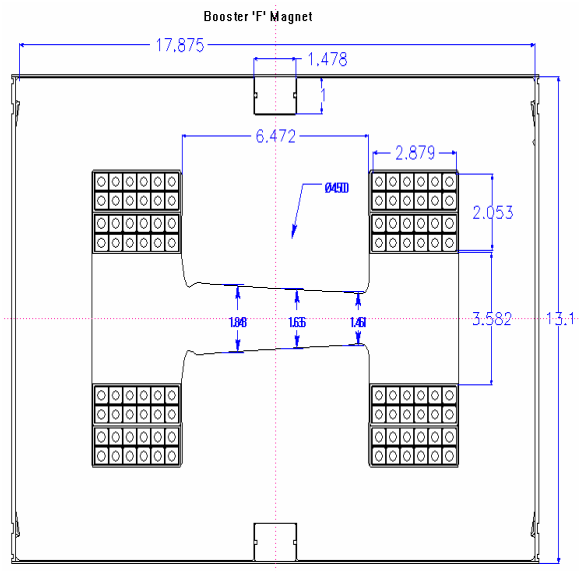
(c) Cross-sectional view of a F-magnet [14]

Figure 3.6: [(a)] Focusing and de-focusing magnets with capacitor banks on a girder; [(b) and (c)] When viewed from the beam direction, tapered pole faces for a combined-function magnet are shown.

3.2 Noise Classification

3.2.1 Electromagnetic Interferences

Electromagnetic interference (EMI) [32] noise results from rapid changes in voltage and current in a power supply. EMI noise transmissions are characterized as either *radiative* or *conductive*. Conductive EMI noise, such as differential-mode (DM) and common-mode (CM) noise, is usually several orders of magnitude higher than the radiative EMI and can be more harmful. The differential-mode voltage (V_{DM}) can be measured between source lines, whereas the common-mode voltage (V_{CM}) is measured between the power lines and ground. Common-mode voltage fluctuations induce common-mode current, in addition to the inherent current ripples arising from sudden potential changes in the power-supply system. The EMI problem is thereby worsened and could result in larger current fluctuations, or the system damage.

3.2.2 Common-Mode Noise and Differential-Mode Noise

The differential-mode noise is smoothed by a 15-Hz low-pass filter in each GMPS unit. Therefore, only the common-mode noise is of concern in the Booster power and magnet systems. As illustrated by Figure 3.7, if common-mode noise appearing on the ground line is not sufficiently smoothed, it could have significant effects on the system. The common-mode voltage (V_{CM}) and differential-mode (V_{DM}) voltage are calculated as follows:

$$\left. \begin{aligned} V_{CM} &= V_{+G} + V_{-G} \\ V_{DM} &= V_{+G} - V_{-G} \end{aligned} \right\} \tag{3.9}$$
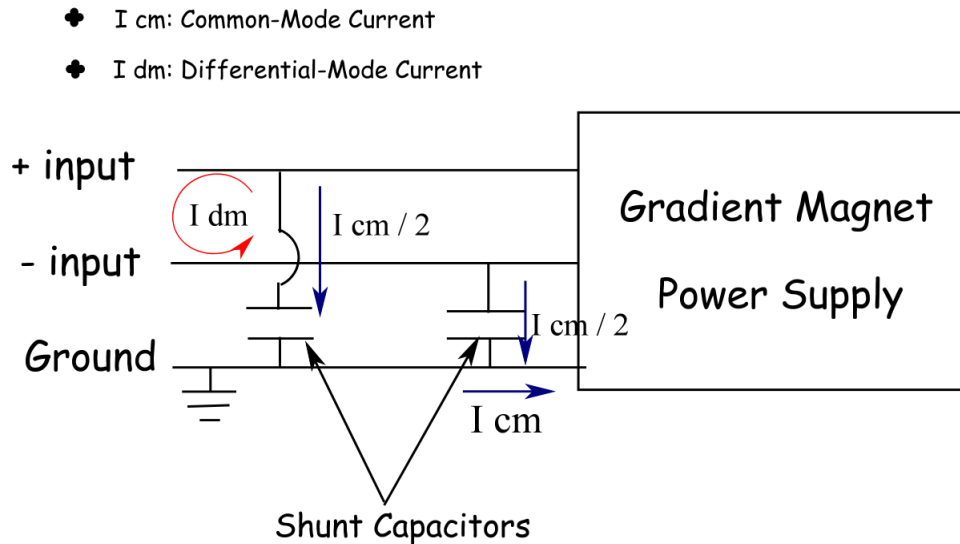
Figure 3.7: Common-mode current and differential-mode current at the Booster GMPS

3.3 Measurement Techniques and Analysis of Common-Mode Noise

The waveforms of both V_{+G} and V_{-G} signals are measured at the two leads (terminals) on the GMPS control rack. The common-mode noise and differential-mode noise are calculated using the math-function keys available on the oscilloscope [1]. As shown in the Figure 3.8, the waveforms of V_+ to ground (V_{+G}) and the inverted voltage of V_- to ground (-V_{-G}) are overlaid (for easy comparison) on the same time scale. The waveforms of V_{+G} and V_{-G} should be 180 degrees out of phase. However, we see phase lags between the two waveforms (V_{+G} and V_{-G}) as shown in Figure 3.8. In this experimental measurement, the inverted V_{-G} is first measured, and then subtracted from V_{+G} to obtain the V_{CM} waveform. For the calculation of differential-mode voltage (V_{DM}), we add up V_{+G} and V_{-G} without

---

[1]The model name of the digital oscilloscope [33] used for the measurements is Agilent 54622A, and the part number 54622-97014.

inversion. Figures 3.10 and 3.11 show V_{+G}, V_{-G}, and well-smoothed differential-mode noise at each GMPS. Figures 3.8 through 3.24 are image files saved directly from the oscilloscope at the time of the measurements. As indicated on the upper frame of each display window shown in Figures 3.8 and 3.9, the voltage divisions are set to 500 mV/div and the sweep speed is set to 20 ms/div. Figures 3.12, 3.13, 3.14, and 3.15 show the impulses of power spectra from a Fourier analysis displayed against the V_{+G} and V_{-G} waveforms over 9 cycles. Here, 9 cycles correspond to the duration of 0.6 second.

Peak-to-peak measurements quantify the potential differences and phase lags between two signals. Potential differences are displayed in Figures 3.16 through 3.19. Phase lags are shown in Figures 3.20 through 3.23. We calculate the fractional difference in amplitudes ($|\frac{\Delta V}{V}|$) by taking the difference between V_{+G} and inverted V_{-G} and dividing by V_{+G}. Figures 3.16 through 3.19 show that there are substantial potential differences in V_{+G} and V_{-G} for each GMPS. The built-in cursor function is used to measure the phase lag between the two waveforms as shown in Figures 3.20 through 3.23. For GMPS 1, there is a phase lag of 0.6 msec between V_{+G} and V_{-G}, and the amplitude of V_{-G} is about 20 % larger than V_{+G}. For GMPS 2, the phase lag is about 4 msec, and the fractional potential difference is 47.4 %. We find that the phase lag and potential differences for each GMPS unit is different. Table 3.3 summarizes the potential difference and the phase lag measured for individual GMPS units.

Table 3.3: Difference in voltage amplitudes and phase lag at each GMPS

GMPS No.	V_{+G} (V)	V_{-G} (V)	$\left|\frac{\Delta V}{V}\right|$	ΔX(msec)
GMPS 1	1.577	1.905	20.8 %	0.6
GMPS 2	3.232	1.699	47.4 %	4.0
GMPS 3	1.598	1.740	8.9 %	1.4
GMPS 4	1.581	1.743	10.2 %	4.6

In summary, the following are the two primary sources of common-mode noise:

(1) phase lags (ΔX) between V_{+G} and V_{-G}

(2) amplitude (potential) difference between V_{+G} and V_{-G}

Because of the common-mode noise, when V_{+G} and V_{-G} are added (point-by-point) on the scope, they do not cancel out each other. The ripples on each waveform add up and the common-mode voltage stands out.

Figure 3.24 shows the current ripples measured on the main magnet bus running through GMPS 1. Because the current signal is small, transducer electronics and a current amplifier (TA22 Texas Instruments) are used to amplify the signals so they can be observed with an oscilloscope. In comparison, Figure 3.25 shows the power spectrum of the O-U noise generated from the new noise module of the ORBIT-FNAL package. We note that the power spectrum of the modeled noise closely matches that of real noise. As shown in Figure 3.24, the power spectra of the current in the common bus are exponentially attenuated above the 15-Hz resonance frequency domain. This illustrates that the bus current contains *non-white*, or *off-white* noise.

3.3.1   Power Spectra of Noise: FFT Analysis

The measured common-mode voltages from all four GMPS units and the current signal with ripples for GMPS 1 are Fourier-analyzed. To provide *real-time* proof of the presence of offending interference in the power-supply system, all the signals are analyzed *on the fly* without being transported to any commercial software for the post-measurement analysis. We are able to perform the *real-time* analysis with the aid of the built-in FFT-function feature on the scope in use. The Figures 3.8 through 3.24 are the real-time graphics saved on the scope. The resolution of a resonant peak, or FFT bin size, is determined by the FFT sampling rate and the number of points. The number of points on the scope that we use is fixed at 2048. As such, the FFT sampling rates and the span of the frequency domain

are controlled in accordance with the Nyquist sampling theorem. In addition, in order to increase the resolution at the frequency peak, the Hanning window is selected over a flat-top or a rectangular window. The following is a list of the FFT settings that we use on the scope:

(1) FFT Sampling Rate, $f_s = 3.53$ kSa/s

(2) FFT bin size, $\Delta f = 1.04$ Hz

(3) Frequency-domain span = 1.67 kHz

(4) Horizontal scale = 167 Hz/div

(5) Vertical scale = 20 dB/div

According to the Nyquist sampling theorem, the oscilloscope that we use determines FFT sampling rate from the chosen span of Frequency domain.

3.4 Equivalent Circuit Model

To find out whether there are any offending resonances floating around the Booster magnet system, serving as noise amplifiers, the equivalent circuit modeling is also carried out. Since a string of 24 magnets in a quadrant of the Booster magnet system are connected in series, they are treated as a transmission line. We employed the B^2 SPICE [34] A/D Version 4, which is one of many versions of commercial SPICE simulators. Figure 3.26 shows the results of AC analysis of the equivalent circuits. The current is peaked at 15 Hz and a cluster of minor peaks are found in a few kHz range. It is suspected that the offending resonances above 15 Hz, in higher frequency region, could amplify the offending noise, when the noise frequencies coincide with those of resonances. The presence of the resonances will enhance the formation of beam halo, eventually resulting in beam loss.
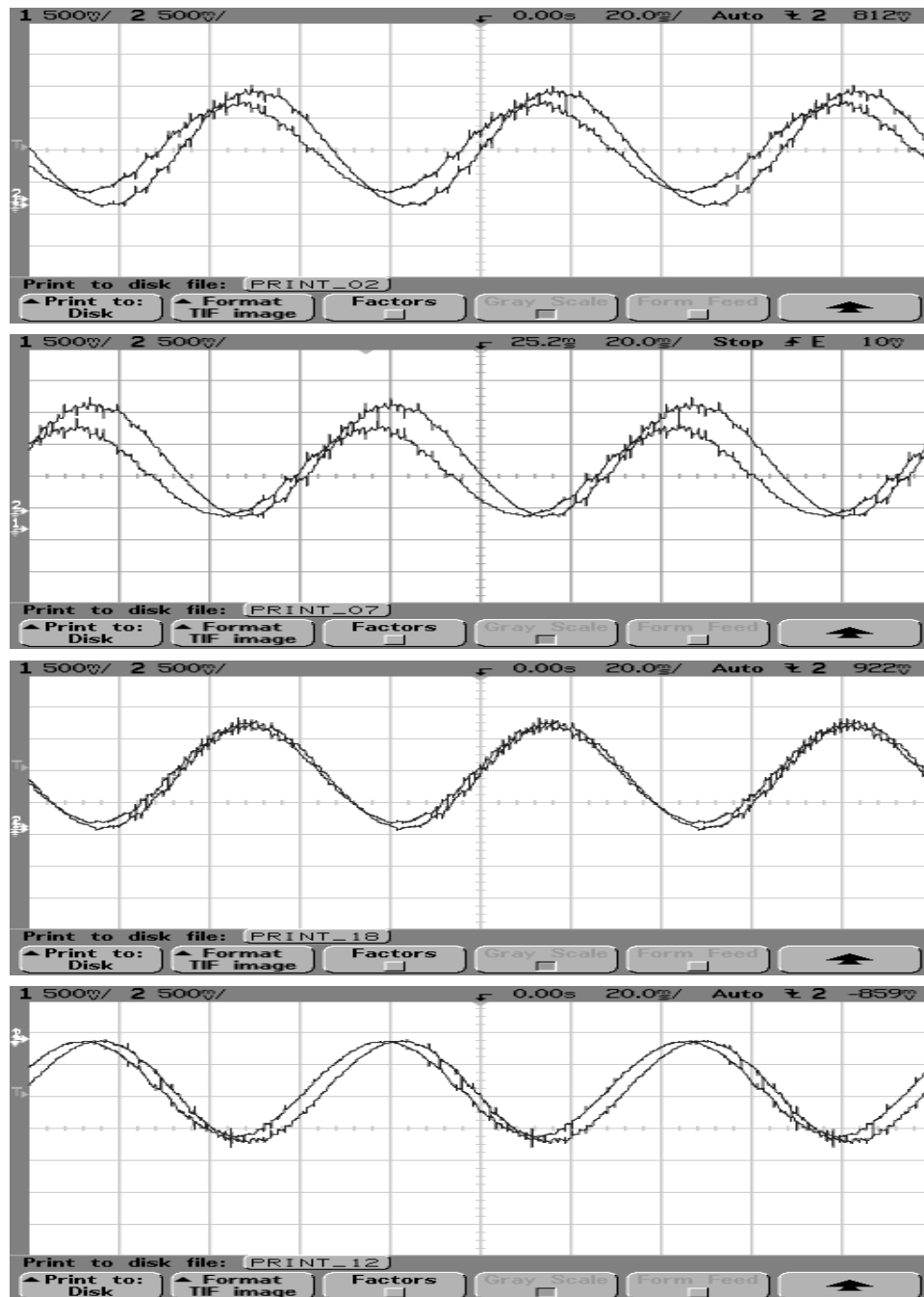
Figure 3.8: The waveforms of V_{+G} and inverted V_{-G}. Progressing from top to bottom, each waveform shown on the oscilloscope display corresponds to GMPS [1] through GMPS [4]. As indicated on the upper edge of each display, the voltage division is set to 500 mV/div and sweep speed to 20 ms/div.
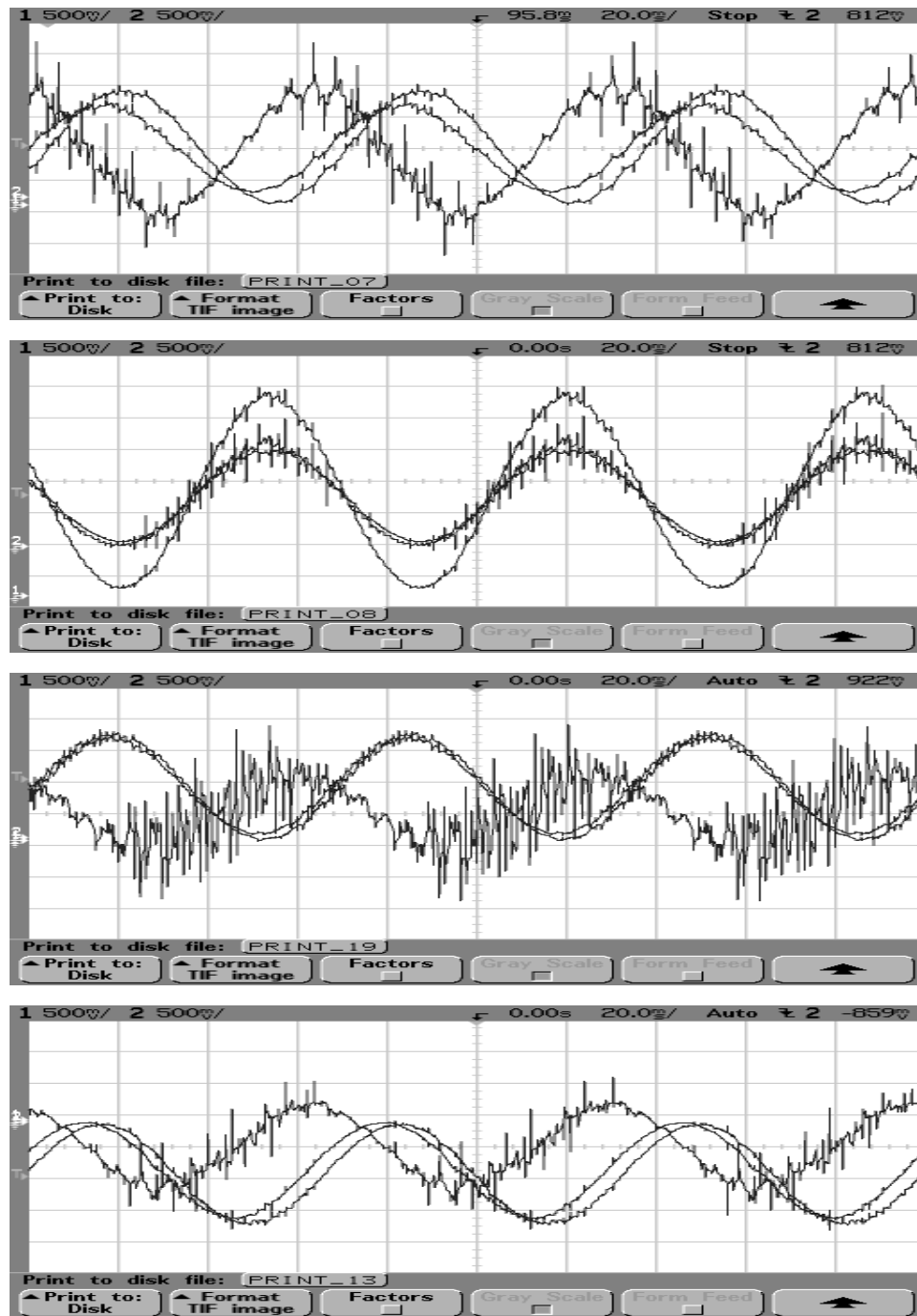
Figure 3.9: The waveforms of V_{CM} are plotted against those of V_{+G} and inverted V_{-G}. Starting from top to bottom, each display corresponds to the GMPS [1] through the GMPS [4]
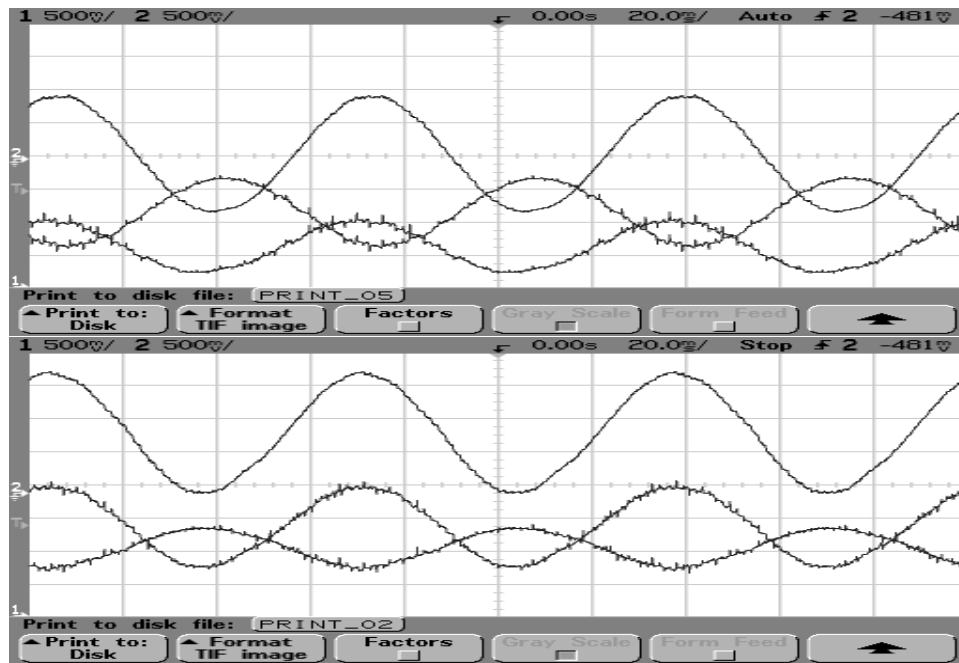
Figure 3.10: The upper waveform is differential-mode voltage (V_{DM}). A pair of lower waveforms are V_{+G} and V_{-G}. [Upper Figure] GMPS 1; [Lower Figure] GMPS 2
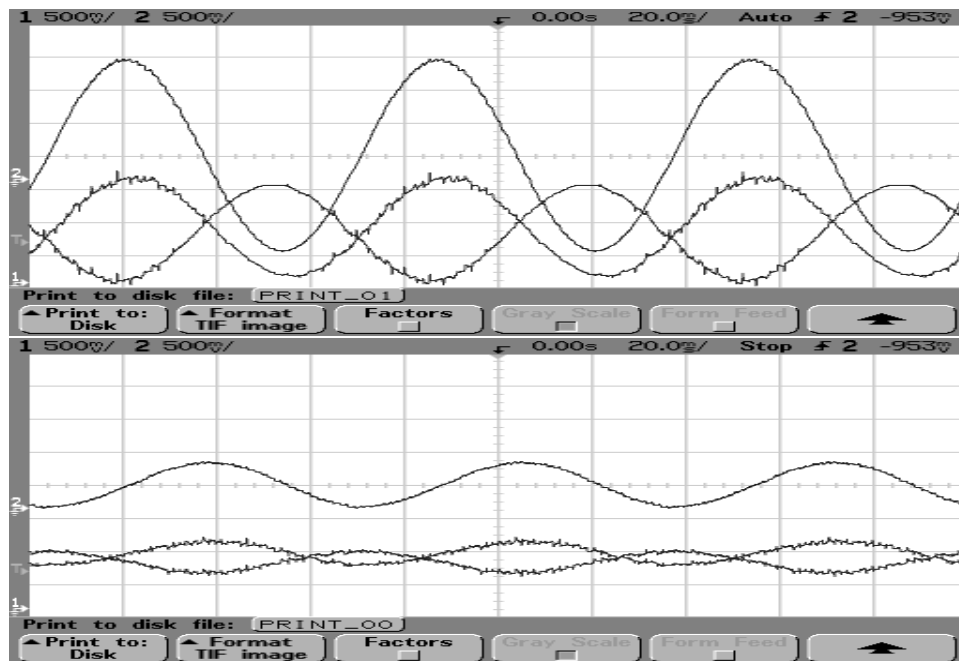
Figure 3.11: [Upper Figure] GMPS 3; [Lower Figure] GMPS 4
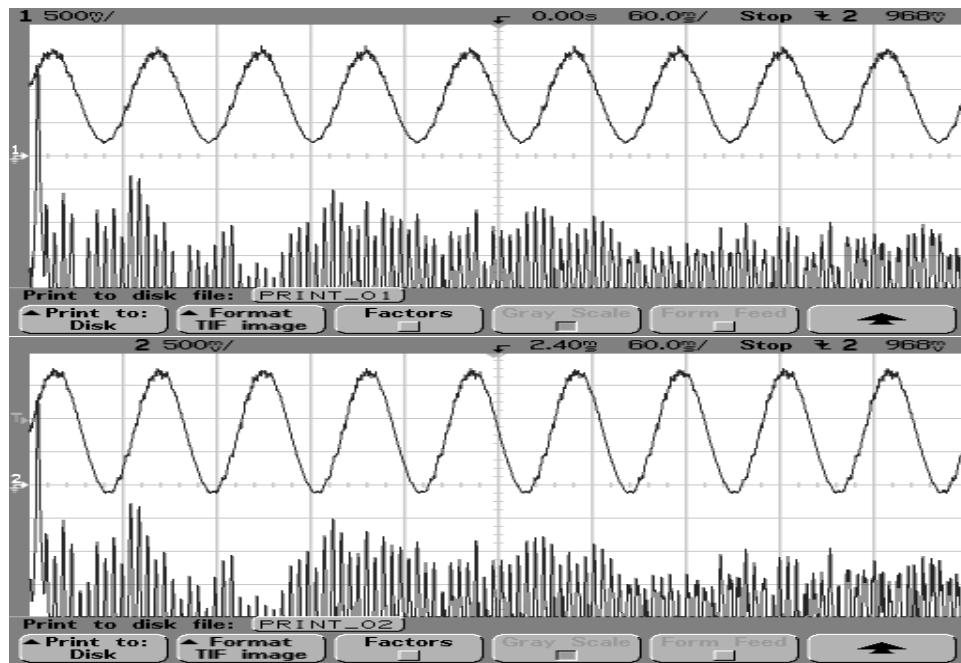
Figure 3.12: [**GMPS 1**] [top] The waveform of V_{+G} and FFT power spectra; [bottom] The waveform of inverted V_{-G} and FFT power spectra
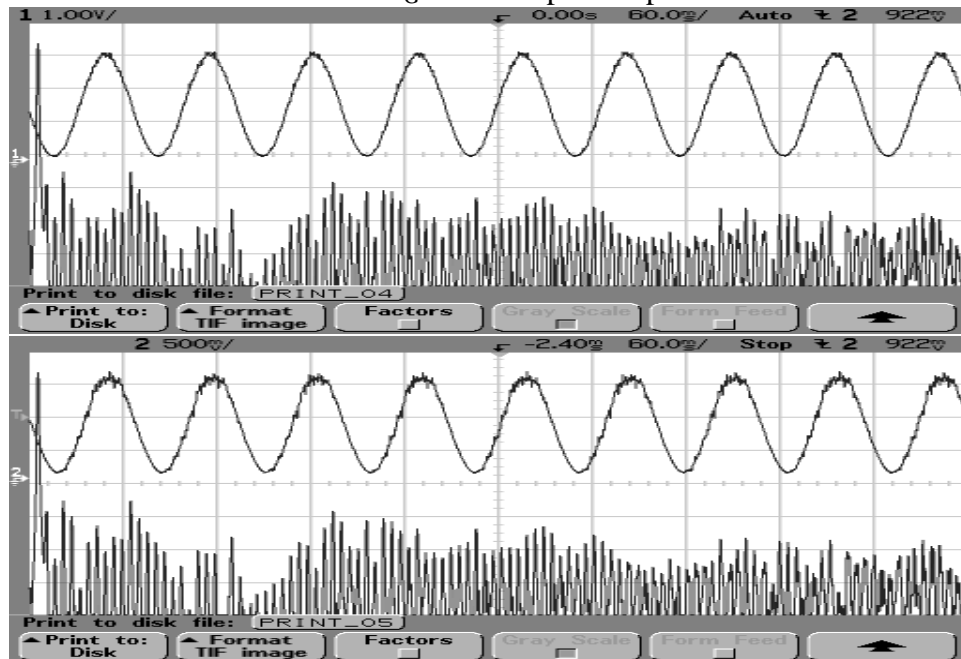
Figure 3.13: [**GMPS 2**] [top] The waveform of V_{+G} and FFT power spectra; [bottom] The waveform of inverted V_{-G} and FFT power spectra; The first resonance peak in lower frequency domain is located at 15 Hz.
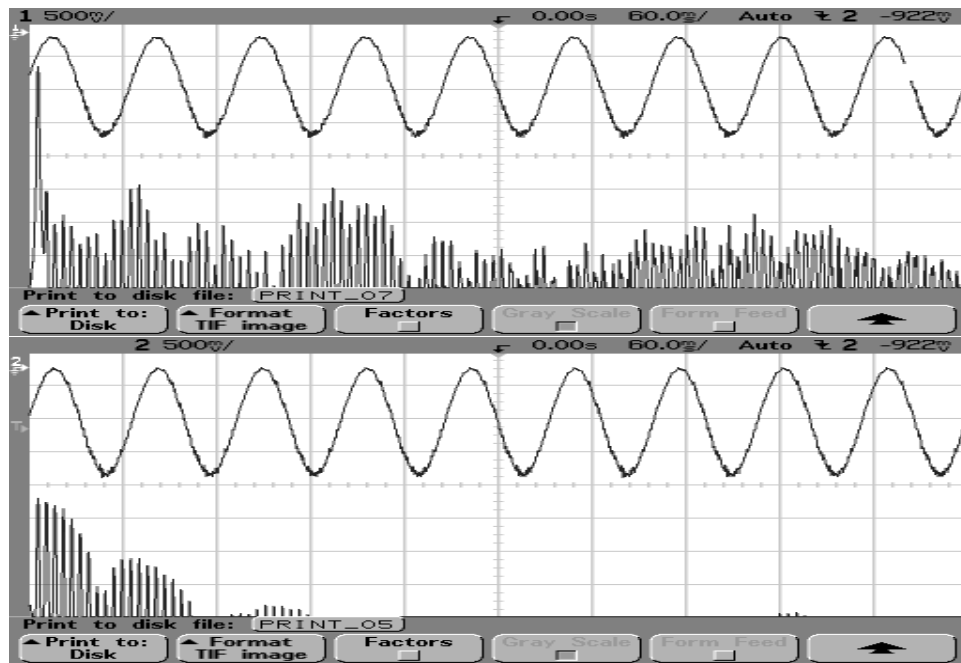
Figure 3.14: [**GMPS 3**] [top] The waveform and power spectra of V_{+G}; [bottom] inverted V_{-G}
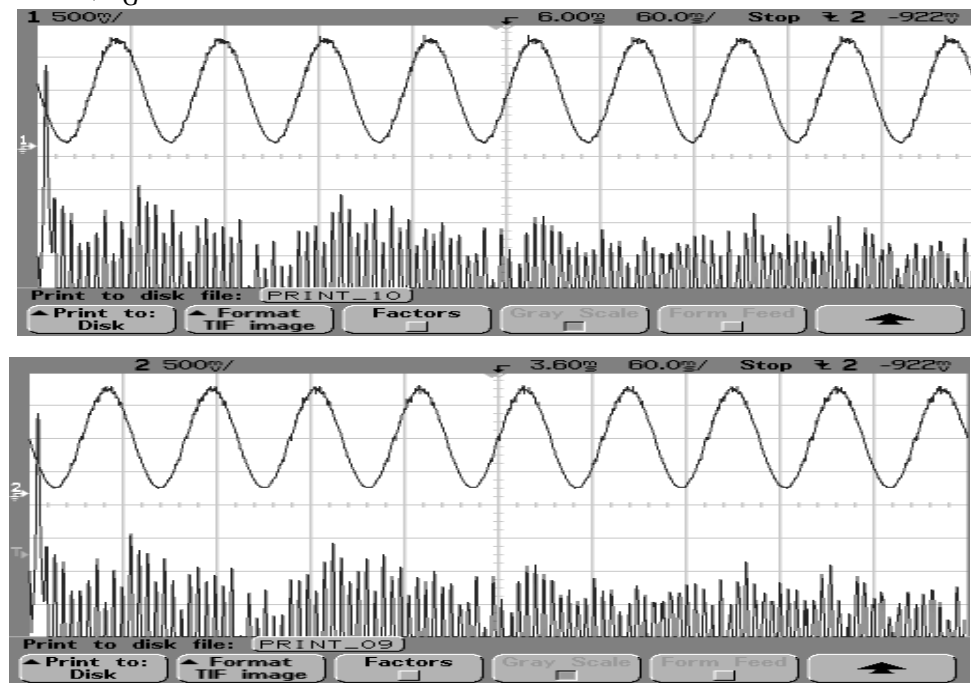
Figure 3.15: [**GMPS 4**] [top] The waveform and power spectra of V_{+G}; [bottom] inverted V_{-G}
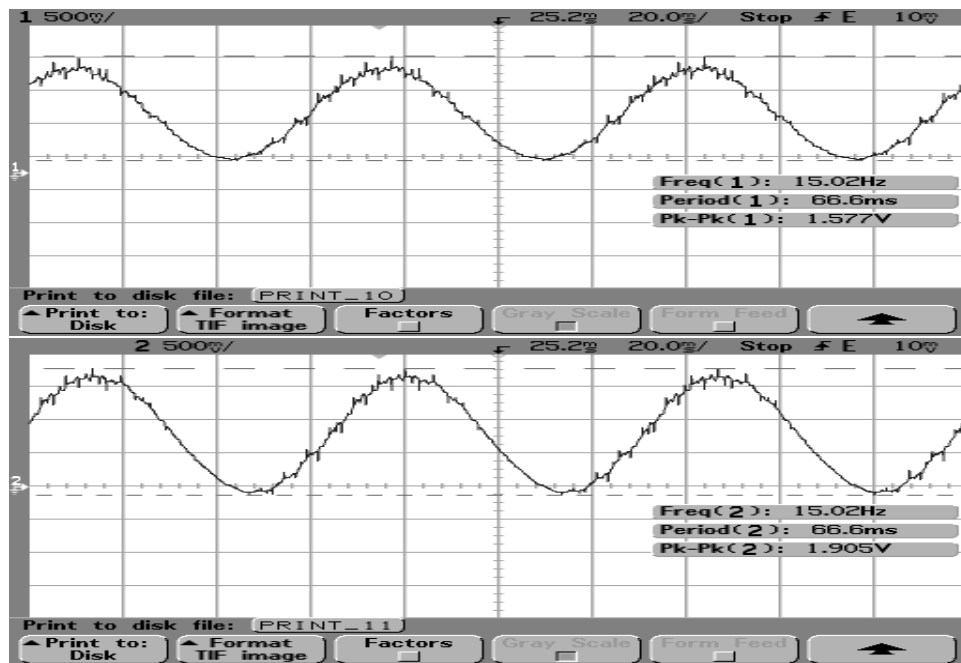
Figure 3.16: [**GMPS 1**] Peak-to-peak amplitudes (Pk-Pk(1) and Pk-Pk(2)) and frequency of each voltage waveform
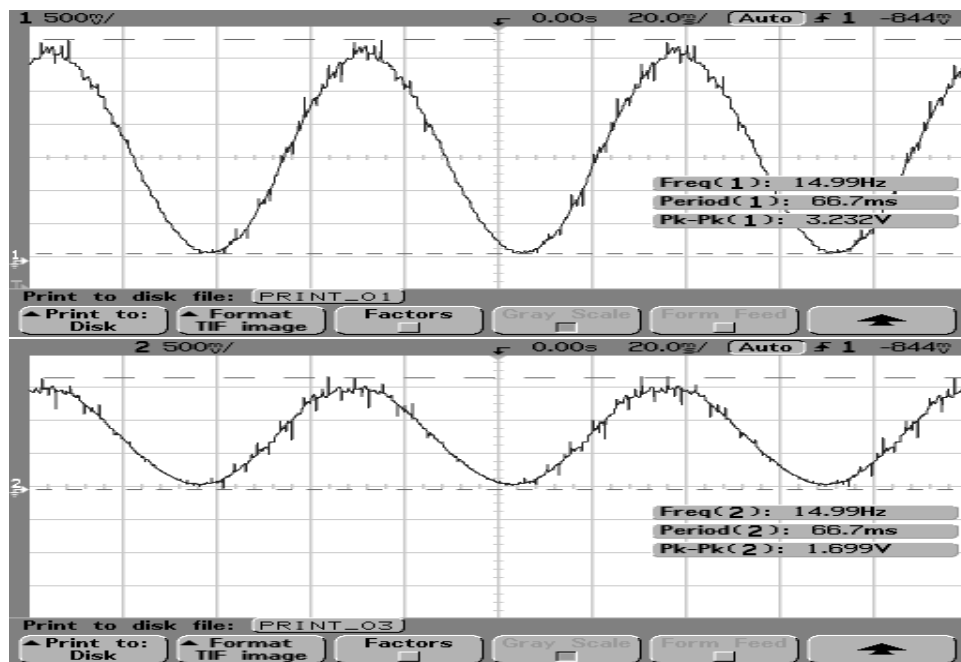
Figure 3.17: [**GMPS 2**] Peak-to-peak amplitudes and frequency of each voltage waveform
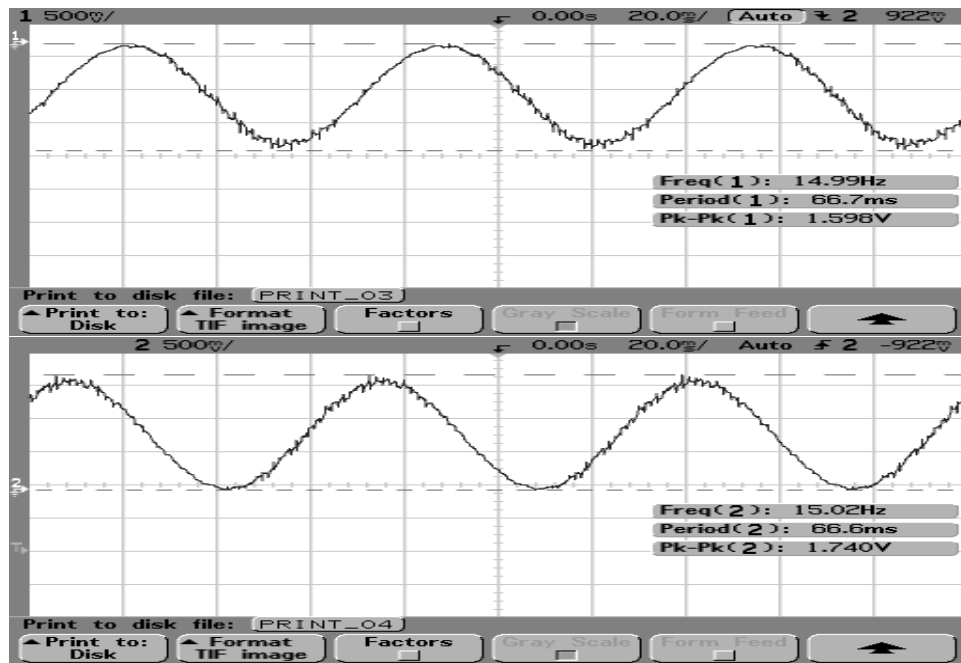
Figure 3.18: [**GMPS 3**] Peak-to-peak amplitudes and frequency of each voltage waveform
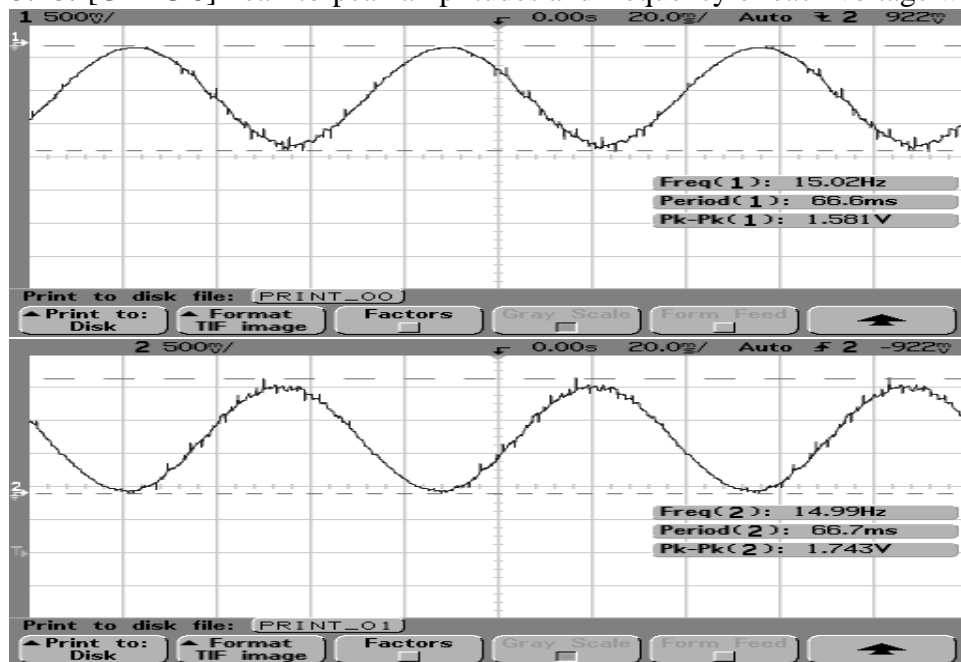
Figure 3.19: [**GMPS 4**] Peak-to-peak amplitudes and frequency of each voltage waveform
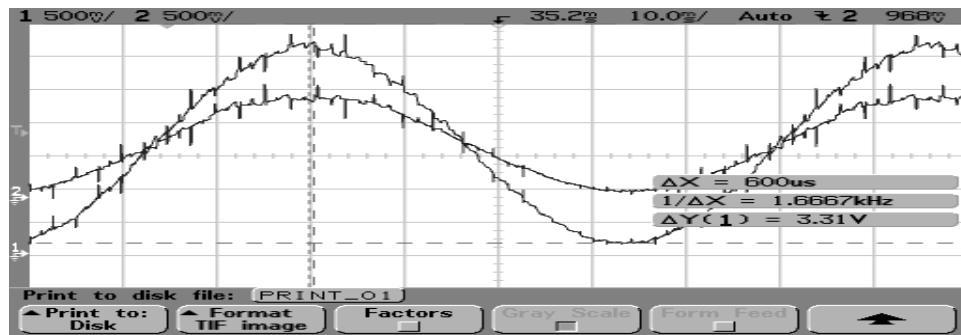
Figure 3.20: [**GMPS 1**] phase lag, ΔX, is 0.6 ms
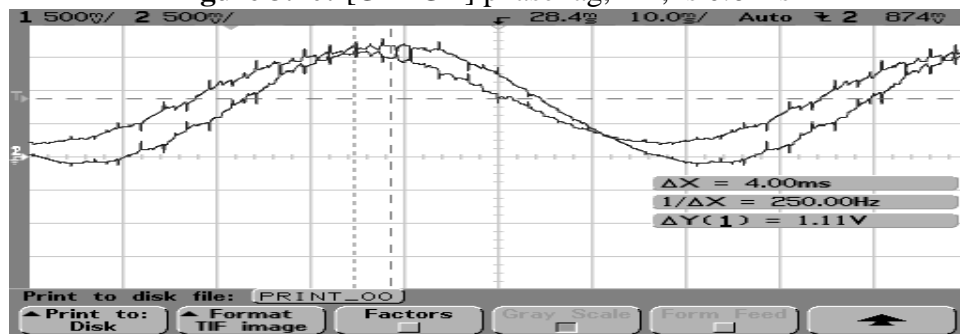
Figure 3.21: [**GMPS 2**] phase lag, ΔX, is 4.0 ms
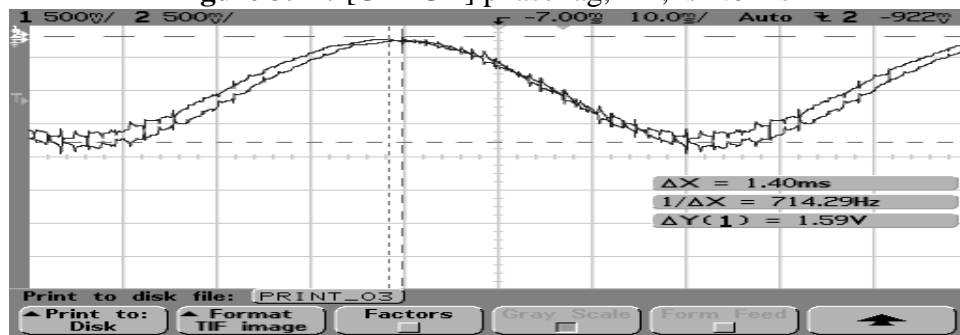
Figure 3.22: [**GMPS 3**] phase lag, ΔX, 1.40 ms
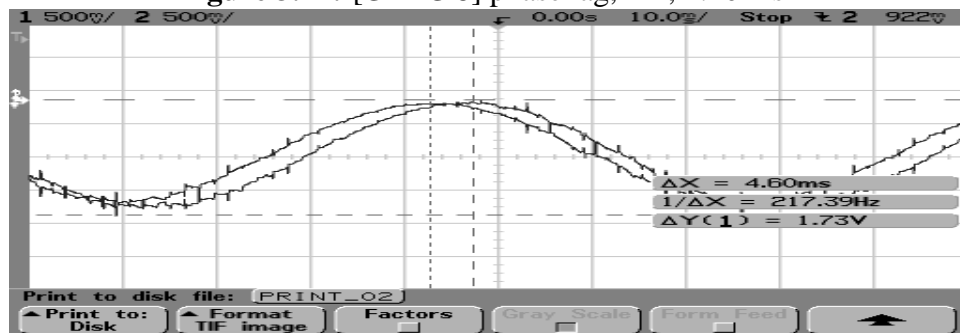
Figure 3.23: [**GMPS 4**] phase lag, ΔX, 4.60 ms
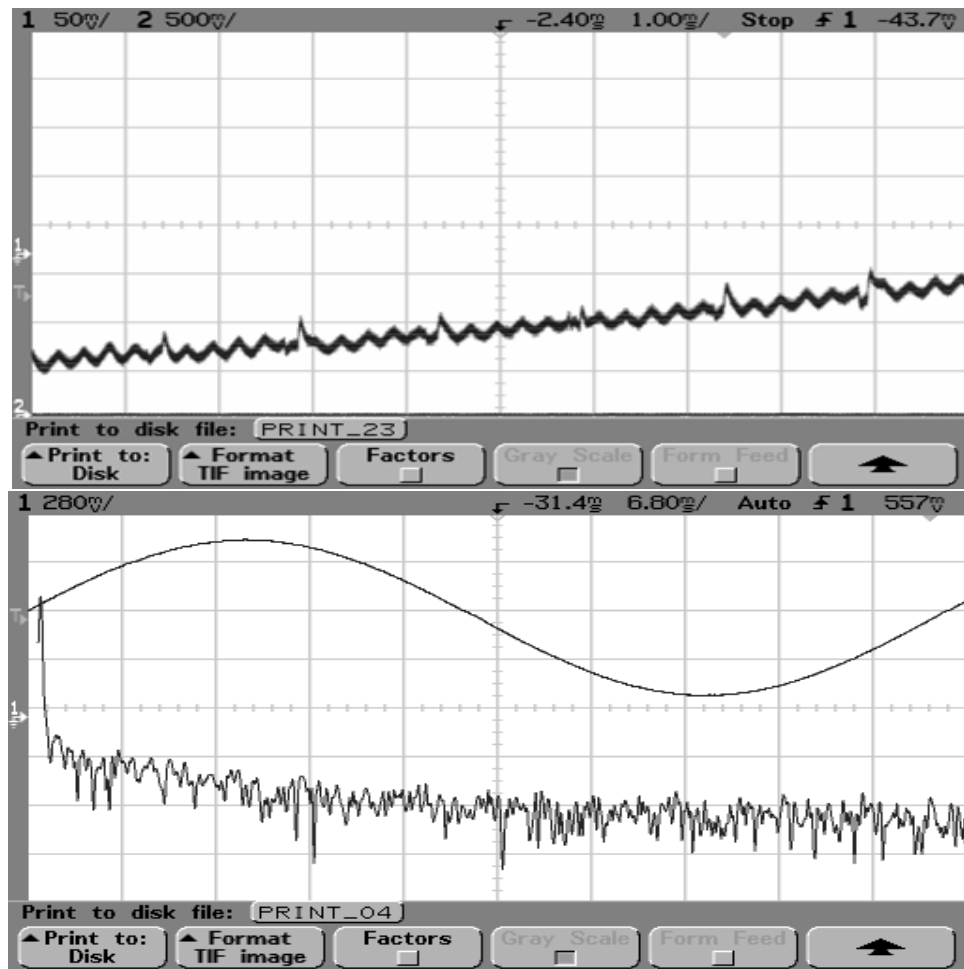
Figure 3.24: [upper] Current ripples on a linear ramp of the sinusoidal waveform. The currents are sampled directly from the magnet bus line at GMPS 1. [lower] FFT impulses and 15-Hz current waveform of one cycle; the horizontal scale is 167 Hz/div and the vertical scale is 20 dB/div.
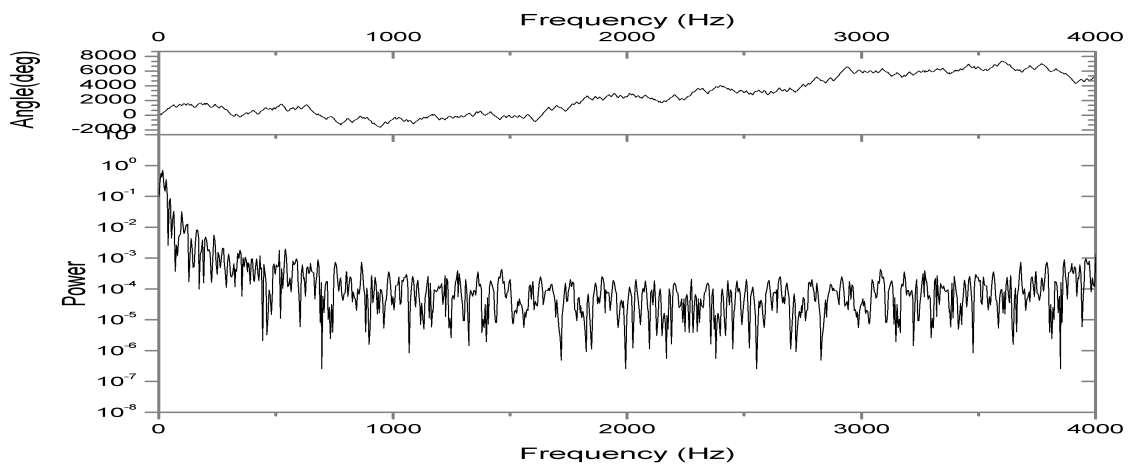
Figure 3.25: The power spectra of Ornstein-Uhlenbeck noise is matched close to that of measured current ripples in Figure 3.24.
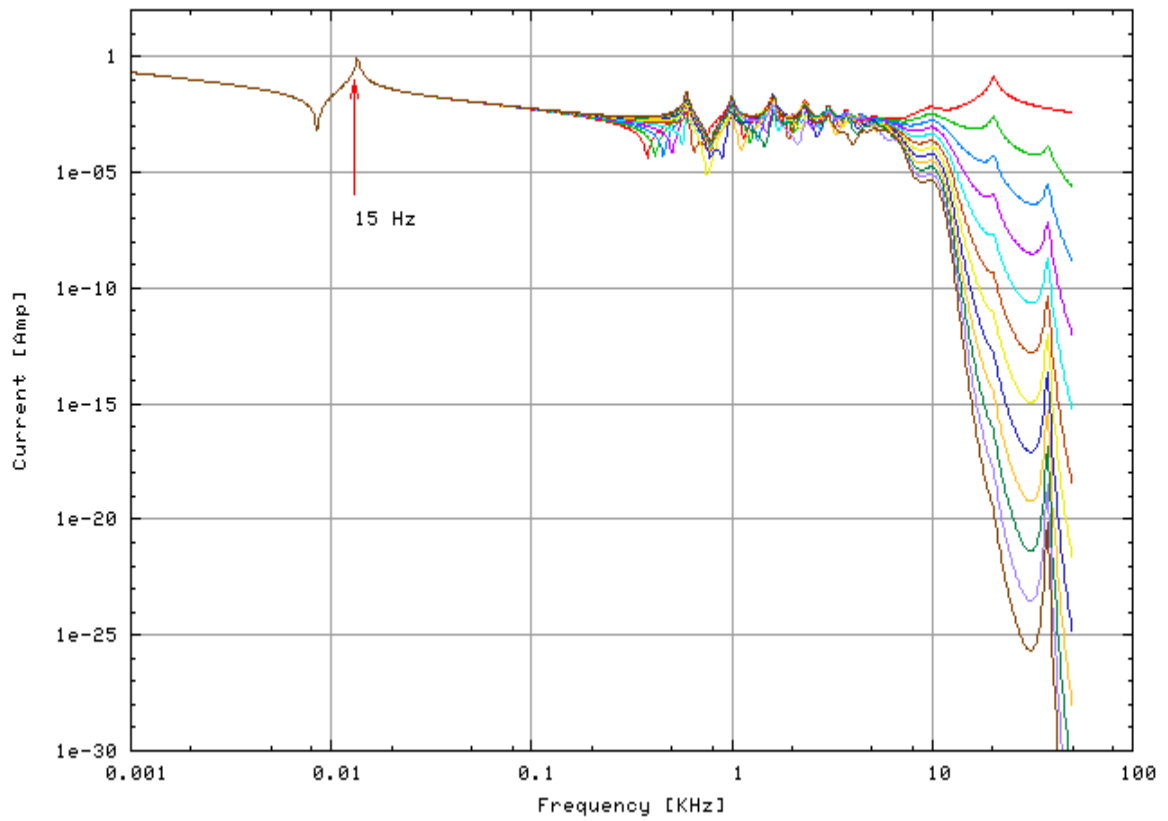
Figure 3.26: [SPICE simulation]: Current vs. Frequency: currents flowing through a string of 12 magnet cells driven by one GMPS. Progressing from top to bottom, the lines correspond to magnet cell [1] through magnet cell [12].

Chapter 4

Impact of GMPS Current Fluctuations on the Booster Beam

In previous chapters, we constructed a realistic stochastic noise model of the Booster. Here, we present and discuss a variety of beam dynamics calculations to investigate adverse (but unavoidable) impact of GMPS current fluctuations on the Booster beam. We first determine values of the stochastic parameters (autocorrelation time, time step, and noise strength) that characterize the GMPS noise, according to the measurements and analyses presented in the preceding chapter.

4.1   Determination of Characteristic Noise Parameters

4.1.1   Autocorrelation Time

In our stochastic noise model, the autocorrelation time (τ_{ac}) represents the memory span of noise in the physical time scale of interest. For example, in special relativity the Lorentz factor ($\beta = v/c$) is used to represent velocity in units of the speed of light (c)[1]. By analogy,

---

[1] c = 2.99792458×10^8 m/s [36]

in numerical calculations and modeling of stochastic noise the time step (Δt) normalized by the autocorrelation time (τ_{ac}) is used to represent a physically meaningful time scale. A normalized time step ($\omega_{ac}\Delta t = \Delta t / \tau_{ac}$) appears in the argument of the exponential function in Eqn. (2.23). The time step (Δt) that is multiplied by the autocorrelation frequency (ω_{ac}) is in units of the autocorrelation time in our model. Our experimental measurements yield an autocorrelation time for the GMPS current ripple in the range of a few miliseconds. In our numerical simulations, this time scale corresponds to about 1,000 tracking turns of the Booster beam at injection energy.

4.1.2 Time Step

Each GMPS drives current through a quadrant of the entire Booster gradient-magnet system. A quadrant is a string of 24 main gradient magnets consisting of 12 resonant cells which are connected in series. Current fluctuation ($\Delta I / I$) originating from each GMPS is transmitted to all magnets in each quadrant of the ring. Therefore, all of the 24 magnets experience the same amount of current ripple. In our stochastic noise model, measured current ripples transform into induced magnetic field fluctuations (cf. Eqn. 2.33), and impinge upon a beam, varying at each tracking turn. Hence, the time step, or noise-sampling rate is chosen to be one revolution time of 2.2 μsec at injection energy.

4.1.3 Noise Strength

According to the measurements of amplitude of current ripples ($\Delta I / I$), as shown in Figure 3.24, the strength of the Booster GMPS noise is on the order of 10^{-4}. Figure 4.1 (a) illustrates how we calculate the amplitude of current ripples sampled from GMPS 1. The deviation of actual current from the base current, or reference current, is measured. Each of four random noise nodes inserted in the Booster ring generates independent stochastic noise. The histograms of noise amplitudes in Figure 4.1 (b) are from each of four random

noise nodes. To verify that the noise module generates the O-U stochastic noise with de-
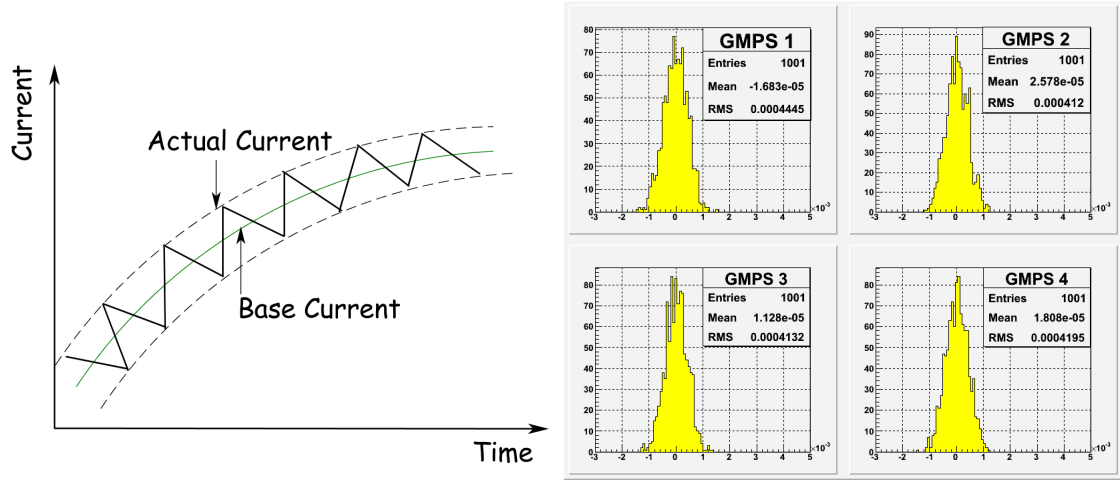
(a) Current ripples on a sinusoidal ramp

(b) Histogram of noise amplitudes at each random noise node; RMS value of each distribution is on the order of 10^{-4}

Figure 4.1: Histogram of noise amplitudes

sired strength, rms values are calculated from each histogram of noise amplitude as shown in the statistics box of Figure 4.1 (b). For the purpose of module verification, sample paths[2] are plotted in Figure 4.2 with different autocorrelation time (τ_{ac}) ranging from one revolution period (T_0) to $10^4 \times T_0$. As described earlier in subsection 4.1.2, the time step is fixed at one revolution period at the Booster injection energy. Figure 4.2 demonstrates that the autocorrelation time governs the pattern of sample path. It is therefore evident that the patterns of all sample paths are *irregular* and *non-periodic*; i.e., *indeterministic*. As stated in subsection 4.1.1, the autocorrelation time of $\sim 10^3 \times T_0$ is chosen as the Booster autocorrelation time.

---

[2] In this context, sample path means the O-U noise sampled at each tracking turn.

(a) $\tau_{ac} = 10^{-3} \times T_0$

(b) $\tau_{ac} = T_0$

(c) $\tau_{ac} = 10 \times T_0$

(d) $\tau_{ac} = 100 \times T_0$

(e) $\tau_{ac} = 10^3 \times T_0$

(f) $\tau_{ac} = 10^4 \times T_0$
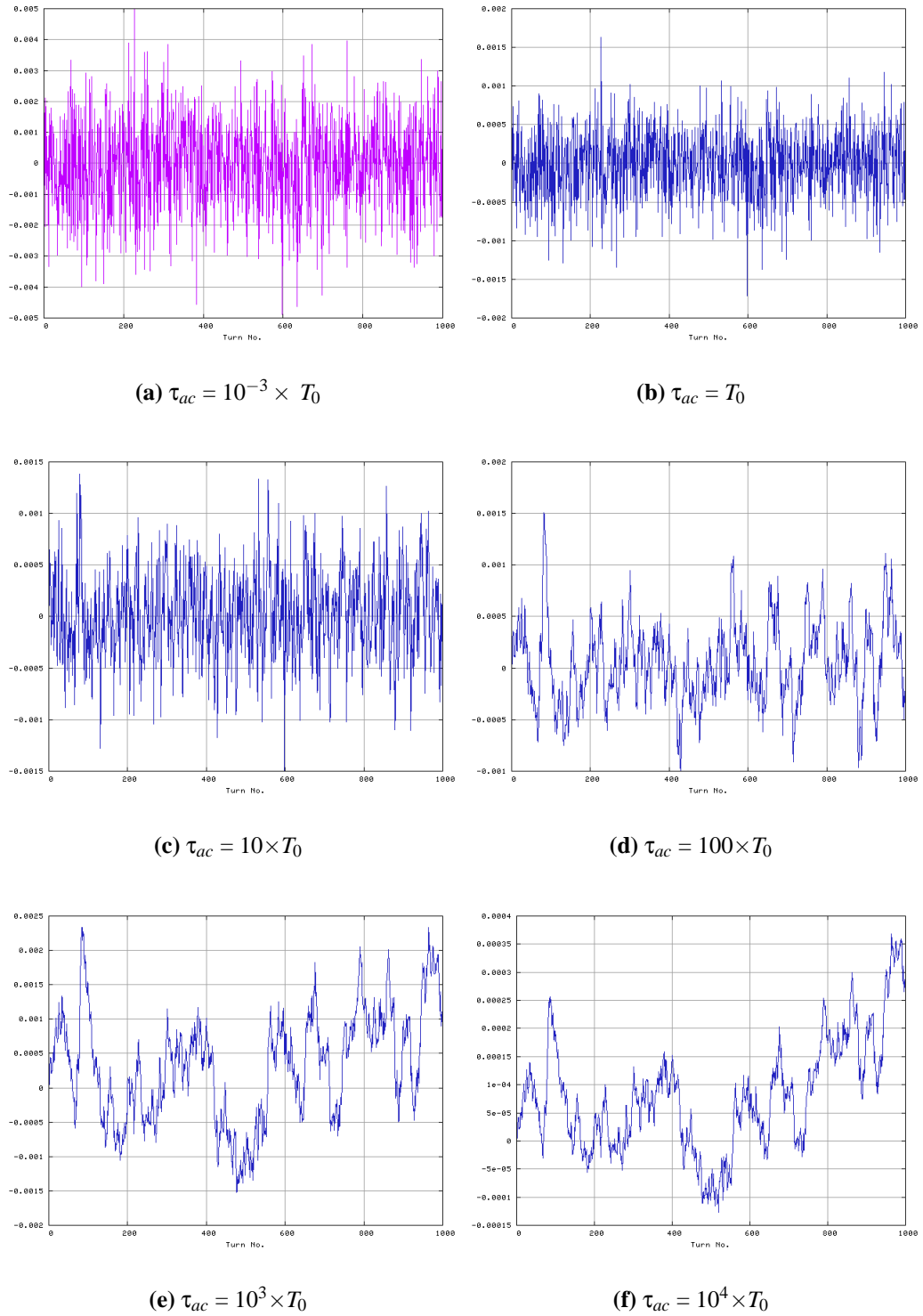
Figure 4.2: Sample paths of the Ornstein-Uhlenbeck noise over 1,000 tracking turns; the autocorrelation time (τ_{ac}) ranges from $10^{-3} \times T_0$ to $10^4 \times T_0$, where T_0 denotes one revolution period.

4.2 Simulation Parameters

The salient ORBIT$\star$ simulation parameters that are used in common for all Booster modeling, including space-charge calculations, are listed in Table 4.1 below.

Table 4.1: Salient Booster simulation parameters for ORBIT$\star$ runs

No. of Injection Turns	11
No. of Maximum Macroparticles	330,000
Harmonic No.	84
Beam Kinetic Energy at Injection	400.0 (MeV)
Beam Intensity	6.0×10^{10} / *RF bucket*
Transverse Beam Distribution	bi-Gaussian
Ring Circumference	474.2 (m)
$\beta_{x,\ inj} \mid \beta_{y,\ inj}$ (optics functions at injection)	6.274 / 19.312 (m)
$\alpha_{x,\ inj} \mid \alpha_{y,\ inj}$	-0.122 / 0.024
$D_{x,\ 0} \mid D_{y,\ 0}$ (dispersion functions)	2.581 / 0.0 (m)
$x_{0,\ inj} \mid y_{0,\ inj}$ (injection beam centroids)	0.0 / 0.0 (mm)
E_{offset} (energy offset)	0.0 (GeV)
$\Delta E / E_{kinetic}$ (relative energy spread of injected particles)[3]	5.1×10^{-4}
$\varepsilon_{x,\ rms,\ inj} \mid \varepsilon_{y,\ rms,\ inj}$ (transverse rms emittances at injection)	1.76 / 1.76 (π-mm-mrad)
V_{rf} (RF voltage)	205.0 (kV/Turn)
$\mathcal{W}/\mathcal{B}$ (effective beam-pipe radius/effective beam radius)	2.0
Longitudinal Space-Charge Bin No.	32
Transverse Space-Charge Bin No.	64 x 64
Smoothing Parameter	$\sim 10^{-4}$
Min. No. of Particles / Longitudinal Space-Charge Bin	16
Min. No. of Particles / Transverse Space-Charge Bin	128
No. of Total Tracking Turns	1,000

In this context, when horizontal and vertical emittances of a beam are approximately equal ($\varepsilon_x \approx \varepsilon_y$), the beam is referred to be a *round beam*. We make a careful choice of simulation parameters according to the latest measurements and actual machine operation

---

[3] The ORBIT$\star$ takes a parameter of energy spread in this way.
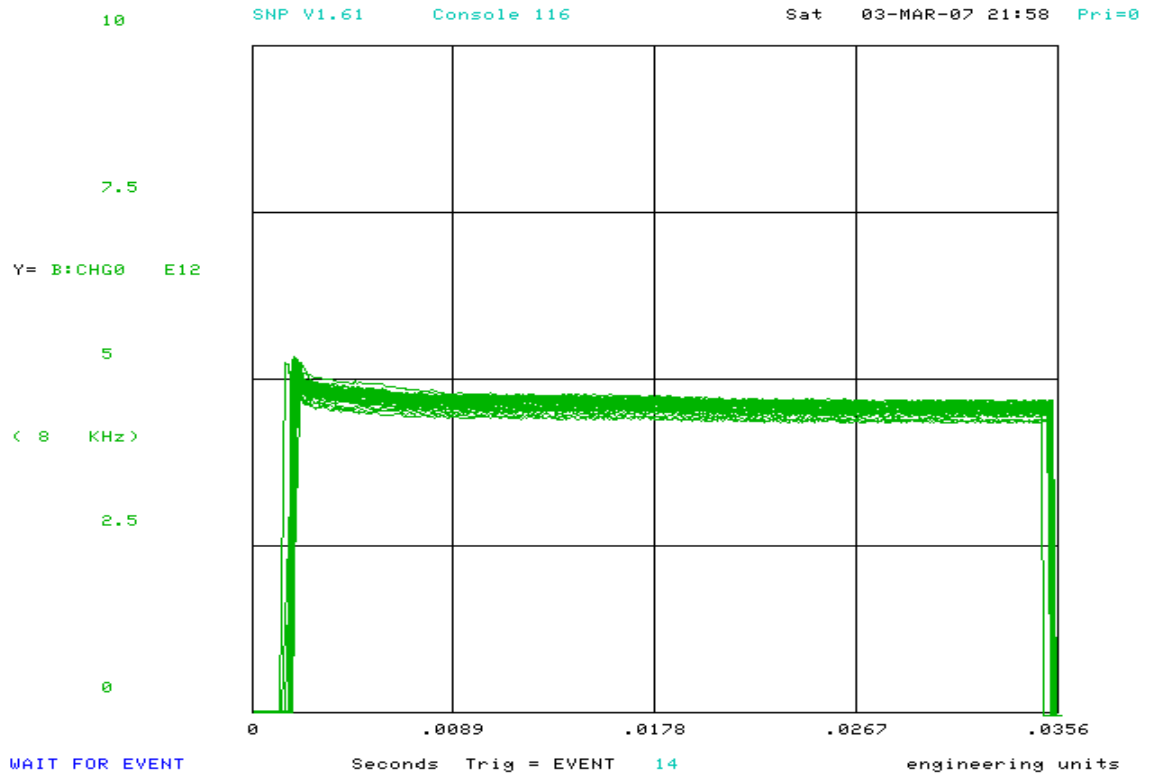
Figure 4.3: ACNET figure of the Booster batch intensity through the entire cycle (B:CHG0). The vertical scale is in the range of 0 and 10 in units of $\times 10^{12}$.

parameters. One example is the Booster beam intensity. What Figure 4.3 shows is an ACNET snapshot of the Booster batch intensity throughout a cycle. Upon completing injection process, the batch intensity amounts to about 5×10^{12} protons. Unless stated otherwise explicitly, we inject ideal *round beams* with axisymmetry into the Booster ring in all simulations to solely investigate the noise effect, coupled to the space charge, on a beam. Optics functions ($\alpha(z)$, $\beta(z)$, *and* $\gamma(z)$) are computed with the Booster lattice using MAD (version 8.23), prior to ORBIT$\star$ simulations. The optics functions at the location of an injection stripping foil (cf. Figure 1.8 and Table 4.1) are chosen as injection Twiss parameters (α_{inj}, β_{inj}, *and* γ_{inj}).

4.3 Beam Diagnostic Calculations and Tracking Results

4.3.1 Parallelized Calculations

In practice, it is not feasible to simulate and track the same number of particles as in actual machine operation. As such, we use macroparticles, each of which represents some fraction of total charge in a machine. Because of statistical fluctuations, it is better to include a sufficient number of macroparticles in simulation. With fixed space-charge bin numbers of $(64 \times 64) \times 32$, we calculate rms emittances from tracking different numbers of total macroparticles. As illustrated by Figure 4.4, when the total number of macropaticles amounts to above 330,000, after injection is complete, the rms emittance values converge with stability. Therefore, considering computation time and the number of macroparticles assigned to each space-charge bin, we determine that 330,000 macroparticles are adequate for our investigation. Hence, each macroparticle represents $\sim 10^5$ real particles, or protons. In order to facilitate tracking of a large number of macroparticles, we implement methods of *parallelized* beam diagnostic calculations. Most of message-passing interfaces occur in the transverse space-charge calculations. Herds of macroparticles are gathered from all running processor nodes, so that the rule of thumb in statistics applies:

The more, the better.

For the Message-Passing Interface (MPI) library, we install the Local Area Multi-computer (LAM) [37] version 7.1.1 under the Scientific Linux Fermi LTS release 4.4. Macroparticle-tracking and beam-diagnostic calculations are conducted from production runs on two local clusters at Fermilab;

The first cluster is 2.8-GHz Pentium 4 Processors with a Myrinet network fabric, and the second cluster is single 3.2-GHz Pentium 640 processors with an Infiniband fabric. The processors on both of the two clusters have an 800-MHz front side bus (FSB)[4]. The node performances are 1400 Megaflops[5]/node and 1729 Megaflops/node, respectively [38, 39].
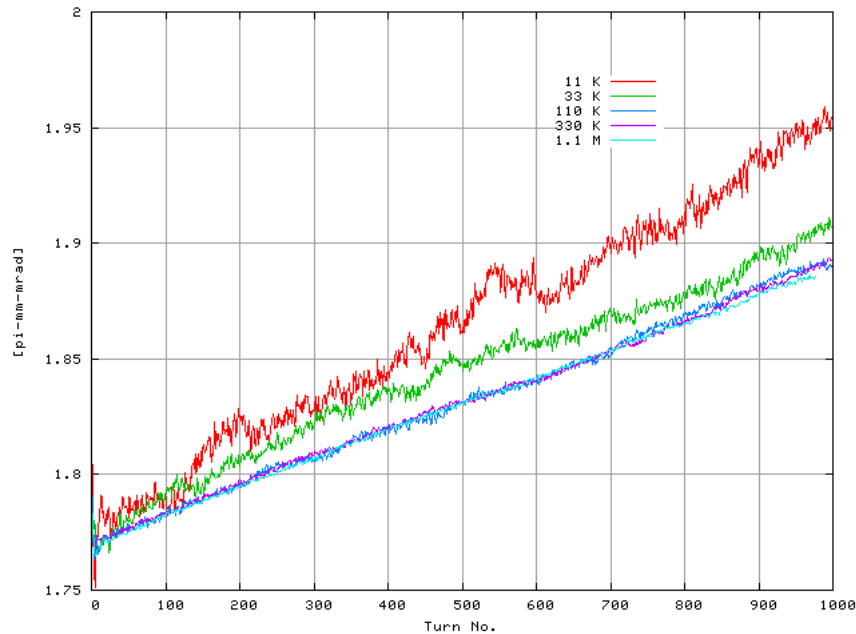
Figure 4.4: RMS emittances with a varying number of total macroparticles and fixed space-charge bin numbers; progressing from top to bottom, each trace corresponds with 11,000, 33,000, 110,000, 330,000, and 1,100,000 macroparticles in total.

---

[4] The front side bus (FBS) connects the processor (CPU) to the system memory. The faster the FSB is the faster data can be transferred to the CPU.

[5] A Megaflop is a measure of a computer's speed expressed as a million floating-point operations per second.

4.3.2 Statistical Emittance: *RMS (Root-Mean-Square) Emittance*

In computational accelerator physics, the statistical emittances, or *rms emittances* are commonly used as a primary beam-diagnostic calculation. The transverse injection coordinates in the ORBIT$\star$ are defined in real (physical) space as a function of azimuthal coordinate (z). Hence, the horizontal coordinates include the effects of horizontal dispersion ($\mathcal{D}_{x0}(z)$). On the other hand, no dispersion effect is included in the vertical coordinates because vertical dispersion ($\mathcal{D}_{y0}(z)$) is zero in the design lattice. Consequently, the following relations are implicitly reflected in the macroparticle coordinates and the calculations of rms emittances and moments in ORBIT$\star$.

$$\begin{cases} x_r(z) & = x_\beta(z) + D_{x0}(z) \cdot \frac{\Delta p}{p_0} \\ y_r(z) & = y_\beta(z) \end{cases} \tag{4.1}$$

In Eqn. (4.1), $x_r(z)$ and $y_r(z)$ denote real-space coordinates, and $x_\beta(z)$ and $y_\beta(z)$ denote betatron coordinates, and $D_{x0}(z)$ and P_0 denote injection horizontal dispersion and design momentum, respectively. The divergence angles, or slopes (x' and y') of the beam trajectory are defined as a derivative of transverse position (x, or y) with respect to longitudinal coordinate (z) as depicted in Figure 4.5. Here, we assume that the transverse momenta ($\mathcal{P}_x$ and $\mathcal{P}_y$) are much smaller than the longitudinal momentum ($\mathcal{P}_z$) as illustrated in Figure 4.5.

$$\mathcal{P}_x, \mathcal{P}_y \ll \mathcal{P}_z \tag{4.2}$$

Then, each of the divergence angles can be represented by a normalized transverse momentum.
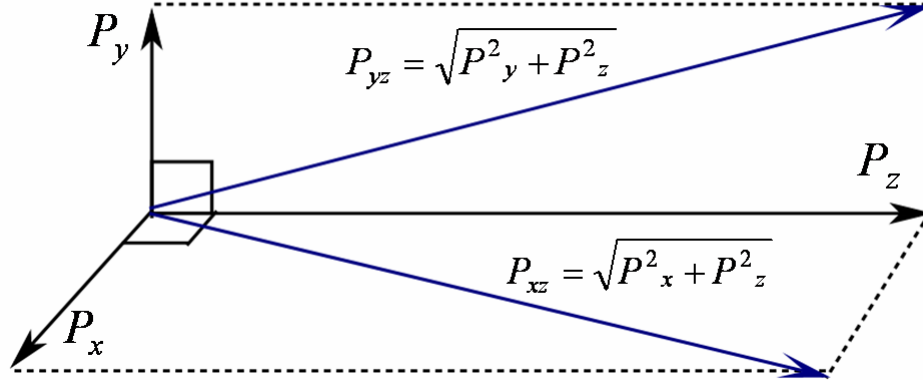
Figure 4.5: Transverse and longitudinal momenta

$$\begin{cases} x' & \equiv dx/dz = v_x/v_z = \mathcal{P}_x/\mathcal{P}_z \approx \mathcal{P}_x/\mathcal{P}_{xz} \\ y' & \equiv dy/dz = v_y/v_z = \mathcal{P}_y/\mathcal{P}_z \approx \mathcal{P}_y/\mathcal{P}_{yz} \end{cases} \tag{4.3}$$

If we consider two transverse planes of $x - z$ and $y - z$ separately as depicted in Figure 4.5, we can define 2-D total momenta in each plane ($\mathcal{P}_{xz}$ and $\mathcal{P}_{yz}$). For instance, to compute the horizontal divergence angle (x'), only horizontal and longitudinal momenta ($\mathcal{P}_x$ and $\mathcal{P}_z$) are included as in Eqn. (4.3). As such, we do not need to consider a 3-D total momentum $\left(\mathcal{P}_{xyz} = \sqrt{\mathcal{P}_x^2 + \mathcal{P}_y^2 + \mathcal{P}_z^2} \right)$: i.e., only total momentum in each transverse plane is needed for the calculations of each divergence angle. Like in Eqn. (4.1), the injection horizontal angles of the ORBIT includes a dispersion term.

$$\begin{cases} x_r'(z) & = x_\beta'(z) + D_{x0}'(z) \cdot \frac{\Delta p}{p_0} \\ y_r'(z) & = y_\beta'(z) \end{cases} \tag{4.4}$$

where $\mathcal{D}_x'(z)$ denote the slope of dispersion. The divergence angles are associated with

transverse momenta as follows:

$$
\begin{cases}
\mathcal{P}_x &= \mathcal{P}_z \cdot x' = (\gamma \beta c m_0) \cdot x' \\
\mathcal{P}_y &= \mathcal{P}_z \cdot y' = (\gamma \beta c m_0) \cdot y'
\end{cases}
\tag{4.5}
$$

As the ORBIT$\star$ employs the 2nd-order central moments[6] in the rms emittance calculations, we need to define the following quantities prior to defining rms emittances.

$$
\begin{cases}
\Delta x &\equiv x - \langle\, x \,\rangle \\
\Delta y &\equiv y - \langle\, y \,\rangle \\
\Delta \mathcal{P}_x &\equiv \mathcal{P}_x - \langle\, \mathcal{P}_x \,\rangle \\
\Delta \mathcal{P}_y &\equiv \mathcal{P}_y - \langle\, \mathcal{P}_y \,\rangle
\end{cases}
\tag{4.6}
$$

In case of the synchrotron motion, $\Delta E (= E - E_s)$ of energy offset and ϕ representing RF phase are used.

$$
\begin{cases}
E^\star &\equiv E/(\omega_0 H) \\
\Delta E^\star &\equiv E^\star - E_s^\star \\
\delta E^\star &\equiv \Delta E^\star - \langle\, \Delta E^\star \,\rangle \\
\Delta \phi &\equiv \phi - \langle\, \phi \,\rangle,
\end{cases}
\tag{4.7}
$$

with ω_0 (= $2\pi f_0$) and H being angular revolution frequency and harmonic number, respectively. Note that the normalization factor of $1/(\omega_0\, H)$ is introduced to transform synchrotron (or longitudinal) coordinates into a pair of canonical conjugate coordinates

---

[6] When a mean value of variable is included in moments calculation, it is referred to as central moments.

$(E^\star, \phi)$. Once we define the 2nd-order central moments[7] of each coordinate in the 6-dimensional space, we define column matrices $\mathcal{M}_{2,\,x}$ $\mathcal{M}_{2,\,y}$, and $\mathcal{M}_{2,\,z}$.

$$\mathcal{M}_{2,\,x} = \begin{bmatrix} \Delta x_\beta \\ \Delta x'_\beta \end{bmatrix} \quad \mathcal{M}_{2,\,y} = \begin{bmatrix} \Delta y_\beta \\ \Delta y'_\beta \end{bmatrix} \quad \mathcal{M}_{2,\,z} = \begin{bmatrix} \delta E \\ \Delta \phi \end{bmatrix} \tag{4.8}$$

Here $\langle\, x\, \rangle$ and $\langle\, y\, \rangle$ are beam centroids and $\langle\, (\Delta x)^2\, \rangle$ and $\langle\, (\Delta y)^2\, \rangle$ denote $\langle\, (x - \langle\, x\, \rangle)^2\, \rangle$ and $\langle\, (y - \langle\, y\, \rangle)^2\, \rangle$, which are the 2nd central moments of a beam in each transverse plane. With the column matrix $\mathcal{M}_{2,\,x}$, we can define 2×2 Σ-matrices [11, 40, 41] in subspaces of trace space: (x_β, x'_β) and (y_β, y'_β)

The off-diagonal elements are concerned with the correlation between position and angle.

$$\Sigma(x_\beta, x'_\beta) \equiv \langle \mathcal{M}_{2,\,x_\beta} \cdot \mathcal{M}^T_{2,\,x_\beta} \rangle$$
$$= \begin{bmatrix} \langle (\Delta x_\beta)^2 \rangle & \langle \Delta x_\beta \Delta x'_\beta \rangle \\ \langle \Delta x'_\beta \Delta x_\beta \rangle & \langle (\Delta x'_\beta)^2 \rangle \end{bmatrix} \tag{4.9}$$

in which $\mathcal{M}^T$ denotes a transpose matrix of $\mathcal{M}$.

$$\varepsilon_{x,\,rms} = \sqrt{\det \Sigma(x_\beta, x'_\beta)}$$
$$= \sqrt{\langle\, (\Delta x_\beta)^2\, \rangle \langle\, (\Delta x'_\beta)^2\, \rangle - \underbrace{\langle\, \Delta x_\beta \Delta x'_\beta\, \rangle^2}_{\text{correlation term}}} \tag{4.10}$$

This quantity is also known as *unnormalized rms emittance*.

In ORBIT$\star$, transverse rms emittances are defined in $(x_\beta, \mathcal{P}_x/P_0)$ and $(y_\beta, \mathcal{P}_y/P_0)$ phase

---

[7] When a mean value of variable is included in moments calculation, it is referred to as central moments.

spaces, following the MAD [30] convention:

$$\Sigma(x_\beta, \mathcal{P}_x) = \begin{bmatrix} \langle (\Delta x_\beta)^2 \rangle & \langle \Delta x_\beta \Delta \mathcal{P}_x \rangle \\ \langle \Delta \mathcal{P}_x \Delta x_\beta \rangle & \langle (\Delta \mathcal{P}_x)^2 \rangle \end{bmatrix} \tag{4.11}$$

$$\begin{aligned} \varepsilon_{x,\,rms} &= \frac{1}{\mathcal{P}_0} \cdot \sqrt{\det \Sigma(x_\beta, \mathcal{P}_x)} \\ &= \frac{1}{\gamma\beta m_0 c} \cdot \sqrt{\langle (\Delta x_\beta)^2 \rangle \langle (\Delta \mathcal{P}_x)^2 \rangle - \langle \Delta x_\beta \Delta \mathcal{P}_x \rangle^2}, \end{aligned} \tag{4.12}$$

in which the transverse momenta ($\mathcal{P}_x$ and $\mathcal{P}_y$) are normalized by the design momentum ($\mathcal{P}_0$). As was stated earlier, if a unnormalized rms emittance is multiplied by the Lorentz factors ($\beta\gamma$), it turns into a normalized rms emittance without momentum dependence. Consequently, the trace-space rms emittance and phase-space rms emittance are related as in Eqn. (4.13) below:

$$\sqrt{\det \Sigma(x_\beta, x_\beta')} = \frac{1}{\gamma\beta m_0 c} \cdot \sqrt{\det \Sigma(x_\beta, \mathcal{P}_x)} \tag{4.13}$$

The Eqns. (4.8) through (4.16) apply likewise to the vertical plane. As in Eqns. (4.13) and (4.15), when beam kinetic energy increases the emittance shrinks. This is termed adiabatic damping. Therefore, to define a truly invariant quantity that is to be preserved regardless of the change in beam kinetic energy, the momentum dependence needs to be removed from the emittance quantity. By eliminating the momentum dependence from the unnormalized rms emittances, we can obtain a true invariant. This quantity is termed *normalized rms emittance*. Under ideal condition, i.e., in the absence of external perturbations, such as nonlinear space-charge force and of couplings, the invariance of a normalized rms emittance is to be preserved. In the longitudinal space, the rms emittance can be defined

utilizing $\Sigma(\delta E, \phi)$ matrix.

$$\Sigma(\delta E, \phi) = \begin{bmatrix} \langle \delta E \rangle^2 & \langle \delta E \Delta \phi \rangle \\ \langle \Delta \phi \delta E \rangle & \langle \Delta \phi \rangle^2 \end{bmatrix} \tag{4.14}$$

$$\begin{aligned} \varepsilon_{z,\,rms} &= \frac{1}{\omega_0 H \cdot \mathcal{P}_0} \sqrt{det\ \Sigma(\delta E, \phi)} \\ &= \frac{1}{\omega_0 H \cdot \gamma \beta m_0 c} \cdot \sqrt{\langle(\delta E)^2\rangle\langle(\Delta\phi)^2\rangle - \langle \delta E \Delta \phi \rangle^2} \end{aligned} \tag{4.15}$$

It should be noted that we employ conjugate longitudinal coordinates of $\left(E/(\omega_0 H),\ \phi\right)$. The energy normalization factor of $1/(\omega_0 H)$ is taken outside of the square root.

$$\begin{cases} \begin{aligned} \varepsilon_{x,\,n,\,rms} &= (\beta\gamma) \cdot \varepsilon_{x,\,rms} \\ &= (\beta\gamma) \cdot \sqrt{\langle(\Delta x_\beta)^2\rangle \cdot \langle(\Delta x_\beta')^2\rangle - \langle \Delta x_\beta \Delta x_\beta' \rangle^2} \\ &= \frac{1}{m_0 c} \cdot \sqrt{\langle(\Delta x_\beta)^2\rangle \cdot \langle(\Delta \mathcal{P}_x)^2\rangle - \langle \Delta x_\beta \Delta \mathcal{P}_x \rangle^2} \\ \varepsilon_{y,\,n,\,rms} &= (\beta\gamma) \cdot \varepsilon_{y,\,rms} \\ &= (\beta\gamma) \cdot \sqrt{\langle(\Delta y_\beta)^2\rangle \cdot \langle(\Delta y_\beta')^2\rangle - \langle \Delta y_\beta \Delta y_\beta' \rangle^2} \\ &= \frac{1}{m_0 c} \cdot \sqrt{\langle(\Delta y)^2\rangle \cdot \langle(\Delta \mathcal{P}_y)^2\rangle - \langle \Delta y \Delta \mathcal{P}_y \rangle^2} \\ \varepsilon_{z,\,n,\,rms} &= (\beta\gamma) \cdot \varepsilon_{z,\,rms} \\ &= \frac{1}{\omega_0 H \cdot m_0 c} \cdot \sqrt{\langle(\delta E)^2\rangle\langle(\Delta\phi)^2\rangle - \langle \delta E \Delta \phi \rangle^2} \end{aligned} \end{cases} \tag{4.16}$$

It is of practical help to bear in mind that for a proton beam at 400 MeV the value of the Lorentz factor $(\beta\gamma)$ is approximately 1.0, such that we can use the unnormalized rms emittance and the normalized rms emittance with no distinction for the Booster beam at injection energy. As a reference, the value of the Lorentz factor $(\beta\gamma)$ at extraction energy (8.0 GeV) is about 10.0. The units of emittance measurement are π-*mm-mrad* at Fermilab.

By convention at Fermilab, beam emittances containing 95 % of the total particles are commonly used:

$$\varepsilon_{x, \, 95, \, rms} \approx 6 \cdot \frac{\sigma_x^2}{\beta_x} = 6 \cdot \varepsilon_{rms} \qquad (4.17)$$

This can be derived from Gaussian probability density distribution [42]. In summary, in the case of a Gaussian beam, normalized rms emittances can be calculated as follows:

$$\begin{cases} \varepsilon_{n, \, rms} & = (\beta\gamma) \cdot \varepsilon_{rms} \\ \varepsilon_{n, \, 95, \, rms} & \approx 6 \cdot (\beta\gamma) \cdot \varepsilon_{rms}, \end{cases} \qquad (4.18)$$

in which *95, n*, and *rms* stand for 95 %, normalized, and root-mean-square, respectively.

4.3.3 Moments

In addition to the rms emittances, moments calculations are used to understand the time evolution of rms beam sizes, or rms beam widths in transverse planes. Since it is necessary to consider beam centroids ($\langle x \rangle$ and $\langle y \rangle$) in calculations, ORBIT$\star$ employs central moments calculations. For the 1st moment calculations, because the central moment calculation vanishes, instead we use beam centroids itself ($\langle x \rangle$ and $\langle y \rangle$) in each plane as in Eqn. (4.19). It is assumed that the density profiles of a beam in transverse planes are *bi-Gaussian*. We first inject a bi-Gaussian beam. Then, rms beam sizes (1 σ) are obtained from the 2nd moments calculation:

$$1^{st} \text{ moments} \begin{cases} \langle x_r \rangle \\ \langle y_r \rangle \end{cases} \qquad (4.19)$$

$$2^{nd} \text{ moments} \begin{cases} \sigma_x^2 & = \langle (\Delta x_r)^2 \rangle \\ \sigma_y^2 & = \langle (\Delta y_r)^2 \rangle \end{cases} \qquad (4.20)$$

Moments of order higher than two are usually referred to as high-order moments.

4.3.4 Actions

Through action-angle transformation, the phase-space area ($\mathcal{A}$) enclosed by the invariant torus, or a closed phase-space curve [43] is equal to 2π times invariant action ($\mathcal{J}$):

$$\mathcal{A}_{x,\,y} = \oint \mathcal{P}(E,\, q)\, dq = \int_0^{2\pi} d\theta\, \mathcal{J}_{x,\,y} = 2\pi \mathcal{J}_{x,\,y} \tag{4.21}$$

with q, $\mathcal{P}$, E, θ, and $\mathcal{J}_{x,\,y}$ being denote generalized transverse coordinates, conjugate momenta, energy, angle, and transverse actions, respectively:

$$\mathcal{A}_z = \oint \phi\, d\tilde{E} = \int_0^{2\pi} d\theta\, \mathcal{J}_z = 2\pi \mathcal{J}_z, \tag{4.22}$$

where $\tilde{E}$ is $E/h\omega_0$, and ϕ and $\mathcal{J}_z$ denote RF-phase angle and longitudinal action, respectively. We define conjugate phase-space coordinates $(x,\, \mathcal{P}_x)$ and $(y,\, \mathcal{P}_y)$ as below:

$$\begin{cases} \mathcal{P}_x & \equiv \alpha_x x + \beta_x x' \\ \mathcal{P}_y & \equiv \alpha_y y + \beta_y y', \end{cases} \tag{4.23}$$

in which x and y denote horizontal and vertical coordinates, and x' and y' denote horizontal and vertical divergence angles, respectively. The Courant-Snyder invariant (I_{cs}) [44] and the action ($\mathcal{J}$) in phase space are related through the Courant-Snyder parameters (α, β, and γ):

$$\begin{cases} I_{CS,\,x} & = x^2 + (\alpha_x x + \beta_x\, x')^2 = x^2 + \mathcal{P}_x^2 = 2\beta_x\, \mathcal{J}_x \\ I_{CS,\,y} & = y^2 + (\alpha_y y + \beta_y\, y')^2 = y^2 + \mathcal{P}_y^2 = 2\beta_y\, \mathcal{J}_y \end{cases} \tag{4.24}$$

$$\mathcal{J} = \frac{1}{2\pi} \cdot \mathcal{A} \tag{4.25}$$

Let us define normalized phase-space coordinates η and ξ:

$$\begin{cases} \eta & \equiv x/\sqrt{\beta_x} \\ \xi & \equiv \sqrt{\beta_x} \cdot \mathcal{P}_x, \end{cases} \tag{4.26}$$

Then, $\eta^2 + \xi^2 = 2\mathcal{I}_x$ is a circle with a radius of $\mathcal{R}$ of $\sqrt{2\mathcal{I}_x}$ on the normalized phase space. If we average the normalized coordinates over all macroparticles, $\langle \eta^2 \rangle = \langle \xi^2 \rangle = \langle \mathcal{I}_x \rangle = \mathcal{R}^2/2$. Therefore, a rms emittance is equivalent to 2 times average action $\mathcal{I}_x$:

$$\varepsilon_{x,\,rms} = \mathcal{A}_{circle}/\pi = 2 \cdot \langle \mathcal{I}_x \rangle \tag{4.27}$$

The action can be a single-particle emittance in phase space. The average action of macroparticles of a beam is thus considered to be a physical quantity comparable to the rms emittance of a beam. The ORBIT$\star$ is now capable of performing parallelized calculation of average actions at each tracking turn. Therefore, the action calculations can be cross-checked to rms emittance calculations.

4.3.5 Longitudinal Space-Charge Calculations

Particle acceleration and longitudinal focusing take place at RF cavities. The transformation of longitudinal coordinates (ΔE, ϕ) from one RF cavity (n) to the next cavity (n+1) is carried out at RF cavity nodes:

$$\begin{cases} \Delta E_{n+1} & = \Delta E_n + \frac{e\mathcal{V}_{rf}}{\mathcal{N}_{cav}}(\sin\phi_n - \sin\phi_s) \\ \phi_{n+1} & = \phi_n + \frac{2\pi\eta\,H}{\mathcal{N}_{cav}\beta^2\,E_s}\Delta E_{n+1}, \end{cases} \tag{4.28}$$

in which η, H, ϕ_s, $\mathcal{V}_{rf}$, $\mathcal{N}_{cav}$, and E_s are slip factor[8], harmonic number, synchronous phase, RF voltage, the number of RF cavities, and synchronous energy, respectively. At the location of a longitudinal space-charge node, the effect of longitudinal space charge is applied as a series of energy kicks, or momentum kicks. The energy kick, or additional energy gain due to space charge is applied when macroparticles pass through RF cavities:

$$\Delta E_{n+1} = \Delta E_n + \frac{eV_{rf}}{\mathcal{N}}(\sin \phi_n - \sin \phi_s) + \frac{eV_{sc}}{\mathcal{N}}, \tag{4.29}$$

in which V_{sc} is total space-charge voltage seen by particles in a beam.

In ORBIT$\star$ simulation, a longitudinal space-charge node first carries out binning the macroparticles in longitudinal direction. After binning the longitudinal beam profile, the node performs the calculation of space-charge potential (V_{sc}) with respect to their RF phase coordinate ϕ in order to obtain line density (λ_{sc}) and bunching factor (B_f):

$$B_f = \frac{\langle \lambda_{sc} \rangle}{\hat{\lambda}_{sc}}, \tag{4.30}$$

where $\langle \lambda_{sc} \rangle$ and $\hat{\lambda}_{sc}$ denote average line density and peak line density, respectively. Assuming that a perfectly conducting smooth wall, the longitudinal space-charge field is associated with the line density gradient by

$$E_{sc} = -\frac{q}{4\pi\varepsilon_0}\frac{g_0}{\gamma}\frac{d\lambda_{sc}}{dz} \tag{4.31}$$

where q, ε_0, g_0, and λ_{sc} denote charge, permittivity of free space, geometric factor [45], and line density. The geometry factor (g_0) is defined as $g_0 \equiv 1 + 2\ln(W/B)$ with W and B being effective beam-pipe wall radius and effective beam radius. A particle whose local line density gradient $d\lambda_{sc}/dz$ is subject to a space-charge potential (V_{sc}) in units of volts

---

[8] The slip factor (η) is a measure of how much off-momentum particles slip in time, or phase relative to a reference particle. The slip factor can be computed as $\eta \equiv \frac{1}{\gamma_{tr}^2} - \frac{1}{\gamma^2}$, with γ_{tr} being transition gamma.

per turn:

$$V_{sc} = \oint ds E_s = -\frac{q}{2\varepsilon_0} \frac{g_0 R}{\gamma^2} \frac{d\lambda_{sc}}{dz} \qquad (4.32)$$

where R is the mean radius of the accelerator. When a herd of macroparticles propagate through at each longitudinal space-charge node, V_{sc} is calculated from binned particles and macroparticle information is updated accordingly:

$$\Delta E_{n+1} = \Delta E_n + \frac{qV_{sc}D_{sc}}{2\pi R} \qquad (4.33)$$

with D_{sc} being the distance to the subsequent space-charge node. After an energy kick is calculated for the phase of each macroparticle, the energy kick is applied to each individual macroparticle. Then, the summation of each individual kick updates the energy spread, or momentum spread:

$$\Delta E_{sc} \propto Z_0 \cdot \frac{d\lambda_{sc}}{dz} \frac{1}{2\gamma^2} (1 + 2\ln(W/B)) \qquad (4.34)$$

in which Z_0, W, and B are free-space impedance, beam pipe radius, and beam radius.

4.3.6 Transverse Space-Charge Calculation: PIC Method

In order to carry out transverse space-charge calculations with drastic reduction of computing time, we choose a macroparticle-tracking approach called Particle-In-Cell (PIC) method. The PIC method begins first with binning macroparticles to a rectangular grid: The PIC method superimposes a grid, or mesh on a bunch of macroparticles at each step. After the binning, the number of macroparticles in each grid cell is counted. Then, the space-charge force acting on each macroparticle is obtained by summing up the fields from binned macroparticles representing charges in each grid.

$$\begin{cases} \mathcal{F}_{sc,\,x}(x,\,y) &= \frac{\mathcal{K}}{N} \Sigma_1^N \frac{x - x_i}{(x - x_i)^2 + (y - y_i)^2} \\ \mathcal{F}_{sc,\,y}(x,\,y) &= \frac{\mathcal{K}}{N} \Sigma_1^N \frac{y - y_i}{(x - x_i)^2 + (y - y_i)^2} \end{cases}, \qquad (4.35)$$

in which $\mathcal{K}$ is perveance defined in Eqn. (4.36) and N is the number of macroparticles:

$$\mathcal{K} = \frac{q^2 \lambda_{sc} r_0}{2\beta^2 \gamma^3 m_0}, \tag{4.36}$$

with r_0, β, and γ being a classical radius of proton and the usual Lorentz factors. Once the transverse space-charge forces are calculated, transverse space-charge angular kicks are applied to each macroparticle:

$$\begin{cases} \Delta x' &= \mathcal{F}_{sc,\,x} \cdot L_{kick} \cdot \lambda_{sc} \\ \Delta y' &= \mathcal{F}_{sc,\,y} \cdot L_{kick} \cdot \lambda_{sc} \end{cases} \tag{4.37}$$

with λ_{sc} and L_{kick} being local line density and longitudinal length over which angular kicks are applied. The forces are then applied as a momentum kick, or impulse to each individual macroparticle. The computing time required for space-charge calculation depends both on the number of macroparticles and the number of mesh cells, or the fineness of the grid. While PIC particles are propagated through beamline elements by means of transport maps provided by the MAD input files (cf. Figure 2.4), transverse kicks are applied to macroparticles. We insert a total of 809 transverse space-charge nodes after each transfer matrix. In our modeling and simulation, a total of 330,000 macroparticles are binned over 64×64 node grids for transverse space-charge calculations. For the space-charge calculations, communications between parallel processors are required. Finally, the method interpolates the force from the grid back to each macroparticle. In the following subsections, we give details of what kind of beam diagnostic calculations are available with the ORBIT$\star$. These diagnostic calculations play a key role of investigating any adverse influences on a beam, resulting from inevitable machine imperfections.

4.3.7 Space-Charge Effects in the Booster

One of the main features of ORBIT⋆ is accurate and fast parallelized calculations of 1-D (longitudinal), 2-D (transverse), and 2.5-D (longitudinal and transverse) space-charge calculations with macroparticles in a ring.

In an effort to reduce space-charge effects, Fermilab linac was upgraded in 1993 from an energy of 200 MeV to 400 MeV. In Figures 4.6, 4.7, and 4.8, the ORBIT⋆ simulations demonstrate that after the injection beam kinetic energy was doubled, the space-charge-induced beam degradations are significantly lowered in the Booster at injection. First, Figures 4.6 and 4.7 demonstrate that the growths of the 2nd moments are substantially reduced by a factor of two at 400 MeV. Second, as illustrated by Figure 4.8, the rms emittance growths due to the effects of full space charge at 400 MeV over 2 msec are significantly weakened and reduced by a factor of two as well. Since the space-charge effect is dependent upon beam intensities, the transverse rms emittances grow fast as the beam intensity increases during the injection process in Figure 4.9. After the injection process is complete, the transverse emittances tend to flatten out and grow slowly and steadily.
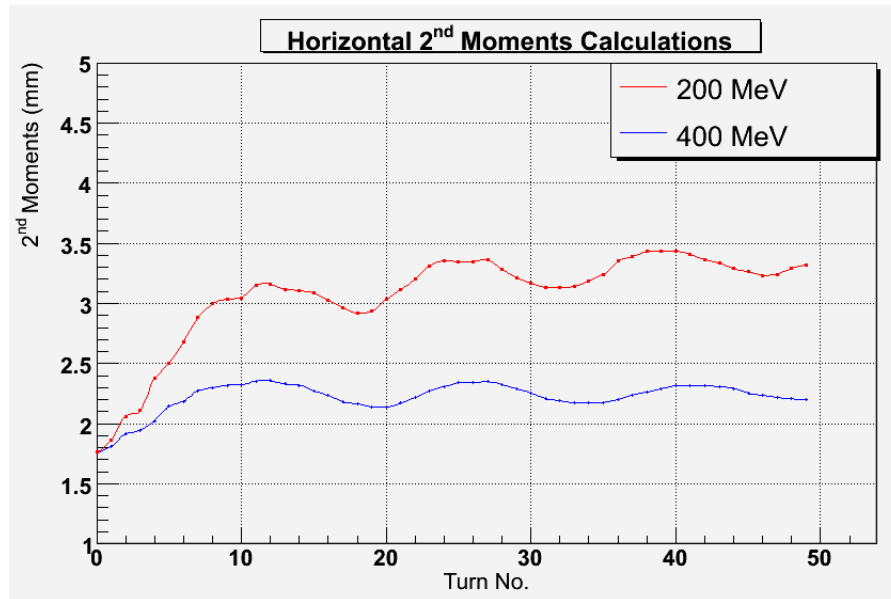
(a) horizontal 2nd moments
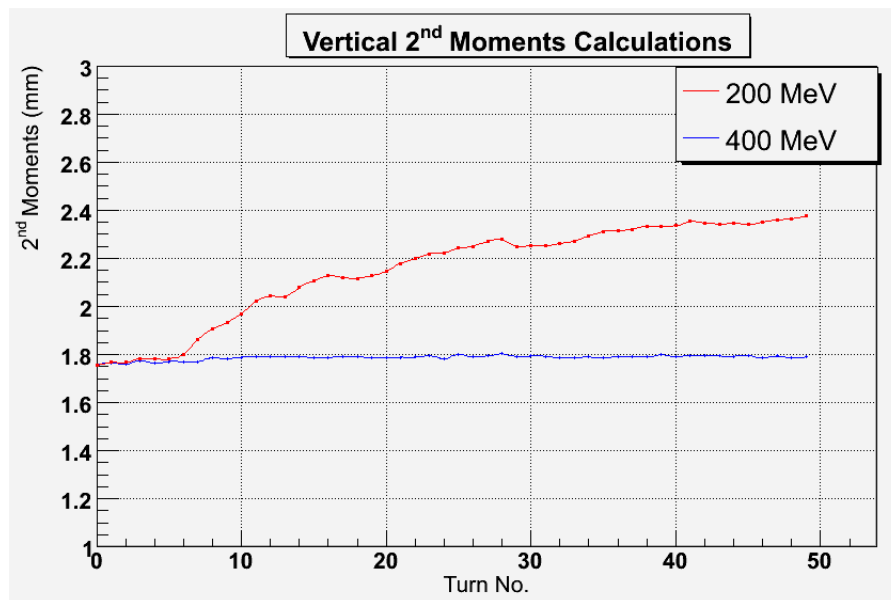
(b) vertical 2nd moments

Figure 4.6: The evolution of 2nd moments of beams over the first 50 turns; the red trace indicates a 200-MeV beam, and the blue trace is for a 400-MeV beam.
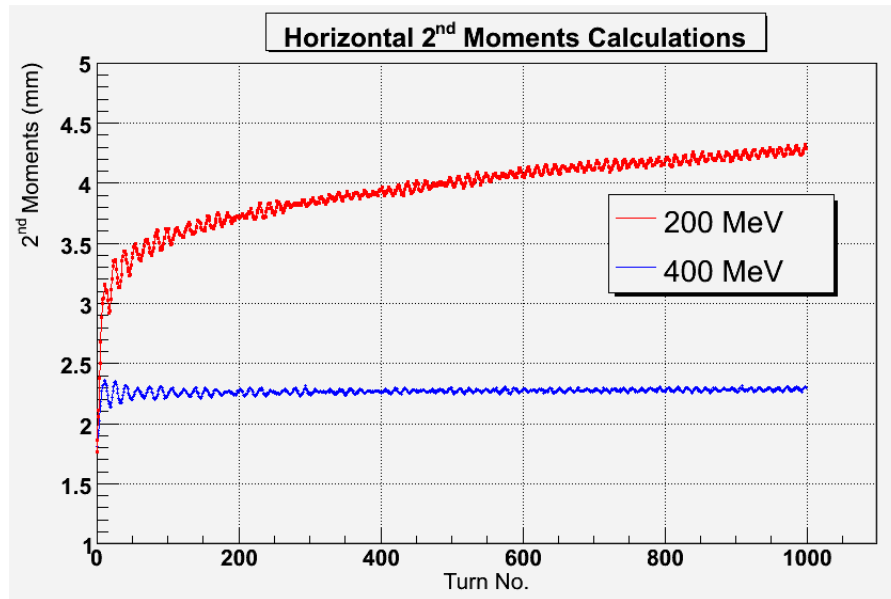
(a) horizontal 2nd moments
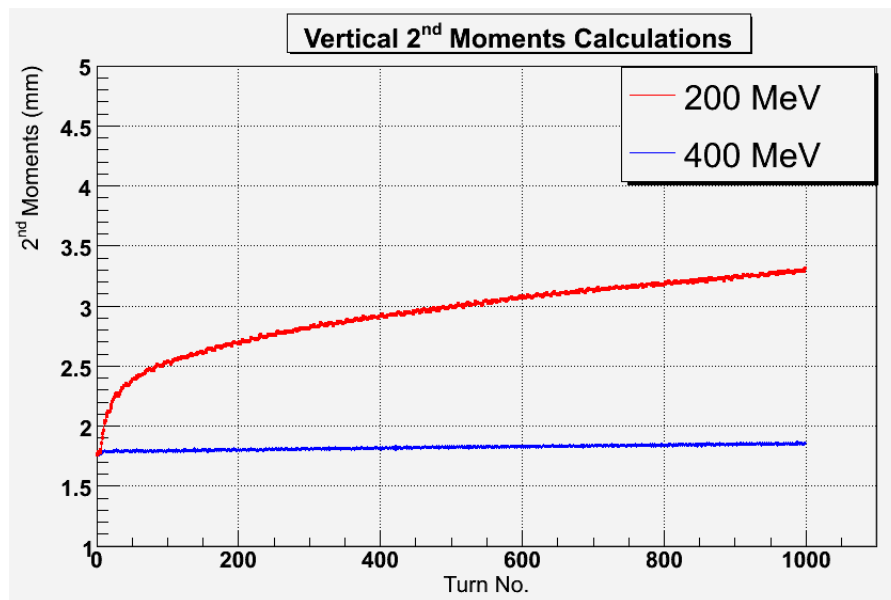
(b) vertical 2nd moments

Figure 4.7: The evolution of 2nd moments in transverse planes arising from space-charge effects over about 2 msec
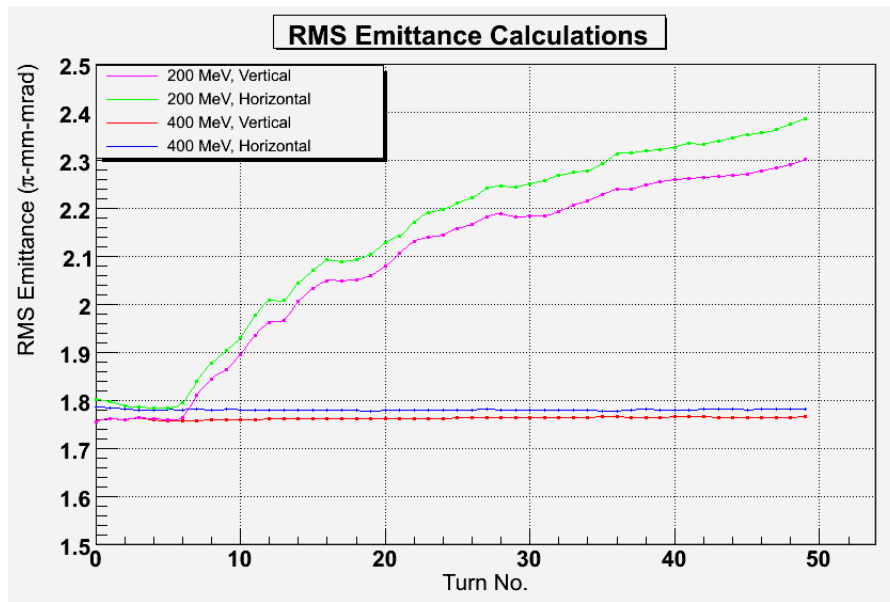
(a) over the first 50 turns
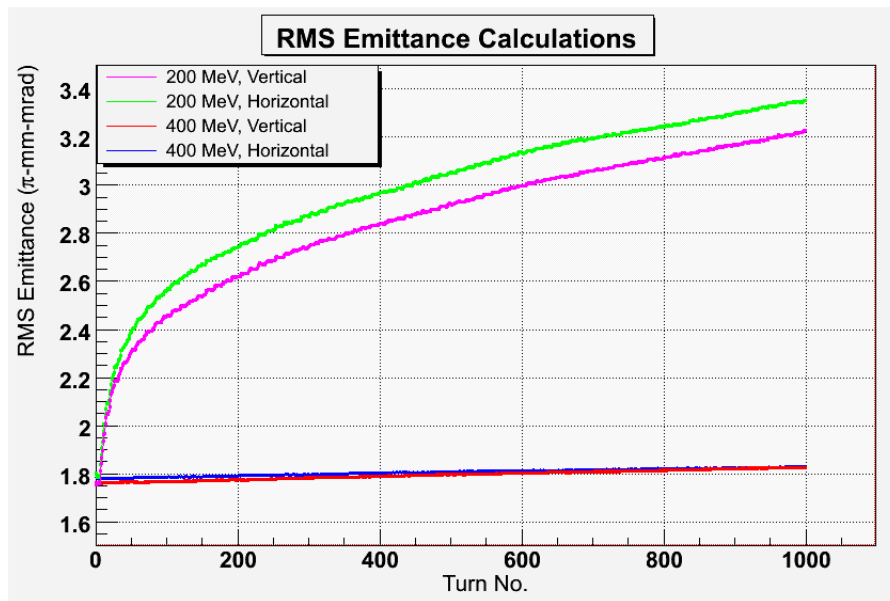
(b) over 1000 turns

Figure 4.8: The evolution of transverse rms emittances arising from space-charge effects
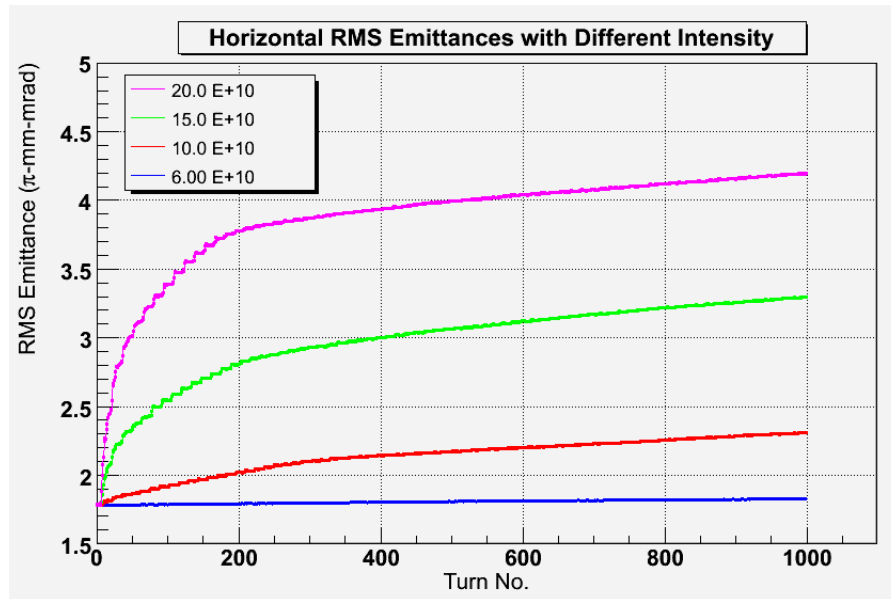
(a) horizontal rms emittances
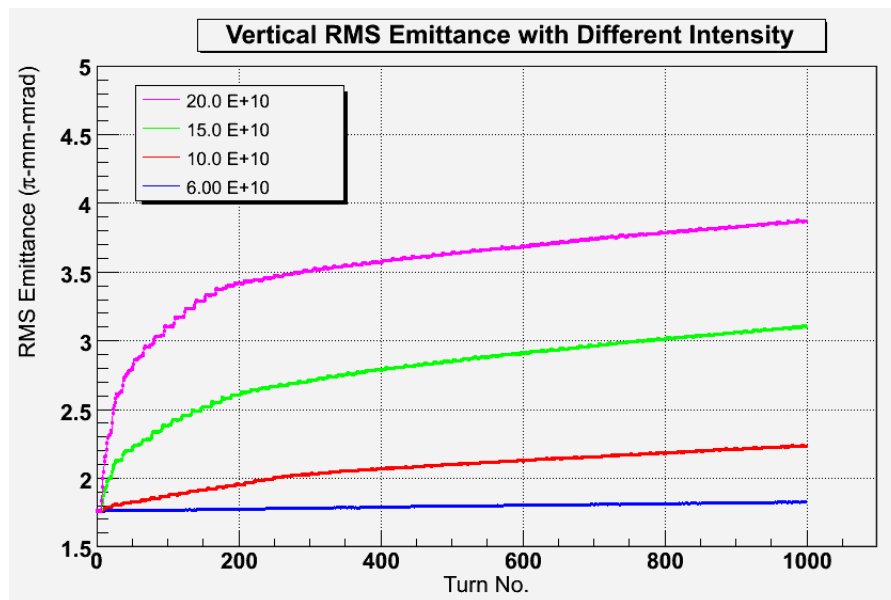
(b) vertical rms emittances

Figure 4.9: The evolutions of rms emittances with different beam intensities including 3-D space-charge effects. The intensities indicated in the legend are the numbers of protons per RF bucket.

4.3.8 Impact of GMPS Current Fluctuations with Space Charge

After inserting random noise nodes, provided with characteristic stochastic noise parameters, into a Booster ring, macroparticles representing the Booster beams are tracked over 1,000 turns in the presence of full space charge.

Figure 4.10 shows that the evolution of transverse rms emittances with the O-U noise[9] coupled to the full space-charge effects (red) and with the space-charge effects alone (blue). To estimate the emittance growth rate, the relative emittance growths $\left(\frac{\Delta\varepsilon}{\varepsilon_0}\right)$ [10] are calculated starting from the injection completion (11th turn) through 1,000 turns, prior to the beam acceleration; this corresponds to the first 2 msec of one cycle over 66.7 msec (15 Hz). In the horizontal plane the relative emittance growth is about 7.5 %, and in the vertical plane the growth is 9.3 %. A total of 330,000 macroparticles, or 30,000 macro particles per each injection turn are simulated and tracked. Upon including O-U noise representing GMPS noise, the process of beam degradation develops, and a more prominent halo formation is found. As a cross-check with the rms emittance calculations, we also compute average actions at each tracking turn including the noise and the full space-charge effects. The rms emittances and average actions are overlaid in Figure 4.11. The calculations of both rms emittances and actions manifest in such a good agreement that beam degradation is substantially enhanced due to *synergistic mechanism* between GMPS-current fluctuations and space-charge effects. Here, we use the term *synergistic mechanism* meaning that the total effects of GMPS noise and space charge are larger than the sum of individual effects. If we lower the Booster batch intensity by an order of one magnitude (5×10^{11}) from the current operational batch intensity under the same conditions, the emittance growths induced by the GMPS noise and space-charge effects are not distinguishable from those of noise alone in the absence of space charge as shown in Figure 4.12. It should be noted that the

---

[9] Here, the O-U noise means the stochastic noise modeled on the GMPS noise measurements.

[10] ε_0 denotes initial emittance, and $\Delta\varepsilon = |\varepsilon - \varepsilon_0|$

space-charge effect is intensity dependent. Thus, if the beam intensity is lowered, so is the space-charge effects. This is a clear signature that only when the space-charge effects are substantial, so does the GMPS noise have a substantial impact on the Booster beam. In addition to the primary beam diagnostic calculations of the rms emittance and average action, we check the transverse couplings.

The calculations of the 2nd-order cross moments $\langle\, x\, y\, \rangle$ for each case are presented in Figure 4.13. A marginal amount of couplings are introduced due to the full space-charge effects in Figure 4.13 (b). When the noise is included alone in the absence of the space charge, couplings are somewhat noticeable in Figure 4.13 (c). When the noise and the full space-charge effects are included, the transverse couplings are substantially amplified. We therefore conclude that the noise impact on a beam is dependent upon the strengths of the space-charge defocusing forces in the Booster. What Figure 4.14 illustrates is the percentage of macroparticles that reside outside of a given average action including the O-U noise and space charge.

Figure 4.15 compares the distributions of transverse single-particle actions (J_x and J_y) at the outset of injection and at the end of 1,000 turns. It is evident that noise-induced beam degradation is enhanced as the time elapses. In Figure 4.16, the phase spaces and cross section of beam particles at injection and at $1,000^{th}$ turn. They show us that the projection of divergence angles (x' and y') are not distorted noticeably due to the O-U noise coupled to the space-charge effects. Whereas the rms values are increased in configuration space (x and y) after 1,000 turns.
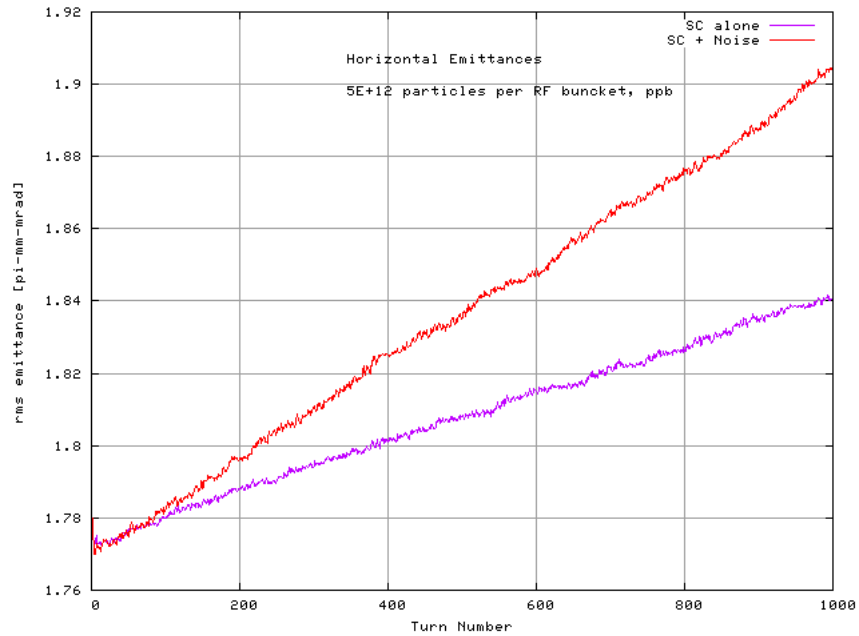
(a) horizontal emittance
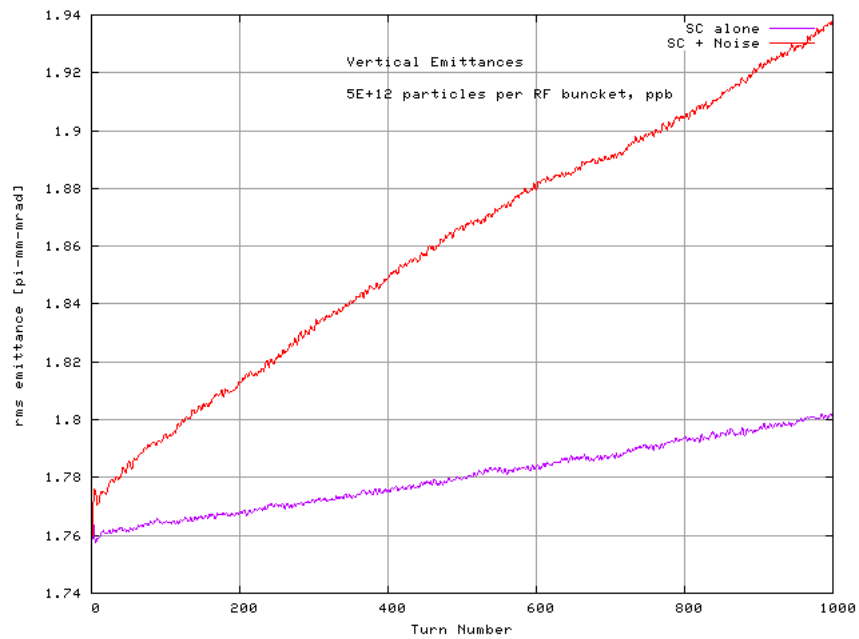
(b) vertical emittance

Figure 4.10: Transverse rms emittance growths starting from the outset of injection through 1,000 tracking turns, or prior to ramping; the noise and space-charge effects in red and the space-charge effects alone in blue. The beam intensity per bucket is 6.0×10^{10} ppb, and the batch intensity is 5.0×10^{12} protons.
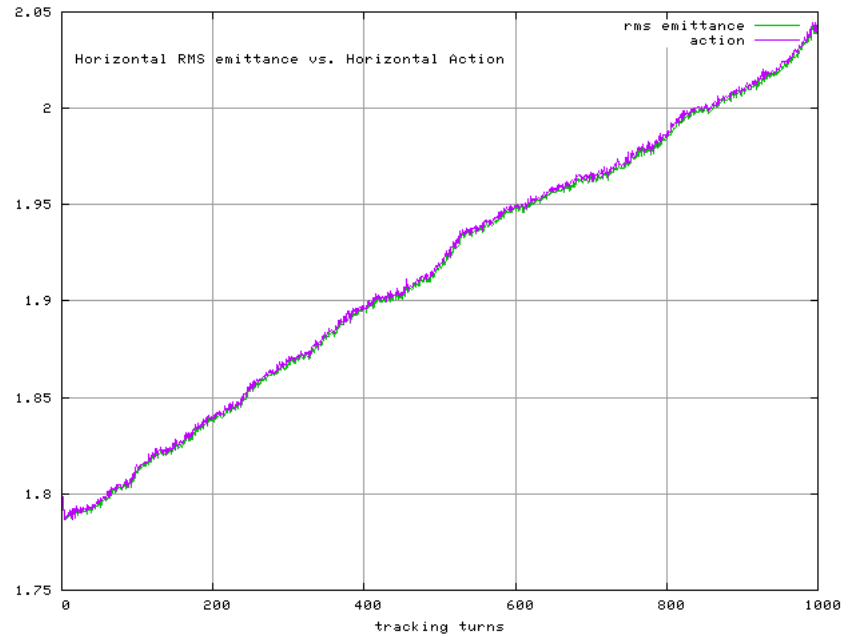
(a) vertical plane
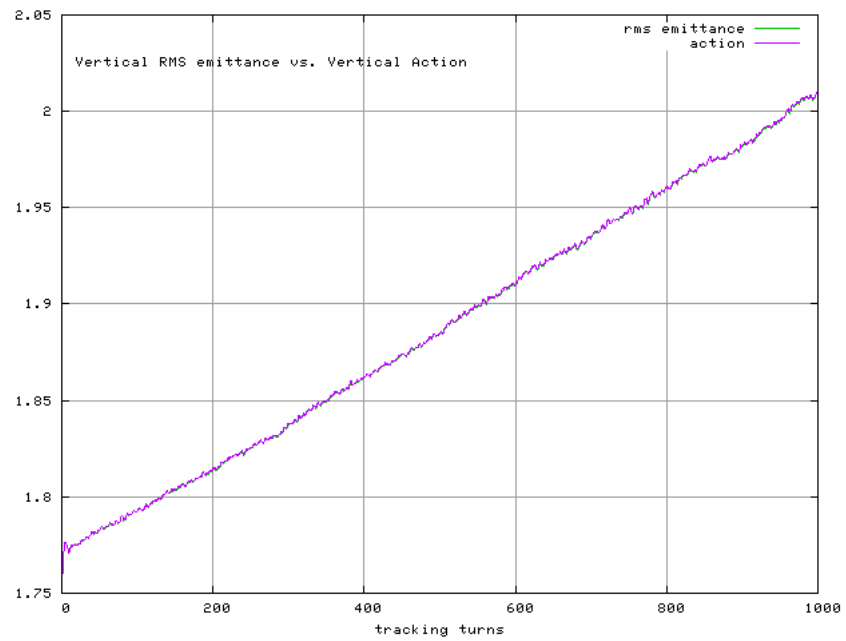
(b) horizontal plane

Figure 4.11: [left] horizontal rms emittance vs. horizontal action; [right] vertical rms emittance vs. vertical action
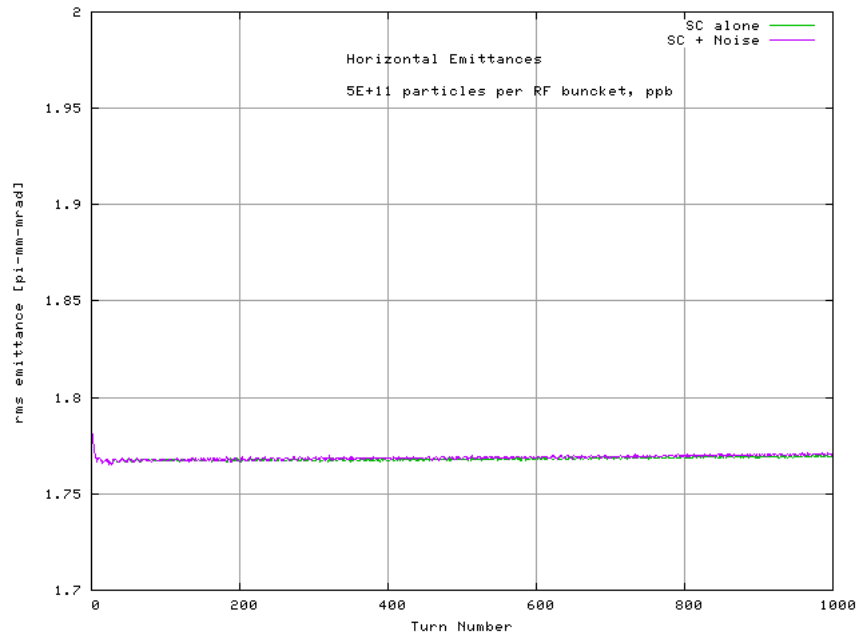
(a) horizontal emittance
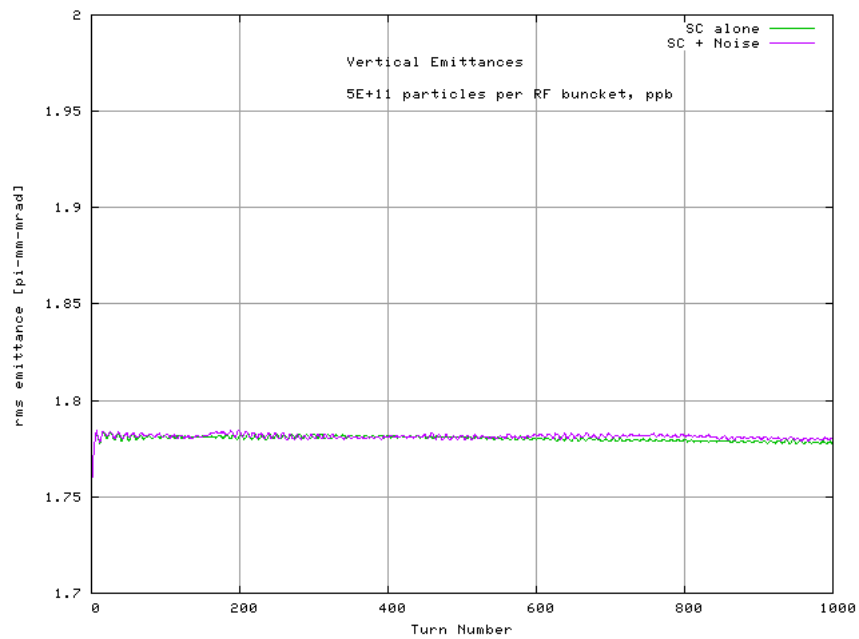
(b) vertical emittance

Figure 4.12: Transverse emittance growths; the noise and space-charge effects in red and the space-charge effects alone in blue. The beam intensity is 6×10^9 ppb, and 5×10^{11} protons in total.

(a) $\langle x y \rangle$: No space charge; no noise

(b) $\langle x y \rangle$: Space charge alone

(c) $\langle x y \rangle$: Noise alone

(d) $\langle x y \rangle$: Noise coupled to space charge
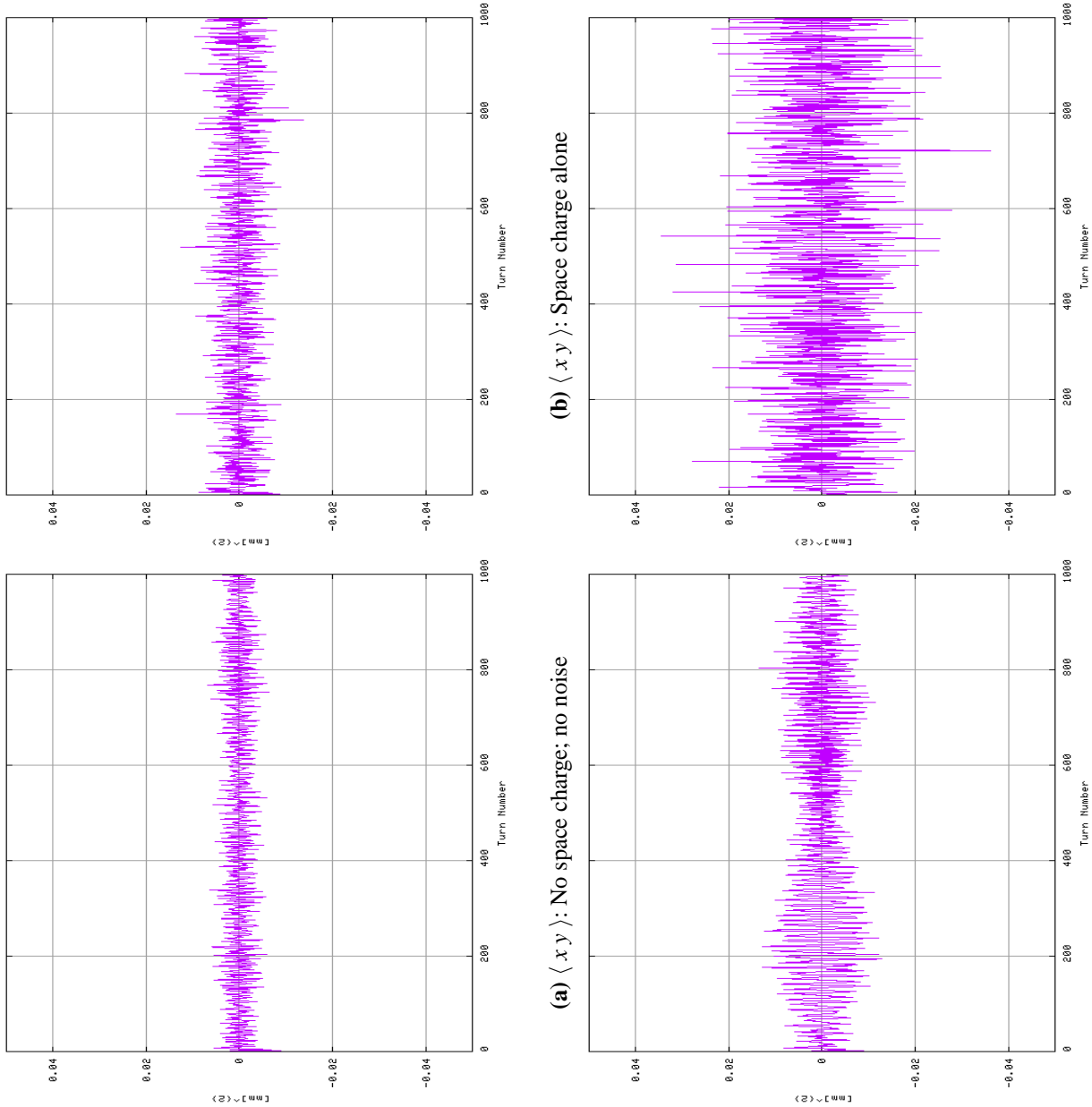
Figure 4.13: Transverse couplings in configuration space
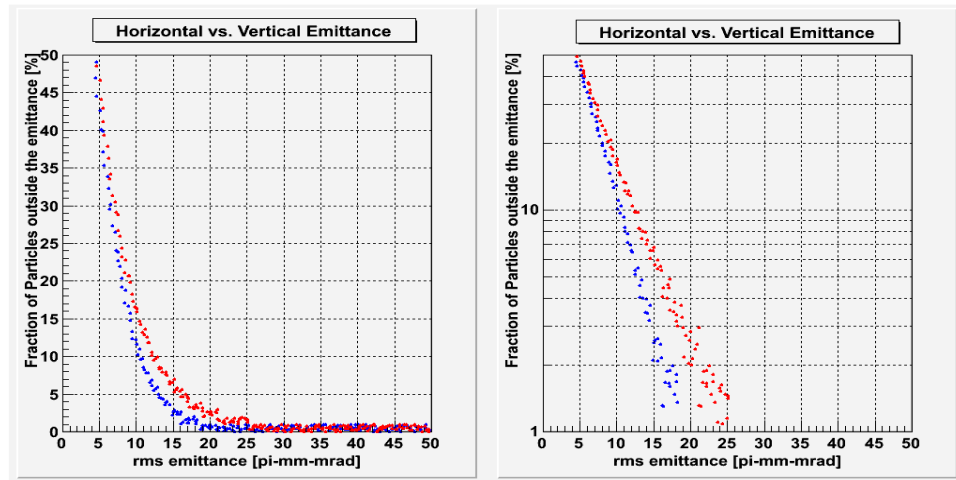
Figure 4.14: Fractional exclusion of macroparticles at a given average action. The blue indicates at the $1^{st}turn$ and the red indicates after 1,000 turns. The vertical axis on the left plot is in linear scale, and the right is on logarithmic scale.
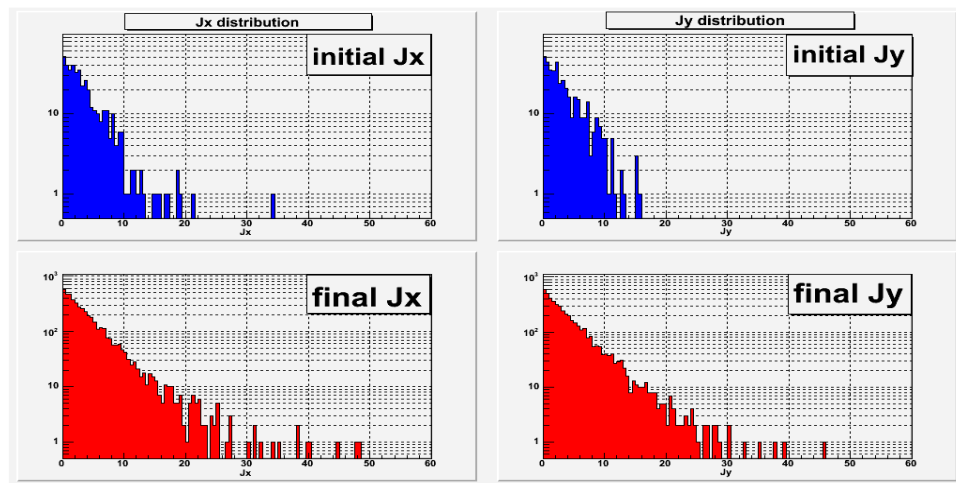
Figure 4.15: The distribution of actions ($\mathcal{I}_x$ and $\mathcal{I}_y$) at the 1st turn and after 1,000 turns. O-U noise and 2.5D space-charge effects are included. Action distribution at the 1st turn is in blue, and action distribution after 1,000 turns in red.
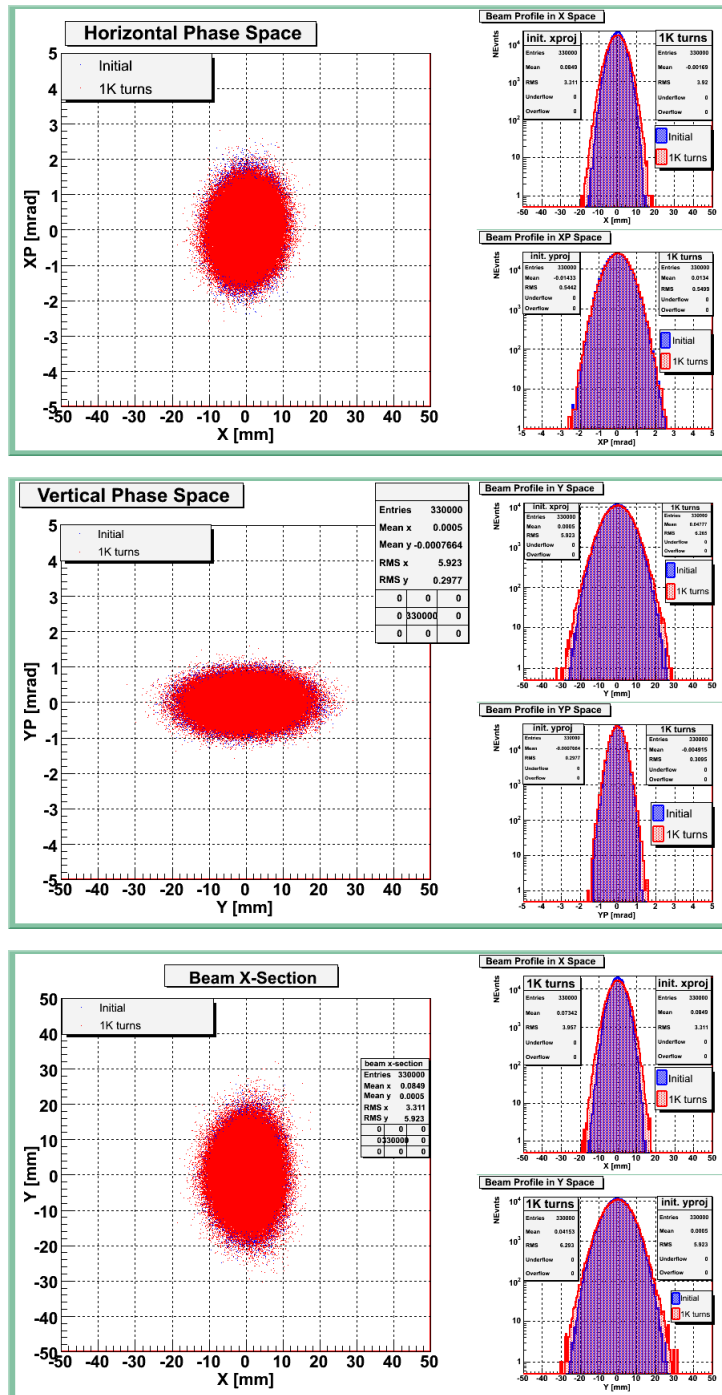
Figure 4.16: Trace spaces and projected profiles in the planes of position and divergence angle; [top] horizontal plane; [middle] vertical plane; [bottom] Beam cross-section and profiles in the horizontal and vertical planes.

4.3.9 Halo Magnitude

The computation of maximum extent of macroparticle coordinates in a beam at each tracking turn is implemented in the Noise module. The Eqn. (4.38) includes only physical coordinates (*x* and *y*) of a maximum-displaced macroparticle at the location of a random noise node [7]. In this dissertation, we refer it to as *halo magnitude* (R_H).

$$\mathcal{R}_{H,\,2D} = \sqrt{x^2 + y^2}\Big|_{Max} \tag{4.38}$$

Figure 4.17 shows the halo magnitudes that are computed at the location of each random noise node representing a GMPS in the Booster ring. Figure 4.18 illustrates the evolution of halo magnitudes in green and smoothed data in blue. Due to the large oscillatory behavior of the halo magnitudes, the data is smoothed. The smoothed curve in Figure 4.19 shows us with clarity a growing pattern of a maximum-displaced macroparticle from the physical center of a magnet aperture.
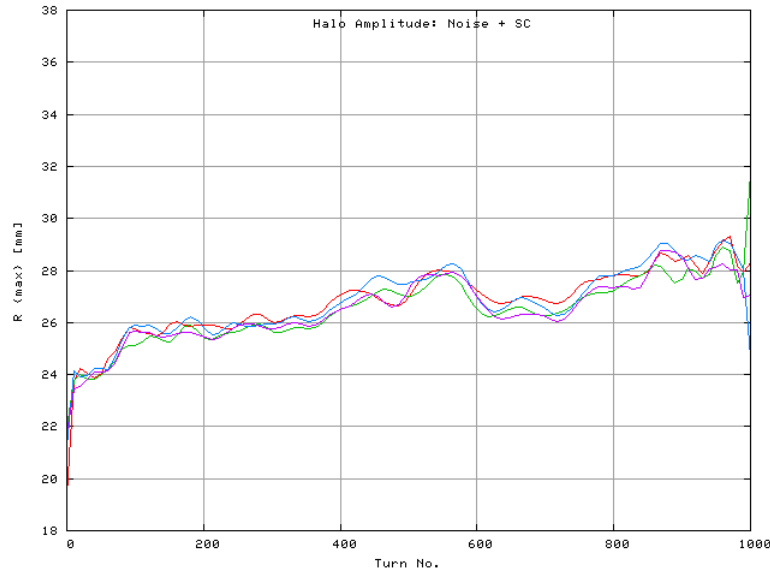
Figure 4.17: Halo magnitudes (R_{max}) at each random noise node
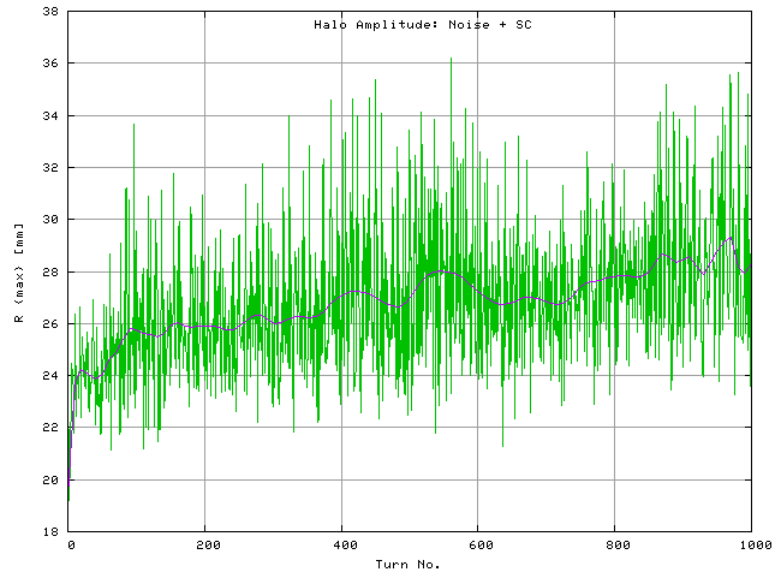
Figure 4.18: Halo magnitudes (R_{max}): noise in the presence of the space-charge effects; the blue trace in the background indicates smoothed curve with spline function.
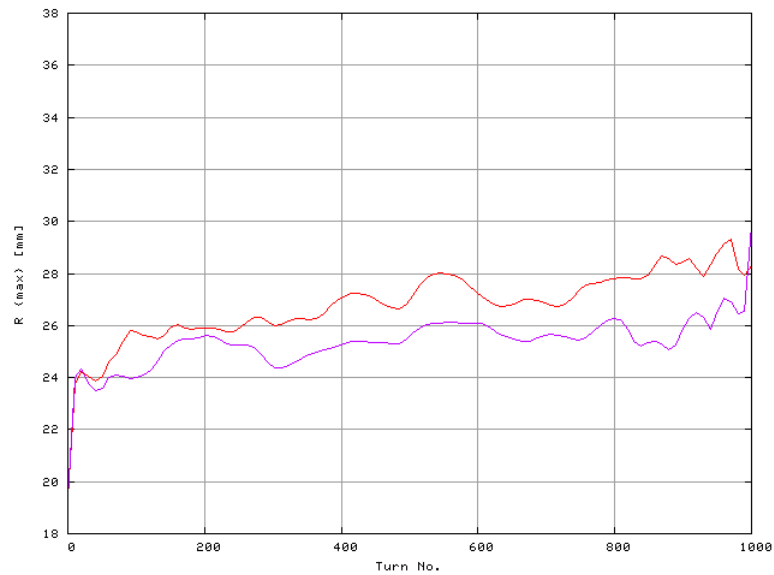
Figure 4.19: Halo magnitudes (R_{max}): noise along with space-charge effects (red) vs. space-charge effects alone (blue)

Magnet Misalignment Model

5.1 Introduction

The previous chapters describe the impact of power-supply current fluctuations on machine performance. In this chapter we focus on the impact of magnet alignment errors in the Booster. Unlike other types of machine imperfections, alignment errors are unavoidably present in all types of accelerators including linear accelerators (linacs) and synchrotrons. We have constructed a magnet misalignment model in order to investigate the impact of lattice-element alignment errors on a beam in the presence of space charge.

In advance of construction of a misalignment model, it is essential to carry out thorough statistical analyses of the raw magnet alignment survey data. The *raw survey data* is a dataset of fiducial coordinates that are measured by the beamline survey team. From these data, we can identify the orientations and alignment errors of each individual beamline element. In the design stages of a new accelerator, all simulations are confined to setting the alignment tolerances for the lattice elements. For an existing accelerator, we have access to yearly-updated survey data. Therefore, we can build a realistic and up-to-date misalignment model.

The Booster lattice is constructed with a number of different beamline elements. These

include focusing and defocusing magnets, corrector packages, straight sections, RF cavities, beam position monitors, beam loss monitors, etc. In this and the next chapter, we focus on modeling the alignment errors for the ninety-six main gradient magnets [1] in the Booster lattice.

Our magnet misalignment model is used as follows:

(1) Through the survey-data analyses, we are able to gain a solid understanding of the most up-to-date alignment issues for the Booster.

(2) It provides guidlines to set priorities and tolerances for future yearly realignment efforts of individual beamline elements.

Once a year, during the long Booster shutdown period, the Survey Alignment and Geodesy (SAG) Group of Fermilab conducts the survey and realigning work on the Booster beamline components. Employing the latest survey data taken in spring 2005, we analyze and calculate the magnitudes and orientations of the magnet misalignments of all types. The data are used to gain an understanding of the types of alignment errors that are currently present, and how they are distributed around the Booster ring. The measurements serve as the most up-to-date input data for realistic macroparticle-tracking simulations, and includes a suite of beam diagnostic calculations. There are no identical gradient magnets in our magnet misalignment model. Each magnet is treated as a unique and individual lattice element with their own alignment errors.

We begin with a discussion of the survey methodology, details of the calculational methods, and survey-data analysis results. The following acronyms are frequently used for convenience and brevity.

---

[1] For brevity, we will frequently refer a main gradient magnet as *magnet* hereafter.

- **SAG**: Survey Alignment and Geodesy

- **FSCS**: Fermilab Site Coordinate Systems

- **CF**: Combined-Function (magnet)

- **LSS**: Long Straight Section

- **SSS**: Short Straight Section

- **MSS**: Mini Straight Section

- **US**: Up Stream

- **DS**: Down Stream

- $(\widetilde{X}, \widetilde{Y}, \widetilde{Z})$: the DUSAF coordinates

- (X, Y, Z): the Cartesian coordinates, or the Frenet-Serret curvilinear coordinates[2]

5.2   Fermilab Site Coordinate Systems

In the early 1990s, a DUSAF [3] coordinate system was established at Fermilab. The DUSAF coordinate system is a right-handed coordinate system with the following definitions [46, 47]:

- **Origin**: The Fermilab Tevatron ring is divided into six sectors starting from A0 through F0. The origin of DUSAF coordinate system is at A0 as indicated in Figure 5.1.

- $\widetilde{Y}$**-axis**: It is also called NORTH axis. As depicted in Figure 5.1 with a red arrow, the

---

[2] Assuming that torsion is zero, the coordinates of a particle on a design orbit in a circular accelerator can be represented by $\vec{r} = \vec{r}_0 + x\hat{x} + y\hat{y}$.

[3] Although the DUSAF coordinate system is selected for the Fermilab Site Coordinate System, the origin of the name DUSAF refers to the four firms that participated in the original NAL site design see: http://history.fnal.gov/visitors.html#DUSAF.

positive Y direction is along the extension line towards the *Neutrino area* from the origin at A0.

- $\widetilde{X}$-**axis**: It is also called EAST axis. The positive X direction extends to the right and perpendicular to the Y-axis.

- $\widetilde{Z}$-**axis**: It is also called ELEVATION axis. The positive direction is upward from the origin and orthogonal to both $\widetilde{X}$- and $\widetilde{Y}$-axis.
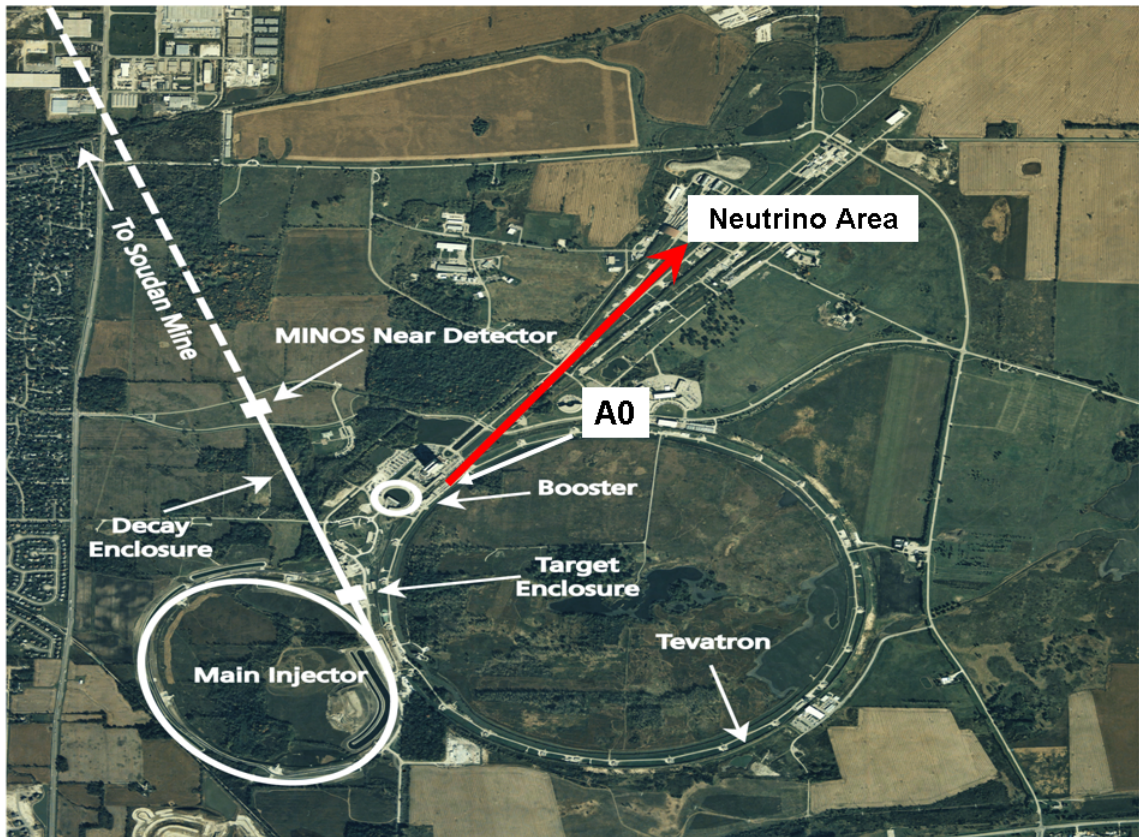
Figure 5.1: An aerial view of the Fermilab site; photo courtesy of Fermilab

It should be noted that the DUSAF coordinate system used by SAG is different from the Frenet-Serret curvilinear coordinate system [48] for circular accelerators and the Cartesian coordinate system for linear accelerators. We use $\widetilde{X}$, $\widetilde{Y}$, and $\widetilde{Z}$ to denote the DUSAF

coordinates in order to differentiate them from the Frenet-Serret and Cartesian coordinates (**X**, **Y**, **Z**). The coordinates defining the origin of the DUSAF coordinate system are as follows:

- $\widetilde{X}$ = 100000.000 ft. (= 30480.06096 m)

- $\widetilde{Y}$ = 100000.000 ft. (= 30480.06096 m)

- $\widetilde{Z}$ = 720.000 ft. (= 219.45644 m)

$\widetilde{Z}$ = 720.000 ft. at A0 indicates that the elevation of A0 is 720 ft. above the DUSAF Datum, which is an arbitrary datum. These arbitrary coordinates at origin are selected in order to make all survey data points positive around the Booster ring for surveyor's convenience [49]. The Fermilab Site Coordinate System (FSCS), which is an assimilated DUSAF coordinate system, is defined for the Booster magnet survey. Its origin and rotation axes are located at A0, preserving the DUSAF coordinate system as nearly as possible. For the unit conversion, the following conversion factor is consistently used.

1 meter = 39.97 US survey inches exactly [4]

5.3 Configuration of the Booster Magnet Cell

The Booster synchrotron has a circumference of 474.2 m. It contains 96 combined-function main gradient magnets. There is a 24-fold symmetry in the Booster lattice. Each period, or cell (defined as SAG) consists of two focusing magnets, two defocusing magnets, two halves of a long straight section, one short straight section, and two mini straight sections. The above-mentioned cell components are symmetrically positioned around the midpoint of a short straight section. The lenghts of all cell components are tabulated in Table 5.1.

---

[4]This unit conversion factor is for the surveyors, and is not the same as in SI (Système International d'Unités; International System of Units). In SI, 1 inch = 0.0254 m exactly.

Table 5.1: Longitudinal distance of the Booster lattice components

Circumference ($\mathcal{C}$)	474.2 (m)
Long Straight Section (LSS)	5.9784 (m)
Short Straight Section (SSS)	1.1753 (m)
Mini Straight Section (MSS)	0.4726 (m)
Longitudinal Distance between Fiducial Points [5]	2.9145 (m)
LSS : SSS : MSS	6.3 : 2.5 : 1.0

5.4 Booster Survey Network

The purpose of the Booster survey is to establish a precision control network for positioning each individual beamline component within the Fermilab Site Coordinate System (FSCS) [47]. As depicted in Figures 5.2 and 5.3, the Booster control network (BooNet) is a system of braced quadrilaterals between the floor monuments, wall monuments, pass points, and tie-rods in the tunnel; between monuments, pass points, and tie-rods, a web-like network is formed. The monuments, pass points, and tie-rods can be understood as designated positions where coordinates are generated. Therefore, by distributing them all around the Booster tunnel, we can form a strengthened Booster survey network.

---

[5] The fiducialized longitudinal distance is assumed to be common to both defocusing and focusing magnets.
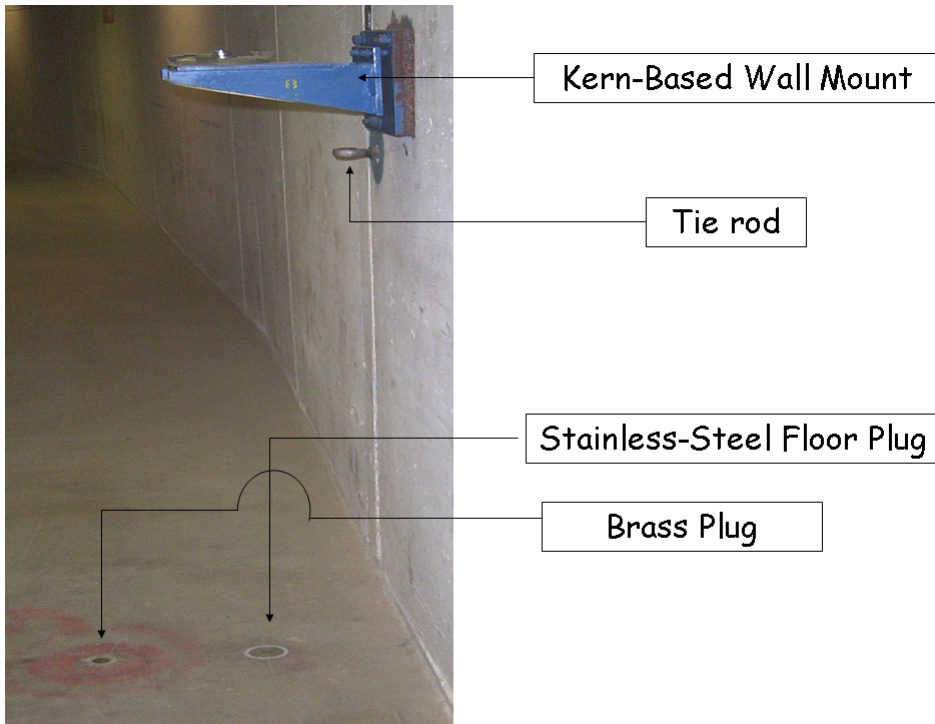
(a) A kern-based wall mount, a tie-rod, and plugs in the Booster tunnel; this photo is at the courtesy of the survey alignment and geodesy (SAG) group of Fermilab

(b) A SMR mounted on a tie rod and a tie adapter

(c) Spherically-Mounted Rectroreflector (SMR) mounted on a brass plug

Figure 5.2: Horizontal and vertical mounts, tie-rod, and SMR
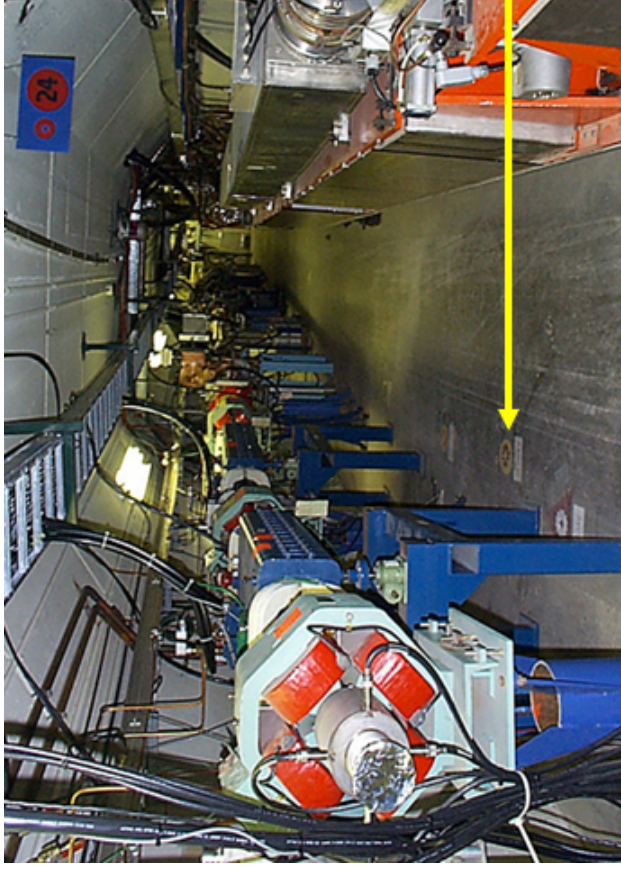
Brass Plugs
Offsets to Beamline
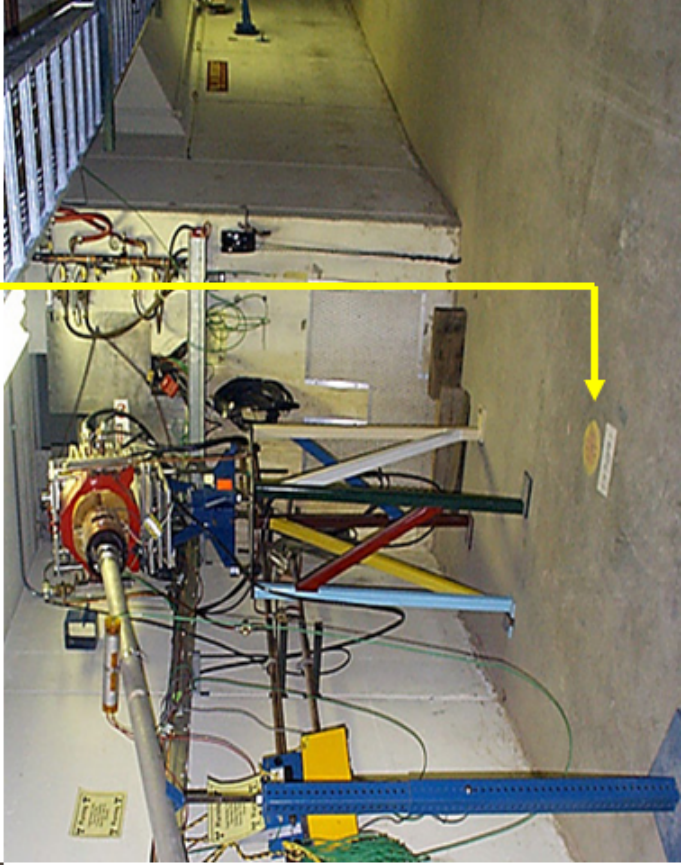
Figure 5.3: Brass plugs on the floor; photos at the courtesy of the SAG of Fermilab

The survey makes use of spherically-mounted retroreflectors (SMR) to improve the performance of the laser-tracker system. The spherically-mounted retroreflectors in conjunctions with a laser-tracker beam are used to locate various devices. A SMR is mounted on a tie adapter supported by a tie-rod bolted into a wall. A pass point is either a permanent, or temporary point installed on a wall, such that a SMR can be attached to it in addition to the monuments. The monuments, tie-rods, and pass points can be considered to be a kind of SMR mounts, or supporting frames [50]. Once SMRs are set up in the Booster survey area, a laser tracker measures horizontal and vertical angles between a pair of mounted SMRs. Figure 5.4 shows a laser tracker that is employed in the Booster survey.

Figure 5.4: An actual laser tracker SMX 4500 in use for survey work at Fermilab

The BooNet was first established in July 1993, and was composed of both horizontal and vertical networks. Before the recent upgrade, the network included a total of 48 floor monuments and 26 tie-rods on the wall. A set of 24 vertical monuments (and another set of 24 horizontal monuments) are equally spaced all around the Booster ring. The vertical monuments, or tie-rods are anchored to the wall, and horizontal monuments are installed on the floor. One horizontal and one vertical monument are positioned at the center of each long straight section (a pair of horizontal and vertical monuments for each superperiod).

In December 2004, as a part of the Booster upgrade plan, the pre-existing Booster control network was densified and tied with additional 59 floor monuments and 125 pass points. The BooNet densification is illustrated by Figure 5.5. Furthermore, the network was up-
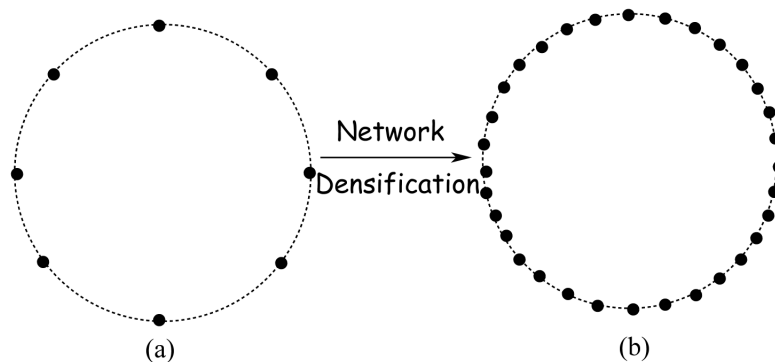
Figure 5.5: Booster network densification viewed from top; the black dots indicate wall monuments and floor monuments in the network.

graded with the aid of the modern technology instruments [51], such as a laser tracker [6] and a digital level[7]. All of three coordinates (Easting, Northing, and Elevation) of each beamline element are first measured with the laser trackers and SMRs. Afterwards, the elevation ($\widetilde{Z}$) data taken with the laser tracker are replaced with the data taken with the digital levels of higher precision. The precision of the laser tracker is 0.5 μm in the radial direction, and

---

[6] The model name of the laser tracker is SMX 4500

[7] The model name of the digital level is Leica NA 3003

0.25 μm in the vertical direction. In between annual survey activities, the vertical positions, or elevations of tie-rods could change or deform over the year. Therefore, the vertical network is remeasured during each shutdown period. There are four additional measurements besides the network measurements:

(1) *as-found* measurements of all of 384 (= 96 × 4) magnet fiducial points, 48 BPMs (Beam Position Monitors) and 19 RF cavities in the Booster. In this context, *as-found* measurements imply survey readings with no adjustments and corrections.

(2) *as-found* measurements of all dipole and quadrupole fiducial points in the 400-MeV transferline.

(3) the determination of the upstream and downstream coordinates ($\widetilde{X}$, $\widetilde{Y}$, and $\widetilde{Z}$) of each beamline component.

(4) archiving the FSCS coordinates of beamline components and further misalignment calculations.

5.5   Magnet Fiducialization

A Booster main gradient magnet is a sector bending magnet (SBEND) with curvature as depicted in Figure 5.6. The rotation angles of the entrance pole face and the exit pole face are zero. Beamline surveyors fiducialize the main gradient magnet with survey fiducial points as a rectilinear object. Figure 5.7 shows a fiducialized body of a main gradient magnet. A proton beam travels through the gradient magnet from upstream end (US) to downstream (DS) end. The side facing radially inward is referred to as *wallside*, and the side facing radially outward is called the *aisleside* [52]. As illustrated by Figures 5.7 and 5.8, the four fiducial points are labeled as A, B, C, and D in a clockwise orientation when viewed from top. According to the schematics of Figure 5.8, the offsets at upstream and downstream of each magnet are calculated. The beam centerline is radially shifted out-

ward by 0.053 inches with the defocusing magnet, and radially inward by 0.042 inches with the focusing magnet [52]. A pair of fiducial points on the gradient magnet are separated by 15.016 inches in the transverse direction, and 114.747 inches in the longitudinal direction. The span of the magnet coils is 113.741 inches, and the longitudinal length of the gradient
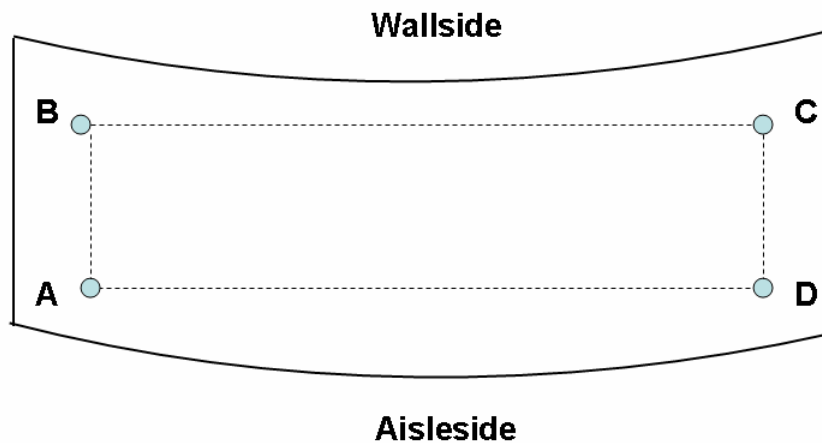
Figure 5.6: A top view of a main magnet of rectangular-bend-magnet (RBEND) type with four fiducial points. The rectangular bend magnet is fiducialized as a rectilinear object (enclosed by dotted lines). The curvature lines are not to scale.
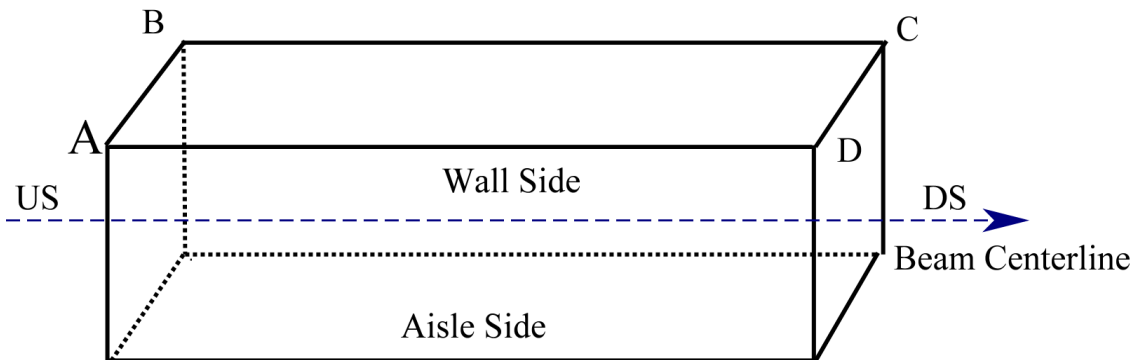
Figure 5.7: A side view of a fiducialized portion of main gradient magnet of the Booster; The blue arrow indicates the beam propagation direction.

physical centerline

B 1.5"

15.016"

0.053"

A

C

D

beam centerline

Wall Side

B **C**

0.042"

A **D**

physical centerline

Aisle Side

113.741" = 2.8890 m

114.747" = 2.9146 m
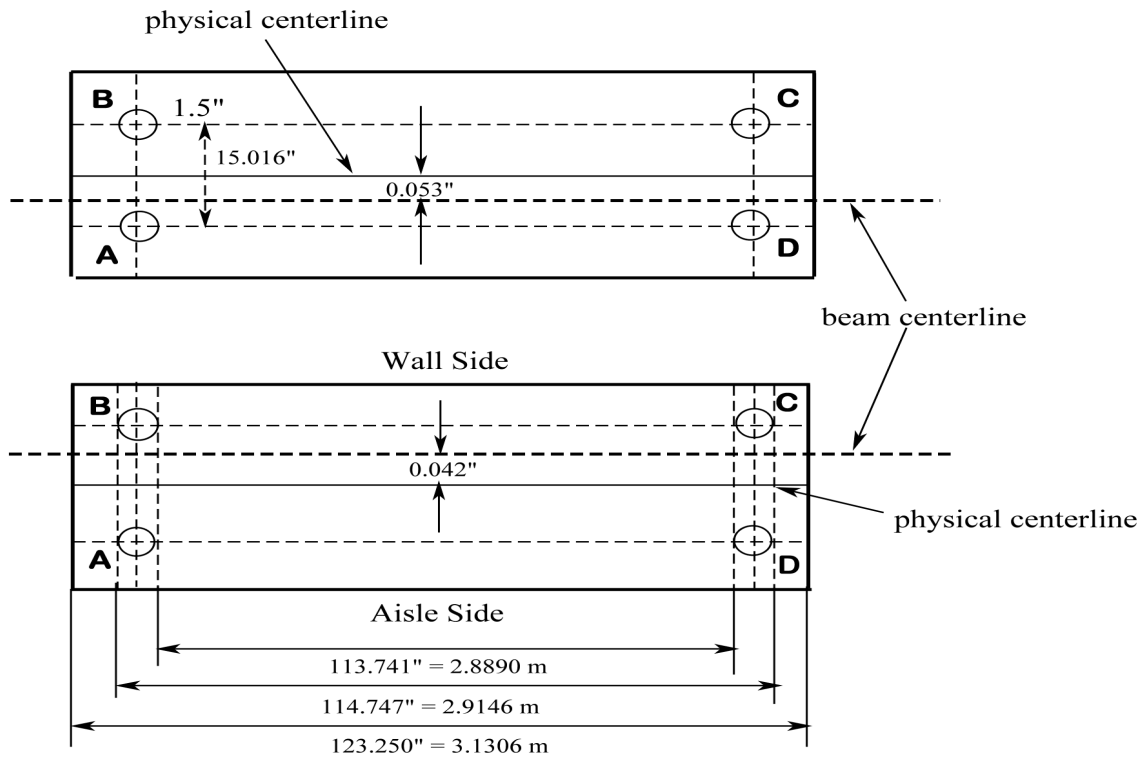
123.250" = 3.1306 m

Figure 5.8: Top views of the main gradient magnets of the Booster. A, B, C, and D indicate four fiducial points. [upper] defocusing magnet [lower] focusing magnet

magnet is 3.1306 meters (=123.250 inches) (i.e., from one end to the other end of the external steel frame of the magnet). This magnet is frequently referred to as a *10-foot long magnet* at Fermilab. The magnet lengths for a focusing magnet and a defocusing magnet are slightly different. However, the distances between fiducial points are intended to be the same for all magnets.

5.6 Types of Magnet Misalignments

After each round of survey measurements, SAG creates a beamsheet file that contains all the coordinates ($\widetilde{X}$, $\widetilde{Y}$, $\widetilde{Z}$) at each fiducial point of all beamline components of

the Booster. By analyzing the raw survey data, the following types of alignment errors (displacements and rotations) are calculated and identified at each gradient magnet;

- radial offset

- vertical offset

- longitudinal (station) offset (mini straight section and long straight section)

- pitch (**X**-rotation)

- yaw (**Y**-rotation)

- roll (**Z**-rotation)

- *twist* (**Z**-rotation with a large roll angle)

It should be noted that although we calculate rotational misalignments using the Fermilab Site coordinates (DUSAF coordinates), we follow the common naming convention of the types of misalignments (pitch, yaw, and roll) according to their rotation axes in the Frenet-Serret coordinates: **X**-rotation, **Y**-rotation, and **Z**-rotation

5.7 Methodology of Magnet Misalignment Calculations

This section gives details of how each type of alignment errors are computed from the raw survey data. From the surveyor's standpoint, the geometry of one magnet cell is considered to be a series of 9 line segments (LSS/2, Defocusing magnet, MSS, Focusing magnet, SSS, Focusing magnet, MSS, Defocusing magnet, and LSS/2) joined together, instead of an arc. As 24 magnet cells constitute the entire Booster ring, the Booster ring is modeled as a 216-sided polygon. By averaging over the coordinates of all upstream and downstream coordinates at each main magnet, we find the Booster centroid, $(\widetilde{X}_c, \widetilde{Y}_c, \widetilde{Z}_c)$ as in Eqn. (5.1): thus, the polygon is centered at the Booster centroid. The black line in
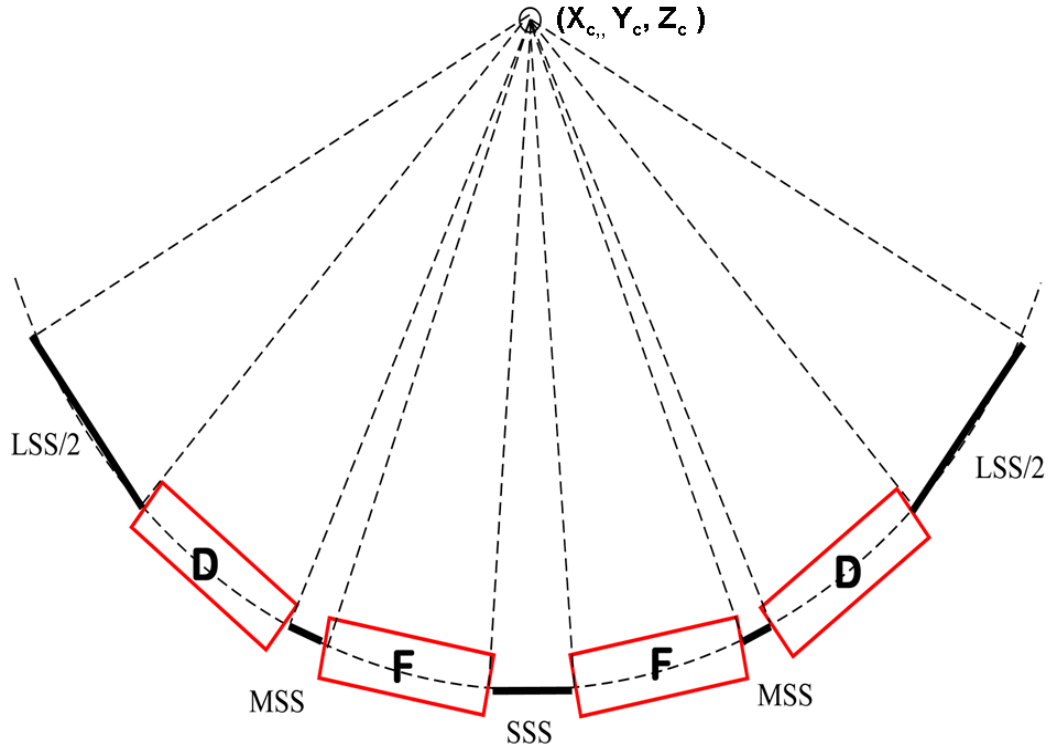
Figure 5.9: The configuration of one magnet cell; Twenty-four cells constitute a 216-sided polygon of the Booster ring

Figure 5.9 represents each of three types of straight sections (MSS, SSS, and LSS), and the red box represents either a focusing or defocusing magnet.

$$
\left.
\begin{aligned}
\widetilde{X}_c = \langle\, \widetilde{X}\, \rangle_{Booster} &= \frac{1}{96 \times 4} \sum_{i=1}^{96\times 4} \widetilde{X}_i = 30396.877 \ (m) \\[2mm]
\widetilde{Y}_c = \langle\, \widetilde{Y}\, \rangle_{Booster} &= \frac{1}{96 \times 4} \sum_{i=1}^{96\times 4} \widetilde{Y}_i = 30306.529 \ (m) \\[2mm]
\widetilde{Z}_c = \langle\, \widetilde{Z}\, \rangle_{Booster} &= \frac{1}{96 \times 4} \sum_{i=1}^{96\times 4} \widetilde{Z}_i = 221.432 \ (m)
\end{aligned}
\right\}
\tag{5.1}
$$

Here $\widetilde{X}_i$, $\widetilde{Y}_i$, and $\widetilde{Z}_i$ denote Fermilab Site Coordinates at each fiducial point on a main magnet. In Eqn. (5.1), because each of 96 main magnets have 4 fiducial points, each of three

coordinates is summed over 384 fiducial points. This implies that by calculating the value of $\widetilde{Z}_c$ the fiducial elevation ($\widetilde{X}$-$\widetilde{Y}$ plane) of the Booster ring ($\langle \widetilde{Z} \rangle_{Booster}$) is determined in the Fermilab Site Coordinate System. The value of $\langle \widetilde{Z} \rangle_{Booster}$ is 221.43197 (m). Since the zero elevation is set at 720.000 (ft.) (= 219.45644 m), the average elevation for 96 gradient magnets is the difference of the two values: that is, 1.97553 (m) above the $\widetilde{Z}_0$ at A0. Furthermore, averaged coordinates at upstream and downstream of each gradient magnet are computed.

$$
\left.
\begin{aligned}
\widetilde{X}_{us} &= \frac{(\widetilde{X}_A + \widetilde{X}_B)}{2} + \Delta_{offset}, \ \widetilde{X}_{ds} = \frac{(\widetilde{X}_C + \widetilde{X}_D)}{2} + \Delta_{offset} \\
\widetilde{Y}_{us} &= \frac{(\widetilde{Y}_A + \widetilde{Y}_B)}{2} + \Delta_{offset}, \ \ \widetilde{Y}_{ds} = \frac{(\widetilde{Y}_C + \widetilde{Y}_D)}{2} + \Delta_{offset} \\
\widetilde{Z}_{us} &= \frac{(\widetilde{Z}_A + \widetilde{Z}_B)}{2}, \qquad\quad \widetilde{Z}_{us} = \frac{(\widetilde{Z}_C + \widetilde{Z}_D)}{2}
\end{aligned}
\right\}
\tag{5.2}
$$

In Eqn (5.2), Δ_{offset} denotes the offset between the physical centerline and the beamline of each type of gradient magnet. The physical centerline is the centerline of physical apertures of a magnet, and the beamline coincides with the design orbit. According to the J. Walton's logbook dated back in September 1973, when the Booster main gradient magnets were physically installed for the first time, the offsets were introduced between a beam centerline and a physical centerline of each magnet. This is determined based upon empirical measurements [53]. As such, surveyors make corrections on *as-found* measurement data every year. The offset for a defocusing magnet is + 0.053 inches (= + 1.346 mm), and - 0.042 inches (= - 1.067 mm) for a focusing magnet. The radially outward direction is set to be positive, radially inward direction to be negative. We define

$$
\left.
\begin{aligned}
\Delta\widetilde{X} &= \widetilde{X}_{ds} - \widetilde{X}_{us} \\
\Delta\widetilde{Y} &= \widetilde{Y}_{ds} - \widetilde{Y}_{us} \\
\Delta\widetilde{Z} &= \widetilde{Z}_{ds} - \widetilde{Z}_{us}
\end{aligned}
\right\}
\tag{5.3}
$$

In Figure 5.10, we first draw a horizontal axis **X1** by extending a line from the upstream
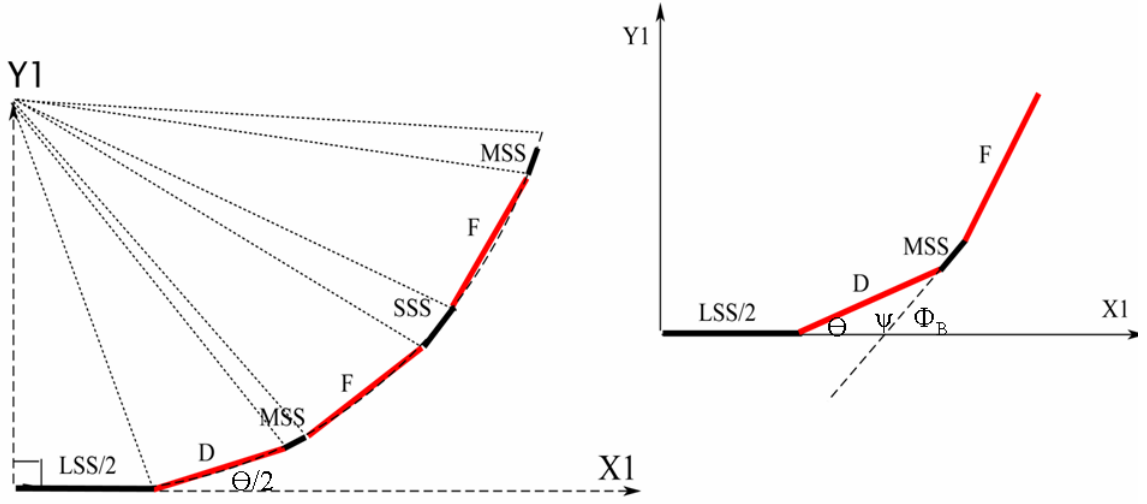
Figure 5.10: The cell components projected onto X1-axis for calculation purpose.

half of a long straight section (LSS/2) towards downstream components. We then draw a vertical axis **Y1** perpendicular to **X1** axis. From the Booster centroid, radial lines are drawn to upstream end and downstream end of each line segment. Each of the station components are projected onto the X1 axis, so that we can compute **X1** and **Y1** coordinates. By definition, the angle Φ_B is equivalent to the bending angle of the corresponding magnet. Thus, the angle Φ_B turns out to be the twice of angle θ_B.

$$\Psi = 180° - \Phi_B$$
$$\theta = (180° - \Psi)/2 \qquad (5.4)$$
$$= \Phi_B/2$$

As we proceed to the downstream component from the first half of the long straight section, the argument angles of trigonometric function are accumulated as described in Eqn. (5.5). The set of equations below illustrate how the projected **X1** and **Y1** coordinates are computed for each cell component. Here θ_D and θ_F denote bending angles of defocusing and

focusing magnet, respectively.

$$
\left.
\begin{aligned}
\widetilde{X}_{LSS/2} &= LSS/2 \\
\widetilde{Y}_{LSS/2} &= 0 \\
\widetilde{X}_D &= \widetilde{X}_{LSS/2} + \mathcal{L}_{long} \cdot \cos(\theta_D/2) \\
\widetilde{Y}_D &= \mathcal{L}_{long} \cdot \sin(\theta_D/2) \\
\widetilde{X}_{MSS/2} &= \widetilde{X}_D + MSS/2 \cdot \cos(\theta_D) \\
\widetilde{Y}_{MSS/2} &= \widetilde{Y}_D + MSS/2 \cdot \sin(\theta_D) \\
\widetilde{X}_F &= \widetilde{X}_{MSS/2} + \mathcal{L}_{long} \cdot \cos(\theta_D + \theta_F/2) \\
\widetilde{Y}_F &= \widetilde{Y}_{MSS/2} + \mathcal{L}_{long} \cdot \sin(\theta_D + \theta_F/2) \\
\widetilde{X}_{SSS/2} &= \widetilde{X}_F + SSS \cdot \cos(\theta_D + \theta_F) \\
\widetilde{Y}_{SSS/2} &= \widetilde{Y}_F + SSS \cdot \sin(\theta_D + \theta_F) \\
\widetilde{X}_F &= \widetilde{X}_{SSS/2} + \mathcal{L}_{long} \cdot \cos(\theta_D + 3 \cdot \theta_F/2) \\
\widetilde{Y}_F &= \widetilde{Y}_{SSS/2} + \mathcal{L}_{long} \cdot \sin(\theta_D + 3 \cdot \theta_F/2) \\
\widetilde{X}_{MSS} &= \widetilde{X}_F + MSS \cdot \cos(\theta_D + 2 \cdot \theta_F) \\
\widetilde{Y}_{MSS} &= \widetilde{Y}_F + MSS \cdot \sin(\theta_D + 2 \cdot \theta_F) \\
\widetilde{X}_D &= \widetilde{X}_{MSS} + \mathcal{L}_{long} \cdot \cos(3 \cdot \theta_D/2 + 2 \cdot \theta_F) \\
\widetilde{Y}_D &= \widetilde{Y}_{MSS} + \mathcal{L}_{long} \cdot \sin(3 \cdot \theta_D/2 + 2 \cdot \theta_F) \\
\widetilde{X}_{LSS/2} &= \widetilde{X}_D + LSS/2 \cdot \cos(2 \cdot \theta_D + 2 \cdot \theta_F) \\
\widetilde{Y}_{LSS/2} &= \widetilde{Y}_D + LSS/2 \cdot \sin(2 \cdot \theta_D + 2 \cdot \theta_F)
\end{aligned}
\right\} \tag{5.5}
$$

Figure 5.10 and a set of equations in Eqn. (5.6) illustrate how the radial distance of each

line segment in a cell is computed from the Booster centroid.

$$
\left.
\begin{aligned}
R_L &= \frac{1}{\sin(2\pi/24)} \cdot \sum_{i=1}^{9} \widetilde{X}_i \approx \frac{12}{\pi} \cdot \sum_{i=1}^{9} \widetilde{X}_i = 75.349 \ (m) \\
R_{D_{us}} &= \sqrt{\widetilde{X}^2_{LSS/2} + (R_L - \widetilde{Y}_{D_{us}})^2} = 75.409 \ (m) \\
R_{D_{ds}} &= \sqrt{\widetilde{X}^2_{D} + (R_L - \widetilde{Y}_{D_{ds}})^2} = 75.493 \ (m) \\
R_{F_{us}} &= \sqrt{\widetilde{X}^2_{MSS} + (R_L - \widetilde{Y}_{MSS})^2} = 75.503 \ (m) \\
R_{F_{ds}} &= \sqrt{\widetilde{X}^2_{F} + (R_L - \widetilde{Y}_{F})^2} = 75.527 \ (m)
\end{aligned}
\right\}
\tag{5.6}
$$

Because of the symmetrical magnet-cell configuration around the midpoint of a short straight section, the computed values in Eqn. (5.6) are repeated after the midpoint. Once the radial distances of each individual cell component from the Booster centroid are computed, the radial offsets (Δr) from each segment radius (R_i) are determined as follows:

$$
\Delta r = \sqrt{(\widetilde{X}_i - \widetilde{X}_c)^2 + (\widetilde{Y}_i - \widetilde{Y}_c)^2} - R_i
\tag{5.7}
$$

5.7.1 Translational Offsets (Displacements)

The translational offsets include radial offsets, vertical offsets, and longitudinal (station) offsets. Of the three types of offsets, we categorize radial and vertical offsets as transverse offsets. For the calculations of radial offsets, each module, or magnet cell is divided into 9 straight-line segments. The calculation scheme is described as follows:

1. Compute the average coordinates of East ($\widetilde{X}$), North ($\widetilde{Y}$) and Elevation ($\widetilde{Z}$). These are the coordinates of the Booster centroid:
   $(\widetilde{X}_c, \widetilde{Y}_c, \widetilde{Z}_c)$

2. Calculate radial distances ($R_{D_{us}}, R_{Dds}, R_{F_{us}}, R_{F_{ds}}$) at both US and DS of each type of magnet (F- and D-magnet) from the ring center.

3. Find the ideal orbit radii at both US and DS of each magnet. Because the configuration of gradient magnets in each cell is D-F—F-D, the symmetry around the SSS needs to be preserved. The only input for calculations is the ratio of bending angles ($R_\theta = \theta_F/\theta_D = 0.8496$) [10, 54].

4. Calculate the radial offsets (Δr) from the ideal orbit radii at both US and DS of each magnet.
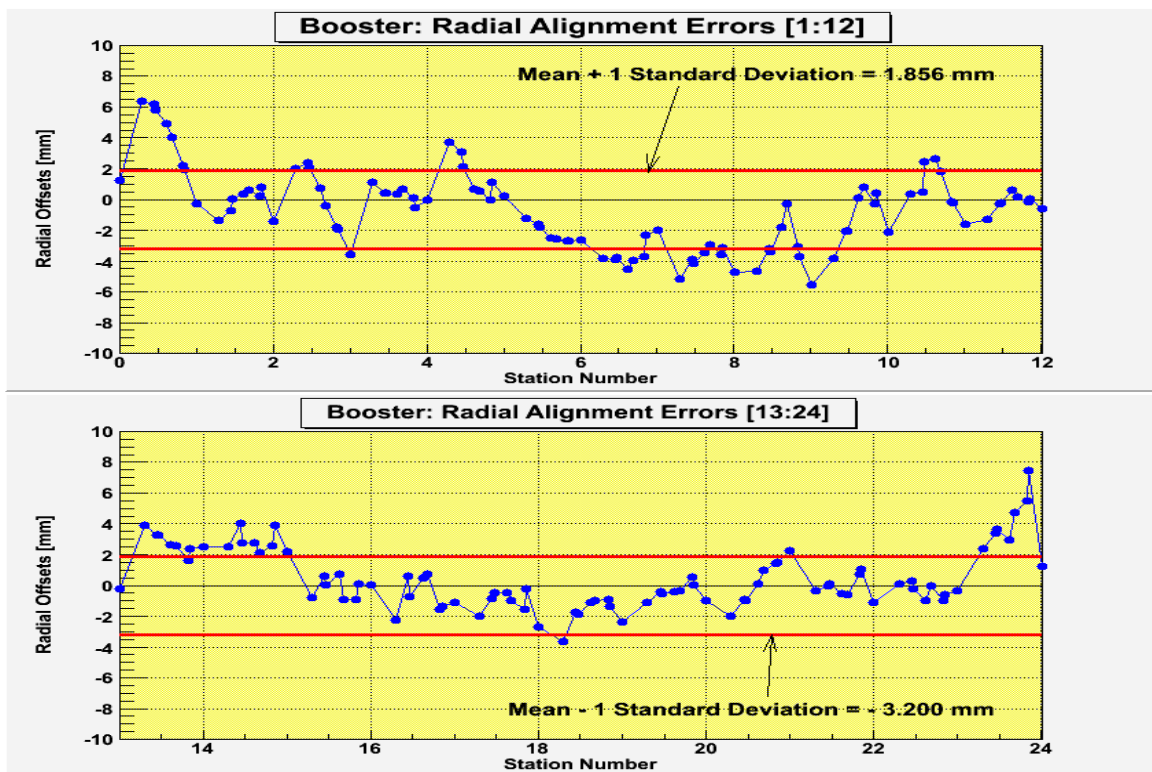
Figure 5.11: Booster-ringwide radial offsets

Figure 5.11 shows the ringwide variations of radial offsets. The vertical axes represent radial offsets in units of mm, and the horizontal axes represent station number. The upper figure is for stations 1 through 12, and the lower figure is for stations 13 through 24. A pair of red horizontal lines indicating *mean ± 1 standard deviation* are drawn to illustrate the fraction of the total numbers of magnets which fall outside of the one standard deviation

(STD) region. The STD is calculated as in Eqn. (5.8) to represent the entire distribution, rather than a sampled distribution. We choose the sample size (N) of 96, which is the total number of main magnets in the Booster. One standard deviation of the radial offsets is 2.53 mm.

$$STD = \sqrt{\frac{\sum_i (x_i - \bar{x})^2}{N}} \tag{5.8}$$

As mentioned earlier, the radial offsets are shown in Figure 5.11, Similarly, the ringwide
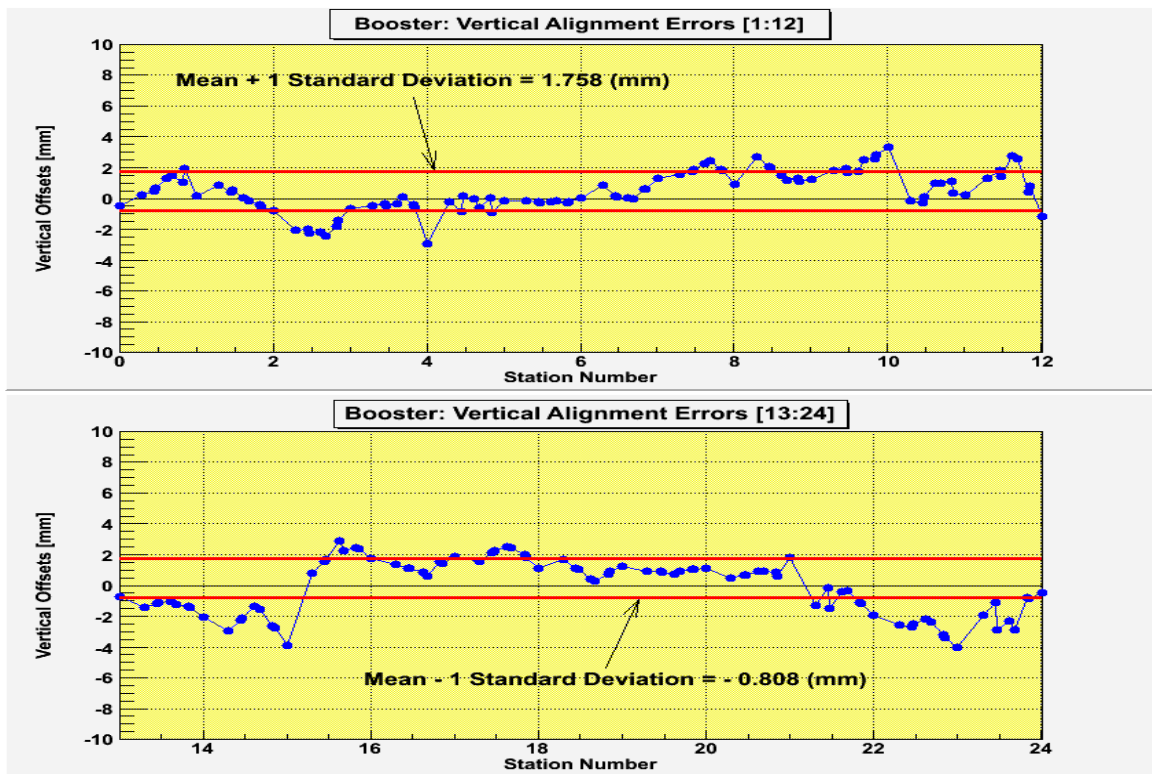
Figure 5.12: Booster-ringwide vertical offsets

variations of the vertical offsets are shown in Figure 5.12. Both Figures 5.11 and 5.12 are plotted using the same range for the vertical. It is clear from the figures that the radial-offset distribution are more widely spread than that of vertical offsets. One standard deviation for the vertical offsets is 1.29 mm. The last type of translational error that exists at the Booster magnets is the longitudinal offset. Figure 5.13 shows the ringwide variation of longitudinal

offsets at each station. In Figure 5.14, each type of translational offsets is presented in a histogram. For ease of comparison, the horizontal scales are the same in all three types of translational offset histograms. In addition, the bin size of each histogram is indicated in the title of the vertical axis. As the statistics boxes in each histogram show, the longitudinal offsets are more widely dispersed than the transverse offsets. We first compute the mean, rms (root-mean-square), and fractional rms for each distribution. We then introduce the *kurtosis* ($\mathcal{K}$), which is a measure of shape distortion from a Gaussian distribution. As defined in Eqn. (5.9), the kurtosis is the 4th central moments (μ^4) normalized by the fourth power of the rms value, or a square of variance (σ^4). To set a kurtosis of a perfect Gaussian
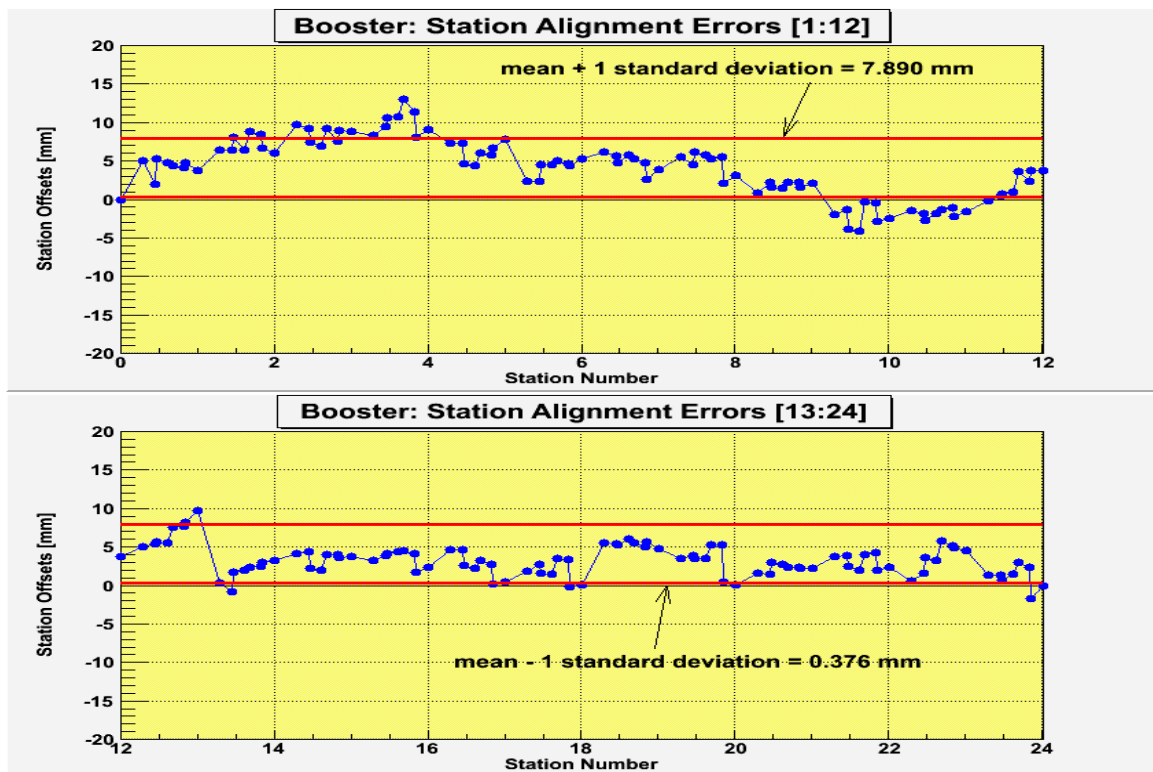
Figure 5.13: Booster-ringwide station offsets

(**a**) radial offsets   (**b**) vertical offsets   (**c**) station offsets
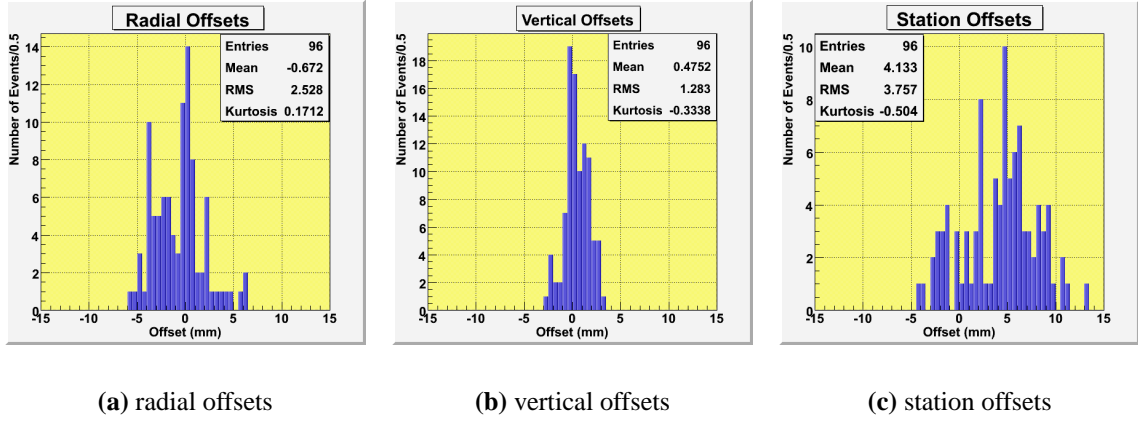
Figure 5.14: The distribution of transverse and longitudinal offsets. The vertical axis is for the number of events, or frequency.

distribution to be zero, 3 !! is subtracted.

$$
\begin{aligned}
\mathcal{K} &= \left.\frac{\mu^4}{\sigma^4}\right|_{actual} - \left.\frac{\mu^4}{\sigma^4}\right|_{Gaussian} \\
&= \left.\frac{(x - \langle x \rangle)^4}{\sigma^4}\right|_{actual} - 3 \text{ !!}
\end{aligned}
\tag{5.9}
$$

Thus, a Gaussian distribution has a kurtosis of zero. Table 5.2 contains the above-mentioned statistical parameters computed from the distributions of each type of the translational offset.

Table 5.2: The statistical parameters for the distributions of translational offsets

	Mean (mm)	RMS (mm)	Kurtosis
radial offsets	-0.672	2.528	0.171
vertical offsets	0.475	1.283	-0.334
station offsets	4.133	3.757	-0.504

5.7.2 Rotational Alignment Errors

Alignment errors arising from magnet rotations around the X-axis, Y-axis, and Z-axis are referred to as *pitch, yaw* and *roll*, respectively. For the calculations of rotational errors, we need to use the transverse and longitudinal distances between fiducial points on a main gradient magnet. The following notations are thus used in this section:

- L_{AD}: longitudinal distance between fiducial points A and D.

- L_{BC}: longitudinal distance between fiducial points B and C.

- L_{AB}: transverse separation between fiducial points A and B.

- L_{CD}: transverse separation between fiducial points C and D.

- $\mathcal{L}_{long}$: average longitudinal distance between fiducial points

$$\mathcal{L}_{long} = (L_{AD} + L_{BC})/2$$

- $\mathcal{L}_{tr}$: average transverse separation between fiducial points

$$\mathcal{L}_{tr} = (L_{AB} + L_{CD})/2$$

- Θ_x: X-rotation angle (pitch)

- Θ_y: Y-rotation angle (yaw)

- Θ_s: Z-rotation angle (roll, twist)

During the course of our analysis of the 2005 survey data, we find a small amount of difference between the wallside and aisleside lengths on each fiducialized magnet [8]. We

---

[8] Because only the main gradient magnets are fiducialized, a fiducialized magnet means a fiducialized main gradient magnet.

therefore average the two fiducialized longitudinal distances on each magnet. We then utilize the average lengths in the calculations of the angles of rotational errors at each magnet location. Figure 5.15 shows the ringwide variation of the differential of longitudinal distance between fiducial points on every magnet (L_{AD} (aisle side) - L_{BC} (wall side)). The ringwide variation of fiducialized longitudinal distance on each magnet is drawn in Figure 5.16. Figure 5.17 shows the histogram of the fiducialized longitudinal distance from all 96 main magnets. For the fiducialized transverse lengths, we average the transverse sep-
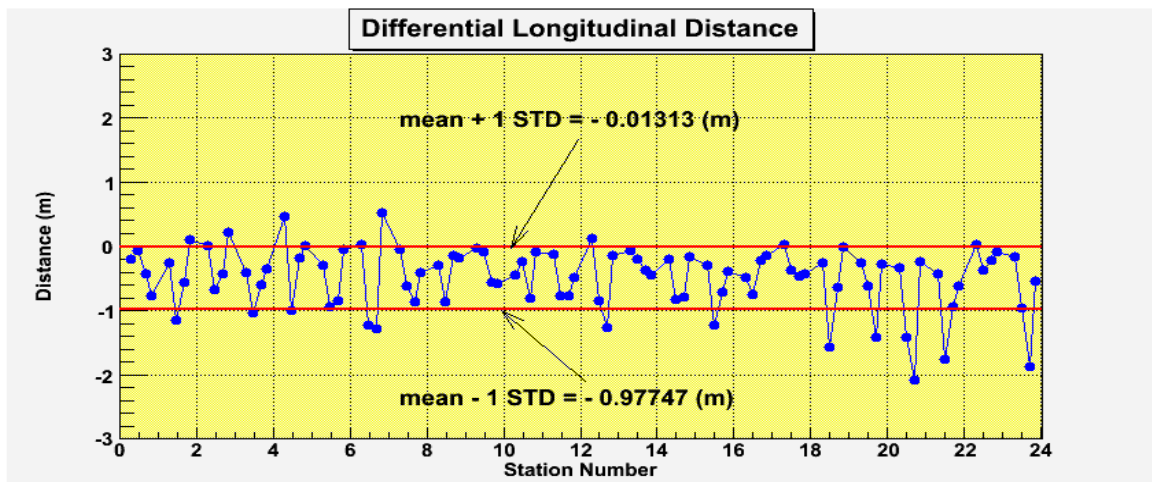
Figure 5.15: The ringwide variation in differential longitudinal distance between fiducial points on each main gradient magnet. Each data point represents the difference between wallside longitudinal distance and aisleside longitudinal distance on each magnet.

arations at the US and DS ends of each magnet. Figure 5.18 shows the ringwide variation of differential transverse distance on each magnet.
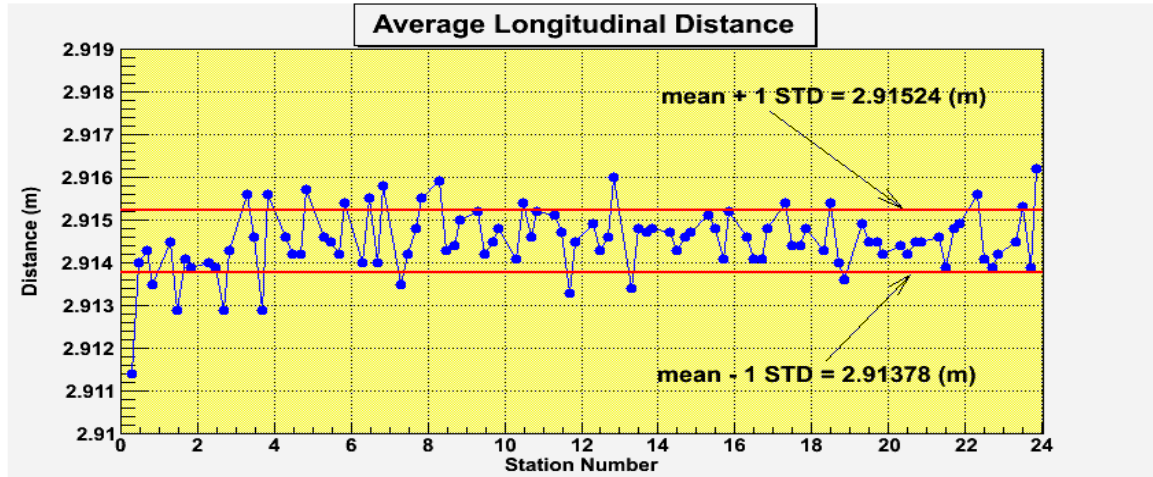
Figure 5.16: The ringwide variation in average longitudinal distance ($\langle L_{long} \rangle$) on each main gradient magnet
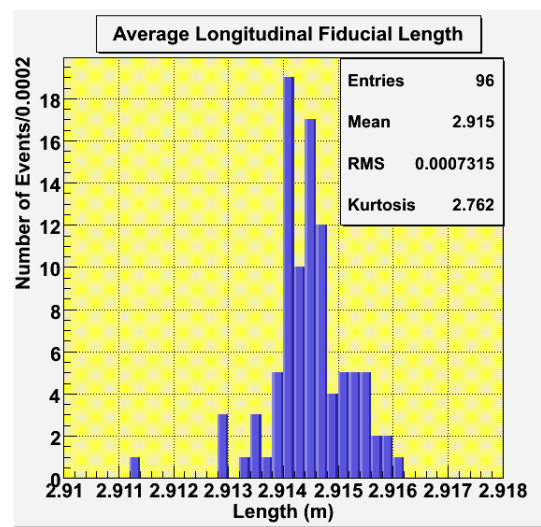
Figure 5.17: The histogram of distribution of average fiducialized longitudinal distance on each magnet

In Figure 5.19, transverse distances at upstream and downstream are overlaid at each magnet. Figure 5.20 shows the histogram of the transverse distances for all main magnets. Once both longitudinal and fiducialized transverse lengths are computed, we proceed to
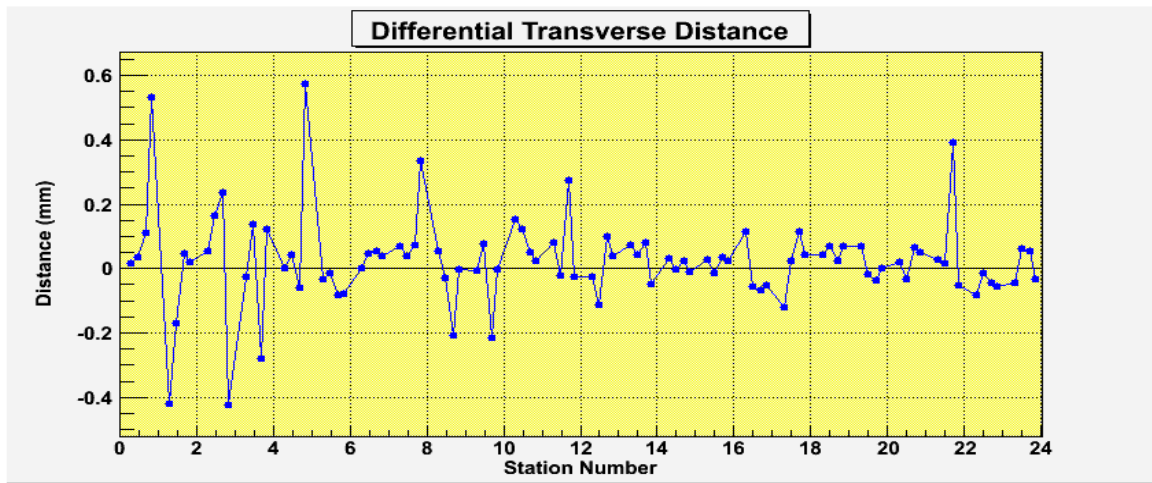
Figure 5.18: Ringwide variation of differential transverse distance (ΔL_{AB} and ΔL_{CD}) between fiducial points
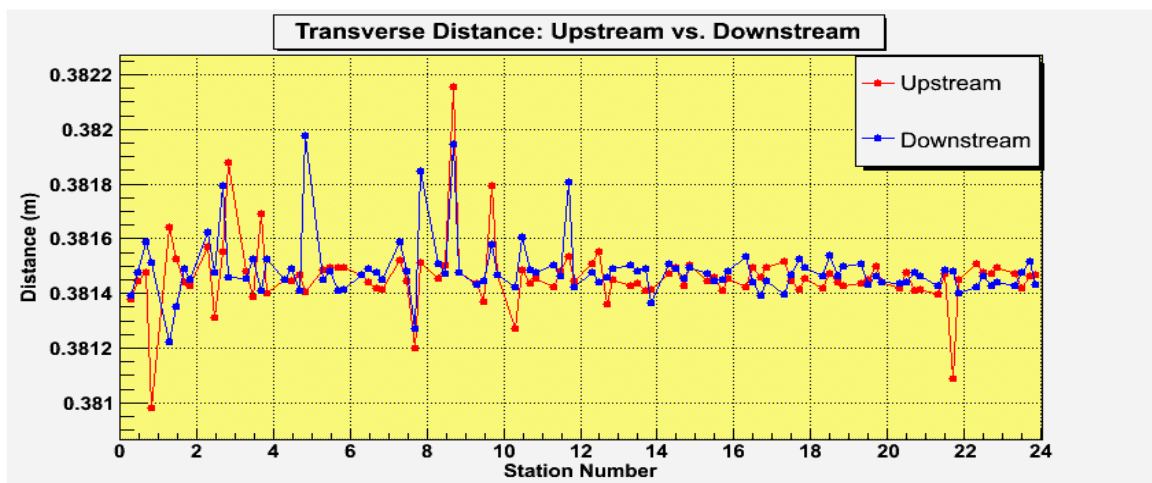
Figure 5.19: Ringwide variation of transverse distance; L_{AB} at upstream and L_{CD} at downstream
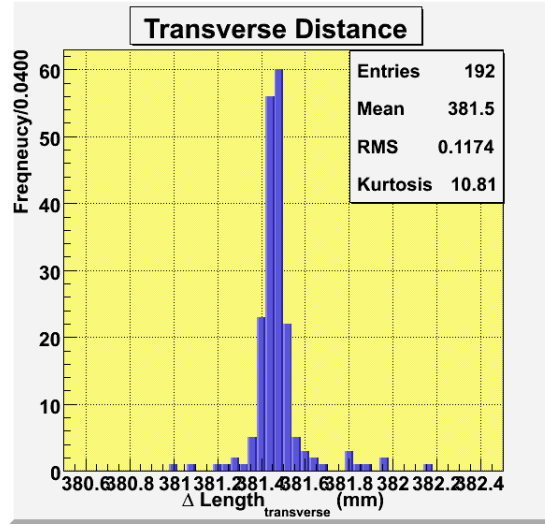
Figure 5.20: The histogram of distribution of fiducialized transverse distance on each magnet

compute the angles and rotational errors. Since the rotational angles are small, we make approximations as in Eqn. (5.10). In particular, the roll angles are determined to be an average of the US and DS angles.

$$
\left.
\begin{aligned}
\langle\, \mathcal{L}_{long}\,\rangle &= \sqrt{(\Delta\widetilde{X})^2 \,+\, (\Delta\widetilde{Y})^2 \,+\, (\Delta\widetilde{Z})^2} \approx \sqrt{(\Delta\widetilde{X})^2 \,+\, (\Delta\widetilde{Y})^2} \\
\langle\, \mathcal{L}_{tr}\,\rangle &= (L_{AB} \,+\, L_{CD})/2 \\
\Theta_x &\approx \Delta\widetilde{Z}/\langle\, \mathcal{L}_{long}\,\rangle \\
\Theta_y &\approx \Delta r/\langle\, \mathcal{L}_{long}\,\rangle \\
\Theta_{z,\, us} &\approx (\widetilde{Z}_B \,-\, \widetilde{Z}_A)/\langle\, \mathcal{L}_{tr}\,\rangle \\
\Theta_{z,\, ds} &\approx (\widetilde{Z}_C \,-\, \widetilde{Z}_D)/\langle\, \mathcal{L}_{tr}\,\rangle \\
\Theta_z &= (\Theta_{z,\, us} + \Theta_{z,\, ds})/2
\end{aligned}
\right\}
\tag{5.10}
$$

As was done for the translational offsets, the station-by-station variations of pitch, yaw, and roll angles are plotted in Figures 5.21 through 5.23. Figure 5.24 shows histograms of each

type of rotation angle.
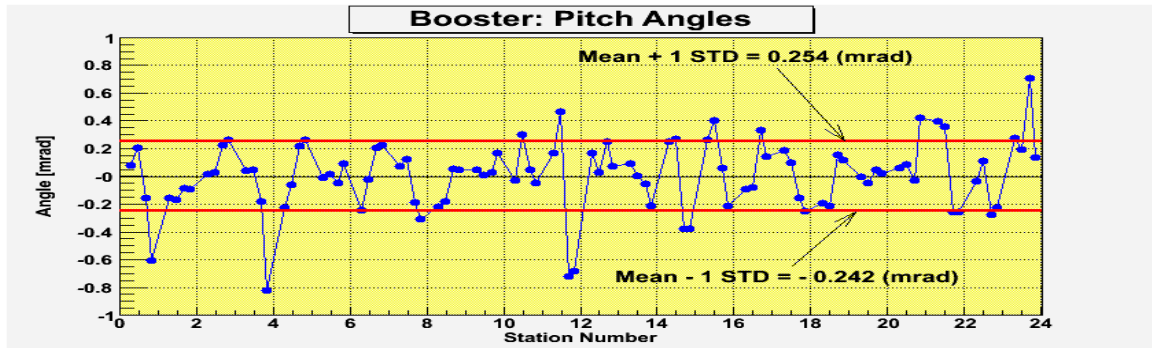
Figure 5.21: Ringwide variation of magnet pitches
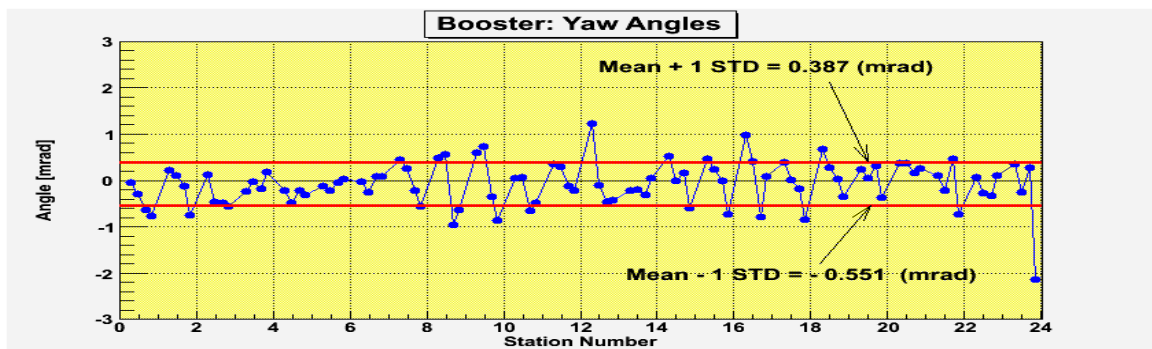
Figure 5.22: Ringwide variation of magnet yaws

Figure 5.23: Ringwide variation of magnet rolls
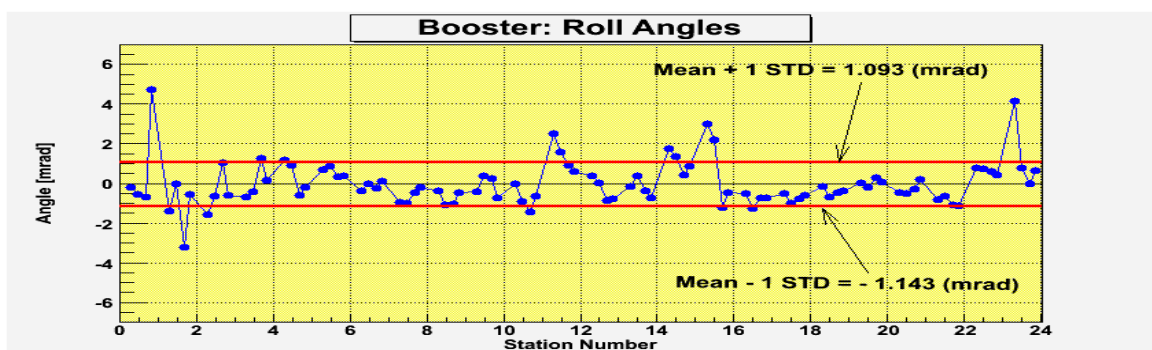
(a) pitch angles   (b) yaw angles   (c) roll angles
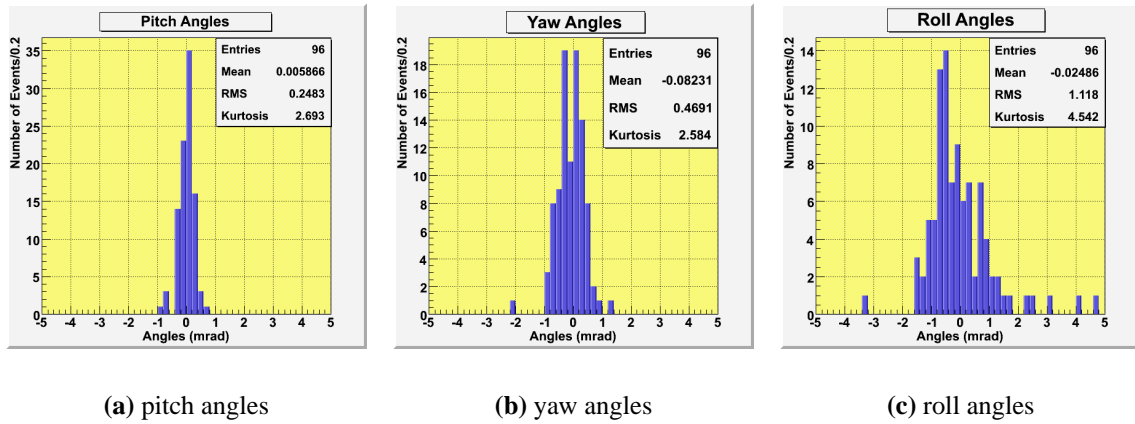
Figure 5.24: The distributions of rotation angles of each type

Similar to Table 5.2, the statistical parameters of rotational errors are summarized in Table 5.3 below. Magnets with roll angles larger than one standard deviation of 1.118 mrad are regarded to be *twisted*. The data points of twisted magnets are outside of the red horizontal lines of standard deviation. Therefore, twisted magnets, or largely rolled magnets can be identified in Figure 5.23. About 20 % of the total magnets fall into this category.

Table 5.3: The statistical parameters for the distributions of rotational errors

Type	Mean	RMS	Kurtosis
transverse magnet length	0.3815 (m)	0.1 (mm)	10.81
longitudinal magnet length	2.915 (m)	0.7 (mm)	2.762
pitch	0.006 (mrad)	0.248 (mrad)	2.693
yaw	-0.082 (mrad)	0.469 (mrad)	2.584
roll	-0.025 (mrad)	1.118 (mrad)	4.542

5.7.3 What and How to Realign

In practice, it would be difficult to realign all of the magnets in the Booster tunnel. Hence, it would be beneficial to identity and list groups of the most-misaligned magnets for each type. We could then proceed to perform partial realignment work, if allowed. In general, magnets with transverse offsets are not difficult to realign. Realigning of pitched magnets is the easiest of all types. Yaw magnets would not be difficult to realign. It is possible but challenging to unroll simple rolls, or rolled magnets with roll angles smaller than one standard deviation. The worst case of all is realigning magnets with station errors. This requires physically moving the magnet girders, rather than mere adjustments. In the following section we list all the magnets identified with large alignment errors. Following the surveyor's magnet naming convention, the first number is the station number, and the second is magnet number in each station. The magnet station number begins from the long straight section 1 (LSS 1) at the foil location. The cell number increments by one, following the direction of the proton beam (the proton beam direction is the reference direction).

A total of 63 fiducial points on 37 main gradient magnets have radial offsets larger than one standard deviation. The magnet numbers are listed in the order of increasing station number.

- 1-1

- 3-4

- 5-1

- 6-2, 6-3, 6-4

- 7-1, 7-2, 7-3

- 8-1, 8-2, 8-3, 8-4

- 9-1, 9-2, 9-3, 9-4

- 10-1

- 11-2

- 13-1, 13-2

- 14-1, 14-2, 14-3, 14-4

- 15-1, 15-2, 15-3, 15-4

- 18-4

- 19-1, 19-4

- 24-1, 24-2, 24-3, 24-4

It is found that a total of 63 fiducial points on 40 main gradient magnets have vertical offsets larger than one standard deviation.

- 1-4

- 3-1, 3-2, 3-3

- 4-4

- 8-1, 8-2, 8-3, 8-4

- 9-1, 9-2

- 10-1, 10-2, 10-3, 10-4,

- 12-2, 12-3

- 13-1

- 14-4

- 15-1, 15-2, 15-3, 15-4

- 16-2, 16-3, 16-4

- 17-4

- 18-1, 18-2, 18-3, 18-4

- 19-1

- 22-4

- 23-1, 23-2, 23-3, 23-4

- 24-1, 24-3U, 24-4

For the case of rotational errors, a total of 17 main gradient magnets are identified as twisted, or largely-rolled magnets.

- 1-4

- 2-1, 2-3

- 3-1

- 4-3, 4-4

- 5-1

- 11-3

- 12-1, 12-2

- 15-1, 15-2

- 16-1, 16-2, 16-3

- 17-2

- 24-1

5.7.4 List of Magnets to Resurvey

Following the surveyor's notation, the fiducial points that need to be remeasured in the next round of survey are listed in Table 5.4 and labeled as follows:

$$[\,station\ number\,] - [\,magnet\ number\,][\,fiducial\ ID\,]$$

Table 5.4: The list of magnets that need resurveying

1-4D	2-4D	4-4D
8-1A	8-1B	8-1C
8-1D		

5.7.5 Types of Rolls

The roll angles, or tilt angles at US and DS of each magnet are computed. We find four different types of rolled magnets, depending on the magnitude and orientation of roll angles at US and DS in the Booster beamline. Table 5.5 contains the fractions of each case of rolled magnets. The twist means large roll regardless of their roll orientation.

Table 5.5: The angle is averaged over US and DS roll angles for each magnet.

Orientation	Total	Twist
Same orientation	69 %	14 %
Opposite orientation	31 %	25 %

5.8   Concluding Remarks

In summary this chapter discusses the calculations and analysis of all types of alignment errors in the Booster main gradient magnets. It lays the framework upon which we build on in the next chapter where the effects of alignment errors on the Booster beam are presented.

Chapter 6

Effects of Magnet Misalignments

In Chapter 5 we use the as-found survey measurement data to determine all types of magnet alignment errors of each individual main gradient magnet. In this chapter we describe beam dynamics calculations using ORBIT$\star$ which include all types of magnet alignment errors in the presence of full space-charge effects. Our misalignment model is based on the misalignment analyses presented in the preceding chapter. Therefore, we also adhere to the same notations and symbols throughout this chapter. We first discuss how the ORBIT$\star$ reflects magnet-alignment errors in macroparticle-tracking simulations. We then follow with investigations of their effects on the Booster beam.

6.1 Rigid Body Motion

In classical mechanics, a rigid body is defined as a system consisting of a large number of point masses, such that the distance between pairs of point masses remain constant even when the body is in motion or under the action of external forces. The magnet fiducialization allows us to describe misaligned magnets as rigid body motion. Here we make an assumption that the distances between fiducial points on a main gradient magnet remain constant. Therefore, the magnet misalignment measured at fiducial points is considered as

idealized rigid body motion.

6.1.1 Transformations of Macroparticle Coordinates

As was previously explained, the magnet alignment errors are calculated in the Fermilab Site Coordinate System, whereas the ORBIT⋆ tracks physical coordinates of macroparticles in the Frenet-Serret coordinate system (cf. section 5.1). In other words, what the ORBIT⋆ tracks is the coordinates of each individual macroparticle, and not the physical coordinates of each beamline element. For convenience in numerical modeling, we fix the coordinate system on the rigid body of each beamline element. When a magnet is misaligned, so is the coordinate system of the misaligned magnet including the origin. If we put it in a different way, in the reference frame of a beamline element, the macroparticle coordinates change in opposite direction, or orientation to the actual alignment errors; that is, the notion of *passive transformation* [55] is employed. Through the passive transformation the misalignment model is simplified resulting in the exactly same physical effects on the Booster beam. Figures 6.1 and 6.2 illustrate the active transformations and the passive transformations of translational offsets and rotational offsets in the $x - y$ plane.
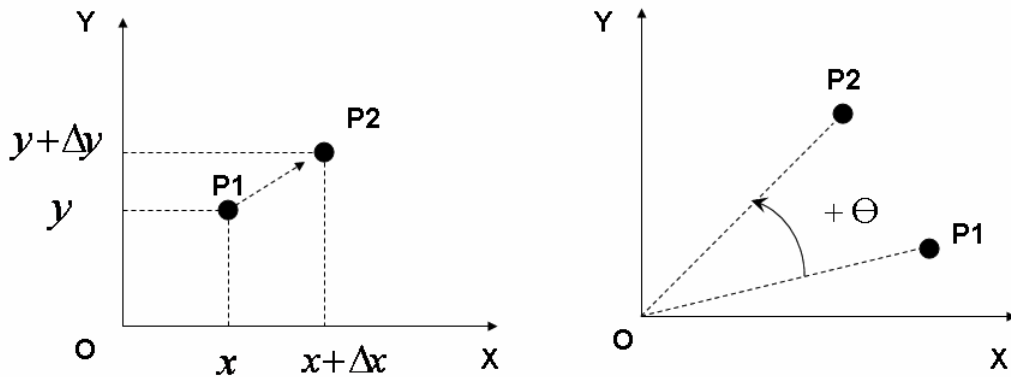
Figure 6.1: Active transformations
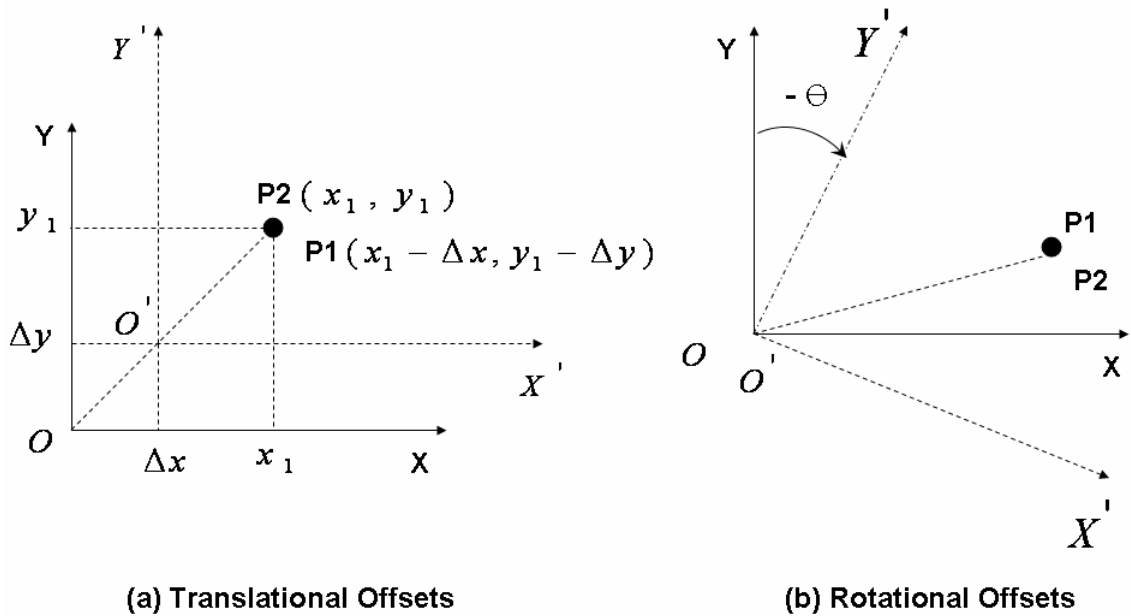
Figure 6.2: Passive transformations

As shown in Figure 6.3, upon entering the upstream face of a misaligned magnet, a herd of macroparticles change their coordinates in a passive fashion. When exiting the downstream face of a misaligned magnet, the ORBIT⋆ restores the changes in macroparticle coordinates that were made on the upstream face. This ensures that the macroparticles are subject to the effects of magnet alignment errors while they are propagated through each misaligned magnet. After leaving each misaligned magnet, and until encountering a subsequent magnet with alignment errors, the macroparticles are free of the effects of alignment errors. Note that in our misalignment model, alignment errors of straight elements [1] are not considered; only alignment errors of gradient magnets. Consequently, the effects of magnet misalignments on macroparticles are simulated as is the actual case in the machine operation. Keeping this idea in mind, we transform macroparticle coordinates in the amounts of translational offsets (δx, δy, δz) and rotational angles ($\delta\theta_x$, $\delta\theta_y$, $\delta\theta_z$) as

---

[1] A straight element is a beamline element without magnetic field, such as drift elements, beam position monitors, etc.
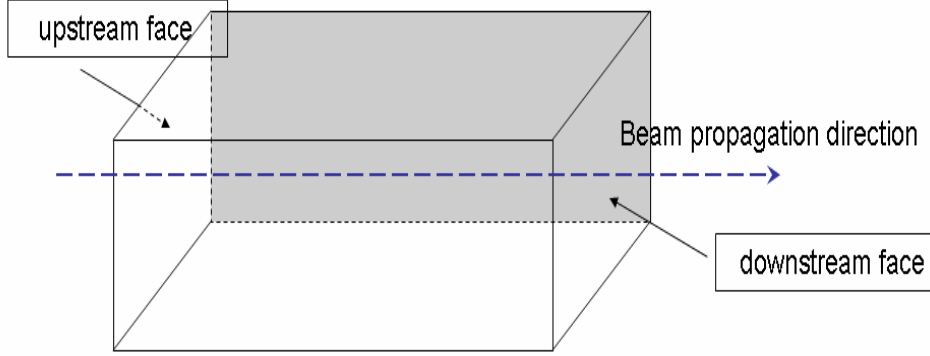
Figure 6.3: Coordinate transformations at magnet faces reflecting alignment errors

calculated in Chapter 5.

In the case of the translational errors, the following transformations with $\mathcal{R}$ matrix are performed as in Eqn. (6.1) and (6.2):

$$\mathcal{R}(\delta x, \ \delta y, \ \delta z) = \begin{bmatrix} 1 - \delta x & 0 & 0 \\ 0 & 1 - \delta y & 0 \\ 0 & 0 & 1 - \delta z \end{bmatrix} \tag{6.1}$$

The $\mathcal{M}_T$ representing an actual transfer map for a misaligned magnet with translational offsets is obtained as follows:

$$\begin{aligned} \mathcal{M}_T &= \mathcal{R}(\delta x, \ \delta y, \ \delta z) \cdot \mathcal{M} \cdot \mathcal{R}^{-1}(\delta x, \ \delta y, \ \delta z) \\ &= \mathcal{R}(\delta x, \ \delta y, \ \delta z) \cdot \mathcal{M} \cdot \mathcal{R}(-\delta x, -\delta y, -\delta z), \end{aligned} \tag{6.2}$$

$$\begin{cases} x \longmapsto x - \delta x, \\ y \longmapsto y - \delta y, \\ z \longmapsto z - \delta z, \end{cases} \tag{6.3}$$

where $\mathcal{M}$ is an *ideal* transfer map supplied by MAD optics calculations prior to the ORBIT$\star$ production runs. Here what is meant by optics calculations is the calculations of optics functions, or lattice functions ($\beta(z)$, $\alpha(z)$, $\gamma(z)$, $\mathcal{D}(z)$, etc.) and transfer maps ($\mathcal{M}$) at each beamline element in an ideal design lattice.

For the rotational errors, the rotation axes characterize the rotation matrices $\mathcal{R}(\theta)$. Thus, an actual transfer map $\mathcal{M}_R$ reflecting rotational alignment errors can be represented as,

$$\mathcal{M}_R = \mathcal{R}(\delta\theta) \cdot \mathcal{M} \cdot \mathcal{R}^{-1}(\delta\theta)$$

$$\mathcal{R}^{-1}(\delta\theta) = \mathcal{R}(-\delta\theta) \tag{6.4}$$

$$\left.\begin{aligned}
\mathcal{R}(\theta_x) &= \begin{pmatrix} 1 & 0 & 0 \\ 0 & \cos\theta_x & -\sin\theta_x \\ 0 & \sin\theta_x & \cos\theta_x \end{pmatrix} \quad
\mathcal{R}(-\theta_x) = \begin{pmatrix} 1 & 0 & 0 \\ 0 & \cos\theta_x & \sin\theta_x \\ 0 & -\sin\theta_x & \cos\theta_x \end{pmatrix} \\[2em]
\mathcal{R}(\theta_y) &= \begin{pmatrix} \cos\theta_y & 0 & -\sin\theta_y \\ 0 & 1 & 0 \\ \sin\theta_y & 0 & \cos\theta_y \end{pmatrix} \quad
\mathcal{R}(-\theta_y) = \begin{pmatrix} \cos\theta_y & 0 & \sin\theta_y \\ 0 & 1 & 0 \\ -\sin\theta_y & 0 & \cos\theta_y \end{pmatrix} \\[2em]
\mathcal{R}(\theta_z) &= \begin{pmatrix} \cos\theta_z & -\sin\theta_z & 0 \\ \sin\theta_z & \cos\theta_z & 0 \\ 0 & 0 & 1 \end{pmatrix} \quad
\mathcal{R}(-\theta_z) = \begin{pmatrix} \cos\theta_z & \sin\theta_z & 0 \\ -\sin\theta_z & \cos\theta_z & 0 \\ 0 & 0 & 1 \end{pmatrix}
\end{aligned}\right\} \tag{6.5}$$

Since the frame of reference is on a misaligned magnet, as mentioned earlier, when a beam enters a rotated magnet, the local coordinate system needs to be first transformed to be aligned with the rotated magnet. Upon leaving the rotated magnet, the local coordinate system needs to be restored. Let ξ be a half of bending angle ($\Theta_B/2$). Using the similarity transformation, a new transformation matrix for local coordinate change at a magnet can be obtained as follows:

$$L(\xi) = \begin{pmatrix} \cos\xi & 0 & \sin\xi \\ 0 & 1 & 0 \\ -\sin\xi & 0 & \cos\xi \end{pmatrix} \tag{6.6}$$

$$\mathbf{R}(\theta_x) = L^{-1}(\xi) \cdot \mathcal{R}(\theta_x) \cdot L(\xi)$$

$$= \begin{pmatrix} \cos\xi & 0 & -\sin\xi \\ 0 & 1 & 0 \\ \sin\xi & 0 & \cos\xi \end{pmatrix} \cdot \begin{pmatrix} 1 & 0 & 0 \\ 0 & \cos\theta_x & \sin\theta_x \\ 0 & -\sin\theta_x & \cos\theta_x \end{pmatrix} \cdot \begin{pmatrix} \cos\xi & 0 & \sin\xi \\ 0 & 1 & 0 \\ -sin\xi & 0 & \cos\xi \end{pmatrix}$$

$$= \begin{pmatrix} \cos^2\xi + \sin^2\xi\cos\theta_x & \sin\xi\cdot\sin\theta_x & \cos\xi\sin\xi - \cos\xi\sin\xi\cos\theta_x \\ -\sin\xi\cdot\sin\theta_x & \cos\theta_x & \cos\xi\sin\theta_x \\ \cos\xi\sin\xi - \cos\xi\sin\xi\cos\theta_x & -\cos\xi\cdot\sin\theta_x & \sin^2\xi + \cos^2\xi\cos\theta_x \end{pmatrix}$$

$$\tag{6.7}$$

Given bending angles of defocusing ($\Phi_{B, D} = 60.67$ (mrad)) and fousing magnets ($\Phi_{B, F}$ = 71.35 (mrad)), and rotational offsets (θ_x, θ_y, θ_z), we can make paraxial approximations.

$$\sin(\xi) \approx \xi, \quad \cos(\xi) \approx 1, \quad \sin(\theta) \approx \theta, \quad \cos(\theta) \approx 1 \tag{6.8}$$

Then, $\mathbf{R}(\theta_x)$ reduces to

$$\mathbf{R}(\theta_x) \approx \begin{pmatrix} 1 & \xi \cdot \theta_x & 0 \\ -\xi \cdot \theta_x & 1 & \theta_x \\ 0 & -\theta_x & 1 \end{pmatrix} \tag{6.9}$$

In the same fashion, we can obtain a total transformation matrix at the entrance of a yawed magnet.

$$\mathbf{R}(\theta_y) = \mathcal{L}^{-1}(\xi) \cdot \mathcal{R}(\theta_y) \cdot \mathcal{L}(\xi)$$
$$= \begin{pmatrix} \cos \theta_y & 0 & \sin \theta_y \\ 0 & 1 & 0 \\ -\sin \theta_y & 0 & \cos \theta_y \end{pmatrix} \tag{6.10}$$

For the case of rolled magnets, the following transformation is required at the entrance of a magnet.

$$\mathbf{R}(\theta_z) = \mathcal{L}^{-1}(\xi) \cdot \mathcal{R}(\theta_z) \cdot \mathcal{L}(\xi)$$
$$= \begin{pmatrix} \cos \xi^2 \cos \theta_z + \sin \xi^2 & \cos \xi \sin \theta_z & \cos \xi \cos \theta_z \sin \xi - \sin \xi \cos \xi \\ -\cos \xi \sin \theta_z & \cos \theta_z & -\sin \xi \sin \theta_z \\ \sin \xi \cos \xi \cos \theta_z - \cos \xi \sin \xi & \sin \xi \sin \theta_z & \sin \xi^2 \cos \theta_z + \cos \xi^2 \end{pmatrix}$$
$$\approx \begin{pmatrix} 1 & \theta_z & 0 \\ -\theta_z & 1 & -\xi \cdot \theta_z \\ 0 & \xi \cdot \theta_z & 1 \end{pmatrix}$$
$$\tag{6.11}$$

These 3×3 rotational matrices transform position coordinates and momentum coordinates

in the following manner:

$$
\begin{pmatrix} \widetilde{x} \\ \widetilde{y} \\ \widetilde{L^\star} \end{pmatrix} = \mathcal{R}(\theta) \begin{pmatrix} x \\ y \\ L^\star \end{pmatrix} \qquad \begin{pmatrix} \widetilde{x'} \\ \widetilde{y'} \\ \widetilde{p^\star} \end{pmatrix} = \mathcal{R}(\theta) \begin{pmatrix} x \\ y \\ p^\star \end{pmatrix}, \tag{6.12}
$$

where $L^\star$ and $p^\star$ denote a half of longitudinal magnet length at each face and normalized momentum (p/p_0), respectively. As mentioned earlier, after translational $(\mathcal{R}^{-1})$ or rotational $(\mathcal{R}^{-1})$ coordinate transformation is carried out on the upstream face, followed by transfer map $(\mathcal{M})$, the ORBIT$\star$ ensures that an inverse transformation $(\mathcal{R}^{-1})^{-1}$ or $(\mathcal{R}^{-1})^{-1}$ is made on the downstream face. Consequently, macroparticles are subject to misalignment-induced field errors only in between an upstream face and a downstream face of a magnet. Once macroparticles leave a misaligned magnet, the particles are free of alignment errors until they enter a subsequent misaligned magnet.

The form of Eqn. (6.4) implies is that alignment errors exist from an upstream face to a downstream face of each misaligned element. In other words, macroparticles are subject to the effects of alignment errors for the duration of transit time through each misaligned element. It is clear that for a perfectly aligned beamline element an actual transfer map reduces to an ideal transfer map, because $\mathcal{R}(\theta)$ reduces to a 3×3 identity matrix. This means that one transfer map is simply used for a beamline element with no alignment errors, or perfectly aligned element. In ORBIT$\star$, the sequence of actions on a beam by one misaligned magnet is a rotational, or translational transformation first, then propagation follows through the magnet, and is completed by reverse transformation. In order to investigate the adverse effect of each type of alignment errors on a beam, we incorporate one type of alignment errors at a time.

6.2 Philosophy of Modeling Magnet Misalignments

A total of 48 focusing and 48 defocusing gradient magnets constitute the Booster design lattice and our Booster misalignment model. Magnets of the same type (either focusing or defocusing) were manufactured to be identical. However, in order to model the present magnet misalignments, each of the main gradient magnets are modeled and treated individually, such that no magnets are considered identical in our model. The following specifications are reflected in our model:

(1) longitudinal length ($\langle L_{long} \rangle$):

The wallside and aisleside lengths of each magnet are averaged to represent the longitudinal length of each magnet.

(2) transverse width (L_{tr}):

Since the ringwide variation of L_{tr} is sufficiently small ($\Delta L_{tr}/L_{tr} = 0.0176$ %), we use the nominal length of 15.016 inches (= 0.38147 m) for upstream and downstream rolls.

(3) bending angles ($\Theta_{B, D}$ and $\Theta_{B, F}$):

We calculate bending angles for defocusing and focusing magnets using different bending radii (ρ_D and ρ_F).

$$
\begin{cases}
\Theta_{B, D} &= \frac{< L_{long} >}{\rho_D} \\
\Theta_{B, F} &= \frac{< L_{long} >}{\rho_F}
\end{cases}
\tag{6.13}
$$

(4) translational offsets (displacements):

radial offsets (δx), vertical offsets (δy), and station (longitudinal) offsets (δz)

(5) rotational errors: pitch ($\delta\theta_x$), yaw ($\delta\theta_y$), roll ($\delta\theta_z$) and twists ($\Delta\theta_z$)[2].

---

[2]We denote $\Delta\theta_z$ for an angular offset larger than 1 standard deviation of the total roll-angle distribution.

6.3 Misalignment-Induced Field Errors

This section deals with the calculations of magnetic-field errors and angular kicks that are induced by magnet alignment errors.

Using the magnetic field on the mid-plane, the magnetic-field coefficient of order n is defined.

$$B_n \equiv \frac{\partial^n B_y}{\partial x^n} \tag{6.14}$$

For instance, $B_0 = B_y$, $B_1 = B' = \partial B_y / \partial x$, $B_2 = B'' = \partial^2 B_y / \partial x^2$, and so on. The magnetic field on the mid-plane ($y = 0$) can be represented using Taylor series expansion.

$$B_x(x, \, 0, \, z) = 0$$
$$B_y(x, \, 0, \, z) = \sum_{n=0}^{\infty} \frac{B_n \cdot x^n}{n!} \tag{6.15}$$
$$B_z(x, \, 0, \, z) = 0$$

The integrated magnetic field of a main magnet can be represented by a multipole expansion.

$$\int B_y \, dz = B_y \langle L_{long} \rangle$$
$$= \langle L_{long} \rangle (B_y \rho) \cdot \sum_{n=0}^{N} \mathcal{K}_n x^n, \tag{6.16}$$

where $\mathcal{K}_n \equiv B_n / (B \rho)$ is taken to be a multipole coefficient of order n. As angular kicks can be superimposed, the kicks can be represented in the form of the multipole expansion as

follows:

$$\Delta x' = \Delta\theta(x)$$

$$= \langle\, L_{long}\,\rangle \sum_{n\,=\,0}^{N} \mathcal{K}_n(\delta x)^n$$

$$= \underbrace{\frac{B\cdot\langle\, L_{long}\,\rangle}{B\rho}}_{\text{dipole kick}} + \underbrace{\frac{B'\cdot\langle\, L_{long}\,\rangle\cdot\delta x}{B\rho}}_{\text{quadrupole kick}} + \underbrace{\frac{B''\cdot\langle\, L_{long}\,\rangle\cdot(\delta x)^2}{B\rho}}_{\text{sextupole kick}} + \ldots \tag{6.17}$$

Referring to Eqn. (6.17), we define a dipole and a quadrupole kick terms. Alignment-error induced dipole field errors can give rise to angular dipole kicks.

$$\Delta\theta\Big|_{dipole} = \frac{\Delta B\langle\, L_{long}\,\rangle}{B\rho}, \tag{6.18}$$

where ΔB denotes induced dipole-field error. Angular quadrupole kicks are induced by translational offsets (δx and δy).

$$\Delta x'\Big|_{quad} = \theta(x\,+\,\delta x) - \theta(x)$$

$$= \langle\, L_{long}\,\rangle\cdot\frac{B'}{B\rho}\cdot\delta x \tag{6.19}$$

$$= \langle\, L_{long}\,\rangle\cdot\mathcal{K}_1\cdot\delta x,$$

$$\Delta y'\Big|_{quad} = \langle\, L_{long}\,\rangle\cdot\mathcal{K}_1\cdot\delta y, \tag{6.20}$$

where $\mathcal{K}_{1,\,D}$ and $\mathcal{K}_{1,\,F}$ are multipole coefficients for defocusing and focusing magnets, respectively. $\mathcal{K}_{1,\,D}$ is given to be - 0.0577069 (m^{-2}) and $\mathcal{K}_{1,\,F}$ is + 0.0542195 (m^{-2}) in the Booster design lattice.

We begin with the field errors that are induced by magnet pitch. Note that as the Booster

main magnet is a combined-function magnet, it could contain all orders of multipole components. In our misalignment model for the Booster, we only take into account dipole and quadrupole components. The higher-order multipole components, such as sextupoles and octupoles, are not considered in our model because the design lattice (version 1.1) that we employ for modeling is a linear lattice containing linear optical elements only. Thus, we consider a bending-, or dipole-field component with a uniform vertical field. Angular kicks ($\Delta x'$ and $\Delta y'$) are originated from induced magnetic fields arising from magnet misalignments. Hence, we first derive induced magnetic fields in order to calculate the amount of angular deflections. For a perfectly-aligned magnet, the magnetic field is given as $\overrightarrow{\mathcal{B}} = (\mathcal{B}_x,\ \mathcal{B}_y,\ \mathcal{B}_z)$, and for a misaligned magnet, the magnetic field is $\overrightarrow{\mathcal{B}^\star} = (\mathcal{B}_x^\star,\ \mathcal{B}_y^\star,\ \mathcal{B}_z^\star)$.

Figure 6.4 illustrates the side view of a pitched magnet with a pitch angle of $\delta\theta_x$. When viewed in radially outward direction, if a magnet is rotated counterclockwise, or the elevation at downstream is positive, then the pitch angle ($\delta\theta_x$) is taken to be positive. Fig-
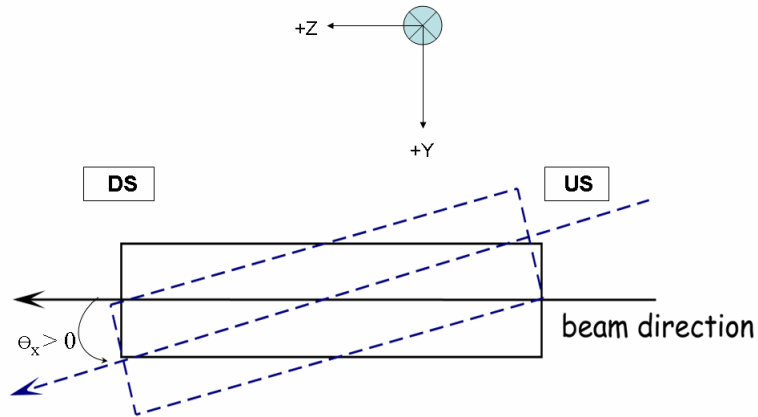
Figure 6.4: A side view of a pitched magnet

ure 6.5 shows dipole-field lines for a pitched maget. With a perfectly-aligned magnet, the magnetic-field components in horizontal and longitudinal directions are zero.

$$\mathcal{B}_x = \mathcal{B}_z = 0 \tag{6.21}$$
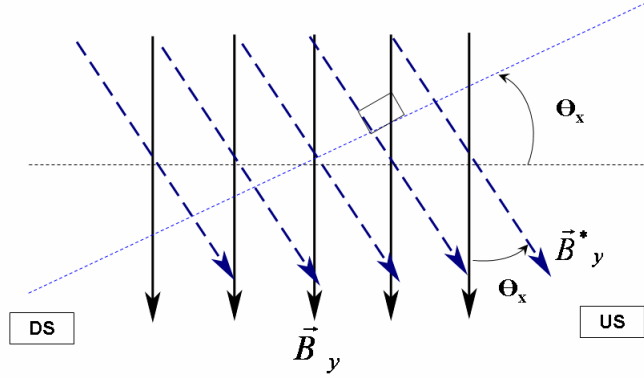
Figure 6.5: Field error due to pitch

$$\mathcal{B}_x^\star = 0, \quad \Delta\mathcal{B}_x = 0 \tag{6.22}$$

Here ΔB_x, ΔB_y and ΔB_z are the magnetic field errors caused by the magnet pitch in each direction. Once we know how much magnetic field errors are induced by each type of alignment errors, we can calculate angular dipole and quadrupole kicks ($\Delta x'$ and $\Delta y'$). A pitched magnet can induce dipole field error deviating from the designed vertical dipole field. However, considering the order of calculated pitch angles, the induced field error is negligible as described below:

$$\overrightarrow{\mathcal{B}_y} = \mathcal{B}_y \hat{y}$$
$$|\overrightarrow{\mathcal{B}_y}| = \mathcal{B}_y \geq 0 \tag{6.23}$$

$$\mathcal{B}_y^\star = \mathcal{B}_y \cos\theta_x$$
$$\Delta\mathcal{B}_y = -\mathcal{B}_y(1 - \cos\theta_x) \tag{6.24}$$
$$\approx -\frac{1}{2}\mathcal{B}_y\theta_x^2 \sim 0$$

According to our analyses of survey data presented in Chapter 5, all types of rotational angles are in the range of a fraction of a mrad. Figure 6.6 (b) shows that $y = \sin(x)$ and $y = x$ are indistinguishable on logarithmic scale for angles smaller than 0.1 rad. Therefore, the

paraxial approximation is sufficiently accurate for the rotational offsets of Booster magnets. Hence, we make paraxial approximations as in Eqn. (6.25).

(a) angle larger than 1 rad **(b)** angle smaller than 0.1 rad
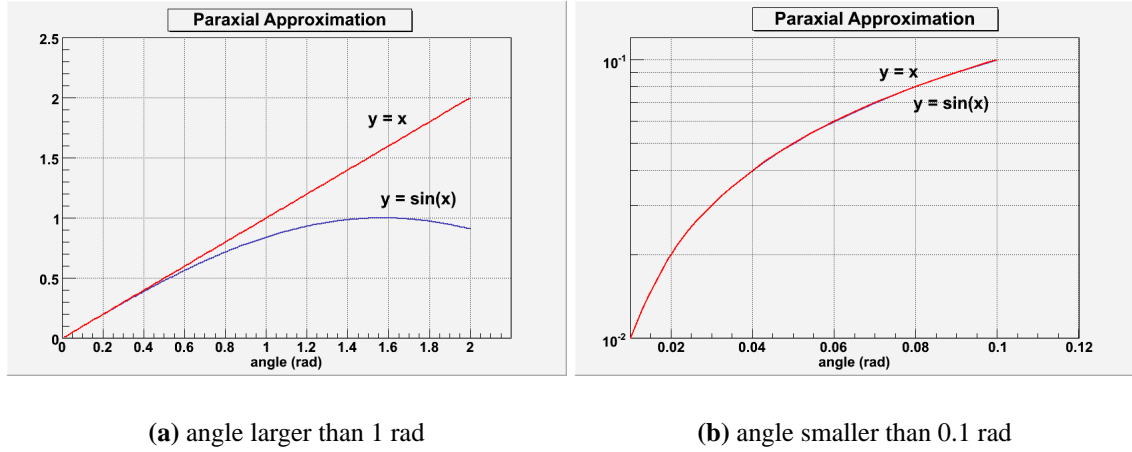
Figure 6.6: $y = \sin(x)$ and $y = x$; the blue trace is for $y = \sin(x)$, and the red trace for $y = x$.

$$\sin\theta \approx \theta, \quad \cos\theta \approx 1, \quad \tan\theta \approx \theta \tag{6.25}$$

If we look into the longitudinal direction for a pitched magnet, the magnet pitch induces $x - y$ coupling as follows.

$$\Delta B_z = - \mathcal{B}_y \sin\theta_x \approx - \mathcal{B}_y\theta_x \tag{6.26}$$

We now turn to angular kicks arising from magnet rolls. Figure 6.7 illustrates dipole-field error arising from a magnet roll.

A histogram of roll angles for all of 96 main magnets is shown in Figure 5.24 (c). The distributions of roll angles for focusing and defocusing magnets are shown separately in Figure 6.8. If a magnet is rotated around the z-axis clockwise when viewed from upstream towards downstream, the roll angle is taken to be positive. The field errors due to magnet
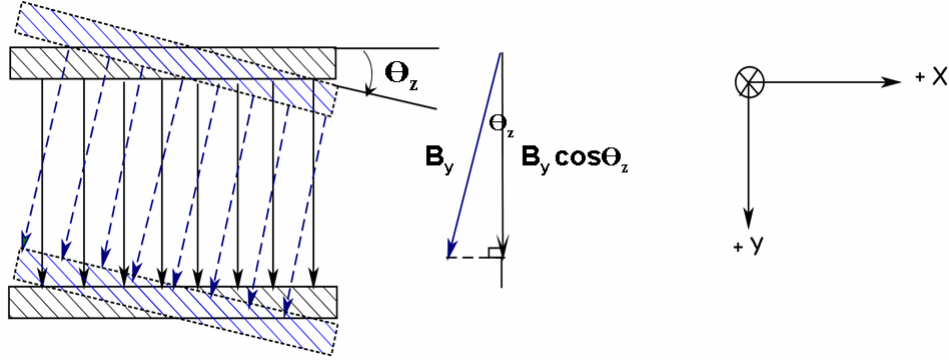
Figure 6.7: A rolled magnet viewed from the beam direction

rolls are

$$\mathcal{B}_y^{\star} = \mathcal{B}_y \cos \theta_z$$

$$\Delta \mathcal{B}_y = -\mathcal{B}_y(1 - \cos \theta_z) \tag{6.27}$$

$$\approx -\frac{1}{2}\mathcal{B}_y \theta_z^2 \sim 0$$

$$\mathcal{B}_x = -\mathcal{B}_y \sin \theta_z \approx -\mathcal{B}_y \theta_z$$

$$\Delta \mathcal{B}_x \approx -\mathcal{B}_y \theta_z \tag{6.28}$$

Vertical angular dipole kick induced by ΔB_x is:

$$\Delta y' \bigg|_{roll,\ dipole} = \frac{\Delta B_x}{B_y} \frac{\langle L_{long} \rangle}{\rho} = -\delta \theta_z \cdot \frac{\langle L_{long} \rangle}{\rho} = -\delta \theta_z \Theta_B \tag{6.29}$$

where Θ_B is bending angle as defined in Eqn. (6.13), and ρ and $\mathcal{P}_0$ are the bending radius and design momentum[3], respectively. These quantities are used to obtain magnetic rigidity ($B\rho$).

$$\mathcal{B}\rho = \gamma m_0 \beta c/e = (10/2.9987) \cdot \mathcal{P}_0 \ (GeV/c) \tag{6.30}$$

---

[3]The design momentum refers to the momentum of a particle on a design orbit.
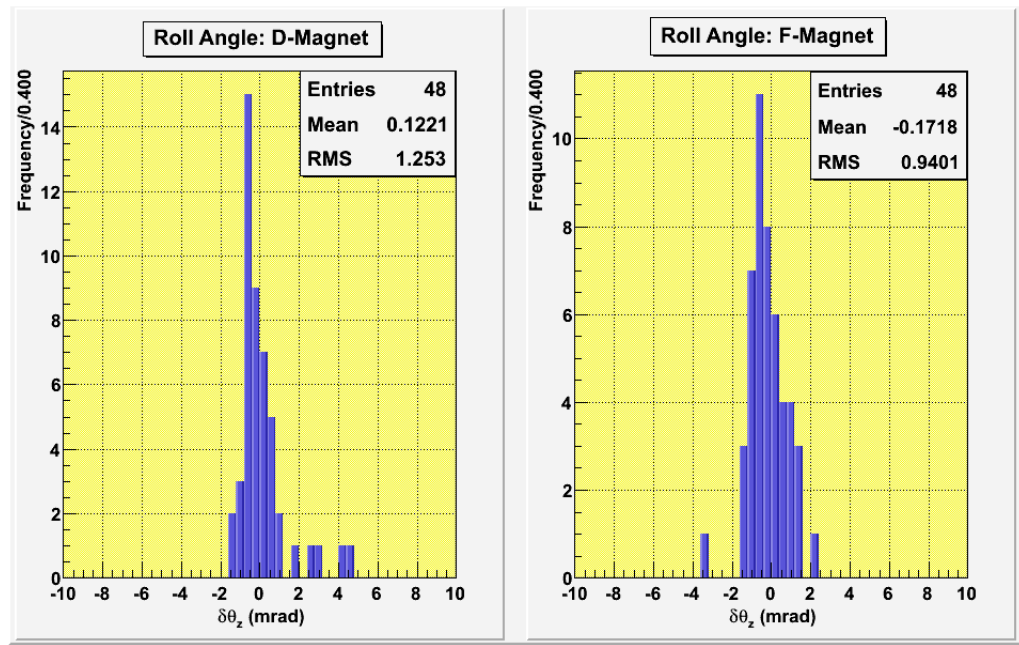
Figure 6.8: Distributions of roll angles in units of mrad: the left figure is for the 48 defo-cusing magnets, and the right figure is for the 48 focusing magnets.

The magnet rigidity characterizes the stiffness of a beam from the bending magnet's stand-point. For the Booster beam at injection energy, the magnetic rigidity is 3.183 (Tesla-meter), and for the beam at extraction the magnetic rigidity is 29.650 (Tesla-meter). Re-ferring to Figure 6.7 and Eqn. (6.29), the orientation of each magnet roll determines the direction of the vertical angular dipole kick ($\Delta y'$), or angular impulse. This is the rea-son why rolled magnets are sorted out by the roll orientation in Chapter 5. Also, since defocusing and focusing magnets have different bending radii, we calculate the average an-gular kick for defocusing magnets and for focusing magnets separately. From Figure 6.8,

$\langle\, \delta\theta_{z,\,D}\,\rangle$ and $\langle\, \delta\theta_{z,\,F}\,\rangle$ are 0.1221 (mrad) and - 0.1718 (mrad), respectively.

$$\langle\, \Delta y'\,\rangle\Big|_{roll,\,dipole} = -\ \Big(\langle\, \delta\theta_{z,\,D}\,\rangle\cdot\langle\,\Theta_{B,\,D}\,\rangle + \langle\, \delta\theta_{z,\,F}\,\rangle\cdot\langle\,\Theta_{B,\,F}\,\rangle\Big)$$

$$= -\ (1.221\times 10^{-4})\cdot(60.67\text{ mrad}) + (1.718\times 10^{-4})\cdot(71.35\text{ mrad})$$

$$= 4.9\ (\mu\text{rad}),$$

(6.31)

where $\delta\theta_{z,\,D}$, $\delta\theta_{z,\,F}$, $\Theta_{B,\,D}$, and $\Theta_{B,\,F}$ are roll angles of defocusing magnets and focusing magnets, and bending angles of defocusing magnets and focusing magnets, respectively. Figure 6.9 shows angular kick distributions for each type of gradient magnet. One thing
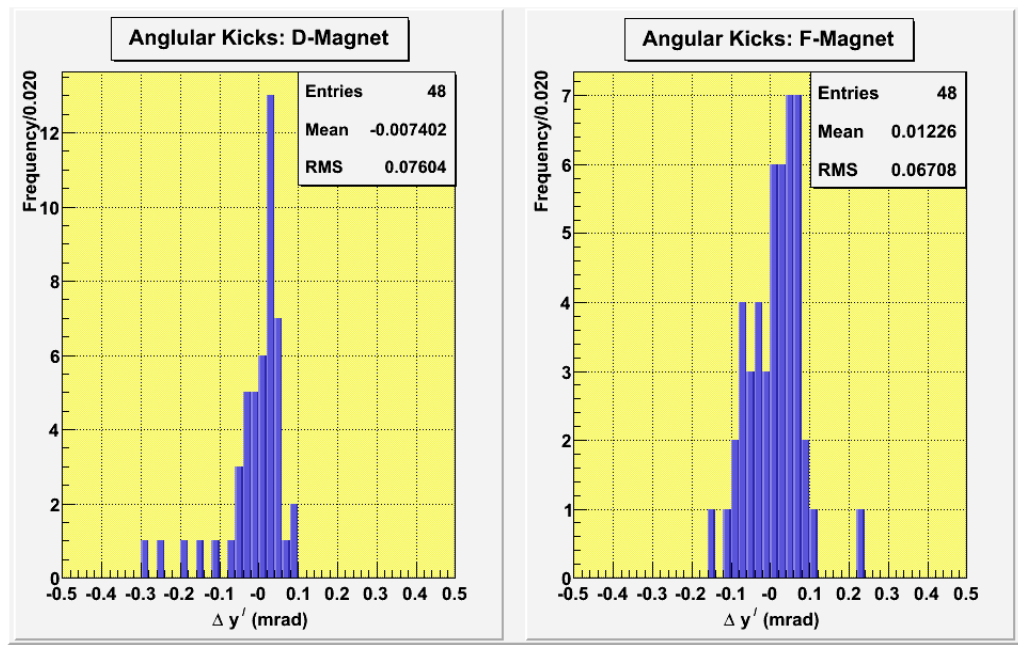
Figure 6.9: Distributions of angular kicks arising from roll angles: the left figure is for the distribution of dipole kicks for the 48 defocusing magnets, and the right figure is for the 48 focusing magnets.

that we need to note in this calculation is that, since the bending radius of the focusing magnet is larger than that of defocusing magnet, such that roll errors for focusing magnets have a larger effect on the beam than the roll errors for defocusing magnets.

The quadrupole components of a gradient magnet also contribute additional angular deflections caused by translational offsets (δx and δy). Since defocusing and focusing magnets have different multipole coefficients ($\mathcal{K}_D$ and $\mathcal{K}_F$) we calculate angular kicks from defocusing magnets and focusing magnets, separately. Given average radial displacements of 0.339 (mm) for defocusing magnets and 0.0819 (mm) for focusing magnets, as shown in Figure 6.10, we calculate horizontal angular kicks as follows:

Figure 6.10: Distributions of radial offsets at gradient magnets: the left figure is for the distribution of radial offsets for the 48 defocusing magnets, and the right figure is for the 48 focusing magnets.

$$\langle \Delta x' \rangle \Big|_{offset, \, quad}$$

$$= \langle L_{long} \rangle \Big(\mathcal{K}_{1, \, D} \langle \delta x \rangle_D + \mathcal{K}_{1, \, F} \langle \delta x \rangle_F \Big)$$

$$= (2.9145 \text{ m}) \cdot \Big\{ (-0.0577069 \, m^{-2})(-0.33865 \text{ mm}) + (0.0542195 \, m^{-2})(0.08185 \text{ mm}) \Big\}$$

$$\approx 70.0 \, (\mu \text{rad})$$

$$(6.32)$$

For the case of vertical angular kicks, as shown in Figure 6.11, the average vertical displacements are 0.05165 (mm) for defocusing magnets and 0.21562 (mm) for focusing magnets. Hence, average vertical kick induced from quadrupole components is 25.4 (μrad).
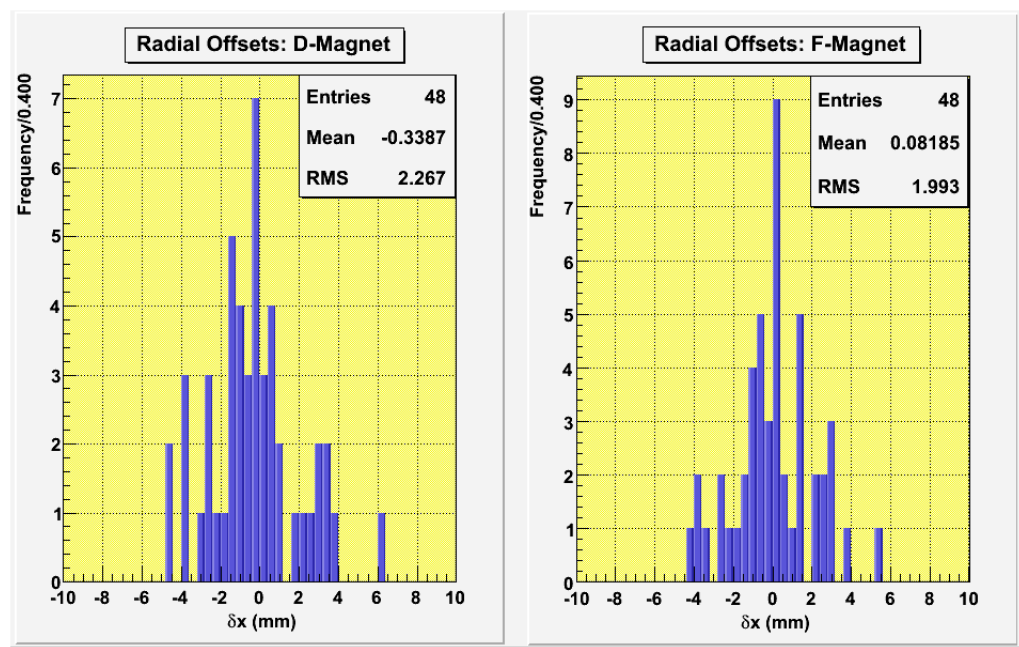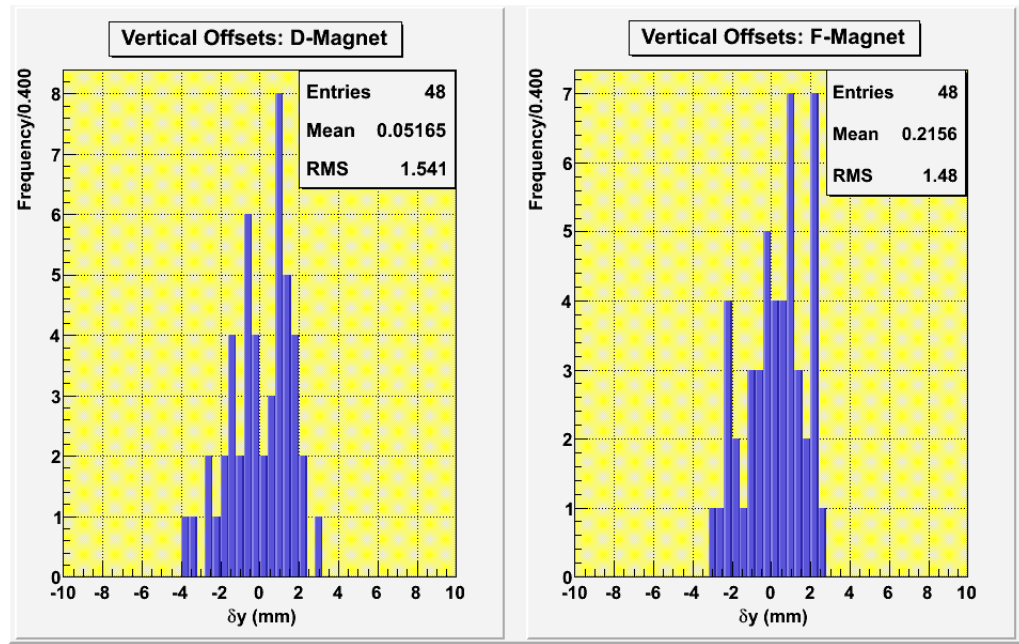

Figure 6.11: Distributions of vertical offsets at gradient magnets: the left figure is for the distribution of vertical offsets from 48 defocusing magnets, and the right is from 48 focusing magnets.

$$\langle \Delta y' \rangle \Big|_{offset,\ quad} = \langle L_{long} \rangle \left(\mathcal{K}_{1,\ D} \cdot \langle \delta y \rangle_D + \mathcal{K}_{1,\ F} \cdot \langle \delta y \rangle_F \right)$$

$$= \langle L_{long} \rangle \cdot \left\{ \mathcal{K}_{1,\ D} \cdot (0.05165 \text{ mm}) + \mathcal{K}_{1,\ F} \cdot (0.21562 \text{ mm}) \right\} \quad (6.33)$$

$$\approx 25.4 \ (\mu\text{rad})$$

From the average angular deflections, we can calculate average momentum kicks, or average transferred momentum, as discussed in section 4.3.2.

$$\langle \Delta \mathcal{P}_x \rangle \Big|_{quad,\ offset} \approx \mathcal{P}_0 \cdot \langle \Delta x' \rangle \Big|_{quad,\ offset}$$

$$= 954.263 \ (MeV/c) \cdot 70.0 \ (\mu\text{rad})$$

$$= 66.8 \ (keV/c) \quad (6.34)$$

$$\langle \Delta \mathcal{P}_y \rangle \Big|_{quad,\ offset} \approx 24.2 \ (keV/c)$$

At the Booster injection energy of 400 (MeV), the design momentum $\mathcal{P}_0$ is 954.263 (MeV/c). All of the above angular deflections can be superimposed and impinge upon a beam. The angular kicks arising from magnet alignment errors leading to closed-orbit distortions are listed in Table 6.1 below.

Table 6.1: Average angular kicks induced by magnet alignment errors

alignment errors	field component	effects
pitch ($\delta\theta_x$)		$x - y$ coupling
roll ($\delta\theta_z$)	dipole	$\langle \Delta y' \rangle = 4.9 \ (\mu\text{rad})$
horizontal offsets (δx)	quadrupole	$\langle \Delta x' \rangle = 70.0 \ (\mu\text{rad})$
vertical offsets (δy)	quadrupole	$\langle \Delta y' \rangle = 25.4 \ (\mu\text{rad})$

6.4 Effects of Magnet Misalignments

6.4.1 rms emittance growth

This section discusses the results of numerical calculations to diagnose beam degradations induced by magnet alignment errors (as presented in Chapter 5) under the influence of space-charge effects. The numerical calculations show that, for pitched magnets the emittance growth is about 2.2 % in the horizontal plane and 4.3 % in the vertical plane. For magnets with station offsets the emittance growth is about 5.0 % in both planes. Figures 6.12, 6.13, and 6.14 show the transverse emittance growths due to alignment errors. Each of the Figures depicts the emittance growths caused by alignment errors with and without space-charge effects. It is clear that in the absence of the space-charge effects, alignment errors do not have adverse effects on a beam. Only in the presence of space charge do alignment errors enhance the beam degradations.
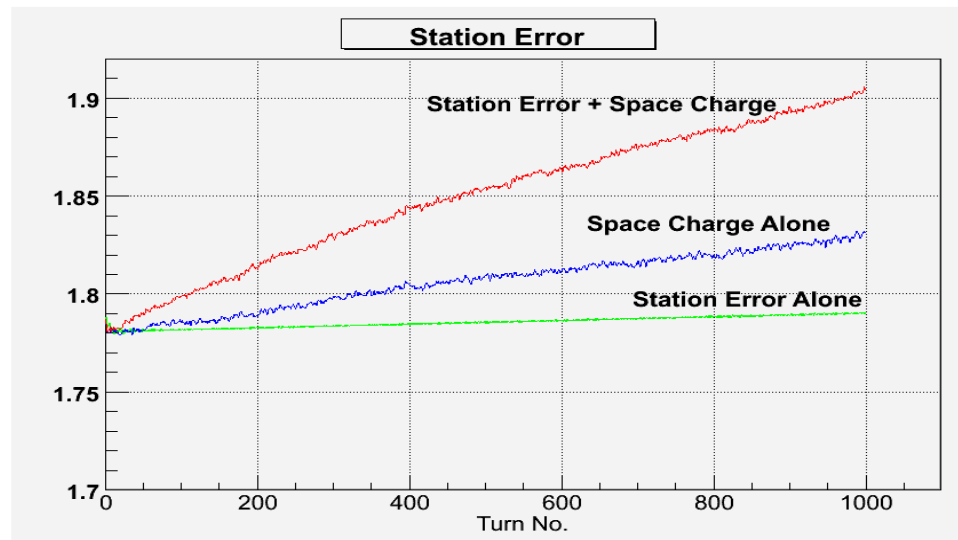
(a) horizontal emittance
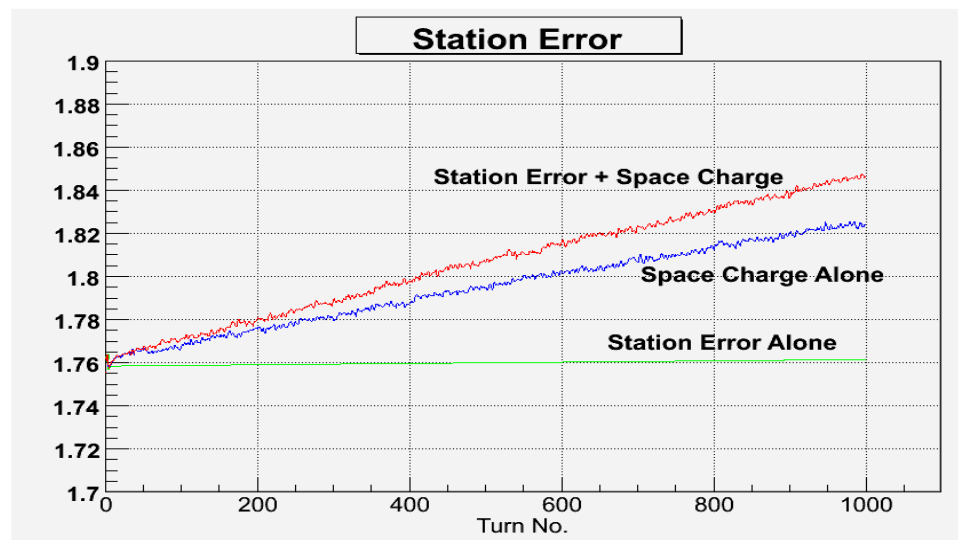
(b) vertical emittance

Figure 6.12: Transverse emittance growth due to station offsets; progressing from bottom to top, station offsets alone, space-charge alone, and station offsets with space-charge effects
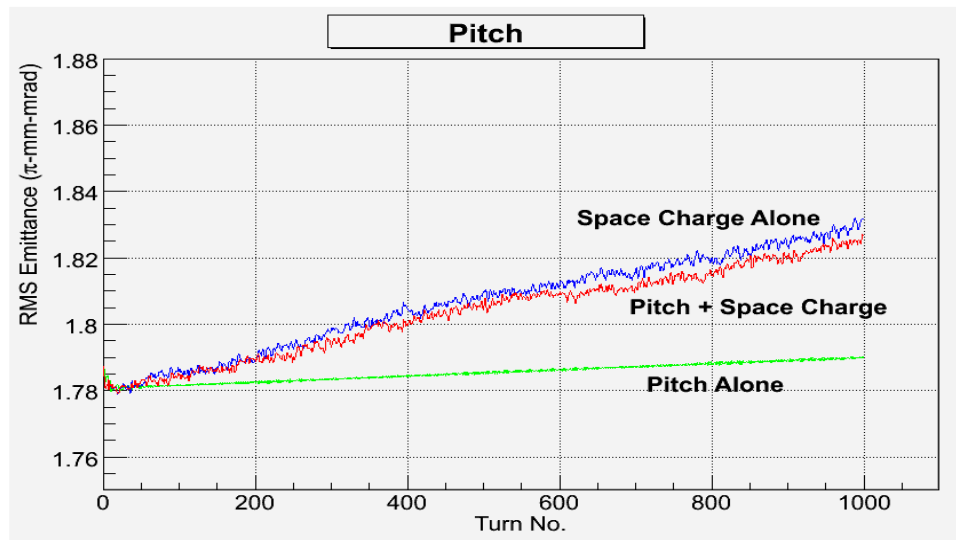
(a) horizontal emittance
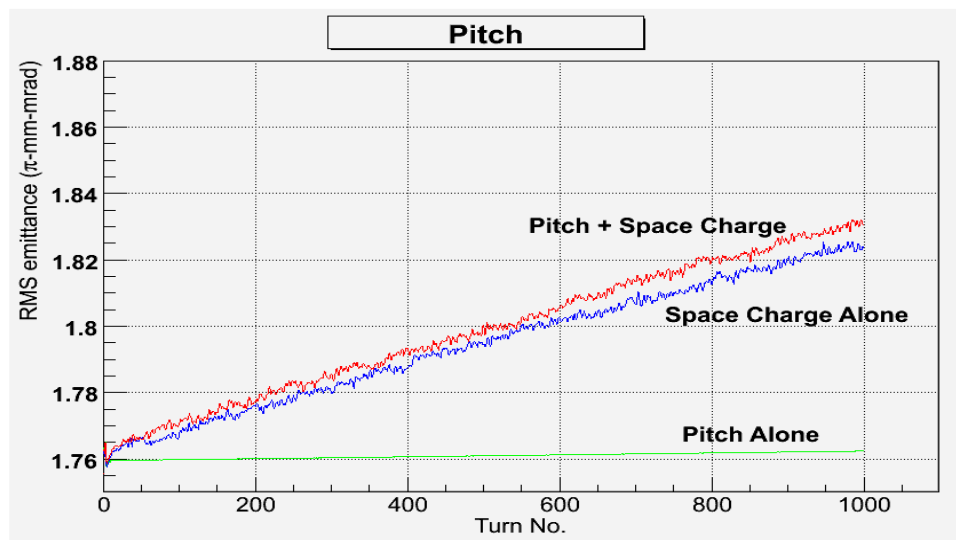
(b) vertical emittance

Figure 6.13: Transverse emittance growth due to magnet pitch; progressing from bottom, pitch alone, space-charge alone, and pitch with space-charge effects
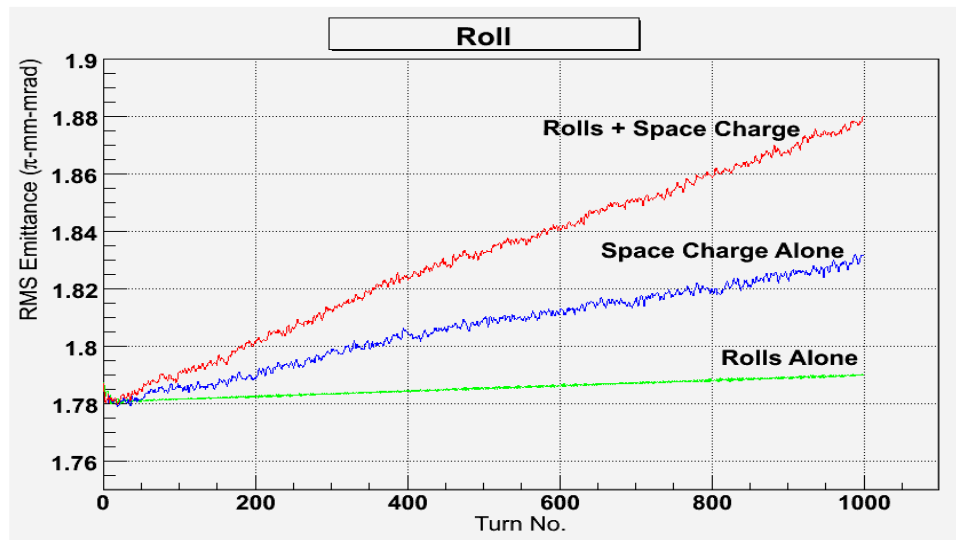
(**a**) horizontal emittance
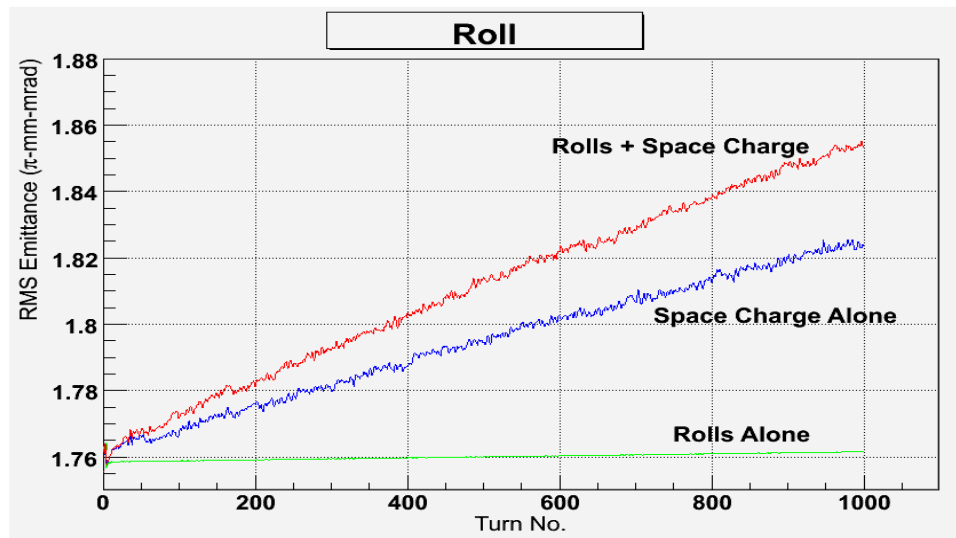
(**b**) vertical emittance

Figure 6.14: Emittance growth due to rolls; progressing from bottom to top, rolls alone, space-charge alone, and rolls with space-charge effects
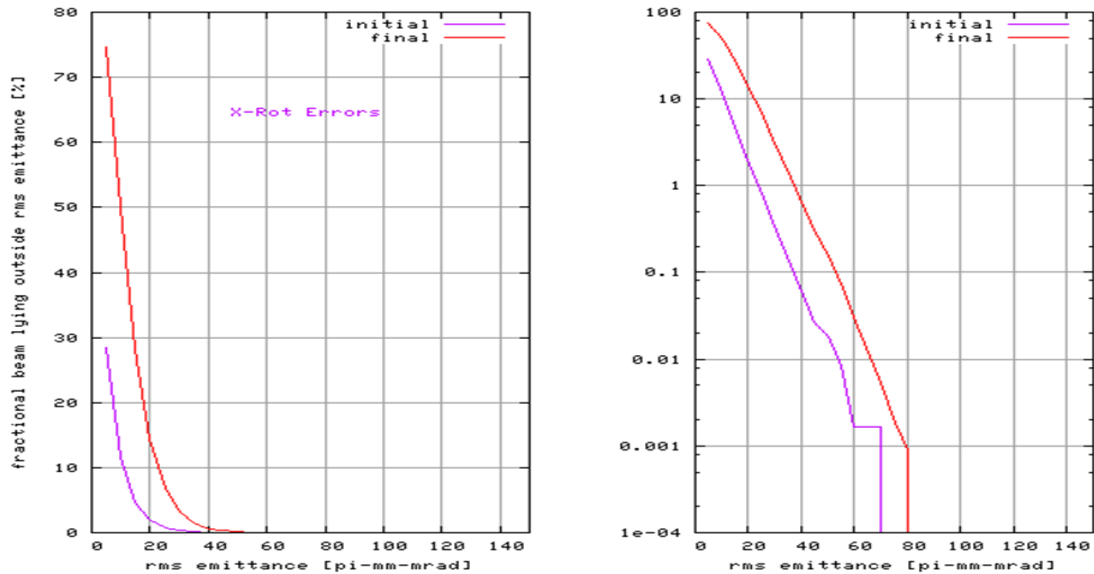
Figure 6.15: Emittance histogram for pitched magnets

Figure 6.15 shows the percentile (or fraction) of a beam at a specific emittance. The blue trace indicates the initial distribution of emittances, and the red trace indicates the final distribution of emittances after 1,000 tracking turns. In the left figure, the vertical axis of percentile is on linear scale, whereas in the right figure is on logarithmic scale. Using a logarithmic scale, the maximum extent of the transverse emittance is more distinguishable.

In case of yawed magnets, Figure 6.16 shows that one percent of total beam has an emittance exceeding 40 π-mm-mrad after 1,000 turns under the influence of space charge. The maximum emittance reaches 90 π-mm-mrad. For rolled magnets, Figure 6.17 shows that one percent of the total beam has an emittance larger than 55 π-mm-mrad after 1,000 turns under space charge effects.
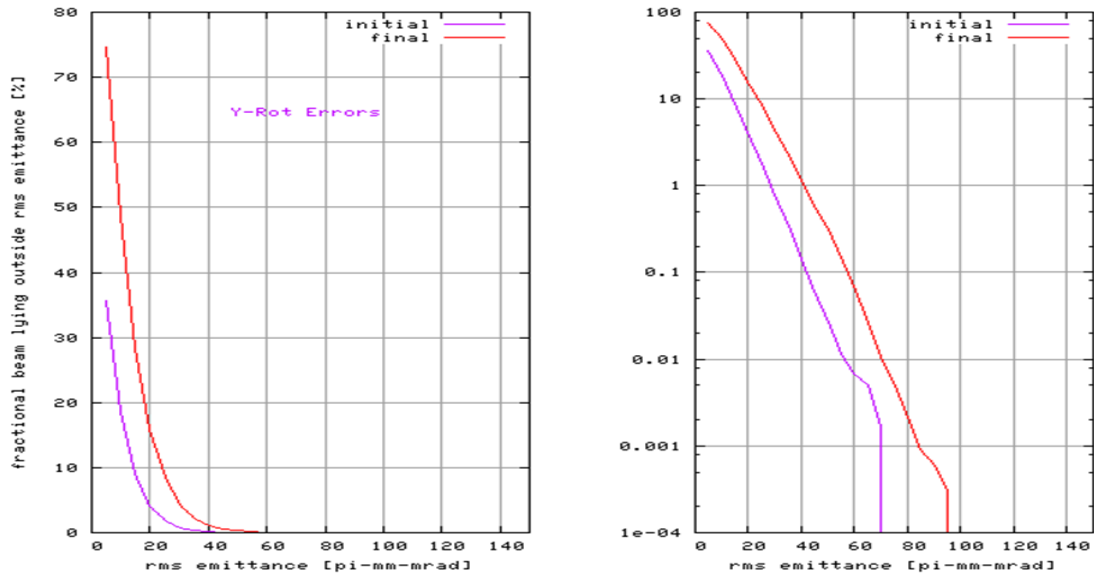
Figure 6.16: Emittance histogram for yawed magnets

Figure 6.18 shows, including magnets with station errors under space-charge effects, one percent of total beam has an emittance larger than 40 π-mm-mrad after the injection period is complete. As stated earlier, once we identify simple rolls and twistors, we can predict how much improvements can be achieved if selected group of rolled magnets are realigned. Figure 6.19 distinctly demonstrates each scenario with rolled magnets. The innermost trace is the case when all magnets are perfectly aligned. About 10 % of total beam have 12 π-mm-mrad. When simple rolls are realigned with twistors left intact, that is only large rolls (twistors) are included, about 10 % of beam has emittance larger than 14 π-mm-mrad. Next, only twistors are realigned, or only simple rolls are included, 10 % of beam has emittance larger than 18 π-mm-mrad. Lastly, no realignment work is done, in other words, including all existing rolls, 10 % of beam emittance larger than 22 π-mm-mrad.
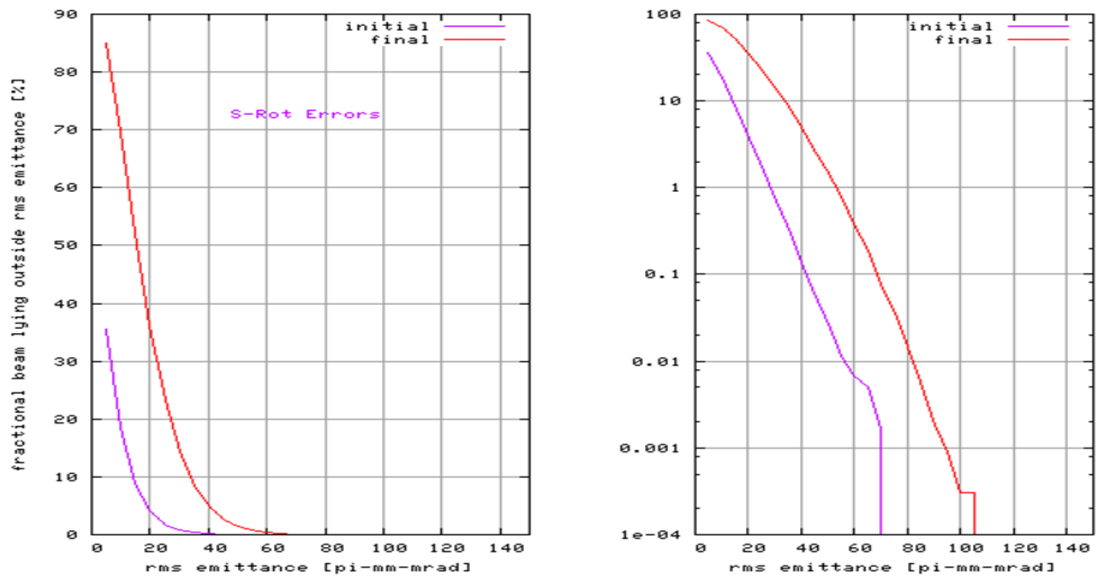
Figure 6.17: Emittance histogram for rolled magnets
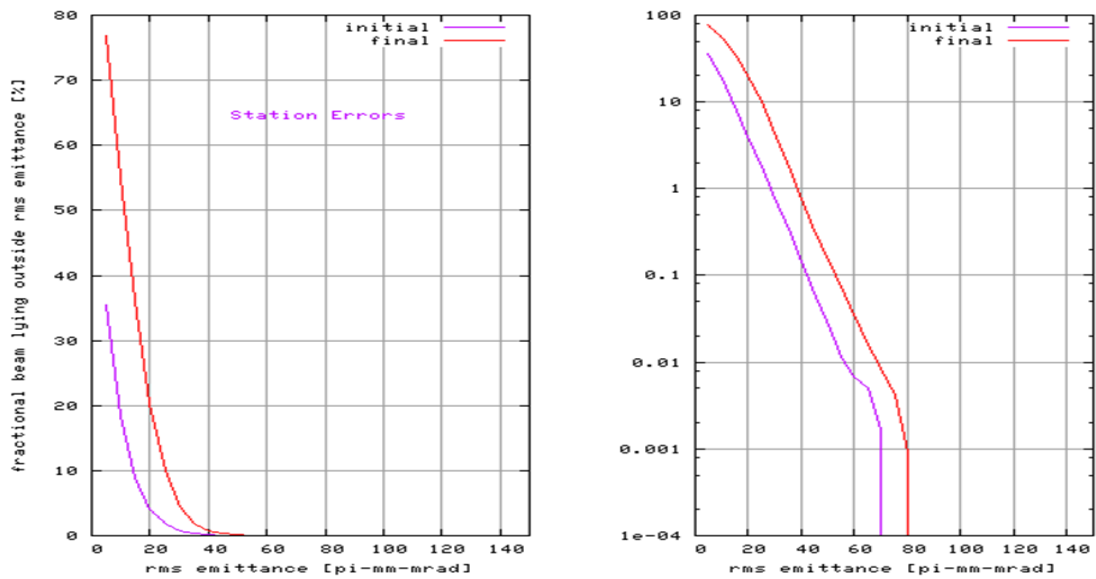
Figure 6.18: Emittance histogram for station-errored magnets

Leaving the twisted magnets intact, if simply-rolled magnets are realigned, much improvement can be made as far as the halo formation is concerned. Figure 6.19 shows the fraction of macroparticles that lie outside of a given rms emittance with different magnet realigning efforts. The upper plot is on linear scale of macroparticle percentage, and the lower plot is shown on a logarithmic scale for clear distinctions between each case scenario of realigning work. Since realignment of beamline elements is quite challenging and time-consuming, it is necessary to prioritize misaligned magnets to realign. Therefore, it is of great interest to predict how much improvement could be made after a selected set of misaligned magnets are realigned. Although, at present it is not known how to repair twisted (largely rolled) magnets, the ORBIT⋆ runs show that twisted magnets are a contributing factor to the halo formation as illustrated by Figure 6.19.
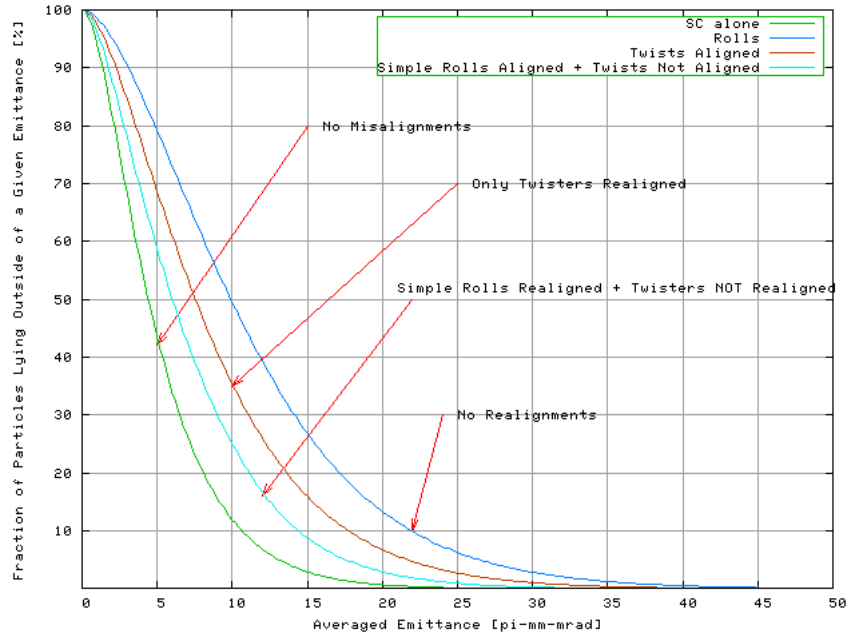
(a) on linear scale
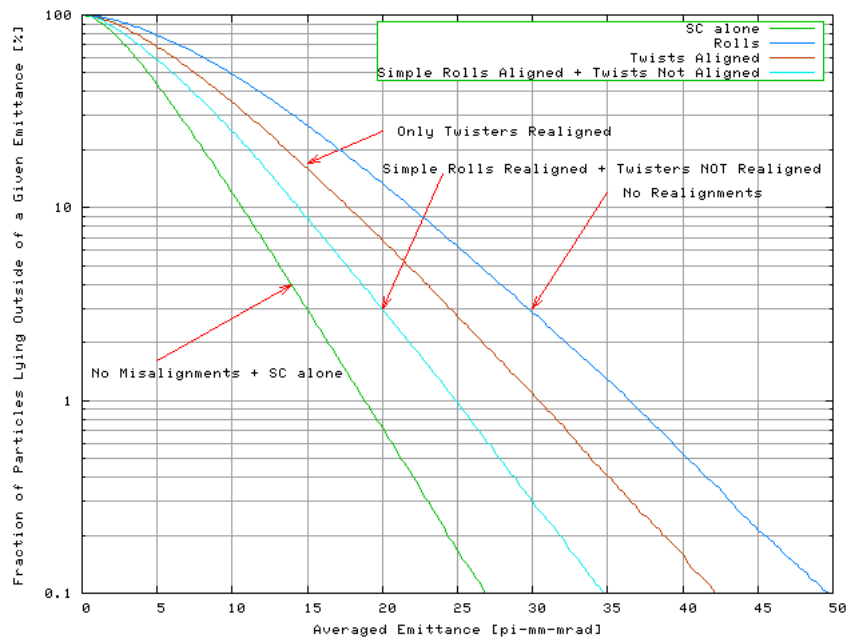
(b) on logarithmic scale

Figure 6.19: emittance histograms before and after realignments

6.5   Concluding Remarks

Since the Booster main magnets are combined-function magnets, magnet misalignments can induce both dipole- and quadrupole-field errors. The induced-field errors result in angular kicks, or momentum kicks, which are superimposed and impinge upon the beam. It is therefore evident that if we could realign any of the misaligned combined-function magnets, then both quadrupole-field and dipole-field errors pertaining to each individual misaligned magnet could be eliminated altogether.

From our misalignment modeling with the up-to-date beamline survey data, we conclude that the effects of magnet rolls and station offsets are larger than the other types of alignment errors that are currently present in the Booster lattice. The aim of our misalignment modeling is twofold: First, as a result of the beam dynamics calculations, it is worthwhile to address selected magnet realignment efforts. As mentioned in section 6.4, priority should be given to *rolled focusing* magnets, and magnets with longitudinal displacements. Second, as no correctors are included in our model, macroparticles are tracked on no-corrector orbit. Instead of planning on magnet realigning efforts, the angular-kick calculations can also help determine, or reset the strengths of corrector magnets (trim dipoles).

In conclusion, we have addressed the benefit of a realignment of selected misaligned magnets, and the benefit of resetting the strengths of corrector magnets in an effort to improve Booster performance.

Chapter 7

Time-Structured Multiturn Injection and Longitudinal Painting

Let's paint the machines red!

In this chapter we discuss microbunch-injection methods that can be applied to the present Booster synchrotron. Methods of synchronous injection into standing RF buckets are investigated under the influence of space charge with the aid of the ESME [3] code. First, the ESME code is briefly described. It is followed by a discussion of simulations for the multiturn-injection models with time structure.

7.1   Introduction to the ESME Simulation Code

ESME is a Fortran program, authored by James MacLachlan of Fermilab, for macroparticle[1] tracking and modeling of RF gymnastics. The older versions are written in Fortran

---

[1] In the context of numerical simulations for particle accelerators, a macroparticle means a simulation particle, or representative particle as individual sources of the space-charge field. Each macroparticle represents the total charge of many real beam particles, or a fractional charge of a total beam charge in distributions in

77, and the latest version is written in Fortran 95. For our injection modeling, the ESME 2003 is used throughout. The program ESME solves a pair of difference equations during n-th turn of a synchronous particle. The synchronous particle is an ideal particle, or reference particle at the center of particle beams. The ideal particle passes the RF gaps at the same RF phase at each turn; thus, there is a *synchronism* between the synchronous particle and the RF electric field.

$$
\left.
\begin{aligned}
\theta_{i,\, n} &= \left[\left(\frac{\tau_{s,\, n-1}}{\tau_{s,\, n}} \right) \cdot \theta_{i,\, n-1} + 2\pi \cdot \left(\frac{\tau_{i,\, n}}{\tau_{s,\, n}} - 1 \right) \right] \\
E_{i,\, n} &= E_{i,\, n-1} + eV \cdot (\phi_{s,\, n} + H \cdot \theta_{i,\, n}) - eV \cdot (\phi_{s,\, n})
\end{aligned}
\right\}
\tag{7.1}
$$

The θ, ϕ, E, τ and H denote RF phase, azimuth angle, energy, revolution period and harmonic number, respectively.

7.2 400-MeV Linac Parameters

Salient parameters of the 400-MeV linac are listed in Table 7.1.

One thing to note in the Table 7.1 is the chopping factor [56]. The chopping factor is defined as the ratio of full bunch length ($\mathcal{L}_{bunch,full}$) to RF wavelength (λ_{rf}). In the case of the 400-MeV transferline, the length of a microbunch spans about 14 % of the RF wavelength (λ_{rf}) in the RF-phase space (Θ) in each individual 201-MHz[2] RF bucket.

$$
\text{chopping factor} = \frac{\mathcal{L}_{bunch,full}}{\lambda_{rf}}
\tag{7.2}
$$

---

energy (ΔE)-azimuth(Θ) phase space. In our simulations, individual macroparticle that we include represents on the order of 10^5 real particles. The macroparticles are then acted upon by the RF system of synchrotrons, or storage rings, or linacs. One of the main capabilities of the ESME is the longitudinal space-charge calculation.

[2] The actual linac RF frequency is 201.25 (MHz). Here we simply refer it to *201-MHz RF* for convenience.

<div align="center">

Table 7.1: Linac Parameters

</div>

Beam Species	H^-
Beam Kinetic Energy	400 (MeV)
RF Frequency	201.25 (MHz)
Full Bunch Length	0.7 (nsec)
Chopping Factor	0.14
$\delta\big|_{max} = \frac{\Delta p}{p}\big|_{max}$	$\pm$ 0.13 %
σ_δ	0.026 %
ε_l	1.0×10^{-3} (eV-s)
Intensity	1.25×10^9

7.3 Booster Synchrotron Parameters

The comprehensive parameters for the Booster ring at injection energy are given in Table 7.2 on the next page. Some machine parameters listed in Table 7.2 are derived from the parameters specified in the Booster design lattice (version 1.1).

Table 7.2: Machine Parameters for Fermilab's Booster at Injection

Ring Radius ($\langle R \rangle$) / Ring Circumference ($2\pi\langle R \rangle = \beta c \cdot T_0$)	75.47 / 474.2 (m)
Injection Kinetic Energy	400 (MeV)
Injection Momentum	954.263 (MeV/c)
Synchronous Energy (E_s)	1.328 (GeV)
β (Lorentz factor)	0.7131
γ (Lorentz factor)	1.426
Revolution Period (T_0)	2.2 (μsec)
Revolution Frequency (f_0)	454.5 (kHz)
No. of Injection Turns	11
Injection Period	24.2 (μsec)
Cycle Time	66.7 (msec)
γ_{tr}	5.4696
α_1 (momentum compaction factor)	0.0172
Phase-Slip Factor ($|\eta|$)	0.458
$\varepsilon_{tr,\,95,\,n}$ (95 % normalized transverse emittance)	12.0 (π-mm-mrad)
RF Frequency Range	38.18 $\sim$ 52.83 (MHz)
ν_x/ν_y (bare tunes)	6.7 / 6.8
betatron frequency ($f_{\beta,x}$, $f_{\beta,y}$)	318.2 / 363.6 (kHz)
Q_s (synchrotron tune)	1.147×10^{-3}
Ω_s (synchrotron frequency)	3.28 (kHz)
T_s (synchrotron period)	305 (μsec)
β_s (longitudinal beta function)	3.0×10^4 (m)
ε_l (longitudinal emittance)	0.25 (eV-s)
Batch Intensity	5.04×10^{12}
Average Beam Current at Injection	420 (mA)
Effective beam radius	0.0325 (m)
Effective beam-pipe radius	0.0653 (m)
Bunching Factor (B_f) (at injection)	~ 0.4
$\frac{\Delta P}{P_0}\big|_{max}$	± 0.15 %
σ_δ	3.0×10^{-4}
$\beta_{x,max}$ / $\beta_{y,max}$	33.7 / 20.5 (m)
$D_{x,max}$ / $D_{y,max}$	3.2 / 0.0 (m)
Cell Type	FOFDOOD (DOODFOF)
Cell Length	20.62 (m)
Gradient Magnets / cell	4
Total Gradient Magnets	96
$V_{rf,\,inj}$ (RF voltage at injection)	205.0 (kV/Turn)
Phase Advance / cell	96 (deg)
ρ_D (bending radius for defocusing magnet)	48.034100 (m)
ρ_F (bending radius for focusing magnet)	40.847086 (m)

Table 7.3: Sampled ESME Parameters for the Booster Simulation

Ring Radius	75.47 (m)
γ^2_{tr}	29.9165
α_1 (momentum compaction factor)	0.0172
No. of Injection Turns	11
Total Charge	6.0×10^{10}
No. of Macroparticles	$\sim 10^5$
Beam Distribution	Elliptical
effective beam radius	0.0325 (mm)
effective beam-pipe radius	0.0653 (mm)
V_{rf}	205.0 (kV/Turn)
Longitudinal Space-Charge Bin No.	512
FFT Bin No.	512

7.4 Microbunch Injection into the Booster

In most simulations, the beams are injected in the longitudinal phase space along a long strip in the direction of RF phase [57]. An injected beam of this type is referred to as a *macrobunch*. In contrast, we use a train of small bunches which are injected into a standing (or stationary) RF bucket with a certain amount of bunch spacing. This type of injected beam with a certain time structure is termed a *microbunch*. For the case of the Booster, each microbunch is 0.7 (nsec) in full length and is separated by 5 (nsec). The synchronous injection repeats for 11 turns for the duration of 24.2 (μsec) with no beam notch.

7.5 Simulations of Microbunch Injection

In this section, we describe how multiturn microbunch injection for the Booster is simulated using the code ESME. First, we generate one microbunch with elliptical distribution

from an initial ESME run. Then, we repeatedly populate the microbunch inside a station-
ary RF bucket to form a train of microbunches. With this time structure, we repeat the
5-microbunch injection over 11 injection turns. In simulation, we track macroparticles on
the order of 10^5 in longitudinal phase space through the ring lattice in the presence of the
longitudinal space-charge force.

7.5.1   Injection with RF-Phase Slip:

Uncontrolled Longitudinal Painting

When a linac-to-ring transfer takes place, RF-bucket mismatch, or longitudinal mis-
match can be parasitically induced. Here we refer to this kind of mismatch as *parasitic
phase slip* in phase space. In this dissertation, we define the longitudinal (RF-**b**ucket)
mismatch factor of R_{bm} for the linac-to-ring transfer.

$$R_{\lambda_{rf}}\Big|_{injection} = \frac{\lambda_{rf,Booster}}{\lambda_{rf,Linac}}\Big|_{injection} = \frac{201.25 \ (MHz)}{38.18 \ (MHz)} = 5.271$$

$$R_{bm} = R_{\lambda_{rf}}\Big|_{mod} = 0.271 = 27.1 \ \% \tag{7.3}$$

According to Eqn. (7.3), a Booster RF bucket can hold 5 microbunches of 201 (MHz)
injected from the 400-MeV transferline. The RF wavelength (λ_{rf}) of the Booster is 26
(nsec) and that of the Transferline is 5 (nsec). The microbunch spacing of 5 (nsec) is
measured between the centers of adjacent RF buckets of 201 (MHz). By calculating a ratio
of RF-bucket wavelengths ($R_{\lambda_{rf}}$), we determine the mismatch factor ($R_{\mathbf{bm}}$). In case of the
Booster injection, the value of R_{bm} is determined to be 0.271. This corresponds to 1.355
(nsec). If the value of $R_{\lambda_{rf}}$ is an integer, then the whole number of sub-buckets are injected
into a standing RF bucket with no mismatch. However, when the value of $R_{\lambda_{rf}}$ is a non-
integer, parasitic phase slip can be induced during the multiturn injection process. Because
of the repeated arrival time errors (RF-phase lags) in subsequent injection turns, we include

a phase lag of about 0.22° for the first turn as shown in Figures 7.1. In accordance with
ESME units for RF phase, the phase offset is calculated in units of degrees as in Eqns. (7.4)
and (7.5).

$$\theta_{offset} = \frac{360°}{H} \times \frac{1.355 \; nsec}{26 \; nsec} \approx 0.22 \; ° \tag{7.4}$$

Here, $\mathcal{L}_{mb}$ denotes microbunch spacing, and H is the Booster harmonic number of 84. Next,
the bunch length is calculated in units of degrees:

$$\mathcal{L}_{mb} = \frac{360 \; °}{84} \times \frac{5 \; nsec}{26 \; nsec} = 0.824 \; °$$

$$\sigma_\theta = \frac{1}{5} \times \mathcal{L}_{bunch,full} = 0.14 \; nsec = 0.023 \; ° \tag{7.5}$$

According to the chopping factor of the 400-MeV transferline, the 201-MHz microbunch
has a full bunch length (5 σ) of 0.7 (nsec). Hence, the rms bunch length of a microbunch is
approximately 0.14 (nsec), or 0.023°. The last parameter to determine is the energy error.
We can compute the rms energy deviation ($\sigma(\Delta E)$) from the synchronous energy (E_s) of
1.338 (GeV):

$$\sigma(\Delta E) = E_s \cdot \beta^2 \cdot \sigma(\delta)$$

$$= (1.338 \; GeV) \cdot (0.7131)^2 \cdot (3 \times 10^{-4}) \approx 0.2 \; (MeV) \tag{7.6}$$

Once we know the maximum extent of the momentum deviation from measurements [58],
we can estimate the rms momentum spread:

$$\frac{\Delta P}{P_0}\bigg|_{max} = \pm \; 0.15 \; \%$$

$$\sigma_\delta \equiv \frac{\delta P}{P_0}\bigg|_{rms} = 0.03 \; \% \tag{7.7}$$

The momentum, or energy spread is important in the injection modeling in that it is neces-
sary to match total emittance of all microbunches captured in a RF bucket to the emittance

of a long bunch, or macrobunch. In our injection model, we particularly mean a *macrobunch*, or *long bunch* by a bunched beam that are distributed uniformly in azimuthal direction. While injected microbunches slip through in RF-phase direction at each turn, the longitudinal phase space is gradually painted with the microbunches. In Figure 7.1, each train of microbunches are colored differently, so that one can tell how longitudinal painting proceeds at each injection turn.

(a) 1st injection

(b) 2nd injection

(c) 3rd injection

(d) 4th injection

(e) 5th injection

(f) 6th injection

(g) 7th injection

(h) 8th injection

(i) 9th injection

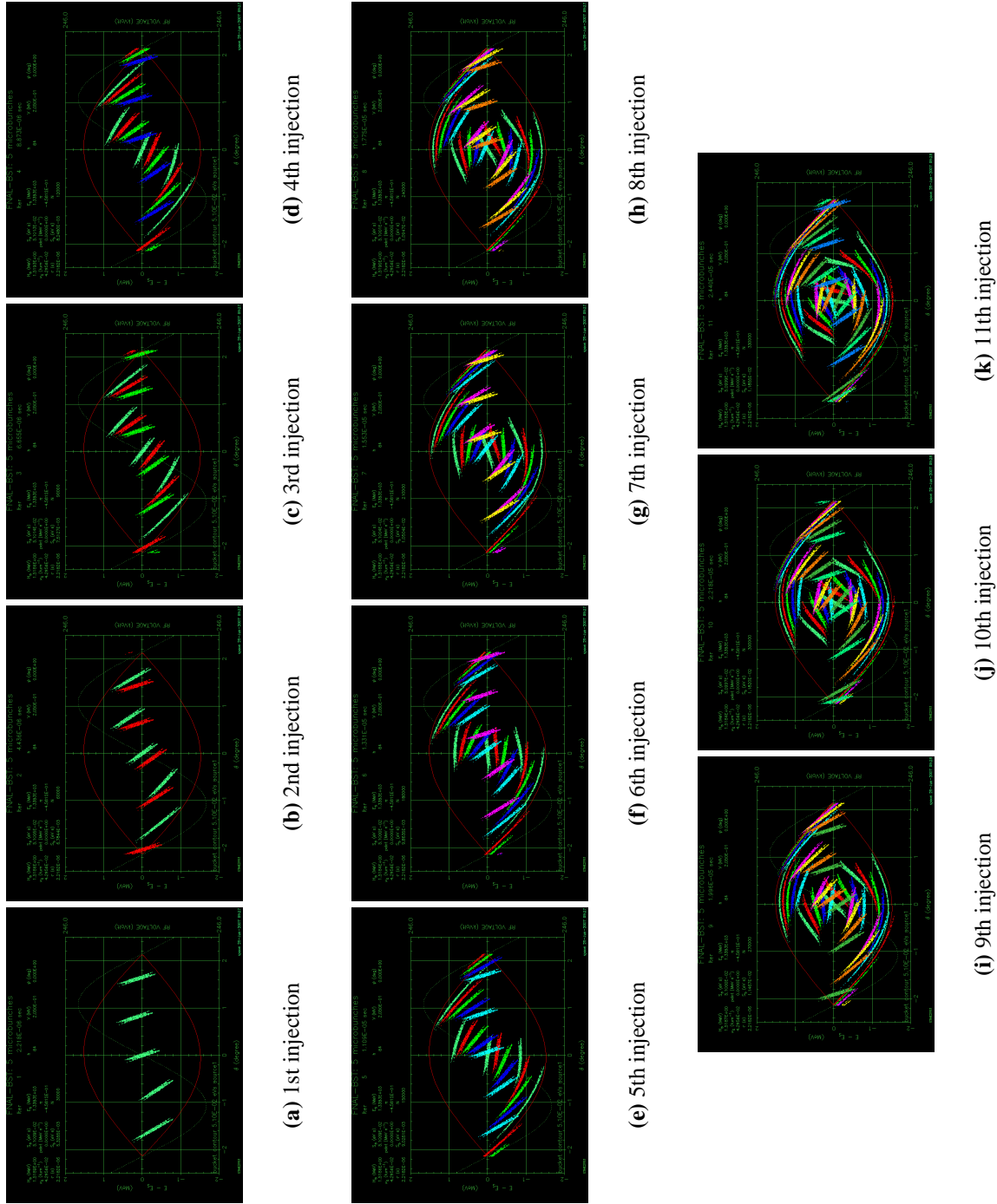**(j)** 10th injection

(k) 11th injection

Figure 7.1: Injection of 5 microbunches with phase slips arising from RF mismatch; the horizontal axis is for RF-phase angle (θ) in units of degree and the vertical axis for ΔE in units of MeV.

7.5.2 3-D Simulations of Microbunch Injection: ESME-ORBIT Simulation

So far, we have discussed the 5-microbunch injection into the Booster using ESME with parasitic longitudinal painting included. By transporting information of macroparticle distribution in θ-ΔE space from the ESME simulations into the ORBIT$\star$, we carry out 3-D space-charge simulations of microbunch injection under the influence of full space-charge effects.

This ESME-ORBIT simulation method allows us to make the best of a variety of features available for RF gymnastics in ESME and macroparticle tracking including both longitudinal and transverse effects of space charge in ORBIT$\star$. Hence, ESME simulations of time-structured multiturn injection can supply ORBIT$\star$ with realistic longitudinal distributions.

Figure 7.2 depicts the flow of the ESME-ORBIT-combined simulations for the microbunch injection into the Booster. Intrinsically, ESME is designed for ring simulations. We, however, use a very small ring ($\langle R \rangle < 1$ (m)) with very large value of transition gamma ($\gamma_{tr} \geq 10^6$) to achieve an approximated linac simulation. By first generating one microbunch from the linac, we spawn a train of 5 microbunches to be injected into the Booster at each turn. After a microbunch passes through the debuncher cavity located about 42.5 meters away from the Linac, the energy spread of a microbunch is reduced. A train of 5 microbunches is then injected into a Booster RF bucket. Over 11 injection turns, we iterate the 5-microbunch injection with phase offsets induced from RF mismatch including 1-D space charge force. Finally, a total of 55 microbunches fill in a Booster bucket with no beam notch. About 9 % beam loss is observed after the microbunch injection process is complete. The distributions of charge density and energy density after the completion of injection process of 11 turns are shown in Figure 7.3 (a) and (b). For comparison, the density profiles of a long bunch with uniform distribution in phase direction are shown in

Figure 7.4. The charge and energy distributions from ESME outputs shown in Figure 7.3 (a) and (b) are matched to those of ORBIT input file shown in Figure 7.5 (e) and (f).
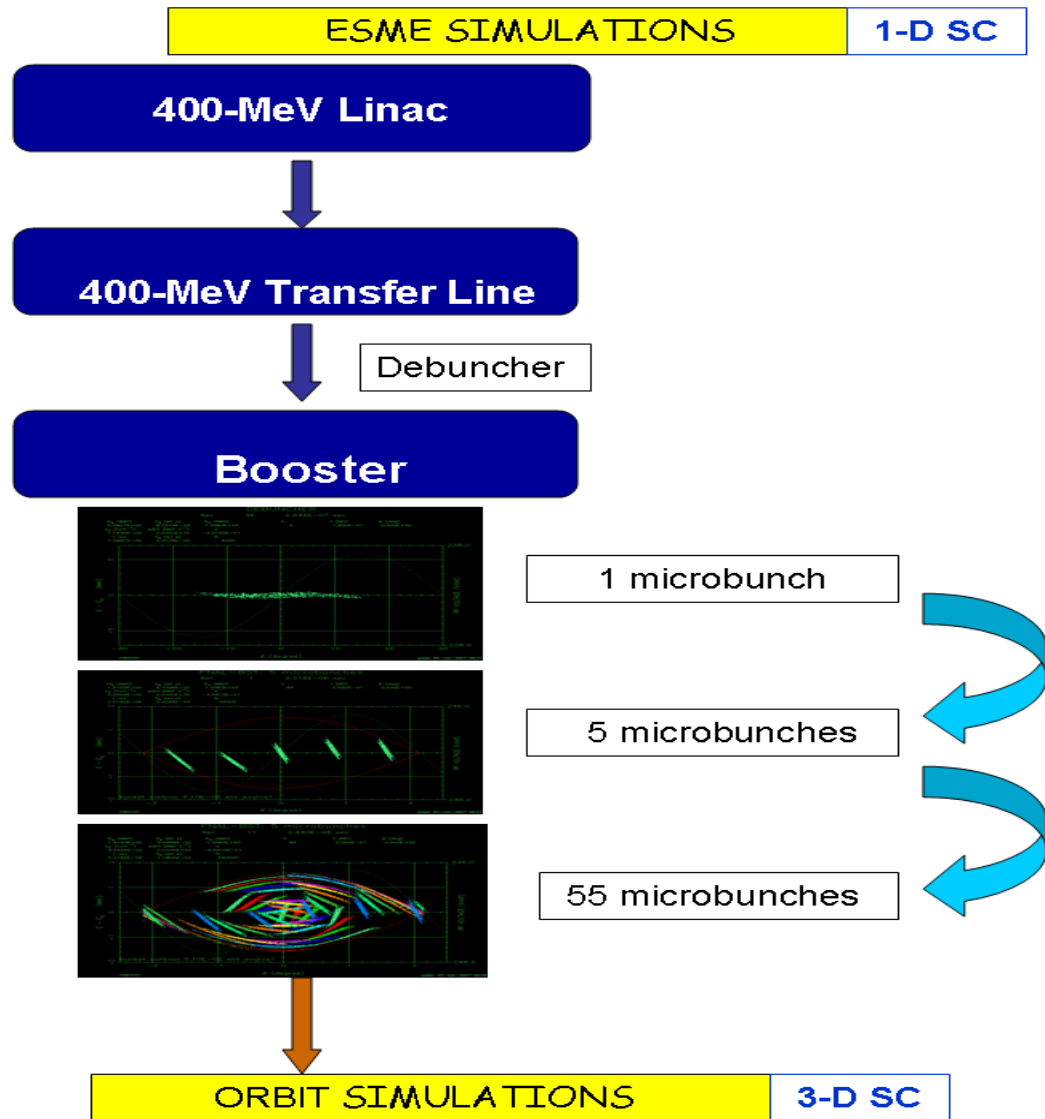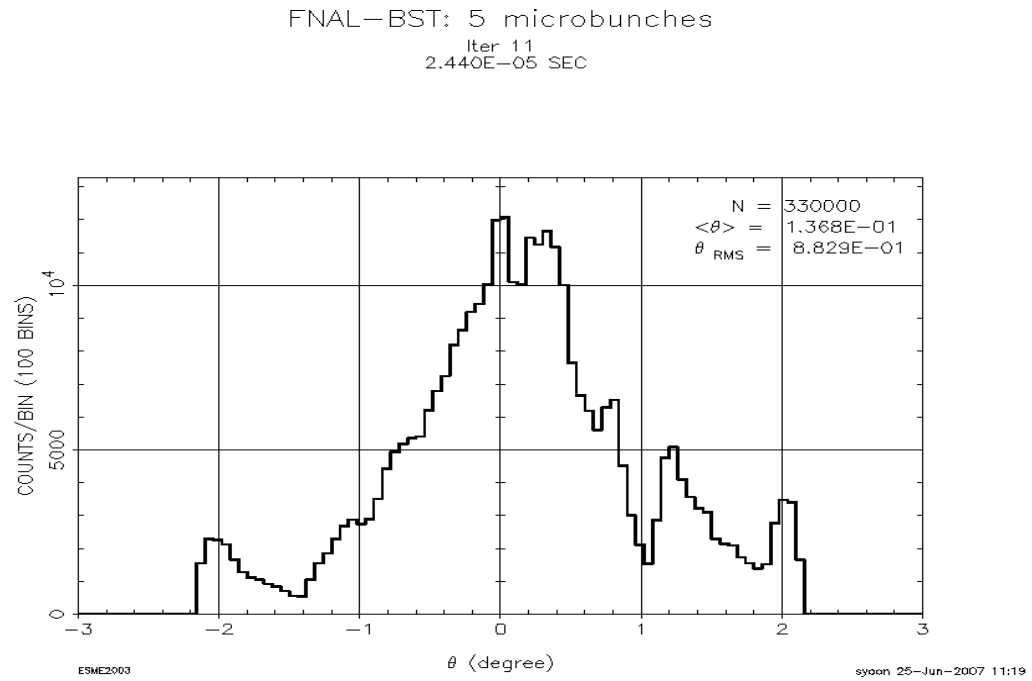

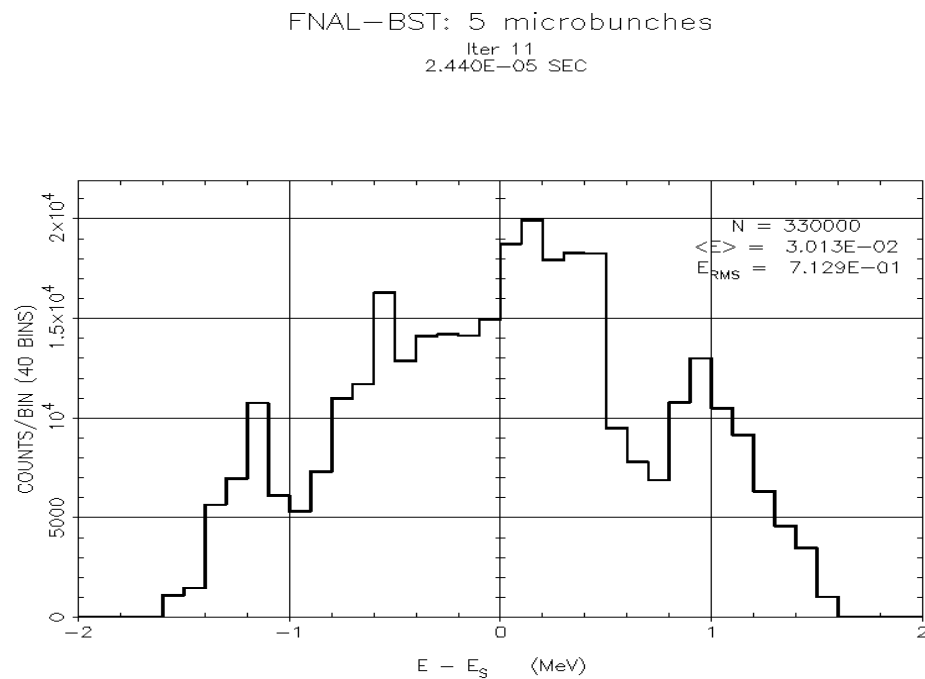**Figure 7.2:** Procedures of ESME-ORBIT-combined simulations including space charge; the SC stands for space charge.

(a) Charge-density distribution of 5 microbunches after the completion of injection process

(b) Energy-density distribution of 5 microbunches after the completion of injection process

Figure 7.3: Longitudinal profiles of 5 microbunches after the injection process is complete

Once the ORBIT takes in the longitudinal information from the ESME simulations, the ORBIT tracks a herd of 330,000 macroparticles starting from 12-th turn through 1,000-th turn with full space-charge nodes included. To achieve the multi-stage EMSE-ORBIT simulation, as illustrated in Figure 7.2, the whole procedure requires about a dozen file processing including unit conversions. For validation purposes, the profiles of 6-D coordinates of input macroparticles are drawn in Figure 7.5. The transverse coordinates (x, x', y, y') provided by a preliminary ORBIT run, and longitudinal coordinates (θ, ΔE) are obtained from the ESME simulations with 5 microbunches. In ESME-ORBIT simulations, it is en-

(a) charge density distribution   (b) energy density distribution
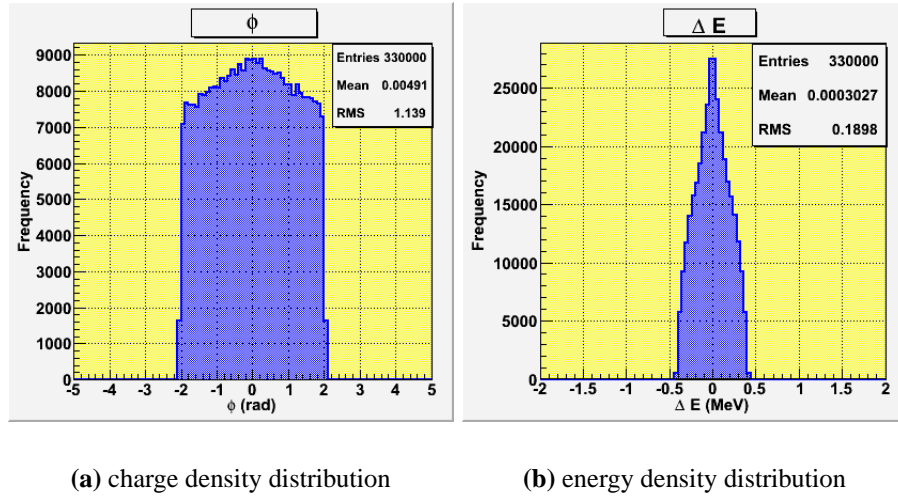
Figure 7.4: A long bunch of longitudinally uniform distribution

sured that the simulation conditions with microbunches are exactly the same as in those of ORBIT-only simulations with longitudinally uniform distribution. Evolution of both horizontal and vertical emittances are shown in Figures 7.6 and 7.7 in comparison with those of a long bunch (or macrobunch). The horizontal emittance grows by 20 % and the vertical emittance by 19 %. In contrast, with a long bunch with longitudinally uniform distribution, transverse emittances grow less than 3 %.
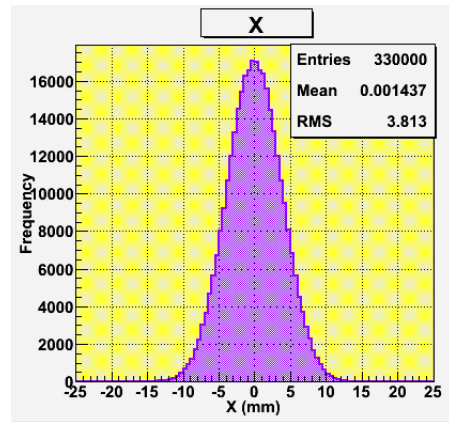
(a) horizontal position profile
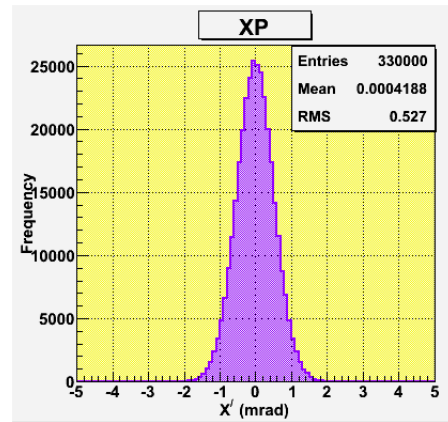
(b) horizontal angle profile
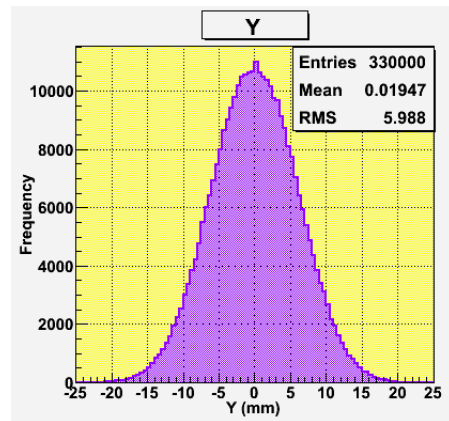
(c) vertical position profile
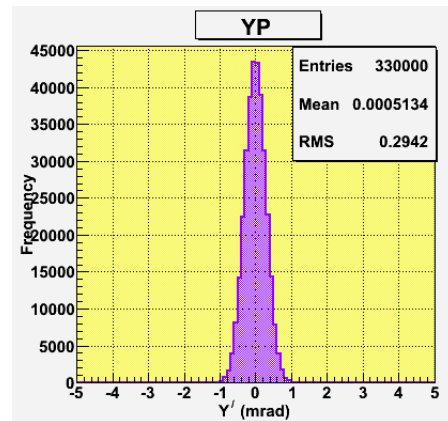
(d) vertical angle profile
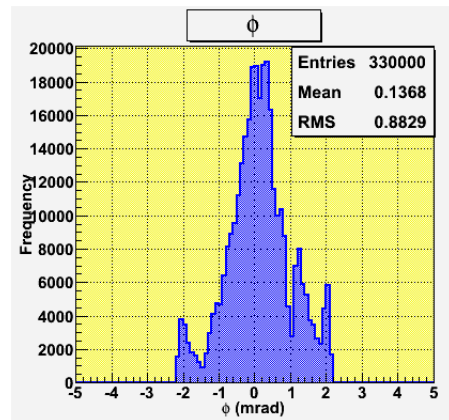
(e) charge density profile
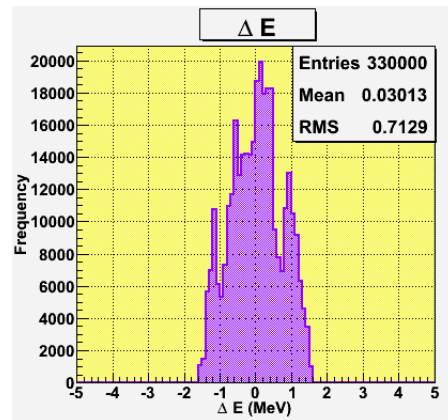
(f) energy profile

Figure 7.5: Validation of an ESME-ORBIT input file
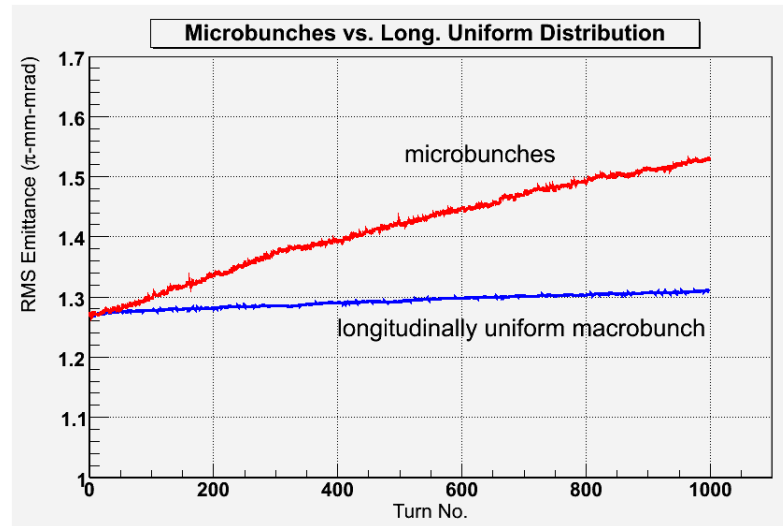
Figure 7.6: Evolution of horizontal emittances of 5 microbunches vs. macrobunch: microbunches are injected with phase slip in the presence of full space-charge effects
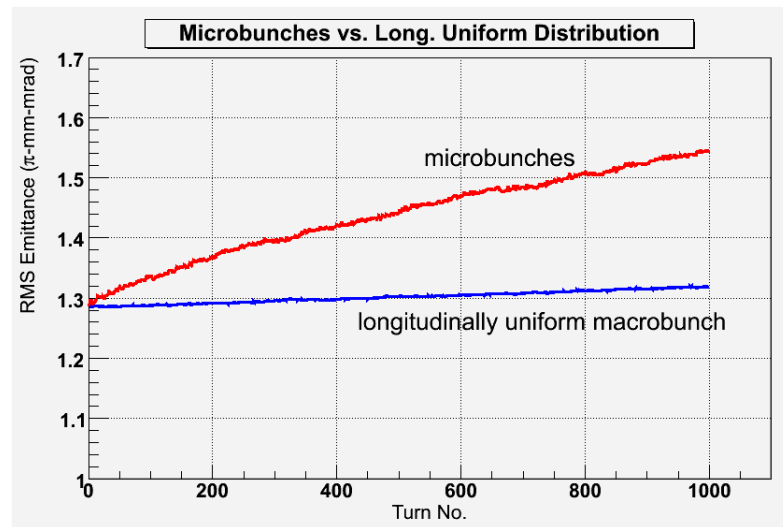
Figure 7.7: Evolution of vertical emittances of 5 microbunches vs. macrobunch: microbunches are injected with phase slip in the presence of full space-charge effects

7.6   Concluding Remarks

Numerical calculations with ESME show that the RF mismatch between the 400-MeV linac and the Booster can parasitically induce longitudinal painting in an uncontrolled fashion. Thus, it would be rather advantageous to utilize RF harmonics of non-integer ratio between machines. From ESME-ORBIT simulations with microbunches, the horizontal emittance grows by 20 % and vertical emittance by 19 % during the injection period. As Eqn. (4.31) explains, space-charge-induced electric field is proportional to the gradient of charge line density. Accordingly, the charge-density distribution from 5-microbunch injection (cf. Figure 7.3 (a)) has larger space-charge effect than the uniform distribution (cf. Figure 7.4 (a)).

We demonstrated the controlled longitudinal painting in RF-phase direction can be considered one way of intensity increase at the Booster injection energy. With a larger number of injection turns (e.g., 300 turns) over a longer injection period (e.g., a few msec), the longitudinal painting scheme can increase beam intensity more effectively. Furthermore, with a dual RF harmonic system, we are able to lower the space-charge effect with higher-intensity beams.

Furthermore, the time-structured multiturn injection with longitudinal painting scheme can also be applied to the 8-GeV Super-Conducting RF (SCRF) linac proton driver and the Main Injector. As a reference, several different injection scenarios with different RF parameters for the Main Injector are presented on the website [63].

Chapter 8

RF Stacking of Protons in the Accumulator

Thus far we have constructed three independent models of the Booster synchrotron. In this chapter we investigate the feasibility of the proposed method [64] of Radio-Frequency (RF) stacking of protons in Fermilab's accumulator. As done in the microbunch model of the Booster in Chapter 7, we utilize numerical calculations using ESME. This RF-stacking process applies various adiabatic RF gymnastics, such that we can achieve nearly emittance-dilution-free stacking [65] in the momentum acceptance of the present Accumulator. As stated in section 1.4.2, this is referred to as momentum stacking of protons in the Accumulator

8.1 Introduction

When the Run2 collider program at Fermilab is terminated around the year of 2009, the present antiproton[1] sources can become available for other Fermilab programs. One possible application is to convert the Antiproton Accumulator into a proton accumulator [64, 66], so that the beam power from the Main Injector could be greatly enhanced.

---

[1]At Fermilab, the antiproton is frequently referred to as *pbar* ($\bar{p}$) for convenience.

The Accumulator has the unique feature of a very large momentum acceptance, which allows the accumulations of several Booster batches of proton beams with small momentum spread.

8.2 Overview of the Antiproton Accumulator

The Fermilab Accumulator is an 8-GeV storage ring that is designed for the collection, cooling, and storage of antiprotons. Antiprotons are produced by impinging a 120 GeV proton beam on an nickel-alloy target. They are collected through a lithium focusing lens and the Fermilab Debuncher ring. The main purpose of the present Accumulator is to accumulate antiprotons. This is achieved by means of momentum stacking of successive pulses of antiprotons from the Debuncher for the duration of several hours, or days. Utilizing both RF and stochastic cooling systems, the RF decelerates the first injected pulse of antiprotons, starting from the injection energy of 8 GeV to the edge of the stack tail, where high-momentum particles reside. The momentum cooling system sweeps the beam accumulated by the RF and injection systems away from the edge of the stack-tail, and decelerates it towards the densely-populated core of the stack. Additional cooling systems maintain the antiprotons in the core with the desired momentum and minimize the transverse beam sizes.

Unbunched, or DC beams of antiprotons are to be extracted from the Debuncher, and transferred to the Accumulator line. The combination of a kicker system and a septum magnet in each ring transfers the DC beam in the horizontal plane. Extraction in the Debuncher occurs just before another antiproton pulse arrives from the target. Figure 8.1 illustrates the layout of the triangle-shaped Accumulator and the Debuncher rings.
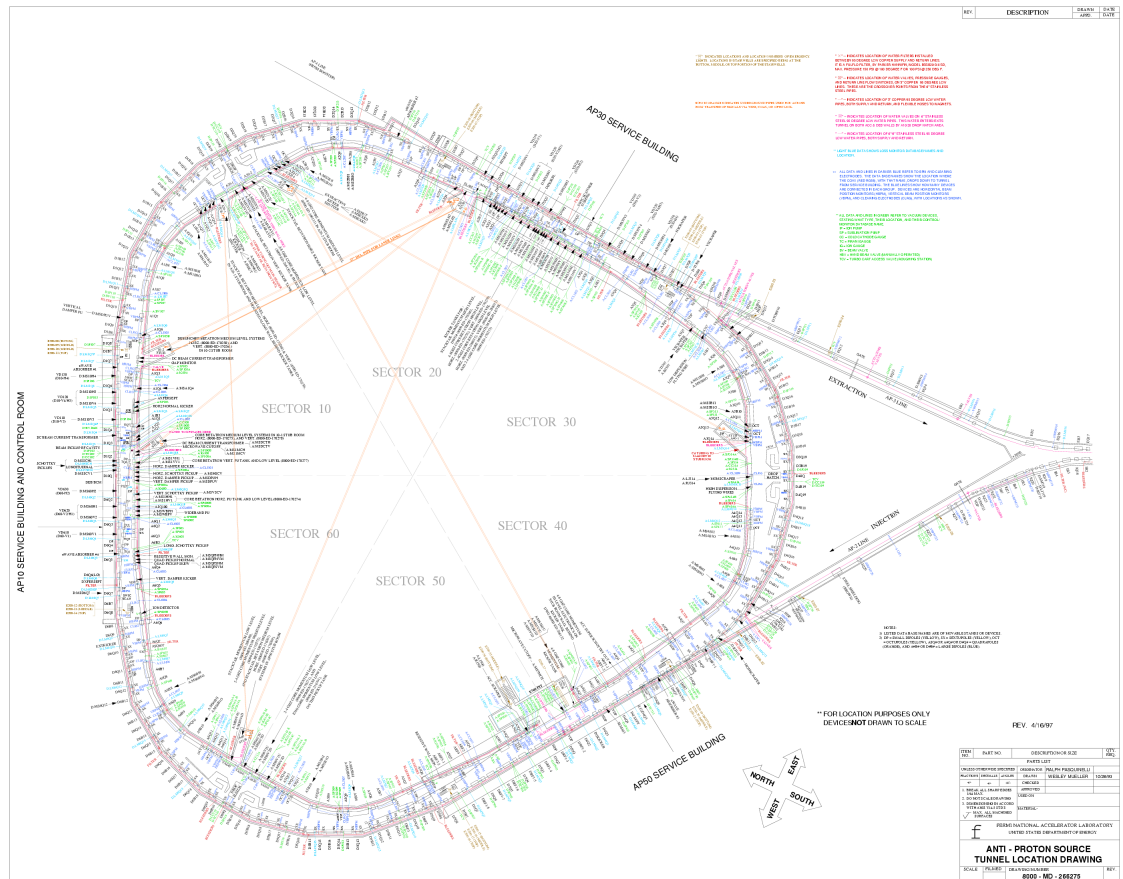
Figure 8.1: A layout of the Debuncher (inner triangle) and the Accumulator (outer triangle) at Fermilab

8.3 Machine Parameters

A comprehensive set of parameters for the Accumulator ring are tabulated in Table 8.1. One can notice that the Accumulator and the Booster are the same in circumference of 474 (m). The lattice of the Accumulator used for this study is the one at injection.

Table 8.1: Selected Accumulator Parameters for Proton Stacking

Beam Specie	H^+
Circumference ($\beta c \cdot \tau_0$)	474.1 (m)
Mean Radius	75.47 (m)
Beam Kinetic Energy	8.0 (GeV)
Total Energy	8.938 (GeV)
Design Momentum	8.889 (GeV/c)
γ_{tr} (Transition Gamma)	5.42173
E_{tr} (Transition Energy)	5.0871 (GeV)
α_c (Momentum Compaction Factor)	0.034
η (phase-slip factor)	0.023
β (normalized velocity)	0.994
γ (relativistic mass factor)	9.5263
Injected Beam Intensity	4×10^{10} (protons per bunch)
Number of Bunches	84
Injected Beam Intensity	3.4×10^{12} (protons per batch)
Number of stacked batches	$3 \sim 4$
Total Beam Intensity after stacking	$1.02 \sim 1.36 \times 10^{13}$
Injected Beam Emittance	0.1 (protons per bunch, eV-s)
Emittance after stacking	≤ 0.5 (per bunch, eV-s)
Longitudinal Bunch Profile	Elliptical
RF Frequency	53 (MHz)
Harmonic Number	84
Peak RF Voltage	250 (kV)
Synchrotron Tune	3×10^{-3}
Synchrotron Period	0.539 (msec)
Stationary Bucket Area	0.65 (eV-s)
Stationary Bucket Height	27 (MeV)
Deceleration Synchronous Phase, ϕ_s	-3 $^\circ$
Deceleration Time	30 (msec)

8.4   Proton-Stacking Procedures

The simulation uses 1,000 macroparticles for each proton pulse to inject under the influence of the longitudinal space-charge effect. The longitudinal beam profile is elliptical. Each of the RF-stacking processes consists of four stages as follows.

The 1st stage is *synchronous injection*. A batch of 84 proton bunches extracted from the Booster are synchronously injected into stationary (or standing) RF buckets of 53 MHz and 250 kV of the Accumulator. One of the captured 84 bunches is as shown in Figure 8.2. The bucket contour is drawn in red in the figure of ΔE-$\Delta\theta$ space. The dotted line drawn in the background of the figure indicates a single RF waveform of 53 MHz in units of kV.
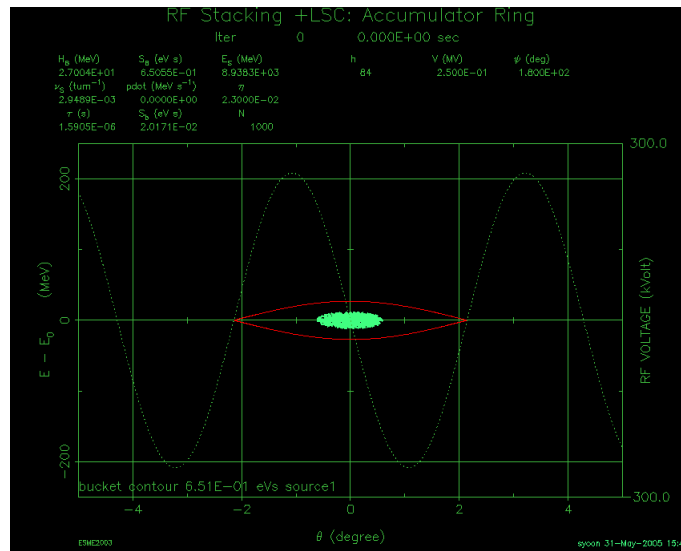
Figure 8.2: 1st pulse: synchronous injection

The 2nd stage is *adiabatic RF-bucket transformation*. When synchrotron parameters vary slowly, satisfying the *adiabatic condition* given as in Eqn. (8.1), we refer the process to a *adiabatic process* [67].

$$\alpha \equiv \frac{1}{\omega_s}\frac{\dot{\omega}_s}{\omega_s} \ll 1, \tag{8.1}$$

where α, ω_s, $\dot{\omega}_s$, and ν_s are the adiabaticity, angular synchrotron frequency, time-derivative

of angular synchrotron frequency, and synchrotron tune, respectively. The adiabaticity (α) is a dimensionless parameter. This implies that the variation of parameters of synchrotron motion is sufficiently slow, such that the longitudinal energy oscillation is negligible in the process; in other words, the fractional change in the Hamiltonian is nearly zero, or $\partial H / \partial t \approx 0$. The longitudinal emittance can therefore be preserved. For this reason, the adiabatic process is a key to emittance-dilution-free stacking. The stationary RF bucket is adiabatically transformed to a moving RF bucket by altering synchronous phase (ϕ_s) from $0°$ to $-3°$ (*Figure 8.3*). For a stationary bucket, a separatrix is symmetric around its center. For a moving bucket, however, the separatrix becomes asymmetric. This process takes about 0.1 msec.
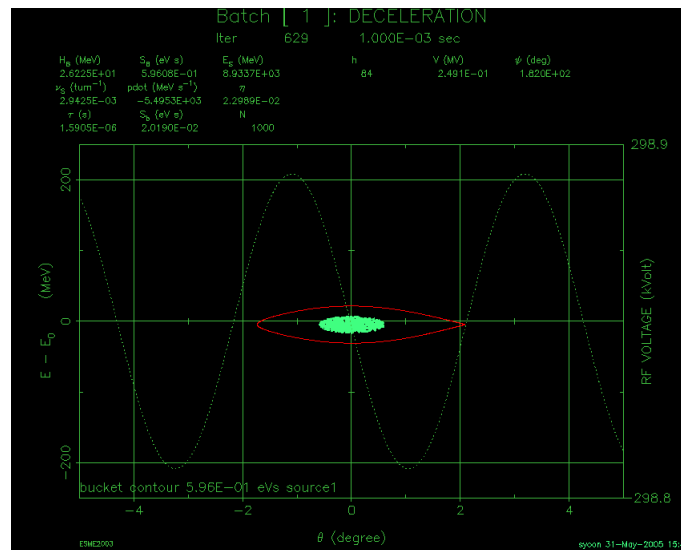
Figure 8.3: 1st pulse: adiabatic transformation

The 3rd stage is a *deceleration* process. At a synchronous phase of $-3.0°$ and RF voltage of 250 kV, the beam is adiabatically decelerated by 150 MeV. This process takes about 30 msec (*Figure 8.4*).

The last stage of stacking the first pulse is *adiabatic debunching*. Towards the end of the deceleration, while the synchronous phase adiabatically changes back to zero, the RF
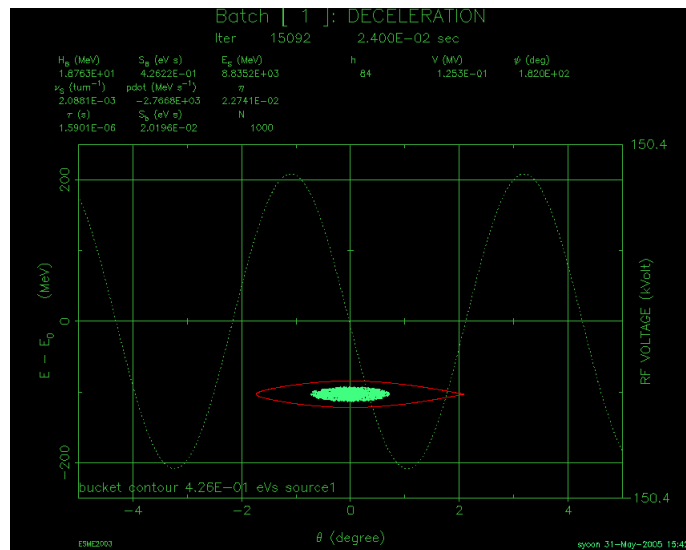
Figure 8.4: 1st pulse: deceleration

voltage is then also adiabatically decreased from 250 kV to zero. As a consequence, the beam is slowly debunched (*Figure 8.5*). The last stage takes about another 30 msec.
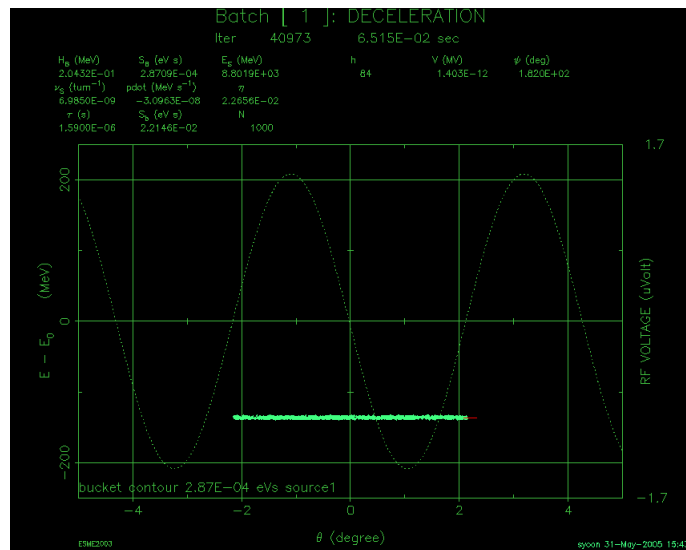

Figure 8.5: 1st pulse: debunched beam

The above multi-stage processes are repeated for the 2nd pulse with the exception that

the deceleration is now reduced to about 143 MeV. The newly injected beam pulse can be added to the 1st pulse that was already deposited. The 2nd batch should be brought as near to the 1st-injected pulse as possible without perturbing the 1st batch considerably. Through this process, the beam intensity is doubled by stacking. During the deceleration process the approaching RF bucket is likely to disturb pre-stacked unbunched beam pulses. This requires laborious attempts to optimize the deceleration of RF waveform, 8.7, and 8.8). The 2nd batch injection is similar to the first-batch injection, but smaller amount of deceleration process is carried out. (*Figures 8.6, 8.7,* and *8.8*). After deceleration and RF bucket
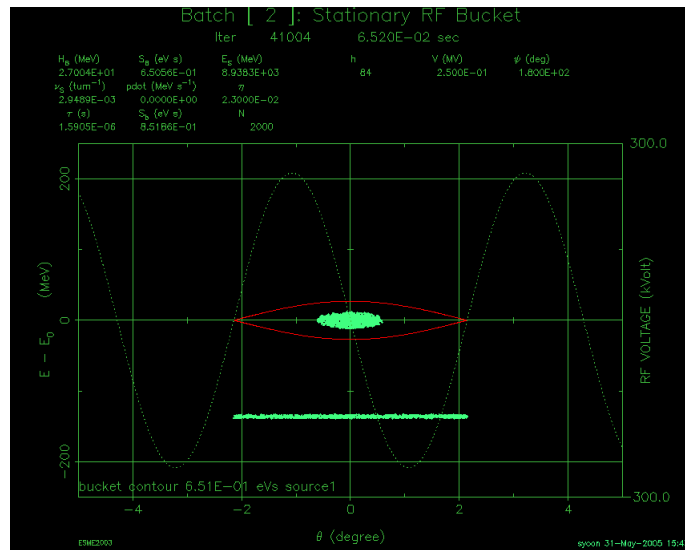
Figure 8.6: 2nd pulse: synchronous injection

transformation are complete, the 2nd beam pulse is adiabatically debunched. After the debunching, we circulate the DC beam for a while to reach the equilibrium state. The third- and the fourth-batch injections proceed in a similar fashion, but with even smaller amount of deceleration than that of 2nd batch. They are shown in Figures 8.9—8.13. After the fourth-batch stacking is completed, the 53-MHz RF system is slowly switched on with RF phase $0°$ to adiabatically recapture the beam (*Figure 8.14*). After the stacked high-intensity beam is rebunched, RF bucket is slowly transformed from a stationary RF
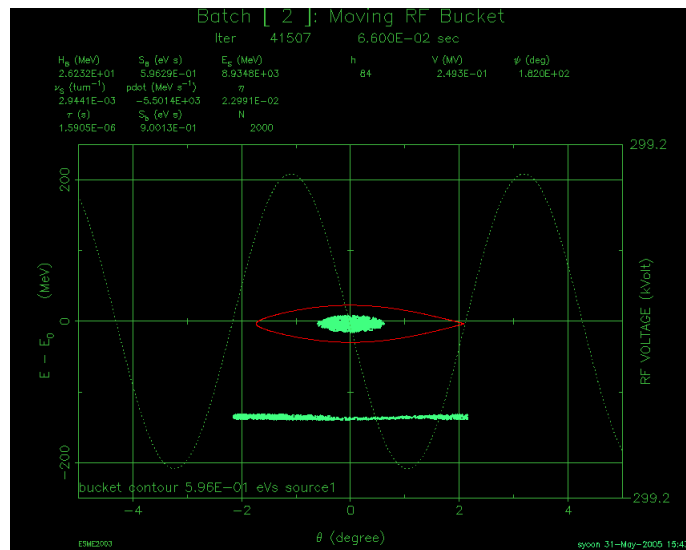
Figure 8.7: 2nd pulse: adiabatic RF-bucket transformation
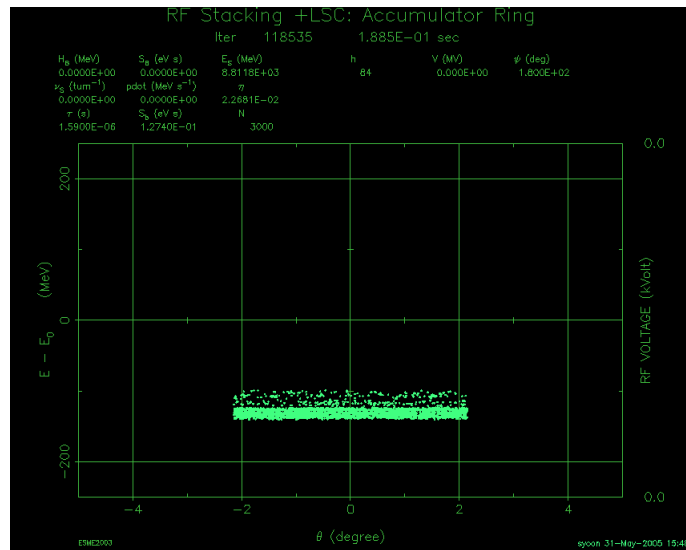
Figure 8.8: 2nd pulse: debunched

bucket back to a moving bucket. And the moving bucket starts acceleration towards the injection orbit for extraction. (*Figure 8.15* and *8.16*). This process would take about 60 msec. Once rebunched high-intensity beams reach to the injection orbit, it is extracted and transferred to the Main Injector or the Recycler.
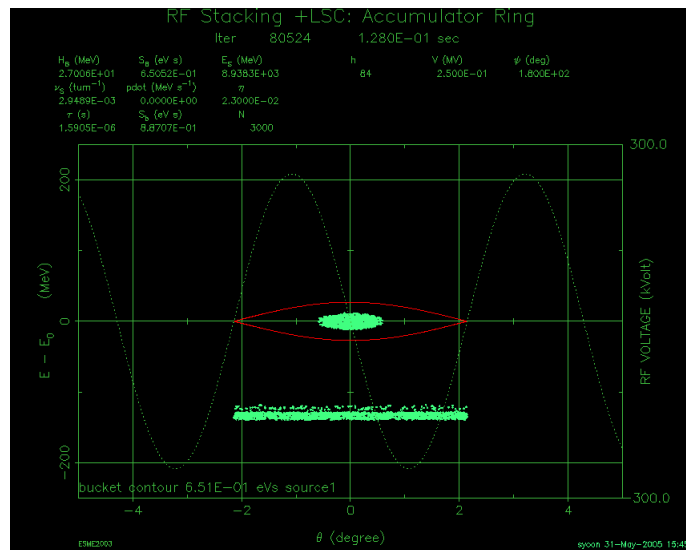
Figure 8.9: 3rd pulse: synchronous injection
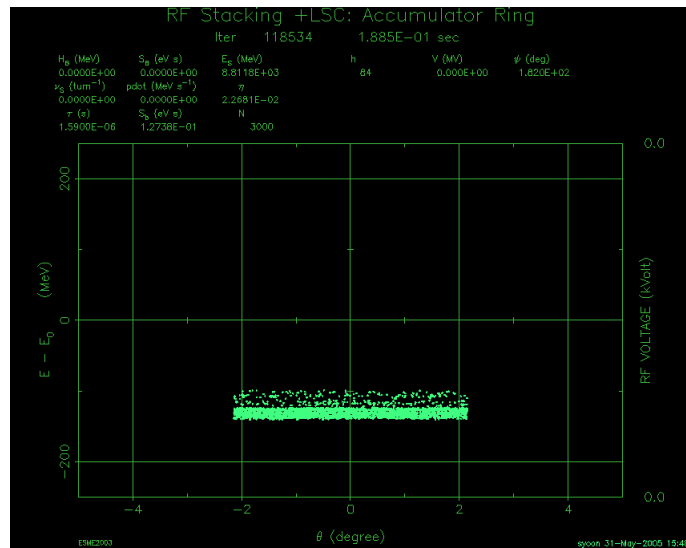
Figure 8.10: 3rd pulse: debunched

8.5   Simulation Results

In the preceding section, we have illustrated the procedure of momentum stacking of proton beams in the longitudinal phase space in Figures from 8.2 through 8.16. In addition, for visualization of the entire momentum-stacking process, an animation has also been
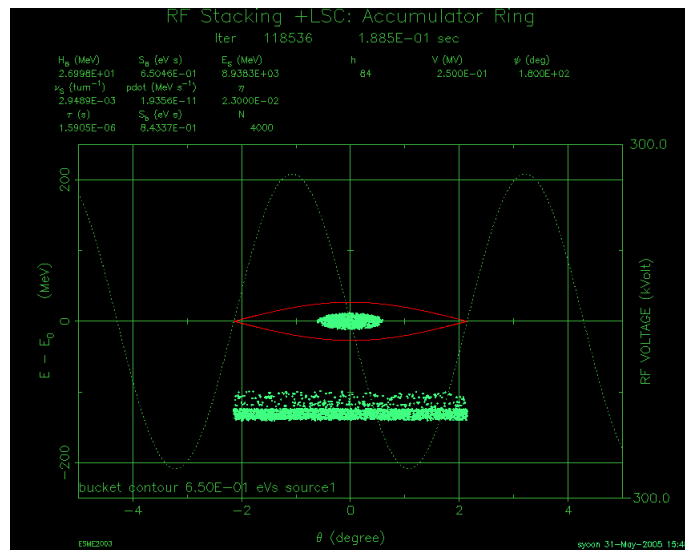
Figure 8.11: 4th pulse: synchronous injection
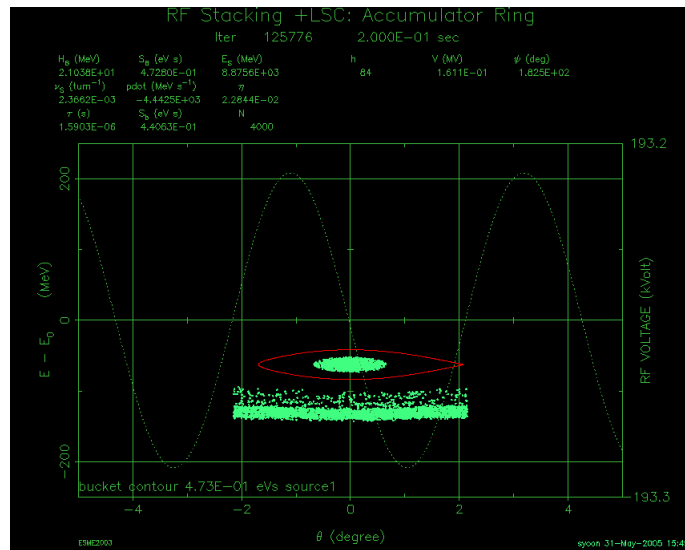
Figure 8.12: 4th pulse: deceleration

created and available on the web [69]. Figure 8.17 shows the energy-density distribution after stacking four batches is complete. There are small gaps between adjacent debunched beams. These gaps are unavoidable in order to minimize the effects of an approaching moving RF bucket on the circulating DC beams in the course of deceleration. A lot of
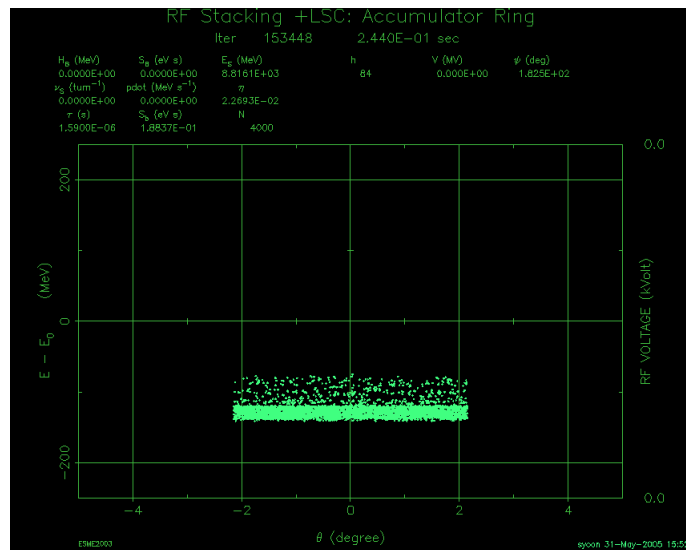
Figure 8.13: 4th pulse: debunched
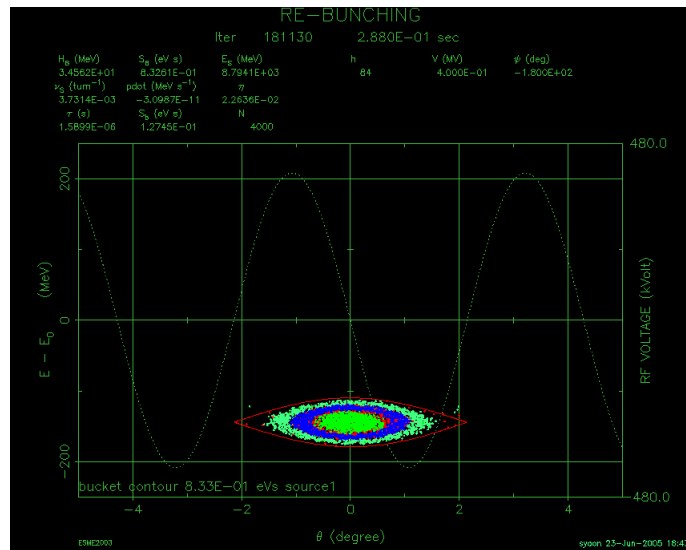
Figure 8.14: RF recapture of a stack of 4 debunched beams

effort goes into the reduction of the gaps between successive batches by optimizing numerous synchrotron and RF parameters (ϕ_s, V_{rf}, ΔE, deceleration time, recapture time, etc.) Stacked beam profile in azimuthal space is illustrated by Figure 8.18. The horizon-
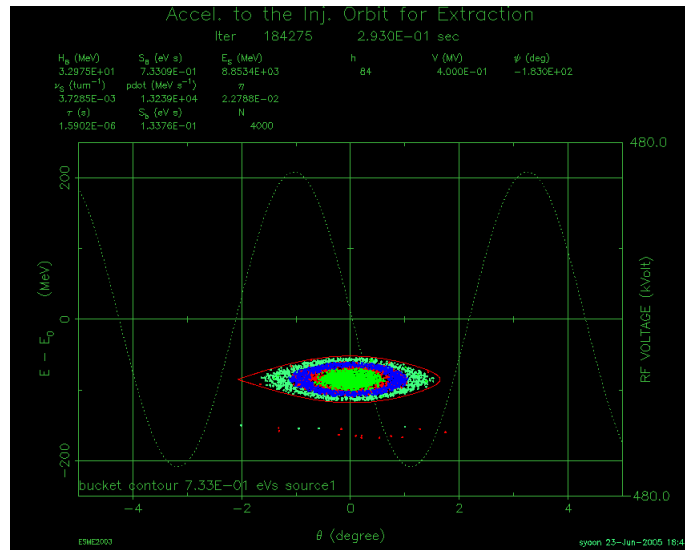
Figure 8.15: Acceleration after RF recapture
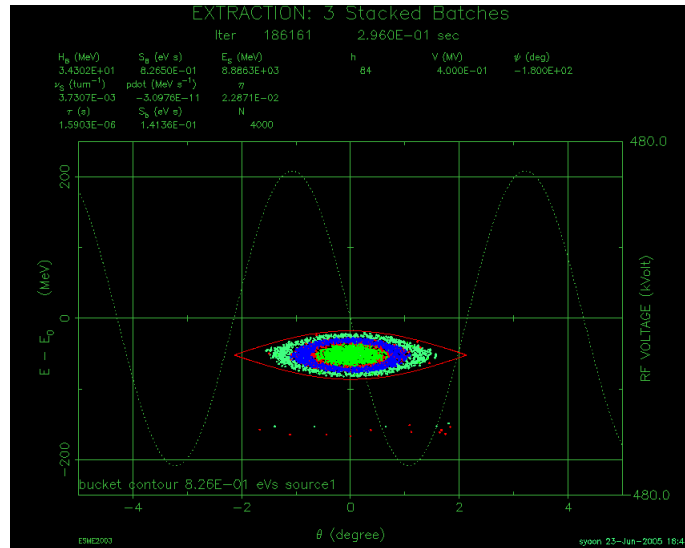
Figure 8.16: Recaptured momentum-stacked beam at injection orbit

tal axis in this plot is in units of degree with the machine circumference considered to be $360°$. A small amount of high-energy stack-tails are also formed in the case of stacking 4 batches; it is, however, much smaller when only 3 batches are stacked. As can be found in Figure 8.19, the azimuthal distribution, or charge-density distribution of stacked three
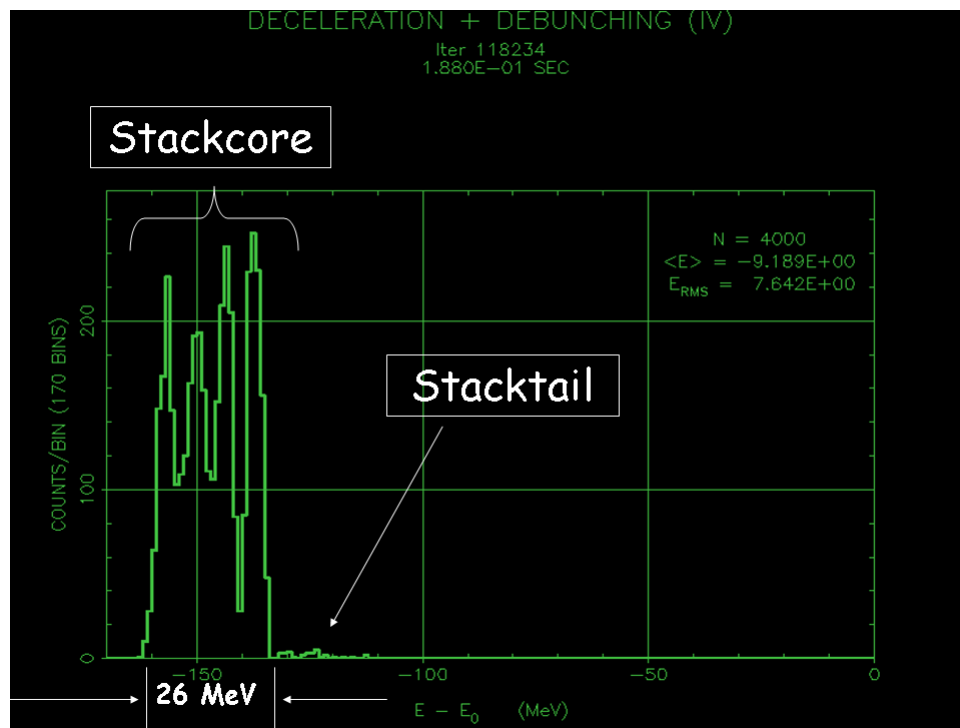
Figure 8.17: Energy-density distribution of four debunched pulses

batches is nearly uniform.

8.6 Discussion

In order to stack high-intensity beams from a few beam pulses of lower intensity we investigated the feasibility of the momentum-stacking method in the presence of the longitudinal space-charge effect. At present, Fermilab is considering the option of transferring stacked beams of high intensity from the Accumulator to the Recycler, or the Main Injector that has large momentum acceptance. One main concern of momentum-stacking is the emittance dilution. The formation of a small amount of *stack-tail* can be clearly seen in Figure 8.17. It is caused by an approaching RF bucket affecting the existing circulating
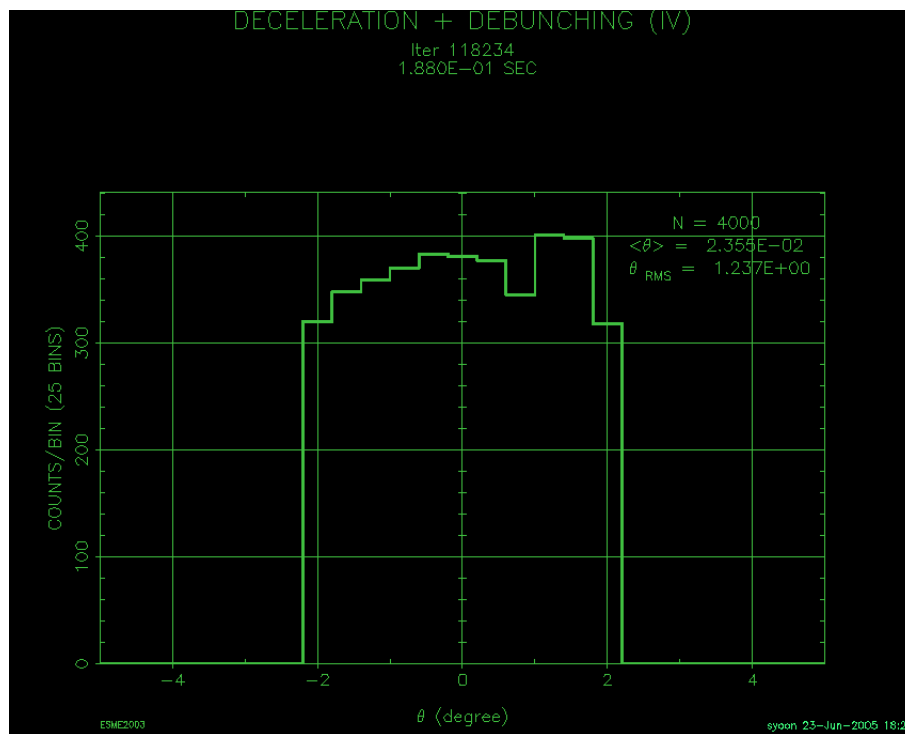
Figure 8.18: Charge-density distribution of four debunched pulses

DC beam during the 2nd, 3rd, and 4th injection process; this is usually referred to as *phase-displacement acceleration* of DC beams. This tail is much smaller when only 3 batches are stacked, since the energy gap between neighboring batches is less tight. There is a trade-off between higher longitudinal beam intensity and smaller stack-tail.

The stack-tail must be dumped before it would enter the Main Injector. One way of eliminating it is to have a momentum collimation in the beam transport line.

The emittance of the stacked beam must be within the acceptance of the Main Injector, which is measured at about 0.7 eV-s when the batch intensity is 8.7×10^{12}. The acceptance would be smaller at higher intensities. Therefore, the allowable emittance after stacking is set to be 0.5 eV-s. This requirement can be met in 3-batch stacking but is more challenging if 4 batches need to be stacked. Figures 8.20 through 8.23 show the evolutions of a few of key parameters in synchrotron beam dynamics during the entire stacking process. The
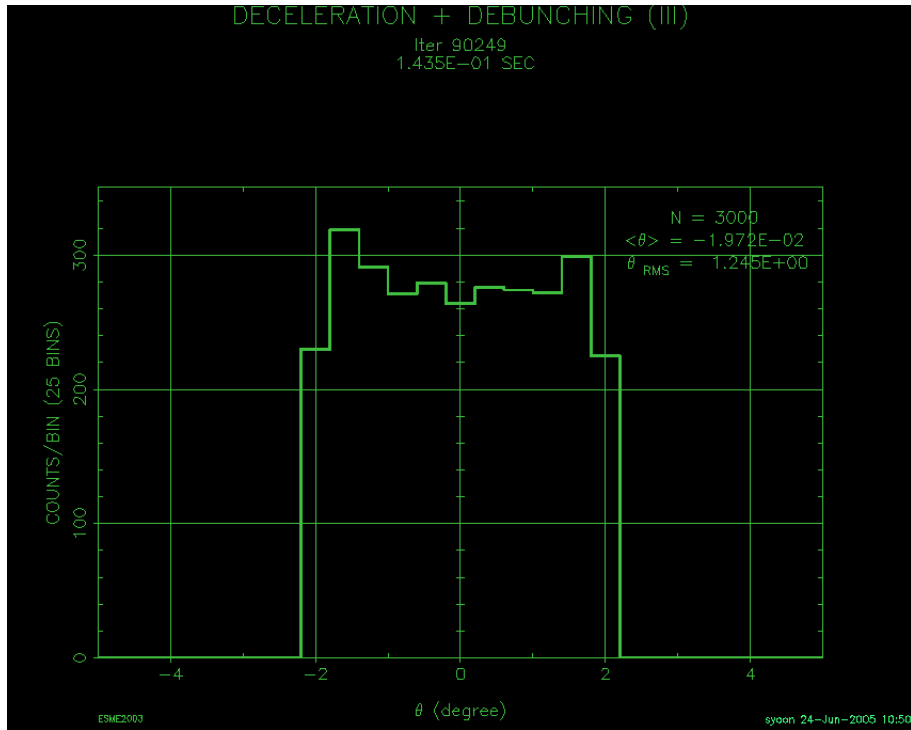
(a) Charge-density distribution
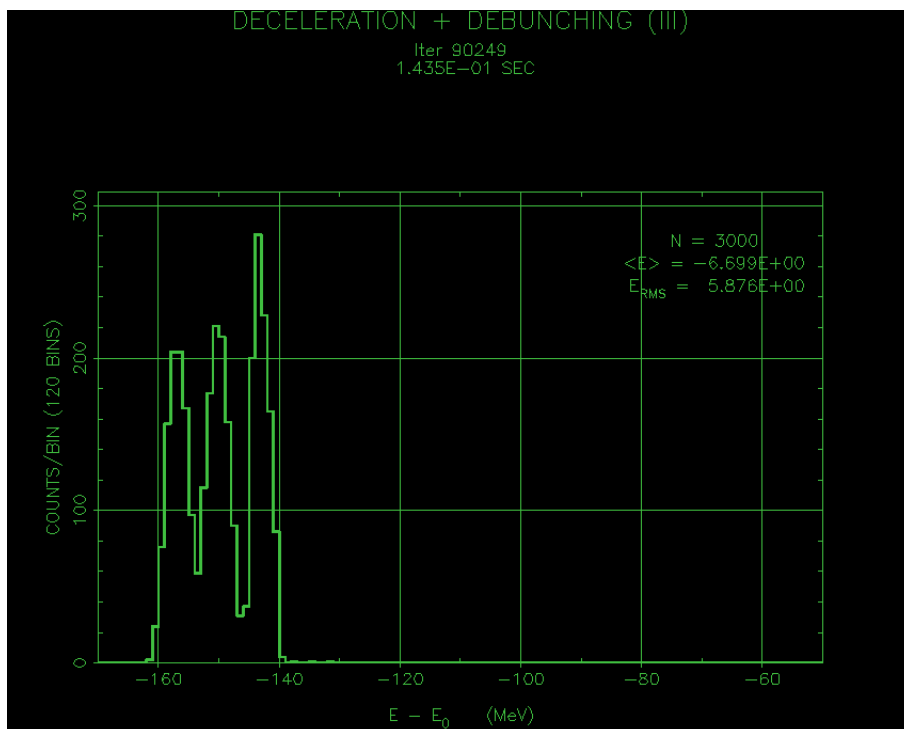
(b) Energy-density distribution

Figure 8.19: Profiles of stacked three batches

evolutions of $\langle \theta \rangle$ and $\langle E \rangle$ are shown in Figures 8.20 and 8.21. As the stacking of the beams progresses the mean energy is slightly decreased. On the other hand, the energy spread, or rms value of the energy increases as the stacking process proceeds, as shown in Figure 8.22. Lastly, the bunching factor (B_f), which was introduced in section 4.3.5, is also calculated throughout the process. The bunching factor is calculated from line density (λ), and it is one of the measures of the effect of the longitudinal space charge. As illustrated in Figure 8.23, the bunching factor is centered around 0.42.
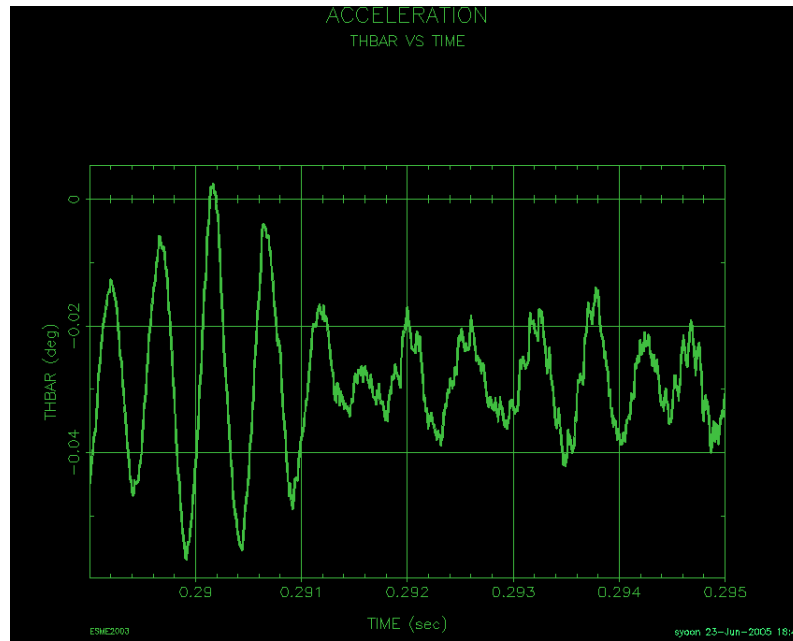
Figure 8.20: $< \theta >$ during the entire RF stacking process

The injection kicker has a mechanical shutter, which is unable to move at 15 Hz. Fortunately, the effective range of the kicker field is small and has no effect on the circulating beam when fired even without the shutter.
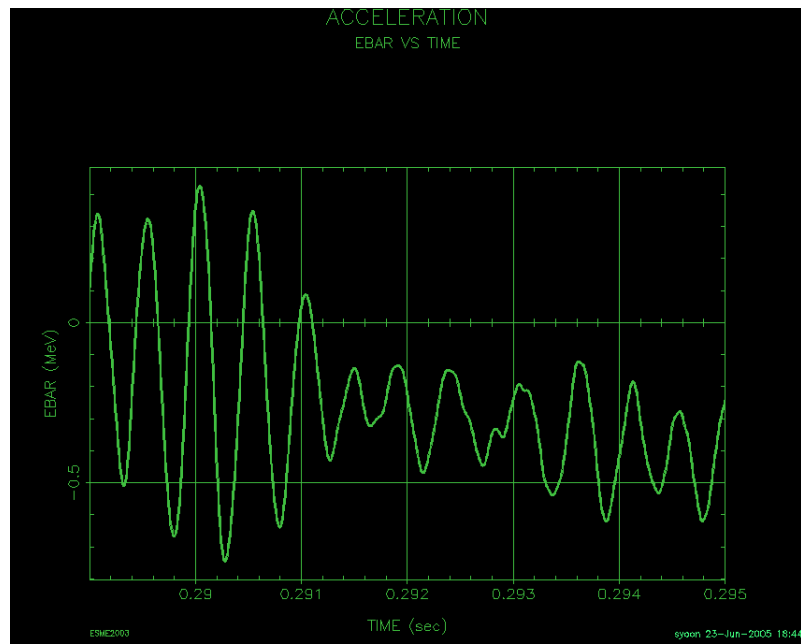
Figure 8.21: $< E >$ during the entire RF stacking process
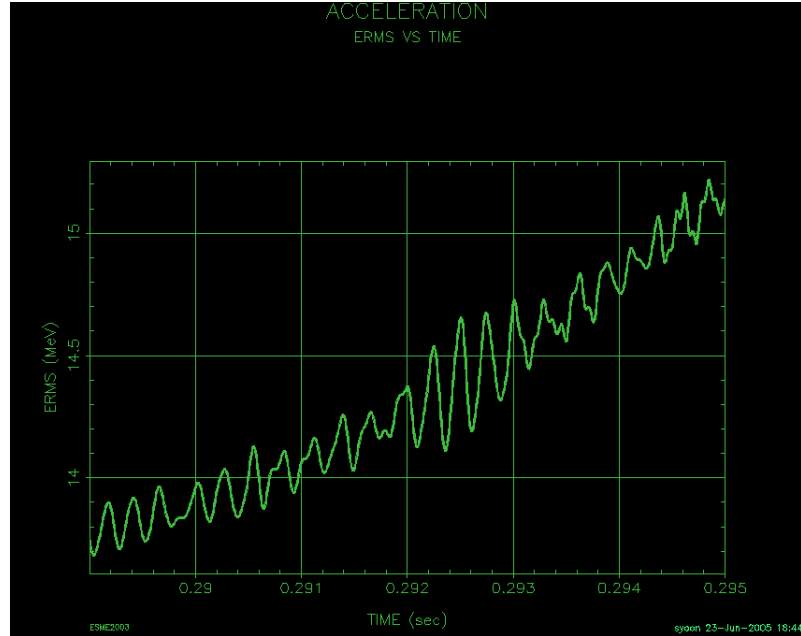
Figure 8.22: The RMS values of energy during the entire RF stacking process
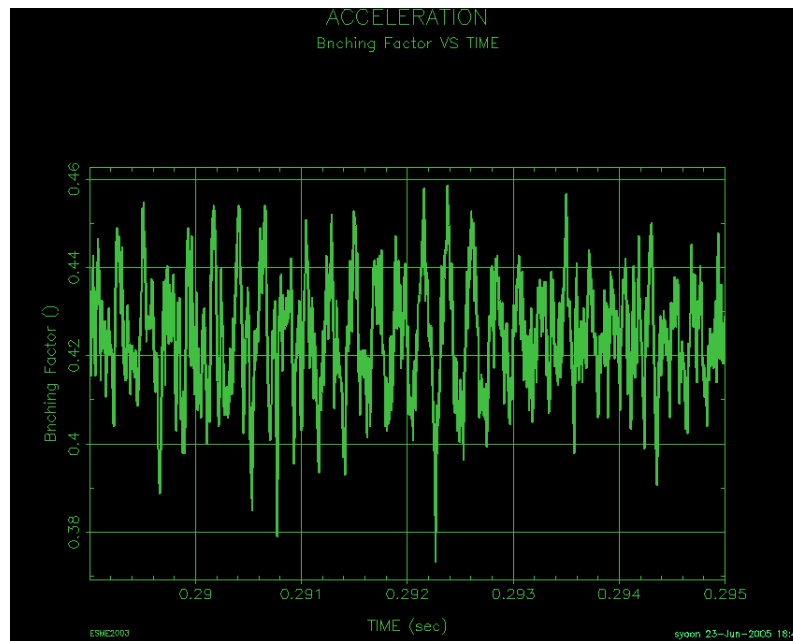
Figure 8.23: The variation of Bunching factor (B_f) during the entire RF stacking process

Bibliography

[1] M. Snir et al., *MPI–The Complete Reference, Vol. 1 and 2*, The MIT Press, 1998

[2] J. Galambos, *ORBIT–A Ring Injection Code With Space Charge*, Proceedings of PAC, New York, 1999

[3] J. A. MacLachlan, *Multiparticle Dynacmics in the E-Φ Tracking Code ESME*, Fermilab-Conf-02/102, 2002

[4] G. E. Uhlenbeck and L. S. Ornstein, Phys. Rev., **34**, 823, 1930, pp. 823—841

[5] P. Langevin, *Sur la Théorie du motion de brownien*, Comptes Rendus Acad. Sci. (Paris), **146**, 1908, pp. 530—533

[6] P. S. Yoon, W. Chou, and C. L. Bohn, *Simulations of Error-Induced Beam Degradation in Fermilab's Booster*, Proceedings of PAC, 2005

[7] C. L. Bohn, *Collective Modes and Colored Noise as Beam Halo Amplifiers*, AIP Conf. Proc.,**737**, 2004, pp. 456—461

[8] P. S. Yoon, P. H. Kasper, B. Oshinowo, and J. R. Lackey, *The Understanding and Analysis of the Booster Magnet Survey Data*, Fermilab Beams-Doc-2491, Sep. 2006

[9] B. Oshinowo and P. H. Kasper, *Beamsheet*, 2006

[10] Booster Staff, *Booster Synchrotron*, Fermilab-TM-405, 1973

[11] S. Y. Lee, *Accelerator Physics*, World Scientific, 1999, pp. 43–44

[12] Fermilab's Booster Homepage, `http://www-ad.fnal.gov/proton/booster/` `booster.html`

[13] R. Tomlin, priv. comm., 2004 $\sim$ 2006

[14] J. Lackey, priv. comm., 2004 $\sim$ 2006

[15] T. Sullivan, E. McCrory, C. Schmidt, R. Florian, B. Worthel, *Linac Rookie*, 1998

[16] S. Kopp, Fermilab-Conf-05-093-AD, *The NuMI Neutrino Beam At Fermilab*

[17] S. Childress, *NuMI/MINOS Overview*, presentation at NBI 2002

[18] M. Popovic, *A Proposed H^- Injection System for the Fermilab Booster*, Fermilab Beams-Doc, 2005

[19] A. Einstein and L. Hopf, Ann. d. Phys., **33**, 1105, 1910

[20] A. Einstein, R. H. Fürth Ed. *Investigations on the Theory of Brownian Movement*, Methuen, London, 1926, Dover Publication, New York, 1956

[21] N. G. Van Kampen, *Stochastic Processes in Physics and Chemistry*, North-Holland, 1992, pp. 39, 53, 73, 225, 232

[22] N. G. Van Kampen, *Stochastic Processes in Physics and Chemistry*, North-Holland, 1981, p. 252

[23] J. L. Doob, *The Brownian Movement and Stochastic Equation*, Annals of Mathematics, **43**, 2, 1942, pp. 351–369

[24] M. G. Wang and G. E. Uhlenbeck, *On the Theory of the Brownian Motion II*, Rev. Mod. Phys. **17**, 2—3, 1945, pp. 323—342

[25] G. I. Taylor, Proc. London Math. Soc. **22**, 196, (1920)

[26] C. L. Bohn and I. Sideris, *Fluctuations Do Matter: Large Noise Enhanced Halos in Charged Particle Beams*, Phys. Rev. Lett, **91**, 264801, 2003,

New York, 2004

[27] S. W. Haney, *Using and Programming the SUPERCODE*, UCRL-ID-118982, 1994

[28] G. E. P. Box and M. E. Muller, *A Note on the Generation of Random Normal Deviates*, Annals Math. Stat.,**29**, 2, 1958, pp. 610–611

[29] W. H. Press, B. P. Flannery, S. A. Teukolsky, *Numerical Recipes in C^{++}*, Cambridge University, Cambridge, 1998, pp. 292–293

[30] H. Grote and F. Iselin, *The MAD (Methodological Accelerator Design) Program*, CERN/SL/90-13 (AP) Rev.5 April 29, 1996

[31] L. Schachinger and R. Talman, *Manual for the Program TeaPot: Non-Interactive Fortran Version*

[32] N. Mohan, T. Undeland, and R. Robbins, *Power Electronics*, John Wiley & Sons, pp. 500–501, 1989

[33] *User's Guide: Agilent 54622A*, 2000

[34] J. Engelbert, T. Nguyen and C. Thurston, *B2 Spice A/D Version 4 User's Manual*, Beige Bag Software, Inc., 2002

[35] P. Horowitz and W. Hill, *The Art of Electronics*, Cambridge University Press, 1989

[36] S. Eidelman, et al., Physics Letters **B 592**, 1 (2004)

[37] LAM-MPI Home Page, `http://www.lam-mpi.org`

[38] D. Holmgren, priv. comm., 2006 *sim* 2007

[39] A. Singh, priv. comm., 2006 *sim* 2007

[40] D. C. Carey, 3rd*-order TRANSPORT with MAD Input*, SLAC-R-530, Oct. 1998

[41] J. Rosenzweig, Fundamentals of Beam Physics ,Oxford University Press, 2003

[42] D. A. Edwards and M. J. Syphers, *An Introduction to the Physics of High Energy Accelerators*, John Wiley & Sons, 1993

[43] H. Goldstein, *Classical Mechanics*, Addison-Wesley, 3rd ed., 2002 ,pp. 484–487

[44] E. D. Courant and H. S. Snyder, *Theory of the Alternating-Gradient Synchrotron*, Annals. Phys. **3**, 1, 1958, pp. 1–48

[45] A. Hoffman, Single beam collective phenomena—longitudinal, Theoretical Aspects of the Behaviour of Beams in Accelerators and Storage Rings, CERN 77-13, 1977

[46] B. Oshinowo, *Fermilab Coordinate Systems*, Fermilab Beams-Doc-1148, 1997

[47] B. Oshinowo, FRICS of Fermilab Survey Alignment and Geodesy (SAG) Group, priv. comm., 2006 $\sim$ 2007

[48] J. Struik, *Lectures on Classical Differential Geometry*, Dover Publication, 2nd ed., 1988

[49] T. Sager of Fermilab Survey Alignment and Geodesy (SAG) Group, priv. comm., 2006

[50] J. Kyle of Fermilab Survey Alignment and Geodesy (SAG) Group, priv. comm., 2007

[51] B. Oshinowo and J. Kyle, *Survey and Alignment of the Fermilab Booster Accelerator*,

[52] J, Walton, Fermilab, September, 1973. Logbook No. 1–3, p. 57,

[53] J. Walton, priv. comm., 2007

[54] P. Kasper, priv. comm., 2006

[55] J. Townsend, *A Modern Approach to Quantum Mechanics*, McGray-Hill, Inc., 1983, p. 47

[56] M. Yamamoto, *Longitudinal Beam Dynamics on 3-GeV PS in JAERI-KEK Joint Project*, Proceedings of EPAC 2002

[57] J. A. MacLachlan, *Injection from 8-GeV Linac Proton Driver into the Main Injector*, `Presentation at the Proton Driver Meeting`, May 2004

[58] J. Amundson, Computational Physics for Accelerators/Computing Division, private communication, 2005

[59] E. McCrory, *Measurement Data*

[60] W. Chou, priv. comm., 2005—2006

[61] P. Lucas, priv. comm., 2005

[62] D. E. Johnson, priv. comm., 2007

[63] P. Y. Yoon, `http://www-ap.fnal.gov/~syoon/SC/FMI.html`

[64] D. McGinnis, *A 2 MegaWatt Multi-Stage Proton Accumulator*, Fermilab Beams-Doc-1782, 2005

[65] J. A. MacLachlan, *RF Stacking without Emittance Dilution*, Fermilab-Conf-00/117

[66] D. McGinnis, *Beam Emittances and RF Structure at the Injection into the Main Injector for the Multi-stage Proton Accumulator*, Fermilab Beams-Doc-2138, 2006

[67] CERN rport 77-13, pp. 63

[68] M. Church and J. Marriner, *The Antiproton Sources: Design and Operation*, Annu. Rev. Nucl. Part. Sci. 1993 43:253—295

[69] P. S. Yoon, `http://www-ap.fnal.gov/~syoon/SC/Accum.html`

8.7 Usage of the New Stochastic Noise Module and the Upgraded TeaPot Module

We describe how to run ORBIT-FNAL package including the new stochastic noise module and an upgraded TeaPot module. The usage of the noise module and the upgraded version of TeaPot module is particularly oriented to the case of Fermilab Booster synchrotron. The following is an exemplary SuperCode script for Fermilab Booster ring. The script contains the nitty-gritty features of ORBIT⋆ only. The lines associated with the noise module and the TeaPot module are placed in shaded blocks.

```
// _____ Start of Script _____


//========================================================================
// [Author] Phil S. Yoon (syoon@fnal.gov)
// [Note]
//  (1) An exemplary SuperCode script for running ORBIT-FNAL
//      in parallel mode including RandomNoiseNodes.
//  (2) Lattice parameters are based upon the Booster design lattice.
//========================================================================
  Integer nRank = MPI_rank();
// === from the Booster MAD lattice v1.1 ===
  Ring::lRing         = 474.202753;//[m]
  Ring::gammaTrans    = 5.445513;
  Ring::harmonicNumber = 84;
  Real rhoD = 48.034101;//[m]
  Real rhoF = 40.847086;
// === MacroParticle Injection ===
```

```
  nMacrosPerTurn     = 30000;

  Integer InjTurns   = 11;

  nMaxMacroParticles = InjTurns * nMacrosPerTurn;

  Real QpBckt        = 6.0e10;

  nReals_Macro       = QpBckt/Real(nMaxMacroParticles);


  Real Vrf = 205.0;//[kV/T]

  Real foilRho = 409.;//[ug/cm**2]
// === File Name ===
  String subName, outF;

  runName = ``Booster'';

  subName = ``.out'';

  outF    = runName  + subName;

  OFstream fio( outF, ios::out );


/////////////////////////////////////
//   Create a Synchronous Particle
/////////////////////////////////////
  Real ESync    = 0.400;//[GeV]

  Real MSync    = 1;

  Integer Charge = 1;

  addSyncPart( MSync, Charge, ESync );

  mainHerd = addMacroHerd( nMaxMacroParticles );
/////////////////////////////
//    Create a Ring
/////////////////////////////
```

```
// a file of Twiss functions generated from MAD:

String MADTW  = ``booster_v11.tw'';

// TeaPot-like lattice:

String MADLAT = ``BST.LAT'';

const Integer nstepTPD = 1,  fringeD = 1;

const Integer nstepTPM = 4,  fringeM = 1;

const Integer nstepTPQ = 4,  fringeQ = 1;

const Integer nstepTPB = 10, fringeB = 1;

const Integer nstepTPS = 4,  fringeS = 1;

const Integer nstepTPK = 4,  fringeK = 1;

Void kick(){ }// leave the subroutine body empty.


// a new method for the Booster lattice:

buildTPlatticeI( MADTW,    MADLAT,

                 nstepTPD, fringeD,

                 nstepTPM, fringeM,

                 nstepTPQ, fringeQ,

                 nstepTPB, fringeB,

                 nstepTPS, fringeS,

                 nstepTPK, fringeK,

                 kick );

Ring::nuX = 6.7; Ring::nuY = 6.8;

if( !nRank )

cerr << ``\n\t\t\t * Finished reading TeaPot-like lattice files ... \n'';

////////////////////////////////////////////////////////////////////

//    Transverse and Longitudinal Distribution Initializer Functions

////////////////////////////////////////////////////////////////////
```

```
  betaXInj = 6.17585; alphaXInj = -0.0939789;

  MXJoho = 100.;

  Real epsX = 1.76;

  epsXLimInj = epsX * (MXJoho + 1) * 2.0;


  xTailFraction = 0.0; xTailFactor = 3.;

  addXInitializer( ``BiGaussX'', JohoXDist );


  betaYInj = 20.023; alphaYInj = -0.029;

  MYJoho = 100.;

  Real epsY = 1.76;

  epsYLimInj = epsY * (MYJoho + 1) * 2.0;


  y0Inj = 0.0; yP0Inj = 0.0;

  yTailFraction = 0.0; yTailFactor = 3.;

  addYInitializer( ``BiGaussY'', JohoYDist );


  phiMinInj = -120.0; phiMaxInj = 120.0;

  EOffset = 0.0;

  deltaEFracInj = 5.1E-4;

  addLongInitializer( ``Uniform'', UniformLongDist );
//////////////////////////
//    Add a Foil Node
//////////////////////////
  addFoil( ``Foil'', 2, -100.00, 100.00, -100.00, 100.00, foilRho );

  useFoilScattering = 0;

  if( !nRank ) cerr << ``\n\t\t\t * Default foil node added. \n'';
```

```
////////////////////////////
//      Add a RF Cavity
////////////////////////////
  Real tFactor;
  Integer nRFHarms = 1;
  RealVector volts(nRFHarms), harmNum(nRFHarms), RFPhase(nRFHarms);
  harmNum(1) = 1;
  RFPhase(1) = 0.;
  volts(1) = Vrf;
  addRFCavity(``RF(1)'',4,nRFHarms,volts,harmNum,RFPhase);
/////////////////////////////////////////////////
//   Add a Longitudinal Space-Charge Node
/////////////////////////////////////////////////
  nLongBins = 32;
  Real b_a  = 2.;
  Integer useAvg = 0;
  Integer nMacroLSCMin  = 128;
  Integer useSpaceCharge = 1;

  addFFTLSpaceCharge(``LSC(1)'',5,ZImped,b_a,useAvg,nMacroLSCMin,useSpaceCharge);
  if(!nRank) cerr << ``\n\t\t\t * added FFT LSpaceCharge node. \n'';
/////////////////////////////////////////////////
//  Add a Transverse Space-Charge Node Set
/////////////////////////////////////////////////
  Integer nxBins = 64, nyBins = 64;
  Real    eps    = 1.e-6;
  Integer nMacroTSCMin = 16;
```

```
addFFTTransSCSet(nxBins,nyBins,eps,nMacroTSCMin);

if( !nRank ) cerr << ''\n\t\t\t * added FFT Transverse SC node set. \n'';
```

```
////////////////////////////////////////
//          Add Noise Nodes
////////////////////////////////////////
```

```
Real T_0 = 2.2E-6;
```

```
Real dT  = T_0;
```

```
Real corrTime = 2.E-3;
```

```
Real Str = 5.0E-4;
```

```
Integer nsteps = 1;
```

```
addRandomNoiseNode(''> NoiseNode [1]'',139,''Noise-1.out'',''Halo-1.out'',
                   dT,corrTime,Str,nsteps);
if( !nRank ) cerr << ''\n\t\t\t * added RandomNoiseNode [1]. \n\n'';
```

```
addRandomNoiseNode(''> NoiseNode [2]'',2279,''Noise-2.out'',''Halo-2.out'',
                   dT,corrTime,Str,nsteps);
if( !nRank ) cerr << ''\n\t\t\t * added RandomNoiseNode [2]. \n\n'';
```

```
addRandomNoiseNode(''> NoiseNode [3]'',4379,''Noise-3.out'',''Halo-3.out'',
                   dT, corrTime,Str,nsteps);
if( !nRank ) cerr << ''\n\t\t\t * added RandomNoiseNode [3]. \n\n'';
```

```
addRandomNoiseNode(''> NoiseNode [4]'',6319,''Noise-4.out'',''Halo-4.out'',
                   dT,corrTime,Str,nsteps);
```

```
  if( !nRank ) cerr << ''\n\t\t\t * added RandomNoiseNode [4]. \n\n'';
```

```
//////////////////////////////////////
//     Add Moment and StatLat Nodes
//////////////////////////////////////
  addMomentNode(''MomentNode(0)'', 7, 2, ''Moments.out'');
  activateMomentNode(1);
  addStatLatNode(''StatLatNode(0)'', 8, ''StatLats.out'');
  activateStatLatNode(1);
//////////////////////////
//   Overall Ring Info
//////////////////////////
  showStart(fio);
  showFoil(fio);
//////////////////////////
//     Tick off the Timer
//////////////////////////
  Real et; timerOn();
  Real time_start, time_stop, time_total;
  time_start = MPI_Wtime0();
/////////////////////
//    Tracking
/////////////////////
  doTurn(1000);
//////////////////////////
//  Streaming Information
//////////////////////////
  OFstream outTP( ''showTP.out'',  ios::out );
```

```
    showTurnInfo(fio); showTurnInfo(cerr);

    showTP(outTP);

    OFstream outN( ''showNoise.out'', ios::out );

    showNoise(outN);

    deactivateMomentNodes();

    deactivateStatLatNodes();

    fio.close();

    quit
// _____ End of Script _____
```

By supplying three characteristic nois parameters to the random-noise adders, desired stochastic noise can be generated. To generate stochastic noise with a different rms value from that of the Booster noise, it might be necessary to tune up the strength parameter. The above set of parameters are selected for the Booster power system only.

Two noise-related output files (Noise.out and Halo.out) are generated from an ORBIT run including the Noise module and the TeaPot module. The format of the *Noise.out* files (Noise-1.out, Noise-2.out, Noise-3.out and Noise-4.out) is two columns delimited by white space. The first column is for tracking turn number and the second is for stochastic noise at each turn. The format of the *Halo.out* files (Halo-1.out, Halo-2.out, Halo-3.out and Halo-4.out) is one data set per line. Each line contains the values for (1) number of turns, (2) accumulated azimuthal position (m), (3) Halo Amplitude I ($A_{H,\,1}$) (mm), and (4) Halo Amplitude II ($A_{H,\,2}$) (mm).

$$
\begin{cases}
\mathcal{A}_{H,\,1} & = \left.\sqrt{x^2+y^2}\,\right|_{Max} \\
\mathcal{A}_{H,\,2} & = \left.\sqrt{(x/\sqrt{\beta_x})^2 + (\sqrt{\beta_x}\cdot x')^2 + (y/\sqrt{\beta_y})^2 + (\sqrt{\beta_y}\cdot y')^2}\,\right|_{Max},
\end{cases}
$$

where β_x and β_y are beta functions.

The next is a script for PBS (Portable Batch System)-LAM (Local Area Multicomputer) job submission. Before using the PBS-LAM script, both PBS scheduler (e.g., Maui, or Torque) and libraries of Local Area Multicomputer (e.g., LAM or OpenMPI) should be available on the cluster. Depending on the local cluster configuration, the contents of the PBS-LAM script are subject to modification.

```
───────────────────────────── Start of Script ─────────────────────────────
#! /bin/bash -x
#========================================================
# [Author] Phil S. Yoon (syoon@fnal.gov)
#
# An example of script for submitting a PBS-LAM run
#========================================================
#PBS -S /bin/bash
#PBS -j oe
#PBS -m n
#PBS -M [your@email.address]
#PBS -l nodes=[requested number of nodes], walltime=[hh:mm:ss]
printf "\n Starting on `hostname` at `date` \n"


#====================================================
EXECUTION_DIR=/where/your/working/directory/is
APP=/where/your/executable/is
ARGS=/where/your/SuperCode/is
#====================================================
if [ -n "${PBS_NODEFILE}" ]; then
 if [ -f ${PBS_NODEFILE} ]; then
    # print the nodenames.
```

```
  # cat ${PBS_NODEFILE}

  set -- `wc -l ${PBS_NODEFILE}`

  NP=$1

 fi

fi

cd ${EXECUTION_DIR}

cat << EOF

  EXECUTION_DIR: ${EXECUTION_DIR}

  PBS_NODEFILE:  ${PBS_NODEFILE}

  PBS_O_WORKDIR: ${PBS_O_WORKDIR}

EOF

cat ${PBS_NODEFILE} > ${PBS_O_WORKDIR}/nodefile.$$

lamboot ${PBS_O_WORKDIR}/nodefile.$$

/path/name/to/mpirun N $APP $ARGS

lamhalt

# Print the End Time

printf "\n Ended at `date`"

exit 0
```

———————————————————— End of Script ————————————